



THÈSE

En vue de l'obtention du DOCTORAT DE L'UNIVERSITÉ DE TOULOUSE

Délivré par l'Université Toulouse 3 - Paul Sabatier

Présentée et soutenue par
BAPTISTE AMOUROUX

Le 27 juin 2019

**Nanoparticules upconverting: vers la microscopie en super-
résolution**

Ecole doctorale : **SDM - SCIENCES DE LA MATIERE - Toulouse**

Spécialité : **Chimie Macromoléculaire et Supramoléculaire**

Unité de recherche :

**IMRCP - Laboratoire des Interactions Moléculaires et Réactivité Chimique et
Photochimique**

Thèse dirigée par

Christophe COUDRET et Fabienne GAUFFRE

Jury

M. Rémi METIVIER, Rapporteur

Mme Fabienne TESTARD, Rapporteuse

M. Thierry GACOIN, Examineur

M. Nicolas MEZAILLES, Examineur

M. Christophe COUDRET, Directeur de thèse

Mme Fabienne GAUFFRE-GUIARDEL, Co-directrice de thèse

Acknowledgements

En premier lieu je tiens à exprimer ma gratitude à mes précédents encadrants de stage (M1 et M2) Barbara Lonetti et Jean-Daniel Marty, sans qui toute cette aventure n'aurait pu démarrer. Vous avez su me donner goût à la recherche au moment où j'aurais pu m'égarer sur les bancs de la fac, et je vous en serai éternellement reconnaissant.

On m'a souvent chambré sur le temps passé dans votre labo mais c'était aussi en grande partie à cause de Jean-Daniel. En effet, je ne pouvais pas quitter les lieux en voyant Castres faire aussi bonne figure. Désormais je peux enfin partir la tête haute, le bouclier de Brennus revenant dans la ville rose.

Je tiens à remercier Monique Mauzac et Christophe Mingotaud, les directeurs successifs du laboratoire des Interactions Moléculaires, Réactivité Chimique et Photochimique (IMRCP) où j'ai réalisé ce doctorat. Je remercie en particulier Christophe Mingotaud en qui j'ai enfin trouvé un aussi grand gourmand que moi, et qui m'aura épaté par son flair pour détecter le moindre gâteau mais aussi par sa capacité à lire les corrélogrammes comme personne.

Ensuite, je veux adresser mes plus vifs remerciements à l'ensemble des personnes qui m'ont fait l'honneur de juger ce travail, de lire ce manuscrit malgré sa longueur, et de supporter la chaleur en ce jour de canicule toulousaine. Chacun avec vos spécialités respectives, vous avez su conduire une discussion riche et exaltante, en faisant un moment d'échange scientifique riche et plein de bienveillance. Mes deux rapporteurs aux domaines d'expertise totalement distincts, Fabienne Testard pour la synthèse de nano-objets et la formation de nanohybride, et Rémi Métivier pour la photophysique et la photochimie, ont permis de faire ressortir les différents points clés de ce travail. Cette discussion a pu être complétée par l'expertise de mes deux examinateurs Thierry Gacoïn et Nicolas Mézailles qui ont amené des précisions sur les différents domaines de chimie explorés. Je tiens à souligner en particulier le rôle de Nicolas Mézailles, président de jury hors pair, pour avoir permis d'amener des détails fins sur la caractérisation chimique des différents systèmes étudiés.

Je tiens à exprimer ma plus profonde gratitude à mes directeurs de thèse Mme Fabienne Goufre, et M. Christophe Coudret pour avoir assuré la direction scientifique de ce travail de recherche, pour la confiance qu'ils m'ont accordée et leur soutien déterminant tout au long de ces trois années.

Il aura été difficile pour toi Fabienne de trouver ta place entre Christophe et moi, mais ton rôle a été très important pour moi, tu as su nous garder les pieds sur terre et nous a permis de maintenir le cap.

Quant à toi Christophe, tu as été non seulement un encadrant, un collègue, mais presque un deuxième parent pendant ces 3 ans (une deuxième maman diront certains). On aura eu plusieurs surnoms (chats noirs, Tic&Tac, etc...) et tout le monde se demande maintenant à qui tu vas bien pouvoir parler. Tu m'as poussé à naviguer sur différents domaines en allant toujours au fond des choses, pour comprendre comment cela fonctionne et refuser le « taken for granted ». Cela a été très formateur pour moi et je t'en remercie, ainsi que pour tout le temps que tu as investi pour moi. Tu peux maintenant souffler un peu et ne plus te faire "engueuler" car tu rentres trop tard à la maison le soir à cause de moi.

Je commencerai ensuite par les IMRCP où j'ai passé la plus grande partie de ces 3 ans, et j'exprime ma reconnaissance à l'ensemble de l'équipe IDEAS : Patricia, Florence B.-M., Diana, Nancy, Véronique, Jean-Claude, Juliette, Charles-Louis, Laure, Fanny, ... J'ai beaucoup apprécié votre gentillesse et la bonne humeur qui régnait au sein de l'équipe, cela a été un plaisir de travailler avec vous.

Je voudrais remercier en particulier Clément, notre Ass Prof national, qui m'a énormément aidé durant ses 3 années. Grâce à toi j'ai aussi pu enrichir mon vocabulaire que ce soit en français lors de nos « joutes verbales » qui avaient le don d'amuser voire d'exaspérer Christophe Coudret, ou en anglais (je n'ose plus parler devant tes enfants avec mon accent). On aura aussi bien déliré à faire de belles images (inkscape, blender), mais tu as hélas pris trop d'avance sur moi pour la 3D, je suis un peu jaloux ! Tu avoueras toutefois que tu avais recours à des moyens déloyaux pour prendre de l'avance, comme m'amener faire un foot et me voir repartir le nez cassé.

Je ne pouvais pas ne pas citer Charles-Louis qui aura vu chaque appareil tomber en panne en croisant mon regard. Il aura eu quelques frayeurs supplémentaires quand il vit un laser se rapprocher de ses appareils et se retrouver entre les mains de "la grande menace".

En parlant de frayer, comment ne pas évoquer Stéphane notre responsable sécurité qui aura vu pousser des cheveux blancs en nous voyant faire des manips toujours plus insolites les unes que les autres, amener des lasers sous des hôtes, chauffer à 300°C, voir débarquer des réacteurs micro-onde, etc ... On aura quand même aussi beaucoup rigolé, en particulier en dehors du labo dans les soirées-jeux que tu organisais.

Je dois aussi beaucoup à Pascale et Anne-Françoise pour leur aide sur la caractérisation de polymères.

Et je n'aurais pas pu ne pas citer la "dream team" de P3R (Mathias, Simon, Olivier, Stéphane) avec qui j'ai eu la chance de collaborer, et j'espère retravailler un jour avec vous. Parmi vous je tiens particulièrement à remercier votre ancien doctorant, Marvin, qui aura été un ami fidèle au cours de ces 3 années pour affronter les différents imprévus du quotidien, préparer les conseils de labo, ou partager un verre en terrasse. Hélas depuis qu'il est devenu un marathonien, je ne peux plus le suivre pour courir avec lui.

Enfin, je remercie les membres de MAPES et SMODD, en particulier Guillaume B. avec qui j'aurais pu partager certaines soirées dans les nombreux bars de Toulouse.

Pour finir, je tiens à remercier 3 membres indispensables des IMRCP :

-Lucie pour son sa bonne humeur et sa folie communicative, toujours à l'écoute des commandes les plus loufoques à n'importe quelle heure.

-Sandrine et Céline, nos gestionnaires, pour leur patience, en particulier avec les 2 chats noirs du labo.

Je tiens à remercier les différents doctorants, post-docs et ingénieurs avec lesquels j'ai eu l'occasion d'interagir aux IMRCP : Ugo, Jean-Noël, Marie, Florian, Jordi, Baptiste M., Aurélie, Cécile, Lucie, Lulu et P'ti Lu, Alix, Claire, Pépé, Delphine, Magali, Paty, Marion M. et "la p'tite Marion".

Je souhaite bon courage à ceux qui deviendront à leur tour docteurs d'ici quelques mois, voire quelques années : Aurélie, Vivien, Aline, Marjorie, Maxime, Camille C., Sara, Ranime, Hai Yen, Barbara et Clémence. Aurélie, la "vieux" du labo, n'aies pas peur, ta rédaction ne se fera pas au dernier moment, ça va bien se passer, pense plutôt aux fruits de la sangria que tu pourras déguster après ta soutenance.

For our Chineses, I will only say "Xiexie" : Fang, Mingxi, Zhiqin, Zhihua.

Je remercie aussi les différents stagiaires que j'ai pu côtoyer, en particulier ceux qui ont qui ont du « subir » le rythme intensif que je leur imposé, dans la bonne humeur, allant jusqu'à partager des

pizza au labo ou prévoir un "budget chocobons" : Kevin, Charlène, Guillaume E, Julie B., Anaïs R., Claire P., Carla, Dmytro, Samy, Tom, Tiphaine, Baptiste, Ivita, Izabela, Gael, Jordan, ...

Je voue aussi toute ma gratitude à Anaïs C. qui fut ma voisine de bureau pendant 3 ans et qui a réussi à me supporter, même lorsque j'utilisais son poulet pendant ses siestes. Je te souhaite une bonne continuation, et pourquoi pas se retrouver à nouveau voisins de bureau dans quelques années.

Pour finir je garde quelques mots pour Qilin et Nadiia, les derniers utilisateurs d'UCNPs à qui j'ai transmis le flambeau. En particulier à Nadiia qui a récupéré ce fardeau, arrivé inopinément dans le monde des plastiques.

J'ai eu la chance de pouvoir partager de nombreux moments conviviaux avec vous (pique-nique, repas, soirées, foot, footing ...) bien que vous ayez eu souvent à faire avec mon fameux "(quart) d'heure toulousain", en particulier les jours de "grosse manip". J'espère que l'on se reverra.

Je voudrais aussi rendre hommage aux différents collaborateurs qui sont intervenus dans ce projet ANR :

-les membres du LASIR Michel Sliwa, Cyril Ruckebush et Aude Bouchet : on aura beaucoup fait la fête ensemble dans les différents congrès où nous nous sommes retrouvés, et le travail avec vous aura été tout aussi agréable. Je regrette juste de partir avant la fin de l'ANR et de ne pas pouvoir voir le résultat final de vos manip. J'espère qu'on restera en contact pour la suite. Merci en particulier à Michel pour tes conseils et ton aide pour préparer mon après-thèse.

-les membres d'Anton Paar France, Anthony Martinet et Olivier Leroux : la collaboration aura été intéressante scientifiquement et humainement même si elle a dû être interrompue par la maison-mère avant la fin du projet. J'ai apprécié les échanges avec vous. Notez bien que pour une fois j'aurais été aussi chic qu'Olivier, le jour de ma soutenance.

-les membres de Cordouan Technologies Boris Pedrono et David Jacob : même si nous n'avons pas pu aller au bout de ce que nous voulions faire, les échanges ont été enrichissant pour vous comme pour moi. Je suis impatient de voir le Vasco Kin® dans le four micro-onde.

Ma thèse étant en codirection entre les IMRCP à Toulouse et l'Institut des Sciences Chimiques de Rennes (ISCR), j'ai eu l'occasion de partager 6 mois très agréables dans l'équipe ICMV devenue COrint.

Je tiens à remercier Jean-Luc et Hurye pour leurs conseils lors de nos réunions et pour m'avoir vu m'initier à la chimie organique dans l'eau. Merci Jean-Luc, j'ai fait ma 1^{ère} colonne avec toi, et je pense que c'est resté un moment mémorable pendant un certain temps.

Je voulais remercier Manu, la technicienne de choc, qui a pu me donner des astuces pratiques en synthèse et que j'ai fait beaucoup rire en compagnie de Solène qui elle était déçu de voir un étudiant de Fabienne ne s'appelant pas Maxime.

Merci à Ludo et Patrick avec qui j'ai partagé de bons moments à parler de science, de nourriture et de bon vin, ou à partager des jeux de sociétés avec Antoine pendant nos repas de midi. Merci aussi à Soizic pour ta gentillesse et ta bienveillance, ainsi que tes remarques pertinentes lors de nos réunions avec Fabienne.

Je ne pourrais jamais remercier assez Gisèle la gestionnaire, qui a dû jongler entre mes missions et mon don pour les "complications administratives".

Pour finir, les non permanents que j'ai pu rencontrer:

-la légion ivoirienne qui a tant bien que mal essayé de m'apprendre leur dialecte mais hélas j'ai tout oublié (Anna, Camille Christelle),

-Nicolas qui partait avec à peu près le même handicap que moi en chimie orga,

-Karl notre stagiaire allemand à qui nous avons inculqué de bonnes bases en français comme la chocolatine en territoire breton,

-Clément (COrint), Mathieu et Maxence (MACSe) qui m'ont bien fait rire à Rennes ou lorsque nous nous sommes vus en congrès.

-Le meilleur pour la fin, Flavien, assez fou pour venir du Japon pour ma soutenance : on a partagé de bons moments au labo et en dehors, bien que Fabienne s'inquiète d'avoir à payer pour nous une fortune en psy à force de ne pas nous voir nous éloigner de la paillasse. Tu as toujours gardé en tête l'idée de collaborer tous les deux sur un sujet commun, et j'espère que cela sera réalisable dans les années futures.

I would like also to thank people from BAM that I visited for 2 months in Berlin. At first I would like to thank Ute Resch-Genger for her kind help to write the proposal for my DAAD grant. Ute did everything to let me work in ideal conditions. I would like to thank also Christian Würth for his help in the lab for handling measurements and treating datas.

Eventually I thank PhD students and postdoc from Ute Resch-genger's group :

-Nithiya and Lorena who helped me a lot during my first days in Berlin ;

-my office's mates Sebastian and Elina for our funny and fruitfull discussions in our office, especially Elina who helped me to find glassware in the lab ;

-Bettina and Melissa for their kind help for the handling of photophysical measurements;

-the two Florian, "kings" of the AFM coupled-confocal microscope ;

-Cui, Oleksandr and all the others biophoton's with whom I could share lunch, or other activities such as climbing

Eventually I was happy to meet Karl David and highly enthusiast to collaborate with you ,but we did not got enough time. I hope we will work together in the future.

Je tiens aussi à remercier les différentes plateformes techniques de Toulouse, sans qui tout ce travail n'aurait pu se réaliser :

-La plateforme de microscopie électronique du CMEAB : Bruno Payré, Dominique Goudenèche, et en particulier Isabelle Fourquaux qui se désespérait de me voir arriver un jour à l'heure et que j'embêtais souvent au milieu de ses repas.

-Nicolas Ratel (CEMES) qui m'a fait découvrir les joies de la cristallographie aux rayons X, et qui aura pris le temps d'expliquer de traiter et même d'analyser les diffractogrammes de mes poudres qui collaient désespérément à la spatule.

-Jean-Michel, notre électronicien toujours disponible et à l'écoute des nos demandes toutes plus loufoques les unes que les autres, allant jusqu'à nous voir bricoler et peindre un ventilateur pour en faire un chopper...

-Le service de RMN (Marc Vedrenne, Pierre Lavedan, Stéphane Massou, Claude Andreu, Caroline Toppan) qui aura eu affaire à des manip pathologiques, sur des nanoparticules inorganiques ou des polymères, ou le mélange des deux. En particulier Caroline, qui a entendu des conversations toutes plus improbables les unes que les autres, comme la fois où on avait tatoué des particules sur une peau de porc...

-Nos informaticiens Edouard et Pascal, qu'on a beaucoup sollicité au cours de ces 3 ans ;

-Corinne Routaboul pour les spectres infrarouges, dont la collection impressionnante de thé en ferait pâlir plus d'un

-Le service de masse de Catherine Claparols.

Pour finir je tiens à remercier nos voisins du SPCMIB qui nous ont souvent dépanné à la dernière minute pour un solvant, un produit ou de l'azote liquide : en particulier Nadine que nous avons bien fait rire, et Thomas pour qui la soutenance se rapproche.

Je ne pouvais pas finir ces quelques lignes sans évoquer Gaëtan, mon binôme ou plutôt mon ami rescapé de master, assez fou pour faire de la RMN du matin au soir et faire des reprises de volée avec des tubes à essai dans le labo. On aura finalement bien mené notre barque, contre vents et marées, bien que peu de personnes auraient mises sur nous il y a quelques années. Bon courage à toi en Alsace, pense à moi si tu as besoin d'un crash test, je serai toujours disponible pour voir tomber en panne un appareil.

Enfin je tiens à remercier ma famille qui m'a apporté son soutien sans faille. En particulier ma maman qui m'aura permis de prévenir les risques d'hypoglycémie de notre directeur Christophe Mingotaud et de Clément par ses nombreux gâteaux; ainsi que les différentes personnes, parents et amis qui ont participé à la soutenance de cette thèse..

| Table of Contents

Introduction.....	1
Chapter I – Literature review and project objectives.....	7
I Optical bioimaging.....	11
I.1 Toward the nanoscale: Super-resolution microscopy.....	12
I.2 Reminder of the specificities of biological media	16
I.3 Inorganic-based nanoparticles: a promising tool for imaging and microscopy.....	18
II Lanthanide-based upconversion.....	20
II.1 Basics of lanthanide spectroscopy	20
II.2 Upconversion mechanisms	22
II.3 Comparison of UCNP mechanism vs standard downconverting luminescence.....	24
III From bulk to nano: UCNP design: towards more emissive material.....	27
III.1 Optimal matrix.....	28
III.1.1 Reducing non-radiative energy losses within the matrix: matrix phonons	28
III.1.2 Favoring the emission: choice of appropriate crystal phase	30
III.2 Chemical composition	31
III.2.1 High sensitizer content:	31
III.2.2 High emitter content for high laser power density.....	33
III.3 Downsizing issue: surface quenching.....	34
III.3.1 Source of surface quenching	34
III.3.2 Energy transfer to the surface (process F).....	34
III.3.3 Solution to surface quenching: towards surface shielding	38
III.3.4 Yb as energy shuttle	39
III.4 Favoring radiative emission (Process D).....	41
III.4.1 UCNP sensitization (process E)	41
IV Towards water-soluble UCNP	42
IV.1 Challenge of surface coating for biology and nanomedecine.....	42

IV.1.1	Importance in Biology.....	42
IV.1.2	Specific issues in Nanomedecine	43
IV.2	Strategies for water-solubilization.....	43
IV.3	Limit of water-solubilization	47
V	Applications of UCNP	50
V.1	Overview on UCNP main applications	50
V.1.1	UCNP as reporter	51
V.1.2	UCNP as actuators	52
V.2	UCNP as a luminescent probe	52
V.2.1	Tm-based UCNP: a multimodal nanolamp	53
V.2.2	UCNP and Super-resolution microscopy	54
VI	Aim of the manuscript.....	56
VII	References	57

Chapter II – Synthesis of ultrasmall UCNP.....65

I-	Litterature review	69
I.1	Theoretical model of synthesis of UCNP	69
I-1-1-	Two phases: one continuous 1 and one discrete 2	69
I-1-2-	Extension to UCNP polymorphs α and β phases.....	71
I.2	Chemical characteristics of NaREF ₄	71
I.3	NaREF ₄ polymorphs: $\alpha \rightarrow \beta$, an Ostwald's step rule	73
I.4	Synthesis of small UCNPs.....	76
I-1-3-	General procedure for UCNP preparation	76
I-1-4-	Towards size reduction	77
I-1-5-	Reproducibility issue	78
I.5	Aim of the chapter	79
II	From small to ultrasmall nanoparticles adapted for super-resolution.....	80

II.1	Small UCNP nanospheres (10-15 nm)	80
II.1.1	Core UCNP	80
II.1.2	Core@shell UCNP	84
II.1.3	Impact of our high sensitizer content	87
II.1.4	Conclusion on small nanospheres	89
II.2	Transposition of nanospheres synthesis from <i>premix</i> to <i>in situ</i> mixing approach.....	89
II.3	Towards sub-5 nm NP obtained via microwave synthesis	91
II.3.1	Reminder about UCNP and microwave synthesis	91
II.3.2	Feasibility of MW heating in OA:ODE without TFA.....	94
II.3.3	Simple microwave heating: high temperature plateau	96
II.3.4	Cycling temperature	104
II.3.5	Chemical characterization	113
III	Model particles for surface chemistry	117
III.1	Fast preparation of UCNP on a small-scale batch.....	117
III.2	Size reduction on UCNP hexagons scale-up issues.....	118
IV	Conclusion on synthesis of ultrasmall UCNP.....	122
V	Experimental section.....	125
V.1	Materials	125
V.2	Synthesis.....	126
V.2.1	Synthesis of cores UCNPs.....	126
V.2.2	Synthesis of core@shell	128
V.2.3	Microwave heatings	129
V.3	Characterization.....	130
V.3.1	Monitoring of the core synthesis, adapted from F. Wang <i>et al.</i> ⁸ : TEM images and image analysis (Image J treatment).....	130
V.3.2	Luminescence monitoring of the shell growth.....	134

V.3.3	Luminescence monitoring of the shell growth with doubling of the reaction time.....	134
V.3.4	Combination of “in situ” introduction and conventional heating, ¹⁹ trial#1	135
V.3.5	Kinetic analysis, combination of “in situ” introduction and conventional heating, ¹⁹ trial#2.....	136
V.3.6	Kinetic analysis, ”in situ” mixing and 30 min microwave oven combination, variable temperature.....	137
V.3.7	Kinetic analysis,”in situ” mixing and 300°C microwave oven combination, variable reaction time.....	138
V.3.8	Typical run for the “as-fast-as-possible” routine and 300°C plateau.....	139
V.3.9	Summary of the TEM analyses	140
VI	References	141

Chapter III – Upconverting nanolamps.....147

I	Introduction.....	151
I.1	Non-linear behaviour	151
I.2	Theoretical models	151
I.3	Aim of the chapter	155
II	Photophysical properties of UCNP	158
II.1	Absorption	158
II.1.1	Absorbance in solution.....	158
II.1.2	Reflectance/transmittance on powder	162
II.2	Emission	163
II.2.1	Experimental considerations	163
II.2.2	Comparative study of UCNPs under steady–state conditions.....	167
II.2.3	Exploration of Tm-based UCNP’s nonlinear behavior	176
III	Quantitative photophysics of the ultrasmall UCNPs.....	183

III.1	Identity card of ultrasmall UCNP nanolamp	184
III.1.1	Steady state.....	184
III.1.2	Time-resolved emission	185
III.1.3	Quantum yield – efficiency	202
IV	Towards our own kinetic model.....	204
IV.1	Description of the model	204
IV.2	Mathematical expression of the model.....	205
IV.3	Data mining of rate constant.....	207
IV.4	Preliminary results	209
V	Conclusion	212
VI	Experimental section	214
VII	References	221

Chapter IV – Upconverting nanohybrid : towards super resolution.....223

I	Introduction.....	227
I.1	Strategy for Blinking UCNP-based nanohybrid	227
I.2	Photochromic dyes	229
I.3	Organic negative T-photochromic dyes	231
I.4	Spiropyran dyes	233
I.4.1	Reversible photoacid	234
I.4.2	Negative photochromic hydrogels.....	235
I.4.3	Photoactivatable “Staples“	237
I.5	Aim of the chapter	238
II	Toward a negative photochromic spiropyran based UCNP nanohybrid.....	239
II.1	Strategy for dye integration: UCNP ligand exchange	239
II.1.1	Removal of OA	239
II.1.2	Different surface functionalization.....	240

II.1.3	Example of quantitative approach followed by NMR	242
II.1.4	Conclusion on the strategies to make nanohybrid.....	247
II.2	Choice of UCNP-dye couple	248
II.3	Synthesis of SP-grafted ligands	251
II.3.1	Triazine route	251
II.3.2	The amide route.....	253
III	Photochemical behavior of amido-BIPS	263
III.1	Parametrization of the dye: use of BIPS-GLT.....	263
III.2	Exploration of P _{1,38} polymer photochromism	268
IV	Towards UCNP@P _{1,38} nanohybrid for super-resolution.....	271
IV.1	Nanohybrid formation	271
IV.2	Impact of the Nanohybrid architecture on P _{1,38} photochemistry	272
IV.3	UCNP-induced Photoswitching of the P _{1,38}	273
V	Conclusion	275
VI	Experimental section	278
VI.1	Material and methods	278
VI.2	The photoisomerization experiments.....	278
VI.3	Protocol for UCNP ligand exchange	278
VI.4	Reactive dye BIPS-TC ₂	279
VI.5	Model compound BIPS-GLT	280
VI.6	Polymer P _{x,(39-x)} x=1.....	281
VI.6.1	Step 1	281
VI.6.2	Step 2.....	281
VI.7	Calculations of k _(MC→SP)	282
VII	References	283
	Conclusion.....	287

Annexes.....	295
I Résumé du chapitre I	297
II Résumé du chapitre II : Synthèse d'UCNP ultrasmall.....	299
III Résumé du chapitre III: Nanolampes Upconverting	303
IV Résumé du chapitre IV: Nanohybride upconverting vers l'imagerie super-résolue ...	307
V Guide de lecture pour le suivi du chapitre III	311

Introduction

“Un voyage de mille lieux commence toujours par un premier pas”

(Lao Tseu)

千里之行始于足下

Couronnées par le prix Nobel 2014, les nouvelles méthodes de microscopie non invasives en super-résolution permettant de dépasser la limite de diffraction sont devenues ces dernières années un sujet en ébullition, attirant des chercheurs de la Chimie (nouvelles sondes), de la Physique (optique, traitement d'image) et de la Biologie (génie génétique). Les retombées de ces avancées en imagerie vont de la Biologie fondamentale à la Médecine.

Mon travail de thèse s'inscrit dans un projet financé par l'Agence Nationale de la Recherche dénommé « BLINK » ayant pour but de mettre au point des nanoparticules luminescentes à clignotement contrôlé comme nouvelles sondes pour l'imagerie en super-résolution.

Outre la présentation de l'intérêt de méthodes dites stochastiques basées sur le clignotement de sources ponctuelles de lumière, la mise au point bibliographique dans le premier chapitre permettra de mettre en évidence l'intérêt et les contraintes d'un tel type d'imagerie. Nous verrons l'intérêt de s'orienter vers des traceurs, les nanoparticules « upconverting », pouvant fonctionner dans l'infrarouge. Après un bref rappel des principaux éléments de spectroscopie et des mécanismes mis en jeu dans ce phénomène fascinant permettant de produire des photons plus énergétiques (UV-visibles) que les photons incidents (proche infrarouge), seront exposées les contraintes liées à une application en imagerie biologique *in cellulo*, donc à terme dans un milieu aqueux. Notre choix ciblé sur les matrices de types NaREF₄ sera également explicité. Animés par notre objectif de microscopie à l'échelle nanométrique, nous nous sommes particulièrement intéressés à obtenir des objets de très petites tailles compatibles avec les enjeux de la super-résolutions. L'objectif que je me suis fixé était d'arriver à synthétiser des objets de taille comparable aux Quantum Dots, les nanoparticules luminescentes de référence à ce jour. Cependant une telle réduction en taille en conservant les propriétés d'émission s'avère très audacieuse. En effet, ce phénomène attractif d'upconversion est en réalité peu efficace, principalement dû à des problèmes de perte d'énergie, en particulier par transfert avec la surface. De ce fait la réduction en taille accentue cet effet. Ces problèmes de management de l'énergie à l'intérieur de la particule seront aussi abordés, en présentant les stratégies générales permettant de limiter les pertes et d'augmenter l'efficacité du phénomène d'upconversion.

Fort de cette description préalable, le chapitre 2 traitera des résultats obtenus pour la synthèse de ces objets. En apparence très facile pour des objets de taille moyenne 10-50 nm ou

micrométrie, la formation ces particuls s'avère bien plus délicate lorsqu'il s'agit de passer en dessous des 10 nm. En effet 2 polymorphes de type NaREF₄ coexistent, la phase thermodynamique apparaissant en cours de synthèse étant la phase d'intérêt, tout le challenge est d'arriver à contrôler la transformation de phase cubique « α », cinétique, généralement de petite taille, vers la phase hexagonale thermodynamique « β », généralement de grande taille). Après un bref rappel mécanistique des problèmes de nucléation et croissance de nanoparticules gouvernées par un mécanisme de murissement d'Ostwald, nous verrons comment à partir d'un schéma général de co-précipitation thermique classique, inspiré de la chimie des oxydes de fer et des Quantum Dots, nous pouvons améliorer le procédé pour arriver à contrôler la séquence d'Ostwald. Dans ce chapitre seront discutés l'importance du mélange et du chauffage à haute température. L'accent sera particulièrement porté sur l'utilisation de four micro-onde. Le process mis au point ne permettant de préparer de quantité assez limitées de particules ultra-petites, nous avons en parallèle mis en place une seconde approche afin de préparer des lots homogènes plus importants pour pouvoir envisager les modifications de surface nécessaires au projet.

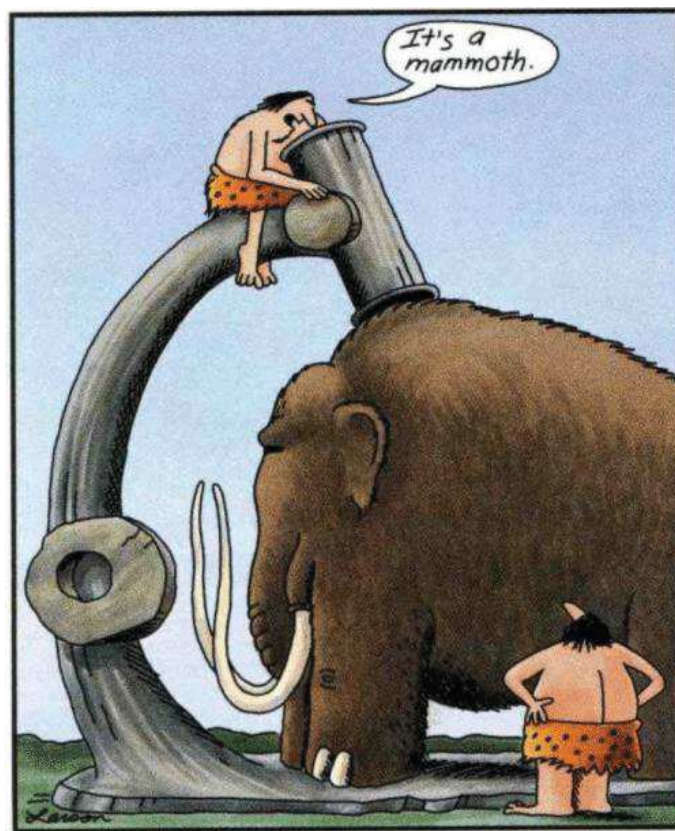
Les résultats recensés pour l'exploration du 2nd chapitre ayant permis la création d'une librairie de nanoparticules de taille, forme, composition et architecture variées, le chapitre suivant est consacré à leur propriétés photophysiques. Une démarche quantitative sera notamment mise en place afin de caractériser complètement le phénomène d'upconversion. Il sera montré notamment comment de simples améliorations, à bas coût, d'un fluorimètre standard permettent d'amener des informations comme la mesure *in situ* de l'absorbance ou la caractérisation colloïdale. Par un travail partagé sur trois sites (Toulouse, Berlin & Lille) sur des appareils de plus en plus sophistiqués seront explorés à la fois l'absorption et l'émission de ces objets. Le comportement non linéaire sera notamment discuté. Dans le cadre des nanoparticules ultra-petites destinée à l'application en super-résolution, l'étude stationnaire de l'émission sera notamment complétée par une étude des temps de vie de luminescence et de l'efficacité (rendement quantique) en fonction de la puissance, afin d'établir la carte d'identité de ces « nanolampes ». A terme, les résultats obtenus ayant pour but de déboucher sur le développement d'un modèle cinétique complexe pour expliquer et prévoir la redistribution d'énergie au sein d'un UCNP, les prémices de ce modèle seront également posés.

Une fois décrites la synthèse et les caractérisations chimique et photochimique, le chapitre 4 traitera de la démarche mise en place pour aller vers la microscopie en super-

résolution. Les particules upconverting étant ultrastable (pas de clignotement, pas de photolyse), tout le challenge de ce projet consiste à « **faire clignoter l'inclignotable** ». De ce fait la stratégie repose sur la conception d'un nanohybride comportant une nanoparticule couverte de "volets" photochromes à sa surface servant à faire fluctuer l'intensité lumineuse globale sortant du nanohybride. Après un rappel bibliographique sur les colorants photochromes réversibles et la justification du choix de colorant de type spiropyrane, nous verrons comment on peut mettre en place le colorant sur la nanoparticule et quelles sont les modifications structurales à faire sur le colorant pour améliorer le recouvrement spectral avec l'émission des UCNPs. Deux principales voies de synthèse de ligand photochromes seront présentées, en particulier une voie permettant de mettre au point des plateformes polymères réactives pouvant laisser libre court à des éventuelles post-fonctionnalisations. A partir de la paramétrisation d'un colorant modèle de structure comparable, un premier polymère sera étudié seul, puis une fois incorporé sur le nanohybride. Outre ces résultats préliminaires seront mentionnées des pistes pour arriver à reproduire nos « fifty shades of blue » !

Chapter I

Literature review and project objectives



Early microscope

“Look deep into nature, and then you will understand everything better” (Albert Einstein)

Contents

I	Optical bioimaging.....	11
I.1	Toward the nanoscale: Super-resolution microscopy.....	12
I.2	Reminder of the specificities of biological media	16
I.3	Inorganic-based nanoparticles: a promising tool for imaging and microscopy.....	18
II	Lanthanide-based upconversion.....	20
II.1	Basics of lanthanide spectroscopy	20
II.2	Upconversion mechanisms	22
II.3	Comparison of UCNP mechanism vs standard downconverting luminescence.....	24
III	From bulk to nano: UCNP design: towards more emissive material	27
III.1	Optimal matrix.....	28
III.1.1	Reducing non-radiative energy losses within the matrix: matrix phonons	28
III.1.2	Favoring the emission: choice of appropriate crystal phase	30
III.2	Chemical composition	31
III.2.1	High sensitizer content:	31
III.2.2	High emitter content for high laser power density	33
III.3	Downsizing issue: surface quenching.....	34
III.3.1	Source of surface quenching	34
III.3.2	Energy transfer to the surface (process F).....	34
III.3.3	Solution to surface quenching: towards surface shielding	38
III.3.4	Yb as energy shuttle	39
III.4	Favoring radiative emission (Process D).....	41
III.4.1	UCNP sensitization (process E)	41
IV	Towards water-soluble UCNP	42
IV.1	Challenge of surface coating for biology and nanomedicine.....	42
IV.1.1	Importance in Biology.....	42

IV.1.2	Specific issues in Nanomedicine	43
IV.2	Strategies for water-solubilization.....	43
IV.3	Limit of water-solubilization	47
V	Applications of UCNP	50
V.1	Overview on UCNP main applications	50
V.1.1	UCNP as reporter	51
V.1.2	UCNP as actuators	52
V.2	UCNP as a luminescent probe	52
V.2.1	Tm-based UCNP: a multimodal nanolamp	53
V.2.2	UCNP and Super-resolution microscopy	54
VI	Aim of the manuscript.....	56
VII	References	57

I Optical bioimaging

The optical observation remains a fundamental of Biology. Since the invention by Antoni Van Leeuwenhoek's in the XVIIth century of the **microscope**, numerous methods have been developed to image biological features at all scales. While the evolution of microscopy tends toward observing cell to sub-cellular structures with an improved resolution, larger scale **imaging techniques** enables one to visualize organ and tissues inside a whole body in 3D. For the latter case, resolution required is usually of several cells. Figure 1 summarizes the scales issues that are relevant in biological imaging, from the biomolecule to the whole organ.

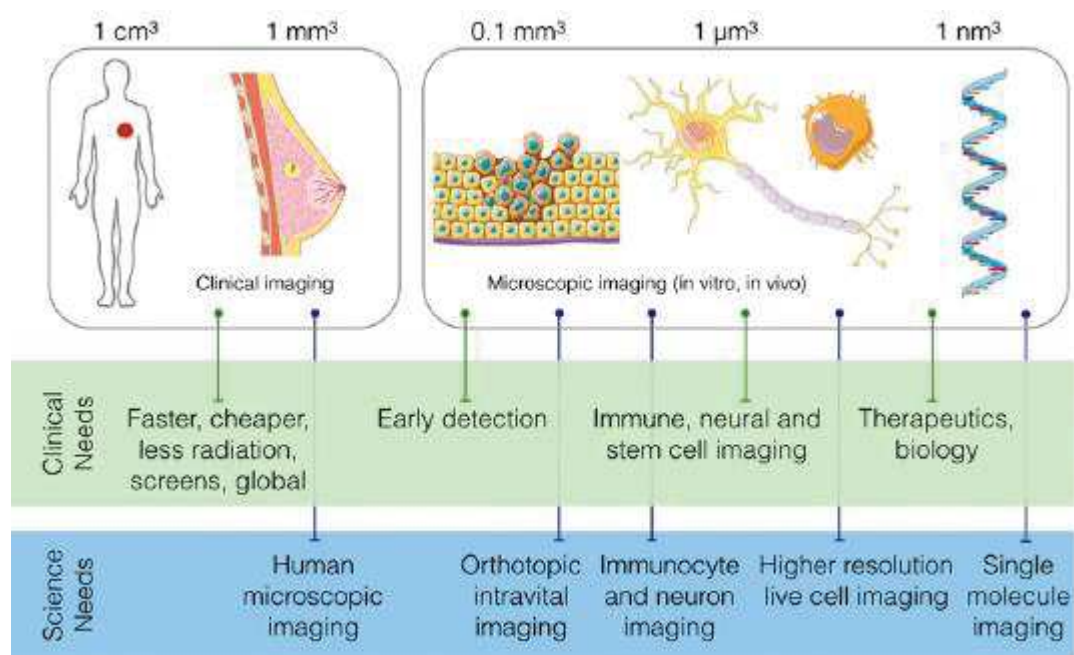


Figure 1. Overview of clinical and basic science imaging needs. Reproduced from¹.

Photoluminescence (PL) is the luminescence resulting from the radiative relaxation of an excited state itself produced by the absorption of light. In other words, it converts high energy photons into lower energy ones. Luminescence measurements are known to be more sensitive than absorption ones and for dilute systems, since the emitted intensity varies linearly with the luminophore concentration. This rule of thumb applies to biological imaging as well, and luminescence imaging techniques are now very popular to observe architectural features. However, as an excited state can decay non radiatively such as by transferring its energy to a quencher, local variations of luminescence is the combination of dye concentration gradients and possible presence of quenching processes: this paves the way to sensing techniques, which are important tools to answer metabolic questions. In parallel, lifetime measurements that are

independent of the dye concentration, are very sensitive to the dye environment and can be used for sensing applications.

I.1 Toward the nanoscale: Super-resolution microscopy

Whichever the PL microscopy technique used, there is a limit in the observation of details in a recorded image: the ability to distinguish two features in close vicinity. Since the mid-XIXth century, it was established that due to diffraction, a point source would give rise to a disk-shaped image if observed by an optical device. This disk called “Airy disk” was further used by Ernst Abbe to establish in 1873 the resolution limit of a microscope. Considering two points separated by a distance d , the minimal distance below which these points cannot be distinguished is when the two Airy disks are tangent:

$$d = \frac{\lambda}{2 n \sin \theta}$$

d : Airy disk diameter (best-focused spot of light),
 $n \sin \theta$: numerical aperture (n =refractive index of the media).

For a long time, this limit was considered to be insurmountable. Considerable investigations in the 90’s led to new techniques collectively termed super-resolution techniques, bypassing this barrier, that were crowned by the 2014 Nobel Prize. Race for an improved image resolution has therefore been central to the biologists, challenging fundamental issues in Physics.

The interest in new, non-invasive, far-field super-resolution is now a hot topic. Expected fallouts span from fundamental biology to medicine. Two families of super-resolution methodologies can be distinguished: the physical approach where the resolution is achieved by altering the excitation beam shape, i.e. patterned illumination spectroscopy (Saturated Structured-Illumination Microscopy SR-SIM, STimulated Emission Depletion STED), and the stochastic approach where the resolution is achieved thanks to probe time-dependent characteristics.

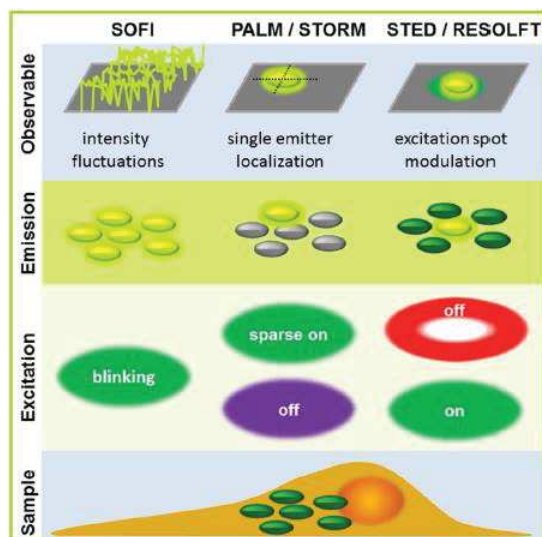


Figure 2. Main super-resolution methods. Reproduced from Y. Lin *et al.* ²

Patterned illumination microscopy: STED

In order to achieve super-resolution, the principle of STED (Stimulated Emission Depletion) relies on limiting the number of excited molecules that can give rise to detectable emission. This is achieved by forcing these excited states to relax to the ground state by stimulated emission. Thus, a first large beam is used to bring the probes in a certain area into their excited state, and another superimposed beam tuned with the dye emission wavelength is applied to relax the excited states. This beam is usually shaped as a doughnut. The simultaneous application of these two beams induces a depletion of the probe's excited state over all the exposed area with the exception of the doughnut center. Careful adjustment of the beam geometries can lead to the survival of very few excited states in a region that can be accurately determined.³

Stochastic approach

The “stochastic approach” is based on the time-dependent dynamics of a population of chromophores under excitation: over a defined time-period not all the probes comprised in a limited domain will be in the same energetic state. The monitoring of this fluctuation over time is therefore employed to localize the emitting centers.

The sub-family of “single molecule localization microscopy” (Photo-Activated Localization Microscopy (PALM), STochastic Optical Reconstruction Microscopy (STORM)) stems on the exploitation of the flickering of luminescent probes: for particular dynamic parameters the probability to have two adjacent probes emitting light at the same time is negligible. By recording multiple consecutive frames and comparing the repartition of the

emitting centers on each frame, one can reconstruct a synthetic image where all emitting centers are localized. Probes however should match several criteria: they must present two states: a bright luminescent “ON” one and a dark “OFF” non-luminescent one. The ON-OFF transformation can be irreversible (bleaching) or not (photochromic). For practical considerations, reversible ones are preferred as they allow for longer experiments, while bleaching leads quickly to the disappearance of emitters’ functionality. The density of probes in the bright states on each frame should also be sparse to be able to position the point spread function as an Airy disc: if a photochromic probe is used it should stay in the OFF state most of time.

The other subfamily is the Stochastic Optical Fluctuation Imaging technique (SOFI). As for the STORM technique, a recording of a set of images is first achieved. However, the image analysis relies here on the time correlation of the luminescence intensity between consecutive frames, pixel by pixel: from the deconvolution of these correlograms is then extracted the position of the point sources of light. This technique, although requiring a heavy mathematical treatment, is particularly less stringent on the dyes’ dynamic parameters; since only spatial fluctuation is needed the dye luminescence may only fluctuate (no need of complete extinction) and the density of point emitters can be higher.^{4,5}

Figure 3 summarizes the optical imaging techniques and compares to other approaches such as MRI or PET:

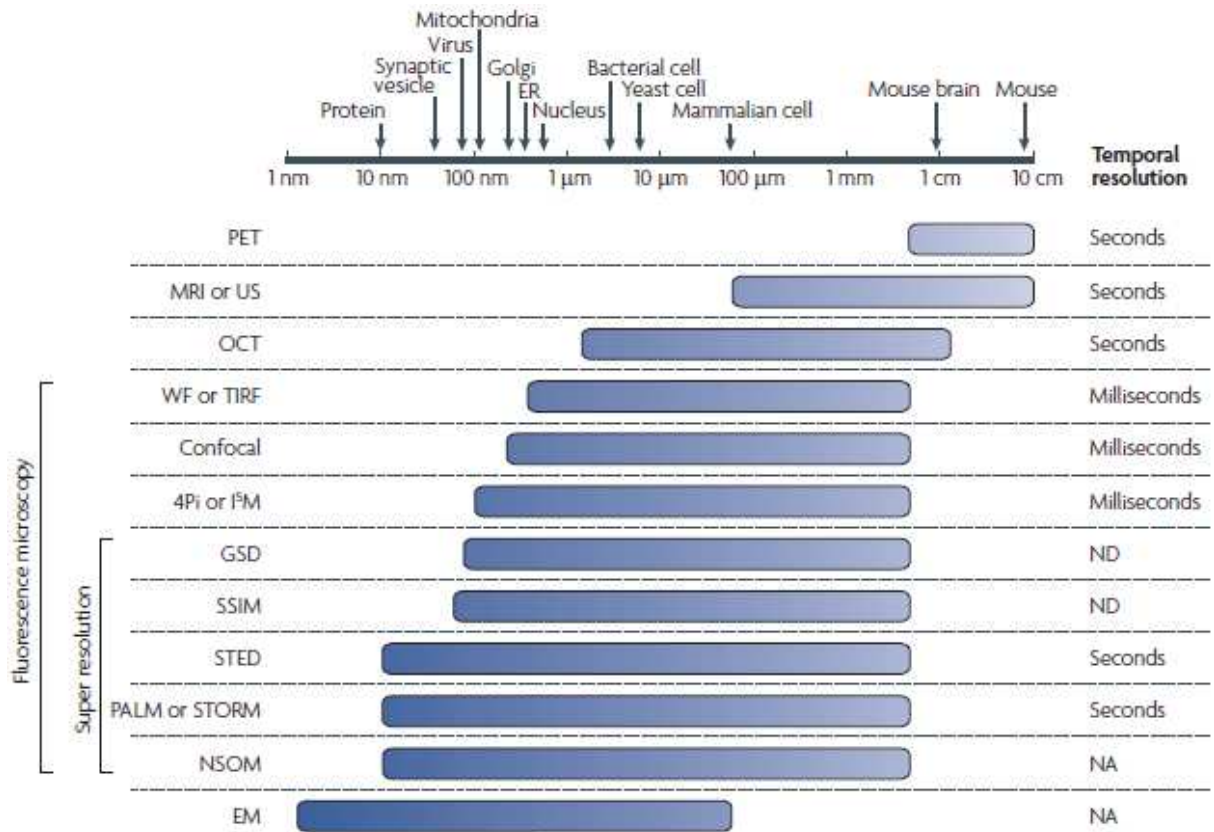


Figure 3. Comparison of the spatial and temporal resolutions of biological imaging techniques. The size scale is logarithmic. Average sizes of biological features are given; specific sizes vary widely among different species and cell lines. The spatial and temporal resolutions are estimates of current practices. The spatial resolution is given for the focal plane. The temporal resolution is not applicable (NA) for electron microscopy (EM) or Near-field Scanning Optical Microscopy (NSOM) because they image static samples. Ground-State Depletion (GSD) and Saturated Structured-Illumination Microscopy (SSIM) have not been shown on biological samples, and thus their temporal resolutions are not determined (ND). ER: endoplasmic reticulum; MRI: Magnetic Resonance Imaging; OCT: Optical Coherence Tomography; PALM: PhotoActivated Localization Microscopy; PET: Positron-Emission Tomography; STED: STimulated Emission Depletion; STORM: Stochastic Optical Reconstruction Microscopy; TIRF: Total Internal Reflection Fluorescence; US: Ultrasound; WF: Wide-Field microscopy. Fig and caption reproduced from ⁶

I.2 Reminder of the specificities of biological media

As imaging is used to explore biological features, one must understand the constraints of biological media, either from the physics' side of *in vivo* imaging or from the chemical aspect in order to take into account the behavior of optical probes in this environment.

Optical constraints of optical bioimaging

In vivo imaging relies on 3 main issues: channeling the light from an external source within tissues, address the site of interest, and retrieve detectable luminescent signal, all of these steps without triggering photodamages.

-Because of their architecture, biological samples can be presented in terms of optics as a scattering and absorbing media. While scattering is fundamental in optical imaging (on large or thick samples),⁷ it can be neglected for cell imaging with a microscopic technique. On the other hand, light absorption can become a severe limitation. Indeed, the penetration depth is dictated by the presence of biological substances competing with the probe absorption. Similarly, the probe emission can also be damped significantly by the surrounding biological compounds. Figure 4 shows the “NIR imaging optical window”, that is the portion of the electromagnetic spectrum for which the deepest light penetration and retrieval can be achieved: it is the convolution of the absorption due to organic matter (UV visible range) and to water (near IR to IR range).

-A corollary issue is photodamaging. Once the light is absorbed, it can trigger photochemical events such as DNA base dimerization, or reactive oxygen species generation. According to the exposure dose, these phenomena can be deleterious for living objects.

-Eventually the signal to noise ratio has to be taken in account: first, if probes are dispersed within the biological sample, a continuous luminescence background will be generated which under wide field illumination will limit the resolution, even with confocal techniques. Second, light absorbed by endogenous biological compounds can lead to autofluorescence also blurring the final image.

-Near IR excitation technique can solve several of these issues:

*it lies typically in the biological transparency window,

*Modern techniques based on non-linear effects (such as 2-photon absorption or Second Harmonic Generation (SHG) approaches) improve the S/R ratio by limiting or even cancelling the sample autofluorescence.

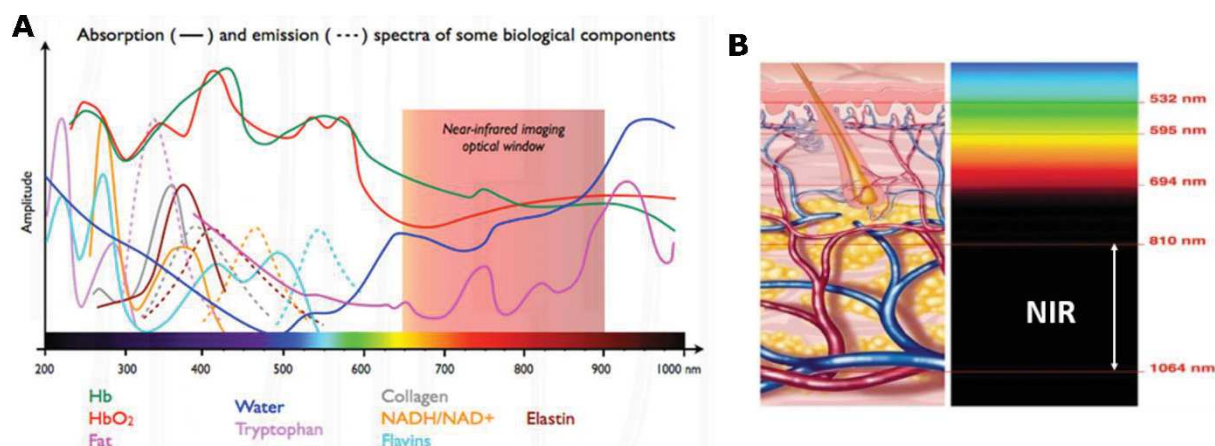


Figure 4. A) Absorption and emission of some biological components. Reproduced from⁸. B) Depth of the light as a function of the wavelength. Reproduced from⁹.

Biological media: a complex chemical reactor

When it comes to the making of dedicated probes, an important point to be taken in account is the biological medium in which the imaging will take place because it may influence the emission properties of the probe and/or the delivery on site of interest. The biological media is a complex system. Its main parameters as far as nanomedicine is concerned can be summarized in the following table 1:

Table 1. Main chemical parameters from a nanomedicine standpoint.

Solvent	water	
Average temperature	37°C	
pH	-Mainly pH=7.4 (blood) -Acidic compartments: Organ: stomach (pH=1.8) in stomach ¹⁰ Cancer tissue (pH _{extracellular} =6.5-6.9) ¹¹ Cellular organelle : lysosome (pH≈4.6) ¹⁰ -Basic compartment: duodenum (pH=8)	
gases	O ₂ , CO ₂	
Main Electrolytes (in decreasing concentration order from top to bottom)	Na ⁺ K ⁺ Ca ²⁺ Mg ²⁺	Cl ⁻ HCO ₃ ⁻ HPO ₄ ²⁻
Biological compounds	Proteins (albumin>90%), carbohydrates, aminoacids, enzymes, etc ...,	
Others	Immune cells (ex : phagocytes)	

Besides genetically engineered proteins that obviously satisfy to the biocompatibility criterion, a lot of work involves xenobiotic probes. As a result, biological probes have to be water-dispersible and stable at least at neutral pH and under oxidation condition (presence of oxygen).

In the present manuscript “solubility” will refer to dispersibility and compatibility with solvent/biological media.

Due to the presence of endogenous electrolytes, some byproduct can be formed due to complexation. Finally, some deleterious aggregation can occur with biological compounds (such as proteins) that can lead to a fast elimination. This requires adapted probe functionalization to have *in vivo* accurate stability and prolonged lifetime.

I.3 Inorganic-based nanoparticles: a promising tool for imaging and microscopy

Over the past two decades, various inorganic nanoparticles¹² have been used as luminescent label in various imaging and microscopy techniques, as recently reported by Enderlein.¹³ Among them, quantum dots (QD) currently have the leadership.¹⁴ These are ultrasmall semiconductors nanoparticles, usually within 2-6 nm size, in which quantum confinement makes their optical absorption and emission properties size-dependent. Therefore, simple size tailoring induces spectral changes. Converting high energy photons into lower energetic ones, the emission spectral window spans from the visible down to the NIR range. They also present large quantum yield,¹⁵ high photochemical and thermal stability. Combined with versatile preparations, these features explain why they are now very popular and easily available in trade. However, QDs suffer from certain limitations: they have generally blinking luminescence, impeding applications such as *in vivo* tracking, but allowing either STED or stochastic-based super-resolution approaches. More critical is the intrinsic toxicity of such materials due to the elements used themselves: typically Cd, Se, Te. It can be reduced (but not cancelled) thanks to complex nanoparticle architecture (i.e. core shell)

Another rising class of NIR absorbing inorganic materials is burgeoning since the beginning of the 2000's (figure 5): upconverting nanoparticles also known as UpConverting NanoPhosphor (UCNPs) and especially lanthanide-based ones.^{16,17} Discovered in the 1960's, upconverting crystals (micrometer scale) were first developed for applications in optics, telecom and laser. Thanks to advances in chemistry and the development of nanoscale objects, UCNP have been brought up to date by Auzel¹⁶ at the end of the 1990's. They present the fascinating properties of being able to convert low energy photons (NIR) into higher energy ones (visible to UV range) with extremely long lifetimes (μ s-ms range).

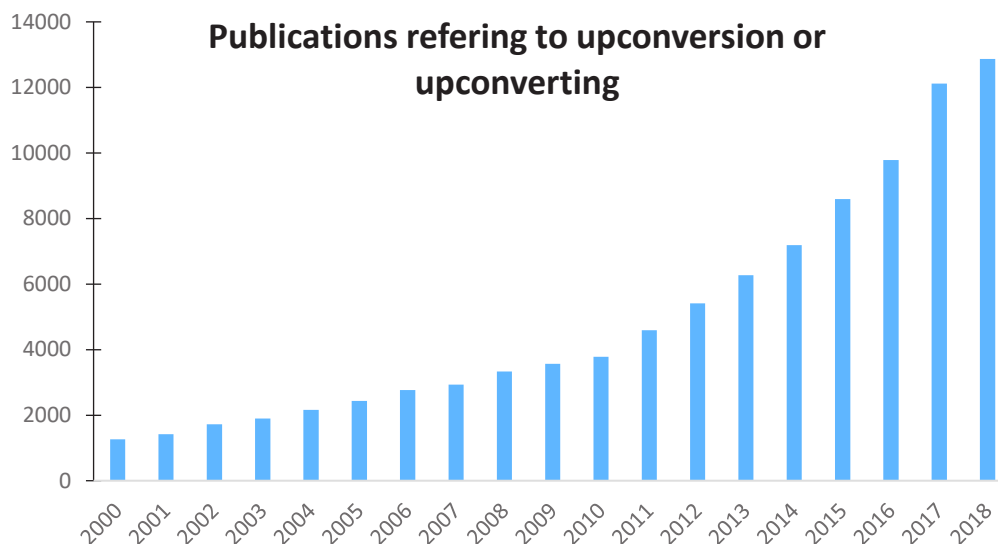


Figure 5. Evolution of the amount of published works referring to upconversion or upconverting, including patents (source: Google Scholar).

UCNPs share the thermal stability with QD.¹⁵ However, they differ from the latter by their emission wavelengths which are no longer sensitive to the crystal size but depend only on the chemical nature of the lanthanides. UCNPs are extremely photostable, showing neither blinking nor bleaching, with a limited toxicity. Thus, they appear as an ideal tool for imaging, especially for tracking. However, this has a cost and such amazing phenomenon has generally quantum yield lower than 1%. The dramatically low apparent emission efficiency is compensated by the total lack of autofluorescence of any biological compound under NIR excitation. Moreover the extremely long UCNP emissions lifetimes allow time-gated detection to remove the eventual back-scattered incident light.¹⁸

The commercial availability of Quantum Dots and their largely explored surface chemistry explain their involvement in a larger number of imaging techniques. However, UCNPs appear as promising challengers due to the several advantages already described and despite the limited number of suppliers. The dare to replace QD by UCNP is still open. Having in mind the development of innovative probes for biological imaging at the smallest scale possible (such as super-resolution), my PhD work was then to contribute to this new field that is nanohybrid probes based on a UCNP inorganic core.

II Lanthanide-based upconversion

We have highlighted the fascinating property of UCNP of converting low energy photons in higher energetic visible to UV emissions. We will now discuss how this phenomenon can occur thanks to the specific spectroscopic characteristics of lanthanides. Then will be shown the main underlying mechanisms and the photophysics particularities of these NPs. From these considerations will be discussed how UCNP have to be designed to present such upconverting behavior.

Although puzzling at first sight, the unusual “upconversion process” draws strongly upon the lanthanide spectroscopic properties. In addition, a complex energy redistribution takes place between all lanthanide ions leading to the final production of higher energy photons. We will now briefly recall the elementary steps of this phenomenon.

II.1 Basics of lanthanide spectroscopy

Trivalent lanthanide ions electronic configurations are characterized by the filling of the f-shell and can be written as $[Xe] 4f^n$ ($n= 0-14$). Electrons in the completely occupied 5s ($5s^2$) and 5p ($5p^6$) orbitals efficiently shield off the 4f-electrons from the chemical environment: the 4f orbitals do not participate in chemical bonding. The spectroscopy of these elements is dominated by the states generated from the 4f-orbitals. These shielded 4f states, mostly governed by spin-orbit coupling, are only weakly affected by the crystal field (contrary to transition metals). These excited states are classically named by their associated spectroscopic terms and are classically gathered in the so-called “Dieke diagrams”. The non-participation of the f-orbitals in the chemical bonding also leads to a weak electron-phonon interaction. This results in a line spectrum whose broadening is mostly due to the crystal field splitting (Stark levels).¹⁹

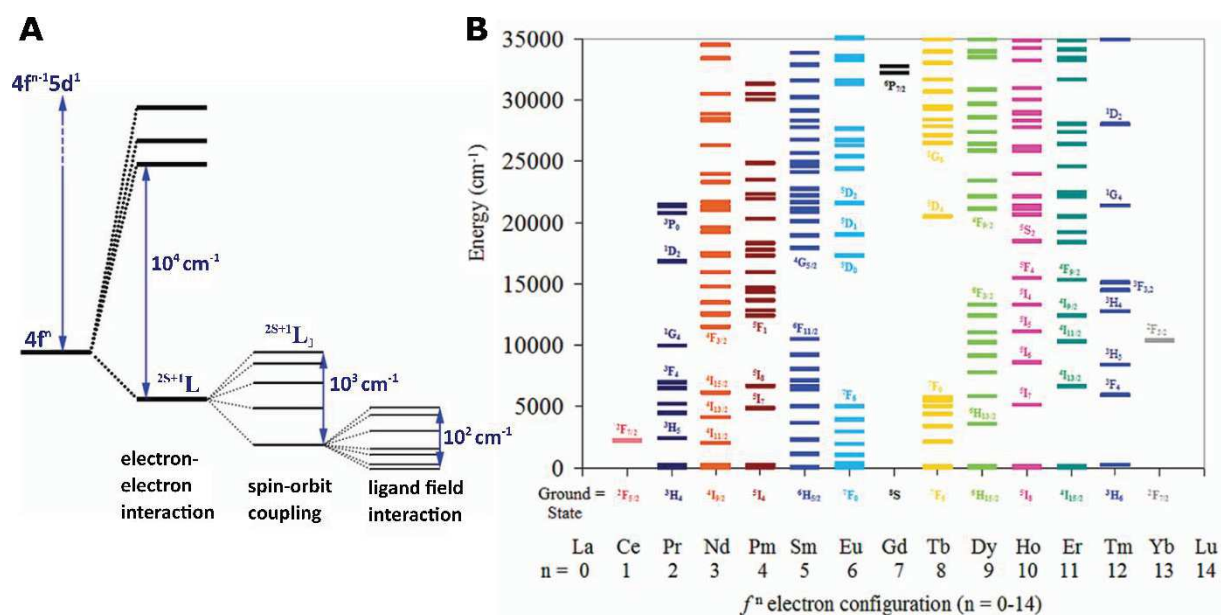


Figure 6. Lanthanide ions energy splitting. A) Origin of the 4f level splitting in lanthanides, reproduced from ²⁰. B) Dieke diagram of lanthanide ions, reproduced from Moore *et al.*²¹

Classically, the interaction of an electromagnetic radiation with matter leads to distinguish three types of transition moments: electric dipole ED, magnetic dipole MD and electric quadrupole EQ. For the lanthanide series, the succession of couplings and interactions leads to complex selection rules (Table 2). Thus, although the number of excited states can be very large, these rules limit the number of possible transitions. The most intense ones are the electric dipole ED transitions. However, involving pairs of 4f states, these are symmetry forbidden²² according to Laporte rules. The forbiddance is partly relaxed when the local crystal field is introduced (Stark effect).²³ Magnetic dipole (MD) and electric quadrupole (EQ) transitions are parity allowed but usually much weaker than the partially allowed ED one. The EQ-transitions are usually neglected. More detail about lanthanides electronic structure characteristics can be found in Bunzli's work.²⁴

Table 2. Selection rules for f–f transitions between spectroscopic levels. a: J = 0 to J' = 0 transitions are always forbidden.²⁴

Operator	Parity	ΔS	ΔL	ΔJ
ED	Opposite	0	≤ 6	≤ 6 (2,4,6 if J or J' = 0)
EM	Same	0	0	0, ± 1
EQ	Same	0	0, $\pm 1, \pm 2$	0, $\pm 1, \pm 2$

It results from the Laporte rule that absorption cross-sections and the emission efficiencies of all lanthanides are very weak, and extremely long luminescence lifetimes (μs - ms) are commonly observed.

However, because the magnitude of the transition moments are bound to the local ligand field and therefore to the host material, it is possible to calculate the radiative rate constants for the emission decays and associated data (lifetime decay, branching ratio, quantum yield). A semi-empirical theory developed by Judd and Ofelt allows one to predict the transition probabilities.²⁵ It relies on the parameterization of the ligand field effect obtained by fitting of the absorption spectrum. Once this achieved, it is possible to calculate the radiative rate constants for the emission decays, and then branching ratios and quantum yields. This requires a well resolved absorption spectrum which is not easy to achieve on nanomaterials.²⁶ May *et al.* have extended this methodology to spectra recorded by reflectance spectroscopy.²⁷

II.2 Upconversion mechanisms

The phenomenon of upconversion can be seen as an « energy accumulation » within a single ion causing it to reach high energy excited states. Decomposition into elementary processes can be a little more complicated. It is now commonly admitted that at least up to six processes can occur:¹⁷

The simplest one, termed ESA (Excited-State Absorption) (fig 7a), involves only a single ion having two excited state separated by the same energy difference. Successive photons absorption can promote the ion in its first (E_1) then second (E_2) excited state. Among Rare-Earths, this situation is encountered for Er^{3+} , Tm^{3+} , Ho^{3+} and Nd^{3+} . Although very simple, this process requires “good” NIR absorption cross sections for the ground *and* the intermediate state, which is a tough constraint.

To bypass the poor NIR absorption, another strategy was proposed based on inter-ion energy transfer. The upconversion results now from multiple energy transfers between a sensitizer and the emitter (fig 7b). The sensitizer is typically ytterbium whose Dieke diagram is particularly simple. As ytterbium has a larger absorption cross section (compared to the other lanthanides) it can be successfully excited at 980nm. This is the so-called Energy Transfer Upconversion (ETU) mechanism. Because the energy transfer depends on the distance between sensitizer and emitter, this mechanism is highly sensitive to doping content. Recently, more complex energy transfer chains were developed that include neodymium. This element is indeed able to absorb at 800 nm and can be used to feed the complete upconversion chain.²⁸ Nevertheless the main issue is the very low absorption cross-section of the lanthanides such as

$1.2 \times 10^{-19} \text{ cm}^2$ (or $31 \text{ L}\cdot\text{mol}^{-1}\cdot\text{cm}^{-1}$)²⁹ at 808 nm and $1.2 \times 10^{-20} \text{ cm}^2$ ($3.1 \text{ L}\cdot\text{mol}^{-1}\cdot\text{cm}^{-1}$)³⁰ at 980 nm respectively for Nd^{3+} and Yb^{3+} .

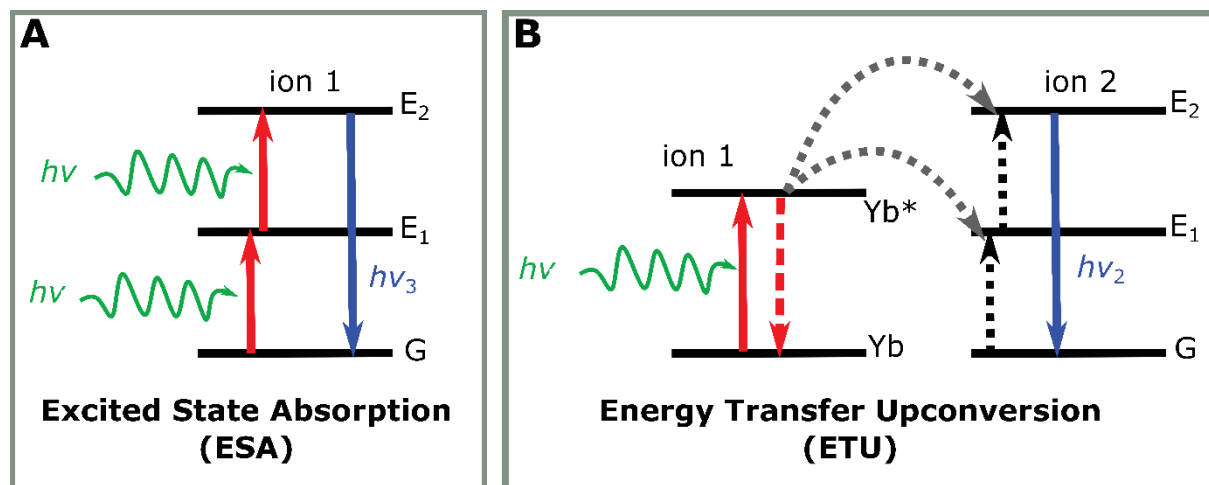


Figure 7. Principal upconverting processes of Ln-doped UCNP. Reproduced with permission from³¹.

Other mechanisms have been described by Auzel,³² involving more complex sequences, for example, three ions for CSU (Cooperative Sensitization Upconversion), or energy looping (photoavalanche PA), but they are less efficient.³¹ Thus in Table 2 are given the order of magnitude of each process' quantum efficiency showing the prevalence of ETU, as proposed by Auzel for comparison purpose. Interestingly, the upconversion phenomenon is also more efficient than the usual non-linear processes achieved by coherent photon absorption (Two-photon or second order harmonic generation SHG).

Table 3. Quantum efficiency comparison of main processes involving 2 photons. Adapted from³². KDP is Potassium dihydrogen phosphate crystal.

	UCNP			SHG	2-photons absorption excitation
	ETU	ESA	CSU		
matrix	$\text{YF}_3:\text{Yb,Er}$	$\text{SrF}_2:\text{Er}$	$\text{YF}_3:\text{Yb,Tm}$	KDP	$\text{CaF}_2:\text{Eu}^{2+}$
Quantum efficiency (cm^2/W)	10^{-3}	10^{-5}	10^{-6}	10^{-11}	10^{-13}

II.3 Comparison of UCNP mechanism vs standard downconverting luminescence

From the lanthanides' Dieke diagram, one can derive a pictorial representation of all the possible processes leading to upconversion in the ETU case. On figure 8 is represented the case of the Yb-Tm pair and the assignment of all detected transitions.

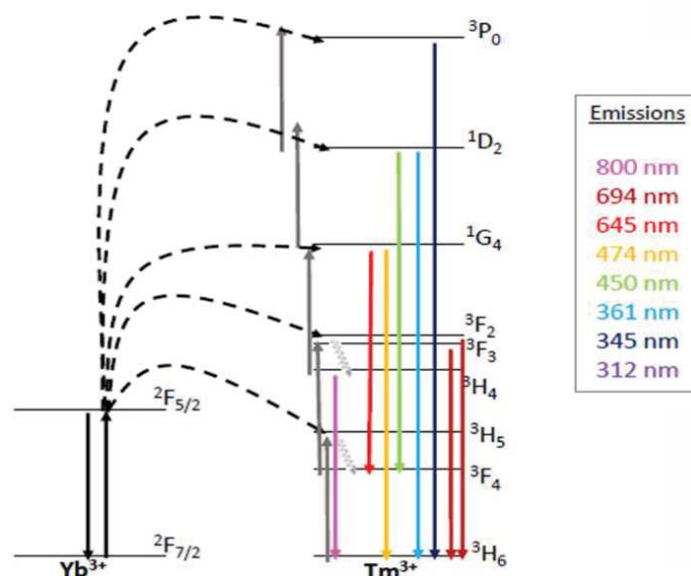


Figure 8. ETU scheme for a Yb: Tm-based UCNP. Dark grey arrows represent the equivalent of energy transfer from one single NIR photon (980 nm) absorption. “Oscillating” light grey arrows are non-radiative relaxations. Dash line arrows are energy transfer between sensitizer and different energy level of thulium emitter.

Compared to standard luminophores, the overall scheme is much more complex. The main feature is that most of the intermediate excited states undergo relaxation processes, but also excitations ones thanks to cross relaxation with excited ytterbium ions. As a result, experimentally measured quantum yield and lifetimes are not absolute values as for standard organic dyes, but more “apparent constant” revealing equilibrium of energy distribution among the excited states. However, following the UCNP research community, they will be treated as usual constant in the present manuscript.

Besides the standard luminescent characteristics (nature of emission, duration, efficiency), it is common to define branching ratio as the proportion of the radiative processes originating from a precise excited state. For example, 1G_4 level gives two emissions respectively at 645 nm ($^1G_4 \rightarrow ^3F_4$) and 474 nm ($^1G_4 \rightarrow ^3H_6$): the branching ratio BR is

$$BR(645nm)_{1G_4} = \frac{Intensity(645nm)}{Intensity(645nm) + Intensity(474nm)}$$

and vice versa for the second band. It should be also noticed that most of emitter energy levels are at the same time producing emission bands and feeding higher energy level.

Dynamics of the energy between levels

From the above-mentioned upconversion diagram, it is possible to establish the kinetic scheme able to reproduce the dynamics of all transient excited states involved in the emission. The general level population rate (dN_i/dt) is therefore the sum of three kinds of elementary processes:

-monomolecular ones: the radiative- (emission absorption) and non-radiative (phonon coupling) one, and

-bimolecular one: the cross relaxations.³³ It is admitted that these processes are derived from dipole-dipole interactions (similarly to classical FRET) and are therefore distance dependent.

The general differential equation is thus:

$$\begin{aligned} \frac{dN_i}{dt} = & \sum_j (N_j A_{ji}^{ED} - N_i A_{ij}^{ED}) + \sum_j (N_j A_{ji}^{MD} - N_i A_{ij}^{MD}) \\ & + (N_{i+1} W_{i+1}^{NR} - N_i W_{i-1}^{NR}) + \sum_{ij, lk} (N_j N_l P_{ij, lk}^{NR} - N_i N_k P_{ij, kl}^{NR}) \end{aligned}$$

A_{ij}^{ED} and A_{ij}^{MD} are the Einstein coefficients (s^{-1}) for electric dipole (ED) and magnetic dipole (MD) radiative transitions from manifold i to j . $W_{i,i-1}^{NR}$ is the non-radiative multiphonon relaxation rate (s^{-1}) from the manifold i to the manifold $i-1$. $P_{ij,kl}^{ET}$ (in nm^3s^{-1}) is the microscopic energy transfer parameter for the transfer of energy for the donor transition from i to j and the acceptor transition from level k to l .

In the case of the Yb:Tm system, 10 ordinary differential equations are necessary to describe all the usual excited states involved in the upconversion process. Complete handling of such a system of equation is difficult as and is usually treated for steady state situations. Yet theoretical predictions are successful especially from the group of the Berkeley Lab's Molecular Foundry.^{34,35}

Typical ETU chemical composition

Within the ETU excitation scheme, upconverting materials are mainly formed by 3 elements (figure 9): a crystalline host matrix in which are dispersed sensitizers and emitters ions.

Thanks to lanthanide chemistry, salts differing only by the lanthanide nature are usually structurally very close, allowing the preparation of mixed element materials that can be considered as a solid solution. It is then possible by adjusting their proportions to tune the distances between optically active ions within the crystal.

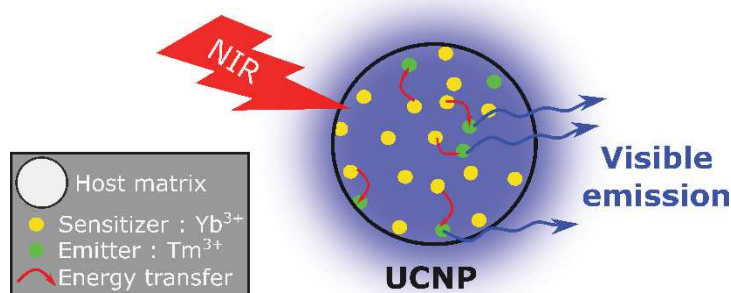


Figure 9. Schematic representation of a UCNP nanoparticle

Typical emission spectra

Depending on the nature of the emitter, specific emission patterns are observable:

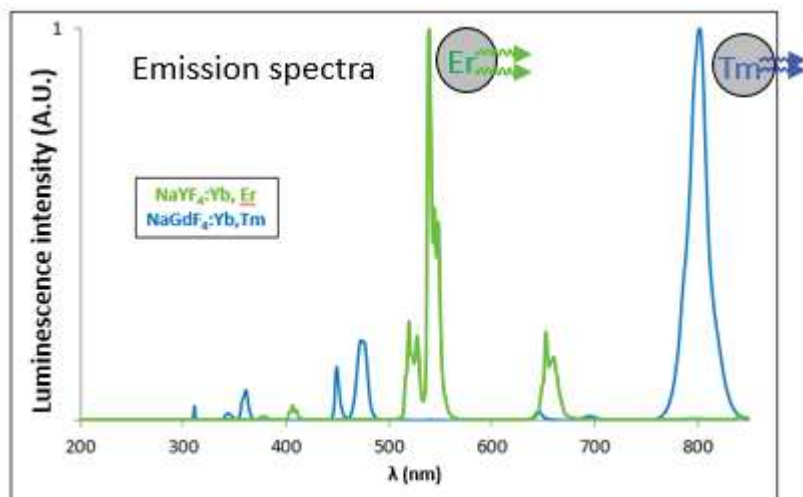


Figure 10. Typical emission spectra of Yb sensitized Er- and Tm-based UCNP. Each spectrum is independently normalized to 1.

Erbium-based UCNP are characterized by two strong emission bands in the green region (525 & 540 nm), one intense band in the red (650nm) and a weak one at 400 nm. Besides, thulium-based UCNP have multiple emission bands ranging from UV (312, 345, 362 nm) to NIR (802)

through blue (450 & 475 nm) and red (650 & 695 nm) emission bands. The position of emission bands is only dependent on the emitter ion. Nevertheless, the intensity ratio between different peaks of one emitter are highly sensitive to the temperature and the excitation source (laser power, shape of the beam (top-hat or Gaussian), pulsed laser or not, etc...).

Pulsed excitation

A less intuitive consequence of the non-linear process is the sensitivity of the energies ratio upon pulsed light.

Appropriate pulsed excitation should be able to modulate and control on demand those emission band ratios in order to promote a desired colored light. However, such a purpose is a new area of investigation and few investigations have focused on it. An interested reader should read as an illustration the work of F.O. Laforge *et al.*³⁶

III From bulk to nano: UCNP design: towards more emissive material

Moving from bulk to highly divided material, especially at the nanoscale, introduces new constraints on the photophysical scheme. Indeed, we will see that the efficiency of the upconversion process depends strongly on the material nature and its size. Thus, maintaining a reasonable efficiency while downsizing the crystal enforces chemical choices such as the host matrix or the surface chemistry.

Figure 11 summarizes the main photophysical processes at work when operating sensitized (ETU) UCNP. They can be sorted into 3 classes:

- based on the type of lanthanide ion: absorption (A), emission (D) and the non-radiative relaxations process (C);

- the cross relaxations related to upconversion (B).

- to this basic intrinsic scheme inside UCNP, other additional energy transfers such as with external sensitizer or acceptor (E, F) can be implemented. The use of a second sensitizer (process E) with higher absorption cross section aims to increase the absorption and eventually switch it to a more favorable wavelength (i.e. from 980 nm which is strongly absorbed by water, to 800 nm) in order to prevent overheating issue for example. The coupling of UCNP with a chromophore acceptor (process F) will be also described as it is particularly of interest to explain energy transfer to the surface quenchers and for applications of UCNP that will be described at the end of the chapter.

Additionally, it can be mentioned that a more sophisticated approach based on the coupling with plasmonic NPs such as gold or silver is currently an area in development to enhance the emission efficiency. This will not be detailed in the present work, but a curious reader can browse the review by Park *et al.*³⁷

Optimization of the overall process aims therefore at reducing all competitive processes that would divert the energy flow out of the upconversion path ($A \rightarrow B \rightarrow D$) or $A \rightarrow B \rightarrow F$. We will now examine how and where the experimental choices to design the UCNPs impact the overall chain of energy transfers.

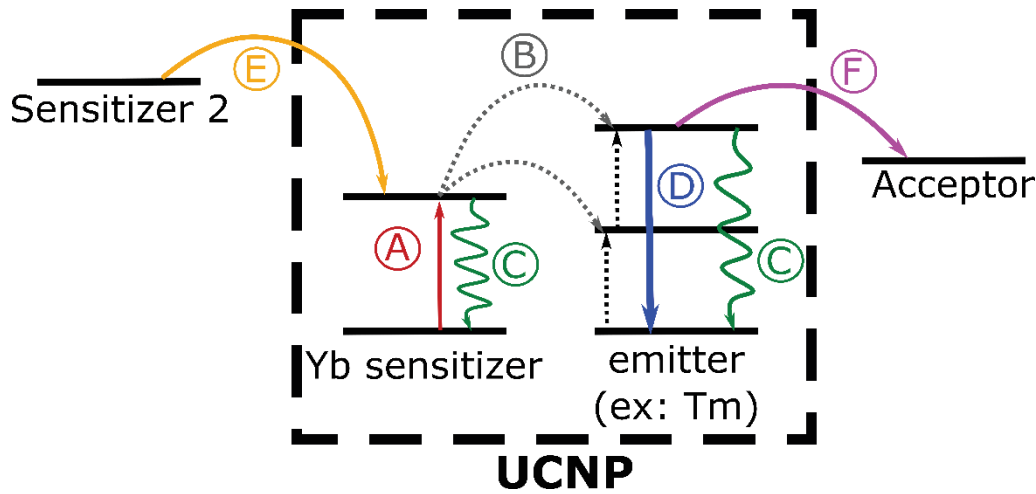


Figure 11. Summary of energy entrance and exit in ETU process: A) Yb Absorption; B) Energy transfer to emitter; C) non-radiative de-excitation; D) Upconversion emission; E) UCNP sensitization; F) Energy transfer involved in FRET application. Dash-line rectangular box indicate phenomenon occurring exclusively inside UCNP crystal, while additional cross relaxation (E-F) are due to coupling respectively with a second sensitizer (E) or FRET acceptor (F).

III.1 Optimal matrix

III.1.1 Reducing non-radiative energy losses within the matrix: matrix phonons

Several theoretical models have been explored in this regard.³⁸ The simplest model developed is the so-called “Energy Gap law” that can be expressed as:³³

$$k_{nr}^{MP} \approx k_{MPR}^0 \exp[-\alpha(\Delta E - \hbar\omega_{cutoff})]$$

where k_{nr}^{MP} is the non-radiative MultiPhonon Relaxation (MPR) rate-constant. This expression states that the larger the number of phonons of energy $\hbar\omega_{cutoff}$ to bridge the gap ΔE , the less efficient the MPR process will be. The parameter α is a function of the nature of the material, the temperature and the number of phonons involved ($\frac{\Delta E}{\hbar\omega_{cutoff}}$).

The more phonons involved, the less efficient will be the process of non-radiative energy losses.

Thus, reducing multiphonon relaxation implies the selection of matrices with the lowest cutoff phonon frequency ($\hbar\omega_{\text{cutoff}}$).

Different kind of inorganic crystals including oxides³⁹ (such as Al_2O_3 ⁴⁰, RE_2O_3 (RE=Rare Earth)⁴¹⁻⁴³, ZnO ⁴⁴, $\text{Bi}_2\text{O}_3\text{-Li}_2\text{O-BaO-PbO}$ ⁴⁵, ZrO_2 ⁴⁶, BaTiO_3 ⁴⁷), oxysulfides⁴⁸, oxyfluorides⁴⁹⁻⁵¹, phosphates⁵², vanadate⁵³, CaF_2 ⁵⁴, and halides⁵⁵⁻⁶¹, have been used as matrix to build upconverting materials.

Table 4 gathers several examples and an estimation of the number of phonons (last column).

Table 4. Comparison of the phonon energy for different matrices. Adapted from R. Diament *et al.*⁶²

Material	Highest phonon energy ($\hbar\omega_{\text{cutoff}}$) in cm^{-1}	Number of phonons equivalent to one photon 980 nm ($\Delta E=10\,200\text{ cm}^{-1}$)
Phosphate glass ⁶²	1200	8.5
Silica glass ⁶²	1100	9.3
Fluoride glass ⁶²	550	18.5
Chalcogenide glass ⁶²	400	25.5
LaPO_4 ⁶²	1050	9.7
YVO_4 ⁵³	890	11.5
YAG (yttrium aluminum garnet) ⁶²	860	11.9
Y_2O_3 ⁶³	550	18.5
$\text{Y}_2\text{O}_2\text{S}$ ⁶⁴	520	19.6
Oxyfluoride or chloride (ex GdOCl) ⁶⁵	500	20.4
ZrO_2 ⁶⁶	500	20.4
NaYF_4 ⁶⁷	350	29.1
LaF_3 ⁶²	300	34
LaCl_3 ⁶²	240	42.5

Compared to other matrices, lanthanide halides show the lowest phonon energies (around 350 cm^{-1})⁶² making them the most efficient for upconversion due to the minimization of non-radiative losses. Unfortunately, among halides, only fluorides are chemically stable.^{39,68} Moreover, since the 70's, laser physicists have demonstrated that the ternary NaYF_4 matrix was more efficient than the binary one YF_3 .⁶⁹ As a result, NaREF_4 appears as the matrix of choice for UCNP nanomaterials.

III.1.2 Favoring the emission: choice of appropriate crystal phase

Local symmetry

Fluoride MREF₄ (M=alkali; RE=Rare Earth), which represent the most commonly used matrix⁶⁹⁻⁷¹ can exist only in 2 crystal phases (figure 12): a cubic (α -MREF₄, space group $Fm\bar{3}m$) crystal and an hexagonal (β -MREF₄, space group $P6_3/m$) gargarinite-like (NaCaREF₆).⁷²

Cubic phase is similar to CaF₂ unit cell in which the Ca²⁺ sites are randomly occupied by $\frac{1}{2}$ RE³⁺ and $\frac{1}{2}$ Na⁺. However, the hexagonal phase presents three kinds of cationic sites: two 9-fold coordinated position occupied respectively by RE³⁺ and randomly $\frac{1}{2}$ RE³⁺ $\frac{1}{2}$ Na⁺; and a 6-fold coordinated occupied by $\frac{1}{2}$ Na⁺ and vacancies.

As explained above, absorption and emission selection rules strongly depend on the local crystal field symmetry (the lower being the better). Within the cubic phase, the Wyckoff sites of lanthanide ions are of high symmetry (O_h symmetry), whereas they have a lower symmetry in the hexagonal one (C_{3h} symmetry). Therefore, it is expected that the hexagonal phase presents a higher upconversion efficiency, since symmetry is lowered and transitions are “less” forbidden. Experimental results show that the hexagonal phase leads to NPs at least one order of magnitude brighter than the cubic one.⁷³⁻⁷⁵

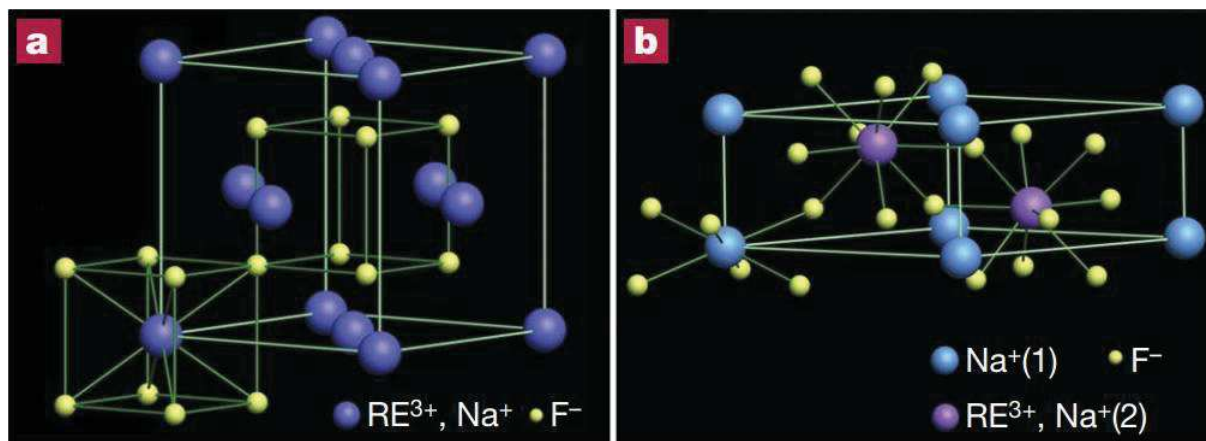


Figure 12. Representation of NaREF₄ polymorphs' unit cells: cubic α -phase (A) and hexagonal β -phase (B). In the cubic phase, equal number of F⁻ cubes contain cations and vacancies. In the hexagonal phase, an ordered array of F⁻ ions offers two kinds of cation sites: Na⁺ sites and Wyckoff sites that can be randomly occupied by either Na⁺ or Re³⁺. Figure and caption reproduced with permission from.⁷⁵

Crystal distortion

A further improvement can be gained by inducing crystal distortion to lower the local RE crystallographic site symmetry. This can be achieved by playing on the ionic radius of the different cations used. As MREF₄ forms solid solutions with various alkali and RE mixture, the

only limit is to induce phase demixion. The main approach relies on the cationic site substitution by alkali such as K^+ or Li^+ .⁷⁶⁻⁷⁹ A more sophisticated approach of crystal distorsion was elaborated by Alivisatos group.⁸⁰ The idea is to corrugate the crystal by co-substituting the RE^{3+} sites. Indeed, in $NaYF_4$ matrix, Y^{3+} (104.1 pm) was substituted at the same time by bigger lanthanides (Gd^{3+} ; 107.8 pm) and smaller ones (Lu^{3+} ; 100.1 pm). As a result, the corrugated crystal revealed an impressive enhancement of the quantum yield efficiency.

III.2 Chemical composition

After having presented the general strategy related to NP general structure (non-radiative energy losses and appropriate crystal symmetry for desired photophysical properties), we shall now investigate how Ln^{3+} ion density impacts the luminescence. It is commonly admitted that the ideal concentrations in terms of Rare Earth molar percentage should be 20% for the sensitizer (Yb) and of 2% and 0.5-1% for the emitters respectively erbium and thulium. This rule is mostly empirical and is justified by considerations related to concentration-induced quenching. However, some groups still work on compositions “outside the box”: dealing with higher sensitizer or emitter content.⁸¹ As the presence of these two dopants can affect not only the photophysics but also nanoparticle crystallization, we will here examine the main issues related to changes in composition.

III.2.1 High sensitizer content:

The sensitizer Yb plays the role of an antenna collecting the NIR light and channeling the energy to the emitters. One can therefore be tempted to change the sensitizer content. Some of the consequences are listed below.

UCNP absorption

Higher sensitizer content was investigated by teams working in $NaYbF_4$ host crystal, mainly Prasad’s group, envisaging ytterbium as being at the same time host matrix and sensitizer.⁸² From 30% to 70% content of ytterbium, luminescence is rising gradually: indeed at 30% and 50% it represents respectively around 3% and 16% of the maximal efficiency observed (at 90%). This gain in efficiency seems to be a consequence of the increased absorption efficiency of the material at 980nm. One could be tempted to move to Yb-only host matrix, however synthesis problems become overwhelming as $NaYbF_4$ tends to lead mostly the cubic phase. It can be noted that this team had to introduce a non-negligible amount of gadolinium (at least 10%) to produce the hexagonal phase.

Interaction with the emitter

Dopant concentration inside the crystal is a key-point for upconverting efficiency. Indeed, the energy transfer mechanism is based on a dipole-dipole coupling and therefore is distance-dependent. Increasing the sensitizer induces a new phenomenon known as concentration quenching detailed in chapter 3.⁸³

An important study by Chen *et al.*⁸⁴ exemplifies the impact of rising sensitizer ytterbium concentration on both Tm^{3+} and Er^{3+} emitters within a YF_3 matrix (figure 13).

Striking difference can be seen by bare eyes between Tm and Er. While poor if no impact can be observed on Tm, keeping a blue-purple emission in the visible range, considerable variation is observed on erbium, upon varying the amount of Yb. The color change from mostly green to red is evidenced by a change in relative intensity of the two main visible emission bands.

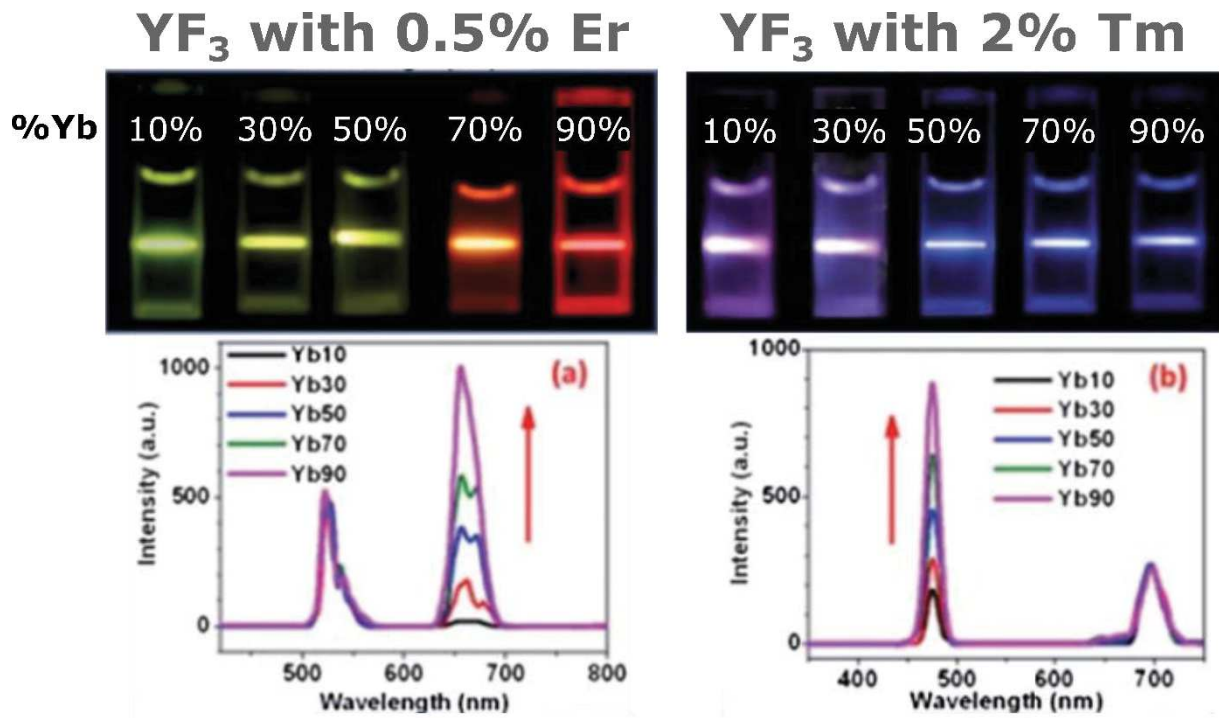


Figure 13. Impact of sensitizer content on the emission color. Adapted from ⁸⁴.

For erbium, the spectacular change in color was explained as an alteration of the upconversion energy path induced by the high level of ytterbium, and mostly by the energy back transfer to the sensitizer from the erbium energy levels responsible of the green emission. A similar mechanism also takes place with Tm but the 700 nm emission is poorly detected by the human eye.

On the other hand, this change in the energy dynamics induced by the increased amount of ytterbium can be exploited to “tune” the emitted light by promoting specifically a desired band. The next question is to know whether it is relevant to increase the emitter content.

III.2.2 High emitter content for high laser power density

Concerning the variation in ion content, it was shown above that enhancement of the sensitizer content can lead to an increased absorption in core@shell structure. Similarly, does an increased emitter content lead to an increased emission? Moreover, is it possible to combine high sensitizer and high emitter content?

As evoked earlier (section III.2), the emission efficiency is limited by the low content of sensitizer (0.5-1% for Tm or 2% for Er) to prevent concentration quenching occurring at higher doping, under usual excitation irradiance such as sub-100 W cm⁻² for the macroscopic measurement of particles.⁸⁵ However, single nanoparticle investigations, such as super-resolution evoked in section I, rely on the use of MW.cm⁻² (i.e. 10⁶ W cm⁻²) power densities. Thus, spectroscopists such as B. Cohen³⁴ and E. Goldys⁸⁵ teams investigated the influence of emitter content under such conditions. Indeed, by turning from tens of kW cm⁻² to MW cm⁻², a tremendous increase by a factor of 200 was observed in Tm-based UCNP luminescence between the usual 0.5% emitter and higher content such as 8%.^{34,85} It can be explained by the following principle: under high laser fluence (MW.cm⁻²) the population of Yb excited-state is increased (until saturation) leading to an increase of ETU probability. If there is a low amount of emitter, they are quickly saturated. However, by increasing the emitters concentration, the excitation energy stored in the sensitizer excited state will be effectively used. This results in luminescence enhancement.

In summary, current trends on doping content management are mainly focused on an increase of emitter content combined to higher laser power density irradiation, forsaking sensitizer enhancement. To the best of our knowledge no significant work explored the combination of simultaneous sensitizer and emitter increased content.

The following sections will briefly expose how an external partner (sensitizer or chromophore acceptor) can interact with the UCNP.

III.3 Downsizing issue: surface quenching

III.3.1 Source of surface quenching

Considering NaREF₄ nanoparticles, the main origin of non-radiative energy losses is due to surface quenching occurring from capping molecules and solvent through CH, OH or NH vibrations, especially in aqueous media.

Most of the efforts in the literature have been focused on the management of the surface quenching which is related to two points: NP size and surface passivation.

Regarding to the size, the smaller the NP, the bigger the surface-to-volume ratio. Thus, size reduction leads to a less favorable surface to volume ratio and a drop of luminescence. As a result, when small size is not a requirement, NP should be as big as possible to maximize the brightness.

III.3.2 Energy transfer to the surface (process F)

As it was briefly announced (section III, figure 11, with the A→B→F pathway), it is possible to imagine an energy transfer between a UCNP and a chromophore at the surrounding. A convenient mechanism commonly invoked in the literature is a FRET (Förster Resonance Energy Transfer) mechanism.

FRET definition

FRET is defined from Förster theory^{86,87} as a short-distance non-radiative dipole-dipole energy transfer between one donor D and one acceptor A, both being small enough to be considered as ponctual. Despite the initial FRET definition for point-to-point energy transfer between molecules such as organic dye, it can be also applied to nanoparticles. This energy transfer is a bimolecular process whose rate constant k_T is:

$$k_T = \frac{1}{\tau_D} \left(\frac{R_0}{r_{DA}} \right)^6 \text{ with } R_0^6 = \frac{9(\ln 10) \kappa^2 \Phi_D J}{128 \pi^5 n^4 N_A} \text{ and } J = \int f_D(\lambda) \epsilon_A(\lambda) \lambda^4 d\lambda$$

N_A : Avogadro constant

n : refractive index of the medium ($n=1.3$ for aqueous media)

r_{DA} : distance donor-acceptor

τ_D : lifetime of the donor excited state, in absence of acceptor

κ^2 : orientation factor (usually fixed at 2/3 for randomly oriented systems)

Φ_D : quantum yield of the donor

$f_D(\lambda)$: emission intensity of the donor at λ , normalized to 1 over the spectral window concerned

$\epsilon_A(\lambda)$: molar extinction coefficient of the acceptor as a function of the wavelengths

Beside the mandatory global spin conservation, critical points are the overlap integral J between donor D and acceptor A spectra, and the orientation factor κ^2 . The first can be computed separately and is usually used to optimize the choice of the pair (D, A) . For a classic pair of dyes, presenting an isotropic distribution of mutual orientations, κ^2 reduces to $2/3$. The theory brings a new parameter, the “Förster radius” (R_0) that enables one to compare the energy transfer rate constant to all the other processes that undergoes the excited state D^* of the donor in the absence of the acceptor. It is convenient to introduce the FRET efficiency E as:

$$E = \frac{k_T}{k_T + \frac{1}{\tau_D}} = \frac{R_0^6}{R_0^6 + r_{DA}^6}$$

When $r_{DA} < R_0$ then $E > 0.5$: in other words, the RET process counts for more than 50% of the total relaxation processes of the donor. Complete extinction occurs at very short distances only (fig14).

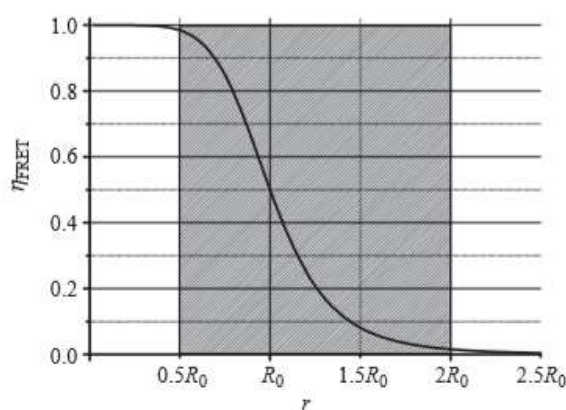


Figure 14. FRET efficiency as a function of the Donor-Acceptor distance. Reproduced from⁸⁶

Thus, different requisites are necessary for an efficient FRET:

- Spectral overlap between donor emission spectrum and the acceptor absorption spectrum;
- close distance between the dipoles;
- donor and acceptor should have respectively a high quantum yield and a high molar extinction coefficient.

Limits of FRET considerations with UCNPs

Once FRET formalism described, we can now focus on its application to energy transfer between UCNPs and surrounding molecules.

The first point to be discussed relies on UCNP quantum yield. In the Forster model, one couples the transition moments between ground and excited states of the donor and the acceptor, and the square of the transition moment μ_{DD^*} figures explicitly in the FRET rate constant. This transition moment is the link via the oscillator strength of the radiative relaxation of D^* to the radiative lifetime τ . For standard dyes, this radiative lifetime is $\frac{\tau_D}{\Phi_D}$, where Φ_D is the fluorescence quantum yield, and τ_D the lifetime of the donor. When UCNPs are concerned it is therefore important to know the radiative lifetime of the level involved in the FRET process. It is not related to the global upconversion quantum yield, but more akin to a branching ratio β defined as $\beta = k_{\text{rad}} / (k_{\text{rad}} + k_{\text{nr}} + k[\text{Yb}^*])$. Very few teams have considered this issue.⁸⁸

It has been admitted within the UCNP community that energy transfers between UCNP and acceptor are occurring by FRET. However, UCNP have an extremely low quantum yield (less than 1%). As a result expected Förster distance should be smaller than the usually expected 1-20 nm range (with conventional bright donor).⁸⁶

Another critical point on UCNP is that emitted light is coming from several emitters disseminated randomly inside a nanoparticle. For a very low emitter content one can neglect the possibility of Tm-Tm energy migration, therefore the contribution of each “emitter-to-acceptor” pairs to the global FRET process should be considered. Establishing a “FRET distance” should be at most computed from a weighted distribution of emitter-acceptor distances (figure 15):

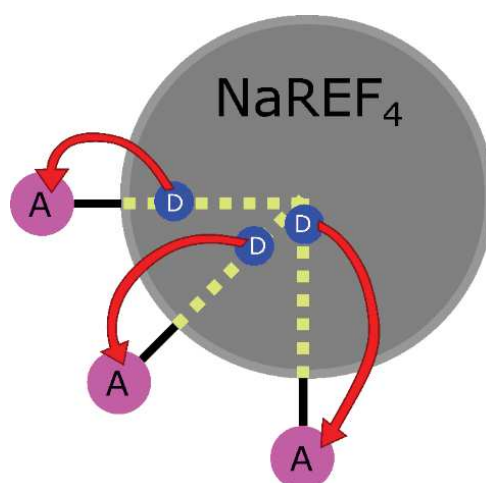


Figure 15. Different configurations of FRET, depending on emitter position. A-labelled pink and D-labelled blue spheres are respectively Acceptor and single emitter. Dark line is used to be the so-called “Forster distance”. Pale yellow dash-line represent UCNP radius. FRET is represented by red arrow.

As a conclusion, FRET with UCNP has to be treated carefully. Indeed, there is uncertainty

-in the dispersion of emitters (donors) inside one UCNP

-in the repartition of acceptor at UCNP surface

-in the definition of the real Förster distance (related to the random emitter localization).

Despite this lack of clarity, an important number of works with UCNP as donor in energy transfer have been reported. Such energy transfer is always described as FRET. Interested readers are addressed for example to work by N. Hildebrandt's team.^{89,90}

Additionally, no reported experiments were setup to assess if energy transfer, between UCNP and an acceptor, could be also coming from long distance mechanism such as trivial transfer.

UCNP Size effect

Large objects have a far larger radius (10-25 nm) than usual reported Förster distance (<10 nm for UCNP). Thus, only emitters placed close enough to the surface may generate an efficient energy transfer. As a result, large nanoparticles with a low surface-to-volume ratio show a reduced surface quenching by FRET compared to the small ones, explaining why downsizing UCNP results in loss of upconversion efficiency.

Thus, from assumed FRET mechanism, a simple strategy to enhance upconversion relies on enhancing the distance between UCNP donor and surface quenchers.

Consequences of NP to surface FRET: an inactive inner “dark layer”

As reported, by May *et al.*⁹¹, and Gargas *et al.*³⁴ it has been admitted that due to surface quenching, an inner “dark” layer (fig 12) being totally surface-quenched can be defined at the NP surface (figure 16).

Extension of Gargas FRET-based model estimated the thickness of this inner “dark” layer as 1.7 nm. As a result, UCNP smaller than 3.4 nm in diameter are not supposed to have a significant emission. Nevertheless, to the best of our knowledge, no experimental data at such critical ultrasmall size have been explored to check the validity of Gargas' model.³³

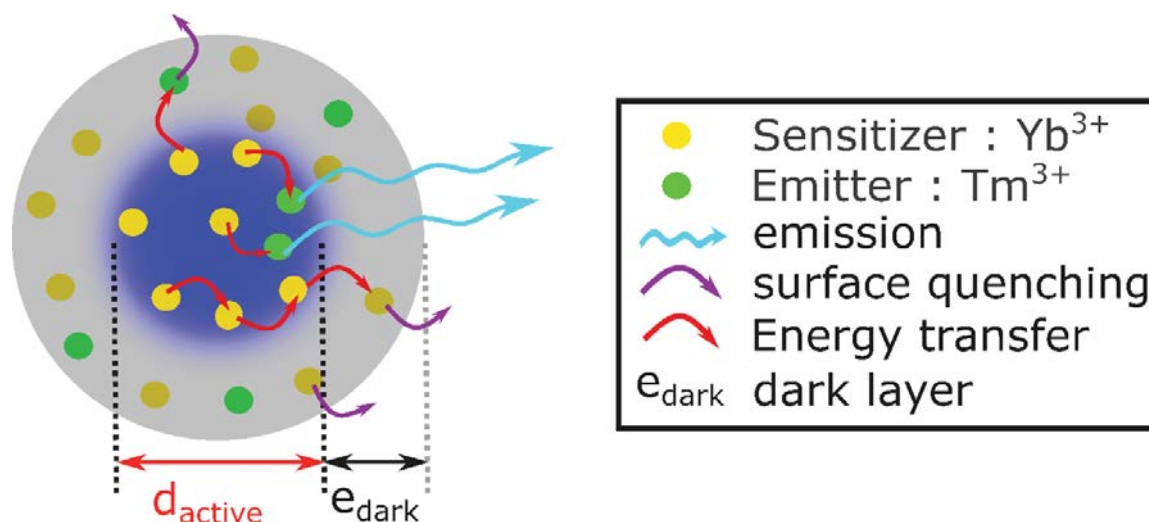


Figure 16. Surface quenching in UCNP

III.3.3 Solution to surface quenching: towards surface shielding

Core@shell structure for luminescence exaltation

The main strategy to overcome surface quenching consists on intercalating an inert spacer, thick enough to shield the surface from molecules at the surface (ligands, solvent, etc ...). It is generally achieved by growing an epitaxial layer of undoped matrix at the surface. This is now a routine architecture on UCNP⁹², as for QD. However, it has been empirically demonstrated that NaYF₄ is a more efficient shielding shell than NaGdF₄. This superiority has been abundantly reported⁹³ and will not be further discussed in this manuscript.

Towards UCNP applications: Core@shell consequence on FRET to a desired acceptor

Concerning doped-core@undoped shell structure, the intercalation of an inert shell (usually 1-6 nm thick layer) between donor and acceptor decreases the probability of presence of emitters. Consequently, compared to core of similar composition, a lower amount of emitters can be involved in such FRET. Thus, a compromise has to be found between luminescence enhancement (higher quantum yield) and “active distance” reduction (number of emitter), as stressed out by Y. Wang *et al.*⁹⁴ revealing more efficient energy transfer on core@shell from singlet oxygen generation by rose bengal acceptor.

To circumvent this issue, some teams investigate doped-core@doped-shell structure while placing sensitizer dopants in core and emitters in shell. However, as it was not explored in the present work, and will not be discussed here either. Interested readers should look for example at publications of A. Pilch *et al.*,⁹⁵ or K. Huang *et al.*⁹⁶

III.3.4 Yb as energy shuttle

As stressed out by C. Ma *et al.*, “the optimal sensitizer concentration in single UCNPs is not limited by the concentration quenching effect as long as surface defects and interior defects can be minimized”.⁹⁷ Especially, Stanley May & Mary Berry⁹¹ and Feng Wang⁹⁸ investigated the role of dopants in energy migration within a UCNP to the surface.

Energy migration in core UCNP

Marry Berry and coworkers⁹¹ have rationalized this phenomenon for Er-doped core UCNP. A rapid energy migration to the surface is occurring via successive energy transfer among Yb ions acting as an energy shuttle. It explains why high sensitizer loading in UCNP leads generally to a reduced luminescence, especially in the case of small UCNP. Such a process is strongly reduced upon addition of an undoped shell suppressing the surface quenching, as it will be more discussed in chapter 3.

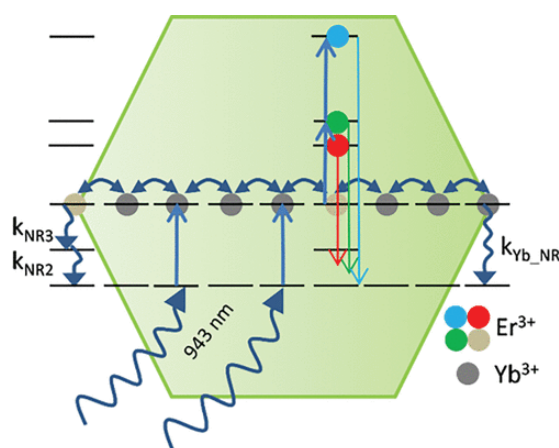


Figure 17. Schematic depiction of the nanoeffect in β -NaYF₄:Yb,Er. Rapid energy migration at the 1 μ m energy-level leads to equilibration between interior and surface sites, such that Er³⁺ (⁴I_{11/2}) and Yb³⁺ (²F_{5/2}) both exhibit enhanced multiphonon relaxation, labeled as k_{NR3} and k_{Yb_NR} , respectively. Figure and caption reproduced from ⁹¹.

Energy migration in core@shell structure

The impact on energy migration within the crystal as a function of the sensitizer content has also been particularly examined by F. Wang’s team working with a standard matrix (NaYF₄ or NaGdF₄.)⁹⁸

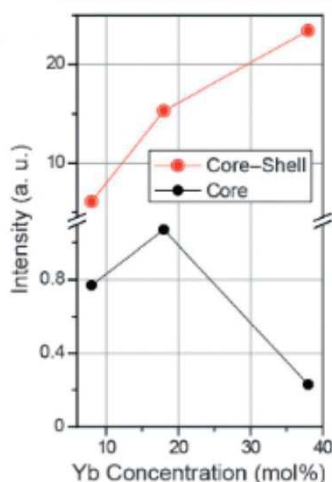


Figure 18. Impact of Yb content on β -UCNP emission intensity compared in NaYF₄:Yb,Er cores and their corresponding core@shell.⁹⁸

On a usual matrix (figure 18), concentration quenching happens above 20% of sensitizer. Nevertheless, core@shell architectures with similar core compositions reveal an increase intensity with sensitizer concentration. Indeed, at such high Yb content, sensitizers are close enough to ensure energy migration to the surface. When the shell is added, the surface cannot quench such energy, leading to luminescence increase. This indicates that high sensitizer content is compatible with core@shell structure to enhance upconversion efficiency. However, this particular exploration is limited to 40%Yb.

Compiling this work of Wang group with the beneficial effect of higher sensitizer content stressed out by Prasad group (section III.2.1), made us think that an original matrix Na(Yb_x-Gd_(1-x))F₄ covered by an undoped NaREF₄ (RE=Gd or Y) shell should lead to the formation of bright objects. Additionally, the work of Prasad⁸² pointed out a second expectation of such a matrix: By rising gadolinium content up to 40%, NP size is lowered, but it remains constant above this value. As a result an original Yb-Gd matrix with at least 40% Gd appears as a good compromise to go towards bright and small UCNPs.

Therefore, most of our work will focus on this original composition to prepare ultrasmall UCNPs: Na(Yb₅₇-Gd_{42%})F₄:Tm_{1%}.

III.4 Favoring radiative emission (Process D)

III.4.1 UCNP sensitization (process E)

As previously described, UCNP main phenomenon is ETU, thanks to Yb sensitization, setting in stone the excitation at 980nm. However, a chromophore, with an efficient absorption cross-section and an excited state higher in energy than the excited Yb one, can be used as a relay to feed UCNP system by transferring energy to Yb excited state. Thus, the new incident light is chosen to excite this new second sensitizer, following sensitization mechanism. UCNP sensitization (figure 11E) can be envisioned for two purposes: either increasing their absorption thanks to dye sensitization, or tune the excitation wavelength.

Absorption enhancement

Absorption enhancement can be achieved thanks to dye sensitization by incorporating highly absorbing antennas.^{99,100} Nevertheless, such approach is not very popular due to the time-consuming design of dye antenna and the low efficiency (one¹⁰⁰ or two⁹⁹ orders of magnitude) compared to upconversion efficiency enhancement with shell growth (up to 4 orders of magnitude).¹⁰¹

Tuning the excitation wavelength to prevent overheating

The main inconvenient of usual UCNP excitation (980 nm) is the overlap with strong water absorption that can induce overheating in biological applications. However, it can be overcome either by pulsing the laser (by pulse excitation or using a chopper), or by exciting with another wavelength which is less absorbed by water.

The latter can be achieved thanks to another Rare Earth (RE) element with adapted cross-section, neodymium, which is absorbing in the 790-810 nm range and used as an antenna to excite ytterbium.²⁸ Indeed, by switching from 980 to 800 nm (figure 19) the excitation laser, water absorption coefficient is 24 times lowered from 0.482 to 0.02 L.mol⁻¹.cm⁻¹ (fig18).¹⁰² This strategy may represent the future for biological applications, but is beyond the scope of this manuscript.

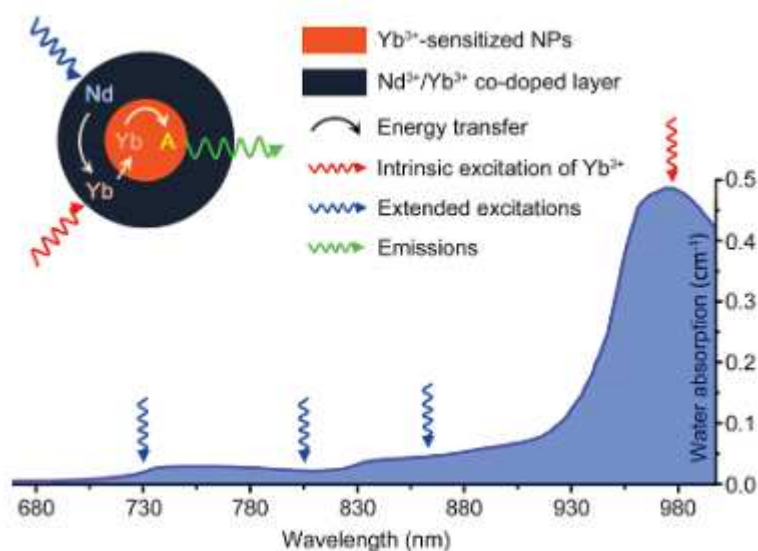


Figure 19. Absorption of water in the NIR and the integration scheme of $\text{Nd}^{3+} \rightarrow \text{Yb}^{3+}$ energy transfer process by introducing neodymium in a Nd/Yb co-doped shell physically separated from the emitters. Figure and caption adapted from ²⁸.

IV Towards water-soluble UCNP

IV.1 Challenge of surface coating for biology and nanomedicine

IV.1.1 Importance in Biology

Usually, the nanoparticle's surface is covered by an organic or inorganic layer, providing mainly solubility and long-term stability. Focusing on inorganic@organic nanohybrid, such assemblies can be prepared following two approaches: in situ formation, or post-modification of NP surface.

However, once exposed to biological content, the surface will likely be modified, changing the complete nanohybrid properties. Nevertheless, organic coating can also give access to other properties (for example by grafting another probe for bimodal imaging), or targeting.

Thanks to the well-known easy NP surface functionalization, a variety of labelling units can be exploited such as small organic molecules (folic acid)¹⁰³, carbohydrates, peptides (RGD)¹⁰⁴, proteins, antibodies, aptamers¹⁰⁵, etc ...

Cell internalization of such nanohybrids is related to their hydrodynamic diameter, surface charge, and shape. It has been demonstrated by S. Zhang *et al.*¹⁰⁶ that the rate of cellular uptake is maximized via endocytose pathway for nanoparticles having a diameter of about 50 nm, thanks to an optimized number of interaction with close cellular surface receptors. Nevertheless, endocytosis is also affected by the shape: anisotropic rods have been shown to

present higher uptake level than isotropic NPs.¹⁰⁷ Moreover, as the plasma membrane is negatively charged, positively charged nanohybrids are more likely to be integrated.

IV.1.2 Specific issues in Nanomedicine

When introduced in the general circulation, two problems can be found: exposition to the immune system, and persistence in the body.

For instance the adsorption of opsonins at the surface can lead to phagocytosis by macrophage (opsonization).¹⁰⁸ Prolonged circulation half-life can be reached by introducing stealth properties, especially thanks to surface PEGylation.¹⁰⁹

Within a whole mammal, nanohybrid elimination is achieved by either renal or hepatic clearance. The current trend in reducing NP toxicity relies on promoting renal elimination in order to have a shorter *in vivo* residence time than the kinetics of the toxic phenomenon (such as metal leaking for example). Kidney filtration is linked to the permeability of the negatively charged glomerulus basement membrane. Experimentally, its threshold allows filtration of any kind of sub-6 nm, and positively charged sub-8nm NPs.¹¹⁰ For other non-biodegradable NPs, hepatobiliary system is usually considered as the only alternative mode of elimination.¹¹⁰

IV.2 Strategies for water-solubilization

As biological medium is mostly aqueous, one can be interested in using water dispersible UCNPs. Two main routes are available: except in the case of hydrothermal synthesis, crude UCNPs synthesized are hydrophobic due to the nature of the ligand (usually oleate OA).

Brightness seems to be more efficient with hydrophobic nanoparticles.¹¹¹ As a result, UCNP are only soluble in apolar solvents such as cyclohexane, toluene, THF, xylene, octadecene, oil. The main application of UCNP being in biology, the challenge is to transfer them into water while keeping the optical properties. This problem became a major issue these ten last years and a lot of strategies have been reported,^{71,112} as we summarize below (figure 20) :

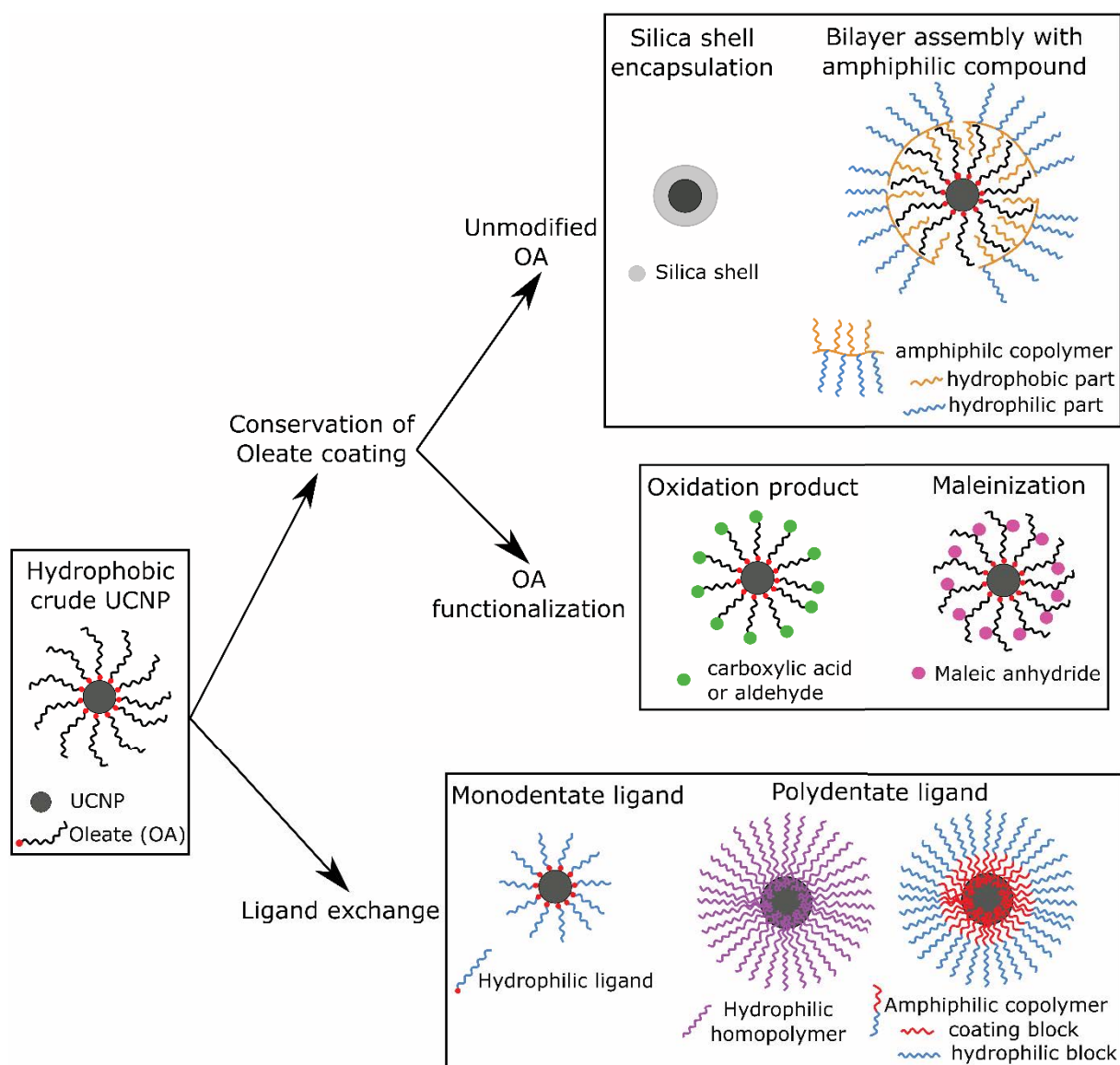


Figure 20. Schematic representation of strategies to get water-soluble UCNPs.

Two points of view are contrasted: maintaining or not the oleate ligand at the surface of UCNPs.

Maintaining OA

The first way is to maintain oleate at the surface. By doing this, there are 2 main approaches: modifying or not the structure of oleate.

The most usual strategy for inorganic nanoparticles (for example zinc oxide or iron oxide) is to maintain the original oleate capping and grow at the surface a silica shell layer. A silica shell can afford directly water-dispersibility, while being a versatile platform for further functionalization such as targeting or coupling with other probes. The drawback of encapsulating UCNPs into a silica shell are the increase in NP polydispersity compared to the

uncoated one, the instability in aqueous solution (in acidic or basic media), and the difficulty to form a thick silica layer.^{113,114}

The second approach when keeping unmodified OA is the use of amphiphilic compounds, such as phospholipids or amphiphilic comb copolymers such as those derived from alternate copolymers of maleic anhydride and various olefins (figure 21). The hydrophobic part (usually long alkyl chains) intercalates between the alkyl chains of oleate, while the hydrophilic one is directed outward. This bilayer assembly is governed by Van der Waals interactions. Contrary to phospholipids, such amphiphilic polymers allow the possibility of multiple functionalizations through anhydride “click chemistry”.

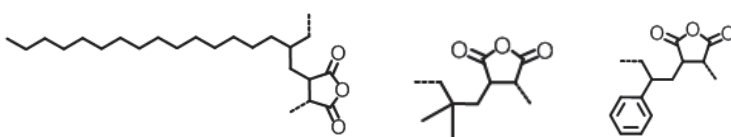


Figure 21. Repetitive units of, from the left to the right, poly(octadecene-*alt*-maleic anhydride) “POMA”, poly(isobutene-*alt*-maleic anhydride) “PIMA”, and poly(styrene-*alt*-maleic anhydride) “PSMA”.

Post-modification on OA

The oleate post-modification pathway is related to the reactivity of the carbon-carbon double bond of ligand (oleate), mainly through oxidation such as ozonolysis,¹¹⁵ epoxidation (m-CPBA),¹¹⁶ or more frequently Lemieux-Von Rudloff oxidation (mixture MnO_4^- , IO_4^-).¹¹⁷ The resulting azelaic acid or aldehyde can be well dispersed in water or ethanol, while keeping the same size and shape.¹¹⁵ Nevertheless, very harsh reaction conditions, long reaction times, low chemical yield associated to a poor colloidal stability in water, and a limited number of ligands can explain why this approach is not commonly used. A different strategy was reported, although only once, by transposing a well-known maleinization^{118,119} reaction from lipids chemistry to NP surface chemistry by E. Peng *et al.*¹²⁰ Despite the attractive post-functionalization perspectives of succinic anhydride grafting in alpha position of the double bond, this strategy remains suspicious while being so unexploited.

Ligand exchange

An alternative of the above described strategy based on keeping OA at the surface, is to clear the latter and build on demand a new organic corona. Such ligand exchange can be achieved either by direct contact with higher affinity ligand, or by the removal of OA in acidic condition (hydrochloric treatment¹²¹ or nitrosyltetrafluoroborate (NOBF_4)¹²² treatment)

followed by surface covering with a new capping ligand. NOBF₄ approach, being performed in organic solvent (DMF), permits a convenient long-term stability in solvent adapted for storage, and a more efficient OA removal.¹²³

Whichever the ligand exchange strategy it has been admitted that the ligand strength of interaction should be in rising order: -SH < -NH₂ < -COOH < -PO₃H.

Despite the risk of NP crosslinking, polydentate ligands ensure a better stabilization due to strong entropic effect. Some usual ligands are listed below (table 5), as an illustration.

Table 5. Usual coating agents suitable for UCNP exchange ligand

	Compound	Capping group	Apparent charge
Monodentate	O-phosphorylethanolamine (AEP) ¹²⁴	-PO ₃ H	(+)
	PEG-Phosphonate or PEG-carboxylate ¹²⁵	-PO ₃ H or -COOH	neutral
	citrate ¹²⁶	-COOH	(-)
	Poly(VinylPyrrolidone) (PVP) ¹²⁷	lactame	neutral
	Poly(Acrylic acid) (PAA) ^{127,128}	-COOH	(-)
Polydentate	Poly(Vinyl Phosphonic Acid) (PVPA) ¹²⁹	-PO ₃ H	(-)
	PAA- <i>b</i> -PEG ¹³⁰	-COOH	neutral
	PVPA- <i>b</i> -PEG ¹²⁹	-PO ₃ H	neutral
	Poly(Allylamine Hydrochloride) (PAH) ¹³¹	-NH ₂	(+)
	Poly(EthyleneImine) (PEI) ¹²⁷	-NH ₂ ; -NH ₃ ⁺	(+)

IV.3 Limit of water-solubilization

Once moving UCNP in aqueous media, following one of the above-described methods, one has to consider the consequences on optical properties and colloidal stability in water and biological media.

Loss of optical properties

Despite various strategies being available for water-solubilization, all of them lead to a drop of upconversion efficiency due to surface quenching from water (sub-section III.3.1).

Stability in water

Due to the presence of endogenous electrolytes (section I.2), some byproduct can be formed due to ion exchange (table 6).

Table 6. Solubility product constant (K_{sp}) at 25°C of some Rare-Earth precipitate, and some apatite under physiological condition (pH=7.4; temperature=37°C).

	K_{sp} at 25°C	K_{sp} at 37°C, pH≈7.4
NaYF ₄	1.6×10^{-26} ¹³²	
CaF ₂	5.3×10^{-9} ¹³³	
YF ₃	8.6×10^{-21} ¹³³	
NaF	7.1×10^{-1} ¹³⁴	
YPO ₄	1.7×10^{-25} ¹³⁵	
GdPO ₄	4×10^{-26} ¹³⁵	
Y(OH) ₃	1.0×10^{-22} ¹³³	
Gd(OH) ₃	1.8×10^{-23} ¹³³	
Ca ₁₀ (PO ₄) ₆ (OH) ₂ calcium hydroxyapatite		7.4×10^{-60} ¹³⁶
Ca ₁₀ (PO ₄) ₆ F ₂ calcium fluorapatite		3.2×10^{-61} ¹³⁶

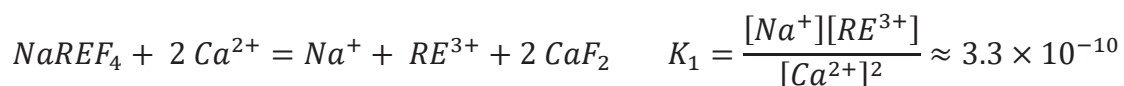
In vitro

At first, precipitation competition with free electrolytes available in blood (such as calcium, potassium and phosphate), have to be envisioned at the *in vitro* scale. Thermodynamic grounds of the particle dissolution can be delineated considering the solubility product of NaREF₄. It was only estimated in one recent publication,¹³² no more precise quantitative comparison can be made.

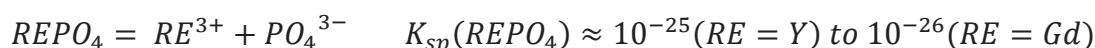


The solubility can be increased by common ion effect: especially the important biological electrolytes calcium and phosphate can indeed form precipitates with the elements contained in the nanoparticle.

Thus, calcium can scavenge fluoride with the formation of fluorine CaF_2 according to



The second reaction is more important: it is the precipitation of rare earth phosphates. It was found that Rare-Earth phosphate and NaREF_4 have similar solubility product ($K_{sp} \approx 10^{-26}$).



Therefore, the reaction between NaREF_4 and phosphate is rather favorable:



Experimentally, NaREF_4 NPs dissolution was noticed *in vitro*, in low NP-concentration condition and exposed to high phosphate content (phosphate buffer).^{132,134} However, some kinetic considerations should also be taken into account, especially the residence-time of nanoparticles in a biological compartment and their surface coating.

To the best of our knowledge only one ligand was proven to afford a protection against water dissolution: poly(Maleic anhydride-*alt*-1-Octadecene)-bis(hexamethylene)triamine (POMA-BHMT).¹³⁷

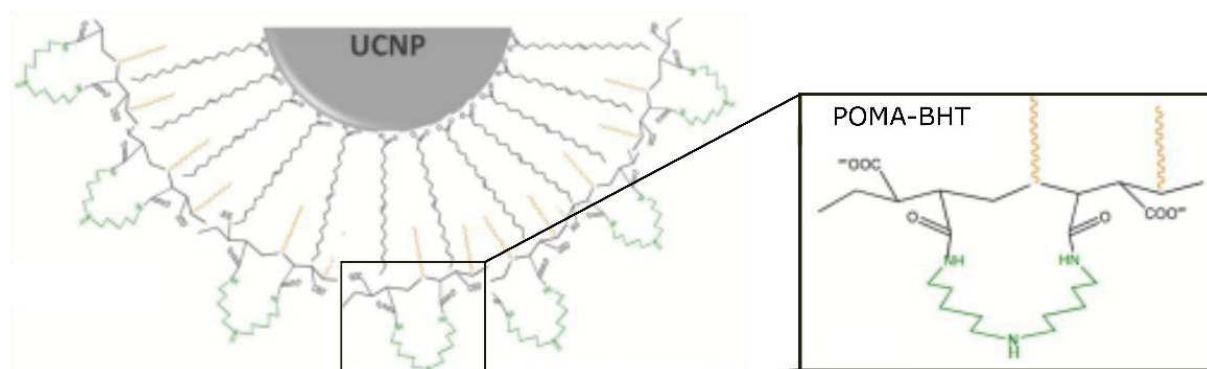


Figure 22. Structure of POMA-BHMT. Reproduced from ¹³⁷.

In vivo

After validation of the first colloidal stability assays with ion competitors in water, a final critical point towards *in vivo* application is the interaction with biological scavenger such as hydroxyapatite. These inorganic complexes¹³⁶ (mainly located in teeth and bones) made of calcium, phosphate and hydroxide have an abysmal solubility product ($\approx 10^{-60}$), but even lower when substituting hydroxide by fluoride ($\approx 10^{-61}$). Thus, it can have a similar deleterious action as Ca^{2+} .

V Applications of UCNP

V.1 Overview on UCNP main applications

Lanthanide-based UCNPs are emerging materials with several applications, until now mainly related to biology (figure 23).¹³⁸ The most evident application is to use them as luminescent nanoprobes for optical imaging. However, UCNP luminescence can be also exploited either as a reporter or an actuator. As reporter, they are used for imaging and sensing. As an actuator, they are used as a local relay to trigger photo-induced transformations, thanks to UCNP UV-visible emissions under NIR excitation.

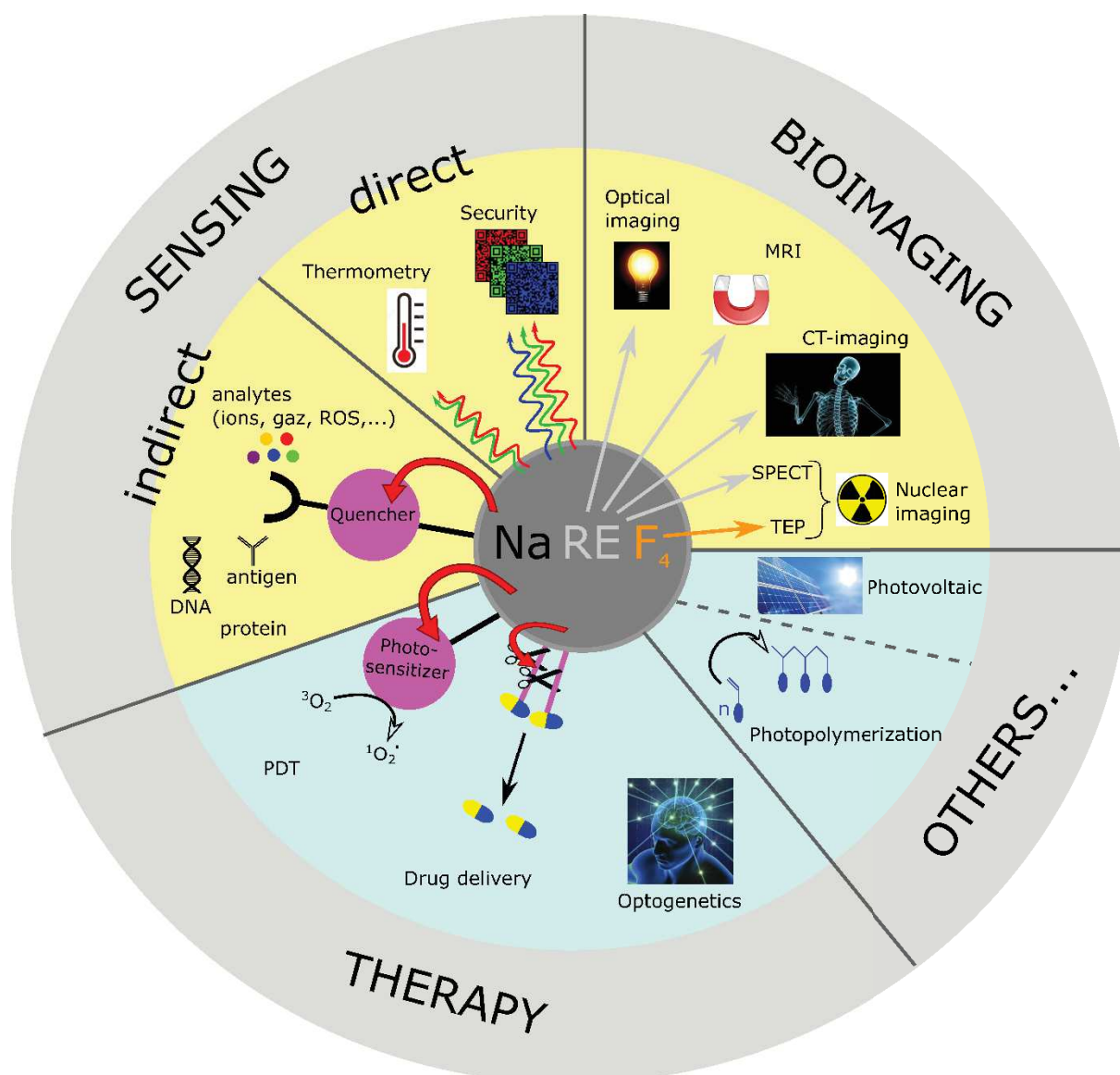


Figure 23. Applications of UCNP classed in two categories: UCNP as reporter (yellow) or actuator (light blue). Red arrow indicates FRET (Förster Resonance Energy Transfer) phenomena with donors such as chromophore (sensing), photosensitizer (PDT), or photocleavable bond (drug release).

V.1.1 UCNP as reporter

Multimodal bioimaging

Thanks to their intrinsic composition, UCNPs give access to others types of imaging techniques, such as MRI, X-ray- (2D) & CT-imaging (3D), and nuclear imaging. Compared to usual probes, i.e. single chromophore or metal complex, NP-based probes allow concentration and confinement of a high amount of single probe inside one nanoparticle, leading to higher signal.

Gadolinium being the ion of choice for MRI (Magnetic Resonance Imaging), due to its high spin number ($s=7/2$), NaGdF₄ appears as an ideal matrix for bimodal MRI/Optical imaging. Nevertheless, MRI and optical imaging have an antagonist behavior regarding the nanoparticle size: The smaller the NPs, the bigger the surface-to-volume ratio is. Thus, with ultrasmall NPs, there is strong surface exchange, leading to a drop of upconversion efficiency but a MRI signal enhancement in the context of Gd-based T₁ agents.¹³⁹ As a result, a compromise has to be established to design such bimodal probes. Lanthanides are heavy metals; hence they are perfectly adapted to X-ray- & CT-imaging to increase contrast. Concerning nuclear imaging, fluoride can be substituted partially by its corresponding radioisotope ¹⁸F for PET (Positron Emission Tomography). However, due to its low half-time (≈ 110 min) it is not a convenient choice. A better strategy for nuclear imaging should be the use of ¹⁵³Sm³⁺ for SPECT (Single Photon Emission Tomography) with $t_{1/2}=46.3$ h. Such isotope can be incorporated by replacing Rare-earth matrix components, either at the early stage of the synthesis, or more easily by contact to UCNP already prepared.¹⁴⁰ Others techniques start to be transposed to UCNP, for example photoacoustic imaging.

In addition, theranostic UCNP-based platform are design by associating imaging modalities to therapy. For example, M. Sun *et al* ¹⁴¹ designed one of the most relevant multimodal nanohybrid, by combining four modalities (optical imaging/MRI/CT-imaging/photoacoustic imaging) with two therapeutics actions (photodynamic and photothermal therapies).

Sensing

Aside from optical imaging, light emitted by UCNP can be used as reporter or actuator.

Direct sensing involves two major applications: thermometry and invisible inks for security. Thermometry imposes the use of Er³⁺-doped UCNP. In erbium spectra the green-to-red and green-to-green intensity ratios, respectively between peaks at 540 & 650 nm, and 525 & 545 nm are varying with temperature. Thus, once calibrated, it can be used as an accurate

temperature sensor. For curiosity, one should address to the work of the leading team of F. Vetrone.¹⁴²

Indirect sensing is based on on/off FRET activation triggered by close contact with the target of interest, as described in FRET subsection (III-3-3). Analytes such as ions, gas (CO₂, O₂, NO₂), reactive oxygen species (ROS, NOS), or biomolecules (antigen, protein, enzyme, RNA, DNA, ...) can be detected.

For more details about sensing application, reader should address to reviews such as B. Gu *et al.*¹⁴³

V.1.2 UCNP as actuators

UCNP-assisted phototherapy

The second kind of applications, as actuator, are mainly based on the use of UCNP as a nanolamp. These nanolamps are used to produce visible to UV light locally in deep-tissue, upon NIR excitation. Hence, usual photoreactive systems are transposed with UCNP, such as photodynamic therapy (PDT), photothermal therapy (PTT), drug-release or optogenetics.

The latter being the most outstanding, it enables the manipulation of membrane ion channels rhodopsin¹⁴⁴ or neuronal activity.^{145,146}

Other (non-biological) applications

UCNP can also trigger non-biological actions. As a result they can be used in photocatalysis, such as photopolymerization application, for example with trithiocarbonate-based RAFT agents.¹⁴⁷

In solar cells, UCNP appear as a good complement to the existing devices (limited to 200-1200 nm for c-Si), as the RE emitters used as antennas should extend the absorbance area to deeper NIR.¹⁴⁸

V.2 UCNP as a luminescent probe

Nanoparticle-based probes

Nanoparticle-based probes are expected to display additional features compared to traditional organic dyes.

*Enhanced photostability, as the luminescent moiety can be shielded from the biological quenchers

*versatile and simple synthesis, enabling large variation of spectroscopic properties and target affinity or the introduction of additional properties leading to multimodal probes

*Eventually, nanoparticle-based probes are intrinsically large, therefore they can be used to address specific metabolic issues such as internalization or trafficking mechanisms.

As for probes based on conventional organic dyes, luminescent nanoparticles based tags are made of two (or more) components: a luminescent core and an organic ligand corona to interface with the biological medium.

Among the versatility of potential UCNP application, our focus is on optical imaging at different scales. The following short section will present how Tm emitter-based UCNP appear as ideal probe to address a unique NP to various optical imaging purposes: from tissue imaging towards tracking and super-resolution.

V.2.1 Tm-based UCNP: a multimodal nanolamp

NIR-to-NIR imaging of tissue

In upconversion condition, Thulium emission spectrum is split into 2 regions: a very intense emission band in the NIR (802 nm) and multiple more or less intense peaks in the visible and UV domains (figure 24).

As a result, it is the only emitter allowing NIR-to-NIR imaging. Thus, both excitation beam and NIR emitted light can go through tissue, allowing a less invasive deep-tissue imaging.

Simultaneous tracking and therapy

Non-blinking NIR emission band is perfectly adapted to tracking, as it allows the continuous monitoring through tissue. On the other hand, the other less emissive bands (mainly UV and blue, or red) are more adapted to excitation of photosensitive systems for example for PDT or drug-release. Thus, local photoeffect can be triggered on demand.

As UCNP are highly nonlinear materials, low excitation power density allows only the super intense NIR band, while the others are gradually revealed at higher power. As a result, a potential clinical application should be declined in two steps:

- 1) At first, under low power laser excitation, a surgeon should localize the NP, as only the NIR band is detectable
- 2) once irradiating the target area, the laser power should be raised, revealing visible and UV emissions, thus triggering local effect.

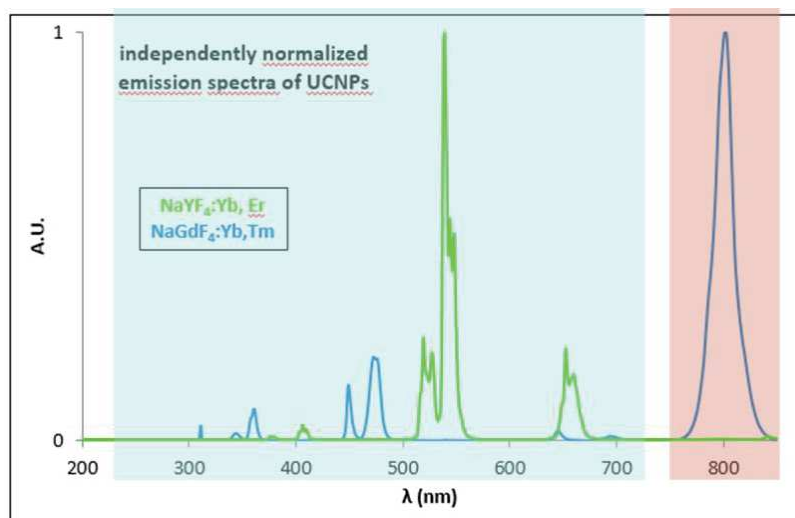


Figure 24. Emission spectra of UCNP. Pink area is attributed to peaks of interest for NIR-to-NIR deep-tissue imaging. Blue area represents emission bands useful to induce local photochemical effect.

V.2.2 UCNP and Super-resolution microscopy

The former subsection revealed the interest of Tm-based UCNP for imaging. But it is not only limited to tissue imaging and can be applied also to modern microscopy techniques such as super-resolution microscopy. As it was already presented at the beginning of the chapter (section I), two main strategies can be distinguished: STED-like methods or stochastic ones. The latter requires the use of light-fluctuating emitter points such as bleaching or blinking. As a result, UCNP are not adapted, in appearance, due to their extreme photostability (no blinking, no bleaching), but STED approach should be envisioned by interacting with the complex Tm

excited states' kinetic network. Indeed, in 2017, the first successful implementations of UCNP for super-resolution microscopy were reported, by using STED methodology (figure 25).¹⁴⁹ The strategy is based on the coupling of 980 nm, for usual ETU phenomenon, with a second one at 808 nm. The second beam induces depopulation of the 3H_4 Tm-level which is responsible of the NIR emission (802 nm). However, it should be noted that such STED methods requires higher emitter content to get a more accurate excited state relaxation where 980 nm and 800 nm beams are superimposed.

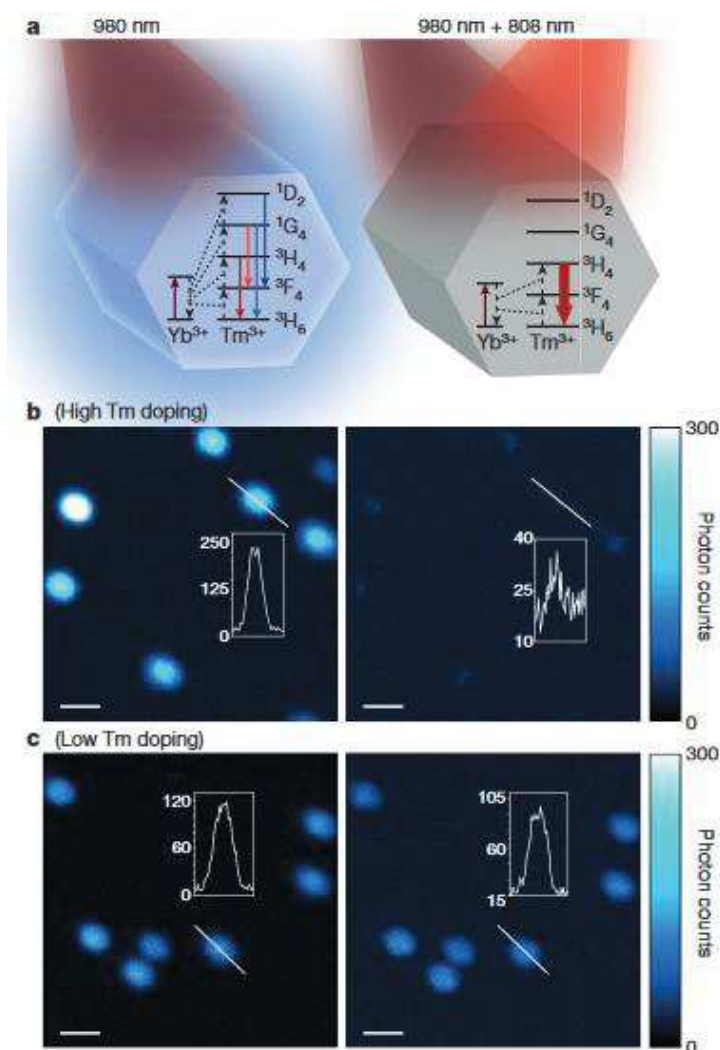


Figure 25. Upconversion luminescence using dual-laser illumination. A) Energy level diagrams of Yb/Tm co-doped UCNPs under 980 nm illumination (left) or both 980 and 808 nm illumination (right). b) Confocal images in 455 nm upconversion emission of 8%Tm-doped UCNP under CW 980 nm laser (left) or under both 980 and 808 nm dual CW laser excitation (right). c) Similar image than B) but with standard 1%Tm doping instead of 8%. For b) and c) the 980 nm and 808 nm laser powers measured at the objective back aperture were 1mW and 5mW respectively. Each inset shows the luminescence signal profile along the diagonal white line in that panel across a typical nanocrystal. Pixel dwell time, 4ms; scale bar, 500 nm. Reproduced from ¹⁴⁹.

Nevertheless, up to now, an area of interest remains unexplored: a stochastic approach for super-resolution with UCNP. Thus, we decided to investigate it, as described in the next subsection and in the last chapter.

VI Aim of the manuscript

My PhD topic is part of an ANR-funded project called BLINK: Luminescent nanoparticles with remote control of blinking for application in super-resolution microscopy and tracking. Hence the aim of my work was at first to design small and bright upconverting nanoparticles suitable for super-resolution microscopy, that had not been demonstrated when the project started (2016). We focused on stochastic imaging, specifically SOFI. As a result, the great challenge is to make the non-blinking UCNP blink.

The idea was to couple small Tm-UCNP with a photochromic shutter in order to build a pseudo-blinking nanohybrid. Tm emitter is chosen as blue emission is more adapted to the reversible photoswitching of the blinking shutter. Moreover, this probe can also be tracked thanks to its NIR emission.

The present manuscript will describe how my work was setup in order to go towards this application.

-**Chapter 2** discusses the synthesis of UCNP nanoparticles from scratch, with a particular attention to size reduction. Compared to the existing strategies, an original hybrid Na(Gd_{42%}-Yb_{57%})F₄ matrix doped by 1%Tm was developed to provide more emissive objects thanks to an increased absorption.

-**Chapter 3** highlights photophysical properties of UCNPs and an original analytical approach to move towards the proposition of a new kinetic model adapted to energy flux migration between dopant energy levels.

-In **Chapter 4** will be developed applications of UCNP as nanolamps.

At first, attempts to characterize the nanolamps by a chemical actinometry approach will be exposed.

Then, application towards SOFI-based super-resolution application will be introduced: from the choice and synthesis of the photochromic shutter, to the design of the water-soluble nanohybrid. First results towards the feasibility of this application will be discussed.

VII References

- 1 Weissleder, R. & Nahrendorf, M. Advancing biomedical imaging. *Proceedings of the National Academy of Sciences* **112**, 14424-14428 (2015).
- 2 Lin, Y., Nienhaus, K. & Nienhaus, G. U. Nanoparticle Probes for Super-Resolution Fluorescence Microscopy. *ChemNanoMat* **4**, 253-264 (2018).
- 3 Willig, K. I., Rizzoli, S. O., Westphal, V., Jahn, R. & Hell, S. W. STED microscopy reveals that synaptotagmin remains clustered after synaptic vesicle exocytosis. *Nature* **440**, 935 (2006).
- 4 Hugelier, S., Eilers, P., Devos, O. & Ruckebusch, C. Improved superresolution microscopy imaging by sparse deconvolution with an interframe penalty. *Journal of Chemometrics* **31**, e2847 (2017).
- 5 Dertinger, T., Colyer, R., Iyer, G., Weiss, S. & Enderlein, J. Fast, background-free, 3D super-resolution optical fluctuation imaging (SOFI). *Proceedings of the National Academy of Sciences* **106**, 22287-22292 (2009).
- 6 Fernández-Suárez, M. & Ting, A. Y. Fluorescent probes for super-resolution imaging in living cells. *Nature Reviews Molecular Cell Biology* **9**, 929 (2008).
- 7 Huang, D. *et al.* Optical coherence tomography. *Science* **254**, 1178-1181 (1991).
- 8 Berger, C. The near infrared (NIR) optical window. <http://www.biomedima.org/en/home/glossary?modality=5&slide=362>, accessed on 06/01/2019.
- 9 Defineyourstyle.co. Intense pulse light treatment. <http://www.defineyourstyle.co.nz/ipl>, accessed on 06/01/2019 (2011).
- 10 Karp, G. *Cell and molecular biology: concepts and experiments*. (John Wiley & Sons, 2009).
- 11 Koltai, T. Cancer: fundamentals behind pH targeting and the double-edged approach. *Oncotargets and therapy* **9**, 6343 (2016).
- 12 Wolfbeis, O. S. An overview of nanoparticles commonly used in fluorescent bioimaging. *Chemical Society Reviews* **44**, 4743-4768 (2015).
- 13 Jin, D. *et al.* Nanoparticles for super-resolution microscopy and single-molecule tracking. *Nature Methods* **15**, 415-423 (2018).
- 14 Resch-Genger, U., Grabolle, M., Cavaliere-Jaricot, S., Nitschke, R. & Nann, T. Quantum dots versus organic dyes as fluorescent labels. *Nature Methods* **5**, 763, (2008).
- 15 Nadort, A. *et al.* Quantitative Imaging of Single Upconversion Nanoparticles in Biological Tissue. *PLOS ONE* **8**, e63292 (2013).
- 16 Auzel, F. Upconversion and Anti-Stokes Processes with f and d Ions in Solids. *Chemical Reviews* **104**, 139-174 (2004).
- 17 Zhou, J., Liu, Q., Feng, W., Sun, Y. & Li, F. Upconversion Luminescent Materials: Advances and Applications. *Chemical Reviews* **115**, 395-465 (2015).
- 18 Leblond, F., Davis, S. C., Valdés, P. A. & Pogue, B. W. Pre-clinical whole-body fluorescence imaging: Review of instruments, methods and applications. *Journal of Photochemistry and Photobiology B: Biology* **98**, 77-94 (2010).
- 19 Bunzli, J. C. Lanthanide luminescence for biomedical analyses and imaging. *Chem Rev* **110**, 2729-2755 (2010).
- 20 Gao, S. & Affronte, M. *Molecular nanomagnets and related phenomena*. Vol. 164 (Springer, 2015).
- 21 Moore, E. G., Samuel, A. P. S. & Raymond, K. N. From Antenna to Assay: Lessons Learned in Lanthanide Luminescence. *Accounts of Chemical Research* **42**, 542-552 (2009).

- 22 Chen, G., Qiu, H., Prasad, P. N. & Chen, X. Upconversion Nanoparticles: Design, Nanochemistry, and Applications in Theranostics. *Chemical Reviews* **114**, 5161-5214 (2014).
- 23 Naccache, R., Yu, Q. & Capobianco, J. A. The Fluoride Host: Nucleation, Growth, and Upconversion of Lanthanide-Doped Nanoparticles. *Advanced Optical Materials* **3**, 482-509 (2015).
- 24 Eliseeva, S. V. & Bünzli, J.-C. G. Lanthanide luminescence for functional materials and bio-sciences. *Chemical Society Reviews* **39**, 189-227 (2010).
- 25 Hehlen, M. P., Brik, M. G. & Krämer, K. W. 50th anniversary of the Judd–Ofelt theory: An experimentalist's view of the formalism and its application. *Journal of Luminescence* **136**, 221-239 (2013).
- 26 Vega, M., Alemany, P., Martin, I. R. & Llanos, J. Structural properties, Judd–Ofelt calculations, and near infrared to visible photon up-conversion in Er³⁺/Yb³⁺ doped BaTiO₃ phosphors under excitation at 1500 nm. *RSC Advances* **7**, 10529-10538 (2017).
- 27 Yao, G., Lin, C., Meng, Q., Stanley May, P. & Berry, M. T. Calculation of Judd-Ofelt parameters for Er³⁺ in β-NaYF₄: Yb³⁺, Er³⁺ from emission intensity ratios and diffuse reflectance spectra. *Journal of Luminescence* **160**, 276-281 (2015).
- 28 Wang, Y.-F. *et al.* Nd³⁺-sensitized upconversion nanophosphors: efficient in vivo bioimaging probes with minimized heating effect. *ACS nano* **7**, 7200-7206 (2013).
- 29 Kushida, T., Marcos, H. & Geusic, J. Laser transition cross section and fluorescence branching ratio for Nd³⁺ in yttrium aluminum garnet. *Physical Review* **167**, 289 (1968).
- 30 Strohhofer, C. *Optical properties of ion beam modified waveguide materials doped with erbium and silver*, Utrecht University, PhD thesis, (2001).
- 31 Lingeshwar Reddy, K., Balaji, R., Kumar, A. & Krishnan, V. Lanthanide Doped Near Infrared Active Upconversion Nanophosphors: Fundamental Concepts, Synthesis Strategies, and Technological Applications. *Small* **14**, 1801304 (2018).
- 32 Auzel, F. Upconversion processes in coupled ion systems. *Journal of Luminescence* **45**, 341-345 (1990).
- 33 Chan, E. M., Gargas, D. J., Schuck, P. J. & Milliron, D. J. Concentrating and Recycling Energy in Lanthanide Codopants for Efficient and Spectrally Pure Emission: The Case of NaYF₄:Er³⁺/Tm³⁺ Upconverting Nanocrystals. *The Journal of Physical Chemistry B* **116**, 10561-10570 (2012).
- 34 Gargas, D. J. *et al.* Engineering bright sub-10-nm upconverting nanocrystals for single-molecule imaging. *Nature Nanotechnology* **9**, 300 (2014).
- 35 Levy, E. S. *et al.* Energy-Looping Nanoparticles: Harnessing Excited-State Absorption for Deep-Tissue Imaging. *ACS Nano* **10**, 8423-8433 (2016).
- 36 Laforge, F. O., Kirschner, M. S. & Rabitz, H. A. Shaped incoherent light for control of kinetics: Optimization of up-conversion hues in phosphors. *The Journal of Chemical Physics* **149**, 054201 (2018).
- 37 Park, W., Lu, D. & Ahn, S. Plasmon enhancement of luminescence upconversion. *Chemical Society Reviews* **44**, 2940-2962 (2015).
- 38 Yu, D., Ballato, J. & Riman, R. E. Temperature-Dependence of Multiphonon Relaxation of Rare-Earth Ions in Solid-State Hosts. *The Journal of Physical Chemistry C* **120**, 9958-9964 (2016).
- 39 Haase, M. & Schafer, H. Upconverting nanoparticles. *Angew Chem Int Ed Engl* **50**, 5808-5829 (2011).
- 40 Dong, B. & Liu, D. P. Optical thermometry through infrared excited green upconversion emissions in Er³⁺–Yb³⁺ codoped Al₂O₃. *Applied Physics Letters* **90**, 181117 (2007).
- 41 Matsuura, D. Red, green, and blue upconversion luminescence of trivalent-rare-earth ion-doped Y₂O₃ nanocrystals. *Applied Physics Letters* **81**, 4526-4528 (2002).

- 42 Vetrone, F., Boyer, J. C., Capobianco, J. A., Speghini, A. & Bettinelli, M. NIR to Visible Upconversion in Nanocrystalline and Bulk $\text{Lu}_2\text{O}_3:\text{Er}^{3+}$. *The Journal of Physical Chemistry B* **106**, 5622-5628 (2002).
- 43 Chen, X., Ma, E. & Liu, G. Energy Levels and Optical Spectroscopy of Er^{3+} in Gd_2O_3 Nanocrystals. *The Journal of Physical Chemistry C* **111**, 10404-10411 (2007).
- 44 Wang, X., Kong, X., Yu, Y., Sun, Y. & Zhang, H. Effect of Annealing on Upconversion Luminescence of $\text{ZnO}:\text{Er}^{3+}$ Nanocrystals and High Thermal Sensitivity. *The Journal of Physical Chemistry C* **111**, 15119-15124 (2007).
- 45 Tripathi, G., Rai, V. K. & Rai, S. B. Upconversion and temperature sensing behavior of Er^{3+} doped $\text{Bi}_2\text{O}_3\text{-Li}_2\text{O-BaO-PbO}$ tertiary glass. *Optical Materials* **30**, 201-206 (2007).
- 46 Solís, D., López-Luke, T., De la Rosa, E., Salas, P. & Angeles-Chavez, C. Surfactant effect on the upconversion emission and decay time of $\text{ZrO}_2:\text{Yb-Er}$ nanocrystals. *Journal of Luminescence* **129**, 449-455 (2009).
- 47 Liu, Y., Pisarski, W. A., Zeng, S., Xu, C. & Yang, Q. Tri-color upconversion luminescence of Rare earth doped BaTiO_3 nanocrystals and lowered color separation. *Opt. Express* **17**, 9089-9098 (2009).
- 48 Hampl, J. *et al.* Upconverting Phosphor Reporters in Immunochromatographic Assays. *Analytical Biochemistry* **288**, 176-187 (2001).
- 49 Feng, L. *et al.* Optical properties of Ho^{3+} -doped novel oxyfluoride glasses. *Journal of Luminescence* **124**, 187-194 (2007).
- 50 Du, Y.-P., Zhang, Y.-W., Sun, L.-D. & Yan, C.-H. Luminescent Monodisperse Nanocrystals of Lanthanide Oxyfluorides Synthesized from Trifluoroacetate Precursors in High-Boiling Solvents. *The Journal of Physical Chemistry C* **112**, 405-415 (2008).
- 51 Pisarski, W. A., Goryczka, T., Pisarska, J., Dominiak-Dzik, G. & Ryba-Romanowski, W. Effect of heat treatment on Er^{3+} containing multicomponent oxyfluoride lead borate glass system. *Journal of Non-Crystalline Solids* **354**, 492-496 (2008).
- 52 Heer, S., Lehmann, O., Haase, M. & Güdel, H.-U. Blue, Green, and Red Upconversion Emission from Lanthanide-Doped LuPO_4 and YbPO_4 Nanocrystals in a Transparent Colloidal Solution. *Angewandte Chemie International Edition* **42**, 3179-3182 (2003).
- 53 Mialon, G. *et al.* High Up-Conversion Efficiency of $\text{YVO}_4:\text{Yb,Er}$ Nanoparticles in Water down to the Single-Particle Level. *The Journal of Physical Chemistry C* **114**, 22449-22454 (2010).
- 54 Wang, G., Peng, Q. & Li, Y. Upconversion Luminescence of Monodisperse $\text{CaF}_2:\text{Yb}^{3+}/\text{Er}^{3+}$ Nanocrystals. *Journal of the American Chemical Society* **131**, 14200-14201 (2009).
- 55 Aebischer, A. *et al.* Structural and Spectroscopic Characterization of Active Sites in a Family of Light-Emitting Sodium Lanthanide Tetrafluorides. *Angewandte Chemie International Edition* **45**, 2802-2806 (2006).
- 56 Schäfer, H., Ptacek, P., Zerzouf, O. & Haase, M. Synthesis and Optical Properties of $\text{KYF}_4/\text{Yb, Er}$ Nanocrystals, and their Surface Modification with Undoped KYF_4 . *Advanced Functional Materials* **18**, 2913-2918 (2008).
- 57 Joubert, M.-F. Photon avalanche upconversion in rare earth laser materials. *Optical Materials* **11**, 181-203 (1999).
- 58 Gamelin, D. R. & Güdel, H. U. Design of Luminescent Inorganic Materials: New Photophysical Processes Studied by Optical Spectroscopy. *Accounts of Chemical Research* **33**, 235-242 (2000).
- 59 Maciel, G., De Araujo, C., Messaddeq, Y. & Aegerter, M. Frequency upconversion in Er^{3+} -doped fluorindate-glasses pumped at $1.48 \mu\text{m}$. *Phys. Rev. B* **55**, 6335-6342 (1997).

- 60 Wang, L., Zhang, Y. & Zhu, Y. One-pot synthesis and strong near-infrared upconversion luminescence of poly(acrylic acid)-functionalized $\text{YF}_3:\text{Yb}^{3+}/\text{Er}^{3+}$ nanocrystals. *Nano Research* **3**, 317-325 (2010).
- 61 Qu, Y., Kong, X., Sun, Y., Zeng, Q. & Zhang, H. Effect of excitation power density on the upconversion luminescence of $\text{LaF}_3:\text{Yb}^{3+}, \text{Er}^{3+}$ nanocrystals. *Journal of Alloys and Compounds* **485**, 493-496 (2009).
- 62 Diamente, P. R., Raudsepp, M. & van Veggel, F. C. J. M. Dispersible Tm^{3+} -Doped Nanoparticles that Exhibit Strong $1.47 \mu\text{m}$ Photoluminescence. *Advanced Functional Materials* **17**, 363-368 (2007).
- 63 Martínez, A. *et al.* Green and red upconverted emission of hydrothermal synthesized $\text{Y}_2\text{O}_3:\text{Er}^{3+}-\text{Yb}^{3+}$ nanophosphors using different solvent ratio conditions. *Materials Science and Engineering: B* **174**, 164-168 (2010).
- 64 Kumar, G. A. *et al.* Synthesis and spectroscopy of color tunable $\text{Y}_2\text{O}_2\text{S}:\text{Yb}^{3+}, \text{Er}^{3+}$ phosphors with intense emission. *Journal of Alloys and Compounds* **513**, 559-565 (2012).
- 65 Li, Y., Wei, X. & Yin, M. Synthesis and upconversion luminescent properties of Er^{3+} doped and $\text{Er}^{3+}-\text{Yb}^{3+}$ codoped GdOCl powders. *Journal of Alloys and Compounds* **509**, 9865-9868 (2011).
- 66 Patra, A., Friend, C. S., Kapoor, R. & Prasad, P. N. Effect of crystal nature on upconversion luminescence in $\text{Er}^{3+}:\text{ZrO}_2$ nanocrystals. *Applied Physics Letters* **83**, 284-286 (2003).
- 67 Ivaturi, A. *et al.* Optimizing infrared to near infrared upconversion quantum yield of β - $\text{NaYF}_4:\text{Er}^{3+}$ in fluoropolymer matrix for photovoltaic devices. *Journal of Applied Physics* **114**, 013505 (2013).
- 68 Wang, F. & Liu, X. Recent advances in the chemistry of lanthanide-doped upconversion nanocrystals. *Chem Soc Rev* **38**, 976-989 (2009).
- 69 Menyuk, N., Dwight, K. & Pierce, J. W. $\text{NaYF}_4 : \text{Yb,Er}$ —an efficient upconversion phosphor. *Applied Physics Letters* **21**, 159-161 (1972).
- 70 Suyver, J. F. *et al.* Novel materials doped with trivalent lanthanides and transition metal ions showing near-infrared to visible photon upconversion. *Optical Materials* **27**, 1111-1130 (2005).
- 71 Sedlmeier, A. & Gorris, H. H. Surface modification and characterization of photon-upconverting nanoparticles for bioanalytical applications. *Chemical Society Reviews* **44**, 1526-1560 (2015).
- 72 Tu, D. *et al.* Breakdown of Crystallographic Site Symmetry in Lanthanide-Doped NaYF_4 Crystals. *Angewandte Chemie International Edition* **52**, 1128-1133 (2013).
- 73 Krämer, K. W. *et al.* Hexagonal Sodium Yttrium Fluoride Based Green and Blue Emitting Upconversion Phosphors. *Chemistry of Materials* **16**, 1244-1251 (2004).
- 74 Liu, C., Wang, H., Li, X. & Chen, D. Monodisperse, size-tunable and highly efficient β - $\text{NaYF}_4:\text{Yb,Er}(\text{Tm})$ up-conversion luminescent nanospheres: controllable synthesis and their surface modifications. *Journal of Materials Chemistry* **19**, 3546-3553 (2009).
- 75 Wang, F. *et al.* Simultaneous phase and size control of upconversion nanocrystals through lanthanide doping. *Nature* **463**, 1061 (2010).
- 76 Chen, G. Y. *et al.* Enhancement of the upconversion radiation in $\text{Y}_2\text{O}_3:\text{Er}^{3+}$ nanocrystals by codoping with Li^+ ions. *Applied Physics Letters* **92**, 113114 (2008).
- 77 Bai, Y. *et al.* The Effect of Li on the Spectrum of Er^{3+} in Li- and Er-Codoped ZnO Nanocrystals. *The Journal of Physical Chemistry C* **112**, 12259-12263 (2008).
- 78 Bai, Y. *et al.* Enhanced upconverted photoluminescence in Er^{3+} and Yb^{3+} codoped ZnO nanocrystals with and without Li^+ ions. *Optics Communications* **281**, 5448-5452 (2008).

- 79 Dou, Q. & Zhang, Y. Tuning of the Structure and Emission Spectra of Upconversion Nanocrystals by Alkali Ion Doping. *Langmuir* **27**, 13236-13241 (2011).
- 80 Wisser, M. D. *et al.* Enhancing Quantum Yield via Local Symmetry Distortion in Lanthanide-Based Upconverting Nanoparticles. *ACS Photonics* **3**, 1523-1530 (2016).
- 81 Wen, S. *et al.* Advances in highly doped upconversion nanoparticles. *Nature Communications* **9**, 2415 (2018).
- 82 Damasco, J. A. *et al.* Size-Tunable and Monodisperse Tm³⁺/Gd³⁺-Doped Hexagonal NaYbF₄ Nanoparticles with Engineered Efficient Near Infrared-to-Near Infrared Upconversion for In Vivo Imaging. *ACS Applied Materials & Interfaces* **6**, 13884-13893 (2014).
- 83 Wang, Z. & Meijerink, A. Concentration Quenching in Upconversion Nanocrystals. *The Journal of Physical Chemistry C* **122**, 26298-26306 (2018).
- 84 Chen, G. *et al.* Lanthanide-doped ultrasmall yttrium fluoride nanoparticles with enhanced multicolor upconversion photoluminescence. *Journal of Materials Chemistry* **22**, 20190-20196 (2012).
- 85 Zhao, J. *et al.* Single-nanocrystal sensitivity achieved by enhanced upconversion luminescence. *Nature Nanotechnology* **8**, 729 (2013).
- 86 Medintz, I. L. & Hildebrandt, N. *FRET-Förster resonance energy transfer: from theory to applications*. (John Wiley & Sons, 2013).
- 87 Valeur, B. & Berberan-Santos, M. N. *Molecular Fluorescence: Principles and Applications*. (Wiley, 2013).
- 88 Dukhno, O. *et al.* Quantitative assessment of energy transfer in upconverting nanoparticles grafted with organic dyes. *Nanoscale* **9**, 11994-12004 (2017).
- 89 Bhuckory, S. *et al.* Core or Shell? Er³⁺ FRET Donors in Upconversion Nanoparticles. *European Journal of Inorganic Chemistry* **2017**, 5186-5195 (2017).
- 90 Mattsson, L., Wegner, K. D., Hildebrandt, N. & Soukka, T. Upconverting nanoparticle to quantum dot FRET for homogeneous double-nano biosensors. *RSC Advances* **5**, 13270-13277 (2015).
- 91 Hossan, M. Y. *et al.* Explaining the Nanoscale Effect in the Upconversion Dynamics of β-NaYF₄:Yb³⁺, Er³⁺ Core and Core-Shell Nanocrystals. *The Journal of Physical Chemistry C* **121**, 16592-16606 (2017).
- 92 Chen, X., Peng, D., Ju, Q. & Wang, F. Photon upconversion in core-shell nanoparticles. *Chemical Society Reviews* **44**, 1318-1330 (2015).
- 93 Haase, M. & Schäfer, H. Upconverting Nanoparticles. *Angewandte Chemie International Edition* **50**, 5808-5829 (2011).
- 94 Wang, Y. *et al.* Critical Shell Thickness of Core/Shell Upconversion Luminescence NanoplatforM for FRET Application. *The Journal of Physical Chemistry Letters* **2**, 2083-2088 (2011).
- 95 Pilch, A. *et al.* Shaping Luminescent Properties of Yb³⁺ and Ho³⁺ Co-Doped Upconverting Core-Shell β-NaYF₄ Nanoparticles by Dopant Distribution and Spacing. *Small* **13**, 1701635 (2017).
- 96 Huang, K. *et al.* A protected excitation-energy reservoir for efficient upconversion luminescence. *Nanoscale* **10**, 250-259 (2018).
- 97 Ma, C. *et al.* Optimal Sensitizer Concentration in Single Upconversion Nanocrystals. *Nano Letters* **17**, 2858-2864 (2017).
- 98 Sun, T., Ma, R., Qiao, X., Fan, X. & Wang, F. Shielding upconversion by surface coating: a study of the emission enhancement factor. *ChemPhysChem* **17**, 766-770 (2016).
- 99 Garfield, D. J. *et al.* Enrichment of molecular antenna triplets amplifies upconverting nanoparticle emission. *Nature Photonics* **12**, 402 (2018).

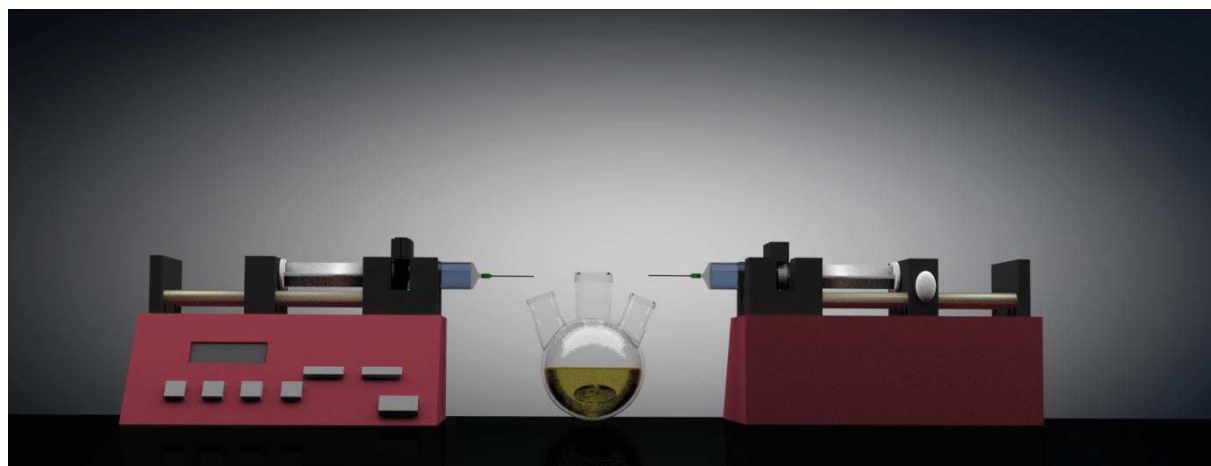
- 100 Wei, W. *et al.* Alleviating luminescence concentration quenching in upconversion nanoparticles through organic dye sensitization. *Journal of the American Chemical Society* **138**, 15130-15133 (2016).
- 101 Würth, C., Fischer, S., Grauel, B., Alivisatos, A. P. & Resch-Genger, U. Quantum yields, surface quenching, and passivation efficiency for ultrasmall core/shell upconverting nanoparticles. *Journal of the American Chemical Society* **140**, 4922-4928 (2018).
- 102 Altavilla, C. *Upconverting nanomaterials: perspectives, synthesis, and applications.* (CRC Press, 2016).
- 103 Chowdhuri, A. R., Laha, D., Pal, S., Karmakar, P. & Sahu, S. K. One-pot synthesis of folic acid encapsulated upconversion nanoscale metal organic frameworks for targeting, imaging and pH responsive drug release. *Dalton Transactions* **45**, 18120-18132 (2016).
- 104 Lee, J. *et al.* RGD peptide–conjugated multimodal NaGdF₄: Yb³⁺/Er³⁺ nanophosphors for upconversion luminescence, MR, and PET imaging of tumor angiogenesis. *Journal of Nuclear Medicine* **54**, 96-103 (2013).
- 105 Ma, L., Liu, F., Lei, Z. & Wang, Z. A novel upconversion@polydopamine core@ shell nanoparticle based aptameric biosensor for biosensing and imaging of cytochrome c inside living cells. *Biosensors and Bioelectronics* **87**, 638-645 (2017).
- 106 Zhang, S., Li, J., Lykotrafitis, G., Bao, G. & Suresh, S. Size-dependent endocytosis of nanoparticles. *Advanced materials* **21**, 419-424 (2009).
- 107 Behzadi, S. *et al.* Cellular uptake of nanoparticles: journey inside the cell. *Chemical Society Reviews* **46**, 4218-4244 (2017).
- 108 Moghimi, S. M., Hunter, A. & Andresen, T. Factors controlling nanoparticle pharmacokinetics: an integrated analysis and perspective. *Annual review of pharmacology and toxicology* **52**, 481-503 (2012).
- 109 Gubala, V. *et al.* Engineered nanomaterials and human health: Part 1. Preparation, functionalization and characterization (IUPAC Technical Report). *Pure and Applied Chemistry* **90**, 1283-1324 (2018).
- 110 Zarschler, K. *et al.* Ultrasmall inorganic nanoparticles: state-of-the-art and perspectives for biomedical applications. *Nanomedicine: Nanotechnology, Biology and Medicine* **12**, 1663-1701 (2016).
- 111 Homann, C. *et al.* NaYF₄: Yb, Er/NaYF₄ core/shell nanocrystals with high upconversion luminescence quantum yield. *Angewandte Chemie International Edition* **57**, 8765-8769 (2018).
- 112 Muhr, V., Wilhelm, S., Hirsch, T. & Wolfbeis, O. S. Upconversion nanoparticles: from hydrophobic to hydrophilic surfaces. *Accounts of chemical research* **47**, 3481-3493 (2014).
- 113 Wang, M. *et al.* NIR-responsive silica-coated NaYbF₄: Er/Tm/Ho upconversion fluorescent nanoparticles with tunable emission colors and their applications in immunolabeling and fluorescent imaging of cancer cells. *The Journal of Physical Chemistry C* **113**, 19021-19027 (2009).
- 114 Idris, N. M. *et al.* In vivo photodynamic therapy using upconversion nanoparticles as remote-controlled nanotransducers. *Nature medicine* **18**, 1580 (2012).
- 115 Zhou, H. P., Xu, C. H., Sun, W. & Yan, C. H. Clean and Flexible Modification Strategy for Carboxyl/Aldehyde-Functionalized Upconversion Nanoparticles and Their Optical Applications. *Advanced Functional Materials* **19**, 3892-3900 (2009).
- 116 Hu, H. *et al.* Facile epoxidation strategy for producing amphiphilic up-converting rare-earth nanophosphors as biological labels. *Chemistry of Materials* **20**, 7003-7009 (2008).

- 117 Chen, Z. *et al.* Versatile synthesis strategy for carboxylic acid– functionalized upconverting nanophosphors as biological labels. *Journal of the American Chemical Society* **130**, 3023-3029 (2008).
- 118 Stefanoiu, F., Candy, L., Vaca-Garcia, C. & Borredon, E. Kinetics and mechanism of the reaction between maleic anhydride and fatty acid esters and the structure of the products. *European journal of lipid science and technology* **110**, 441-447 (2008).
- 119 Bickford, W., Krauczunas, P. & Wheeler, D. The reaction of nonconjugated unsaturated fatty acid esters with maleic anhydride. *Oil and Soap* **19**, 23-27 (1942).
- 120 Peng, E., Ding, J. & Xue, J. M. Succinic anhydride functionalized alkenoic ligands: a facile route to synthesize water dispersible nanocrystals. *Journal of Materials Chemistry* **22**, 13832-13840 (2012).
- 121 Bogdan, N., Vetrone, F., Ozin, G. A. & Capobianco, J. A. Synthesis of ligand-free colloiddally stable water dispersible brightly luminescent lanthanide-doped upconverting nanoparticles. *Nano letters* **11**, 835-840 (2011).
- 122 Dong, A. *et al.* A generalized ligand-exchange strategy enabling sequential surface functionalization of colloidal nanocrystals. *Journal of the American Chemical Society* **133**, 998-1006 (2010).
- 123 Cichos, J. & Karbowiak, M. Spectroscopic characterization of ligands on the surface of water dispersible NaGdF₄: Ln³⁺ nanocrystals. *Applied Surface Science* **258**, 5610-5618 (2012).
- 124 Fedoryshin, L. L., Tavares, A. J., Petryayeva, E., Doughan, S. & Krull, U. J. Near-infrared-triggered anticancer drug release from upconverting nanoparticles. *ACS applied materials & interfaces* **6**, 13600-13606 (2014).
- 125 He, H. *et al.* Bispecific Antibody-Functionalized Upconversion Nanoprobe. *Analytical chemistry* **90**, 3024-3029 (2018).
- 126 Zhou, J. *et al.* Fluorine-18-labeled Gd³⁺/Yb³⁺/Er³⁺ co-doped NaYF₄ nanophosphors for multimodality PET/MR/UCL imaging. *Biomaterials* **32**, 1148-1156 (2011).
- 127 Jin, J. *et al.* Polymer-Coated NaYF₄:Yb³⁺, Er³⁺ Upconversion Nanoparticles for Charge-Dependent Cellular Imaging. *ACS Nano* **5**, 7838-7847 (2011).
- 128 Zhao, L. *et al.* Stem cell labeling using polyethylenimine conjugated (α-NaYbF₄: Tm³⁺)/CaF₂ upconversion nanoparticles. *Theranostics* **3**, 249 (2013).
- 129 Markiewicz, K. H. *et al.* Advantages of poly(vinyl phosphonic acid)-based double hydrophilic block copolymers for the stabilization of iron oxide nanoparticles. *Polymer Chemistry* **7**, 6391-6399 (2016).
- 130 Pinkerton, N. M. *et al.* Ionic Flash NanoPrecipitation (iFNP) for the facile, one-step synthesis of inorganic–organic hybrid nanoparticles in water. *Nanoscale* **9**, 1403-1408 (2017).
- 131 Li, X. *et al.* Dependence between cytotoxicity and dynamic subcellular localization of up-conversion nanoparticles with different surface charges. *RSC Advances* **7**, 33502-33509 (2017).
- 132 Lahtinen, S. *et al.* Disintegration of hexagonal NaYF₄: Yb³⁺, Er³⁺ upconverting nanoparticles in aqueous media: The role of fluoride in solubility equilibrium. *The Journal of Physical Chemistry C* **121**, 656-665 (2016).
- 133 Campus virtual exastas, Constantes de solubilidad. https://campus.exactas.uba.ar/pluginfile.php/111271/mod_resource/content/0/Constantes%20de%20solubilidad.pdf, accessed on 09/01/2019 (s.d.).
- 134 Lisjak, D., Plohl, O., Ponikvar-Svet, M. & Majaron, B. Dissolution of upconverting fluoride nanoparticles in aqueous suspensions. *RSC advances* **5**, 27393-27397 (2015).
- 135 Firsching, F. H. & Brune, S. N. Solubility products of the trivalent rare-earth phosphates. *Journal of Chemical and Engineering Data* **36**, 93-95 (1991).

- 136 Rey, C., Combes, C., Drouet, C. & Sfihi, H. in *Fluorine and Health* 279-331 (Elsevier, 2008).
- 137 Plohl, O. *et al.* Amphiphilic coatings for the protection of upconverting nanoparticles against dissolution in aqueous media. *Dalton Transactions* **46**, 6975-6984 (2017).
- 138 Bouzigues, C., Gacoin, T. & Alexandrou, A. Biological Applications of Rare-Earth Based Nanoparticles. *ACS Nano* **5**, 8488-8505 (2011).
- 139 Johnson, N. J., Oakden, W., Stanisz, G. J., Scott Prosser, R. & van Veggel, F. C. Size-tunable, ultrasmall NaGdF₄ nanoparticles: insights into their T1 MRI contrast enhancement. *Chemistry of Materials* **23**, 3714-3722 (2011).
- 140 Sun, Y. *et al.* Radioisotope post-labeling upconversion nanophosphors for in vivo quantitative tracking. *Biomaterials* **34**, 2289-2295 (2013).
- 141 Sun, M. *et al.* Hierarchical Plasmonic Nanorods and Upconversion Core–Satellite Nanoassemblies for Multimodal Imaging-Guided Combination Phototherapy. *Advanced Materials* **28**, 898-904 (2016).
- 142 Vetrone, F. *et al.* Temperature sensing using fluorescent nanothermometers. *ACS nano* **4**, 3254-3258 (2010).
- 143 Gu, B. & Zhang, Q. Recent advances on functionalized upconversion nanoparticles for detection of small molecules and ions in biosystems. *Advanced Science* **5**, 1700609 (2018).
- 144 Wang, Z., Hu, M., Ai, X., Zhang, Z. & Xing, B. Near-Infrared Manipulation of Membrane Ion Channels via Upconversion Optogenetics. *Advanced Biosystems* **3**, 1800233 (2019).
- 145 Chen, S. *et al.* Near-infrared deep brain stimulation via upconversion nanoparticle-mediated optogenetics. *Science* **359**, 679-684 (2018).
- 146 Wang, Y. *et al.* Tetherless near-infrared control of brain activity in behaving animals using fully implantable upconversion microdevices. *Biomaterials* **142**, 136-148 (2017).
- 147 Xie, Z. *et al.* Construction of hierarchical polymer brushes on upconversion nanoparticles via NIR-light-initiated RAFT polymerization. *ACS applied materials & interfaces* **9**, 30414-30425 (2017).
- 148 Méndez-Ramos, J., Ruiz-Morales, J., Acosta-Mora, P., Del-Castillo, J. & Yanes, A. Rare-earth doped nano-glass-ceramics for extending spectral response of water-splitting semiconductor electrodes by high intense UV-blue up-conversion: turning the sun into blue. *Journal of Power Sources* **238**, 313-317 (2013).
- 149 Liu, Y. *et al.* Amplified stimulated emission in upconversion nanoparticles for super-resolution nanoscopy. *Nature* **543**, 229 (2017).

Chapter II

Synthesis of ultrasmall UCNPs



“Plutôt que de maudire les ténèbres, allumons une chandelle, si petite
soit-elle” (Confucius)

与其诅咒黑暗，不如点燃蜡烛

Contents

I- Litterature review	69
I.1 Theoretical model of synthesis of UCNP	69
I-1-1- Two phases: one continuous 1 and one discrete 2	69
I-1-2- Extension to UCNP polymorphs α and β phases	71
I.2 Chemical characteristics of NaREF ₄	71
I.3 NaREF ₄ polymorphs: $\alpha \rightarrow \beta$, an Ostwald's step rule	73
I.4 Synthesis of small UCNPs	76
I-1-3- General procedure for UCNP preparation	76
I-1-4- Towards size reduction	77
I-1-5- Reproducibility issue	78
I.5 Aim of the chapter	79
II From small to ultrasmall nanoparticles adapted for super-resolution	80
II.1 Small UCNP nanospheres (10-15 nm)	80
II.1.1 Core UCNP	80
II.1.2 Core@shell UCNP	84
II.1.3 Impact of our high sensitizer content	87
II.1.4 Conclusion on small nanospheres	89
II.2 Transposition of nanospheres synthesis from <i>premix</i> to <i>in situ</i> mixing approach	89
II.3 Towards sub-5 nm NP obtained via microwave synthesis	91
II.3.1 Reminder about UCNP and microwave synthesis	91
II.3.2 Feasibility of MW heating in OA:ODE without TFA	94
II.3.3 Simple microwave heating: high temperature plateau	96
II.3.4 Cycling temperature	104
II.3.5 Chemical characterization	113
III Model particles for surface chemistry	117
III.1 Fast preparation of UCNP on a small-scale batch	117

III.2	Size reduction on UCNP hexagons scale-up issues.....	118
IV	Conclusion on synthesis of ultrasmall UCNP	122
V	Experimental section.....	125
V.1	Materials	125
V.2	Synthesis.....	126
V.2.1	Synthesis of cores UCNP.....	126
V.2.2	Synthesis of core@shell	128
V.2.3	Microwave heatings	129
V.3	Characterization.....	130
V.3.1	Monitoring of the core synthesis, adapted from F. Wang <i>et al.</i> ⁸ : TEM images and image analysis (Image J treatment).....	130
V.3.2	Luminescence monitoring of the shell growth.....	134
V.3.3	Luminescence monitoring of the shell growth with doubling of the reaction time. 134	
V.3.4	Combination of “in situ” introduction and conventional heating, ¹⁹ trial#1	135
V.3.5	Kinetic analysis, combination of “ <i>in situ</i> ” introduction and conventional heating, ¹⁹ trial#2.....	136
V.3.6	Kinetic analysis, “ <i>in situ</i> ” mixing and 30 min microwave oven combination, variable temperature.....	137
V.3.7	Kinetic analysis, “ <i>in situ</i> ” mixing and 300°C microwave oven combination, variable reaction time.....	138
V.3.8	Typical run for the “as-fast-as-possible” routine and 300°C plateau.....	139
V.3.9	Summary of the TEM analyses	140
VI	References	141

I- Litterature review

I.1 Theoretical model of synthesis of UCNP

Theoretical aspects of the preparation of nanocrystals can be found in the literature. In particular, an important amount of work has been dedicated to the synthesis of quantum dots as their emission properties are strongly bound to their size. The general frame of the Lifshitz-Slyozov-Wagner (LSW) theory is a biphasic system with a continuous phase and a dilute discrete one: spherical independent particles grow and exchange matter by dissolution/precipitation process. When the Ostwald ripening regime is established, the amount of dissolved material is quasi-negligible and the driving-force of the changes of the particles' shape is the minimization of the interface between the two phases. The particle size distribution (PSD) $F(t, r)$ presents a self-similar behavior: $F(t, r) = A(r^*(t)) \cdot g(\rho)$ with r^* being a critical radius, and $\rho = r(t)/r^*(t)$ an adimensioned length parameter. For the LSW theory, the critical radius is the mean of the PSD and defines the size where the growth rate is null: $\left(\frac{dr}{dt}\right)_{r^*(t)} = 0$. The normalized, scaled size-distribution function $g(\rho)$ gives the shape of the distribution.¹

These results were then adapted to UCNPs: the main difficulty is the presence of two polymorphs, the cubic and hexagonal phases. Therefore it requires a triphasic system (one continuous phase and two discrete ones). As expected, the succession of crystalline phase follows the empirical rule of Ostwald's "rule of phases": the polymorphic phases appear by order of increasing stability. In this section the main results achieved by the team of Talapin *et al.* will be recalled, then, their adaptation to the presence of two polymorphs will be presented.

I-1-1- Two phases: one continuous 1 and one discrete 2

General growth kinetic scheme

The growth mechanism is based on continuous exchange of material between nanoparticles with the continuous phase. Classical hypotheses are that nanoparticles stay far away from each other and the surface changes do not affect the steady state regime that is established quickly around the growing center. Key equations describe the transport, the surface reaction and the size changes, and lead to the following expression

$$\frac{dr}{dt} = U_m D \frac{[M]_\infty - \frac{k_r^{-1}}{r}}{r + \frac{D}{k_r}}$$

Where dr/dt is the radius growth rate, U_m the molar volume of the crystal phase, D the diffusion coefficient of the dissolved precursor, $[M]_\infty$ the concentration of dissolved precursor in the bulk solution and k_r^1 and k_r^{-1} are the radius dependent rate constants of deposition and dissolution respectively. The improvements of the work by Talapin *et al.*² are that a general expression for the radius change is given without simplifying constraints and that the radius dependent kinetic rates constant are related to equilibrium one via the use of transfer coefficients. Rate constants are size-dependent and differ from those related to a “flat” surface (when the thermodynamic equilibrium is reached), respectively k_{flat}^1 and k_{flat}^{-1} . In the model developed by Talapin, a dependence of the rate constants with r is expressed as

$$k_r^1 = k_{flat}^1 e^{-a \frac{2\gamma U_m}{rRT}} \quad \text{and} \quad k_r^{-1} = k_{flat}^{-1} e^{-b \frac{2\gamma U_m}{rRT}} \quad \text{with} \quad a+b=1, \quad a \quad \text{and} \quad b \quad \text{being} \quad \text{the} \quad \text{transfer} \quad \text{coefficients} \quad \text{usually} \quad \text{taken} \quad \text{as} \quad a=b=1/2. \quad \text{Therefore} \quad \frac{k_r^{-1}}{k_r^1} = \frac{k_{flat}^{-1}}{k_{flat}^1} e^{-\frac{2\gamma U_m}{rRT}}$$

At the equilibrium, when the surface is flat, the concentration of monomer is $[M]_e$ defined from the solubility product $K_s = [M]_e = \frac{k_{flat}^{-1}}{k_{flat}^1}$. The super-saturation being $S = [M]_\infty/[M]_e$ the radius change with time becomes

$$\frac{dr}{dt} = U_m D \frac{S - e^{-\frac{2\gamma U_m}{rRT}}}{r + \frac{D}{k_{flat}^1} e^{a \frac{2\gamma U_m}{rRT}}}$$

The magnitude of term $\frac{D}{k_{flat}^1}$ allows one to distinguish two regimes: diffusion controlled when $D \ll k_{flat}^1$ and reaction controlled otherwise.

It can also be seen that if $r = r^* = (2\gamma U_m)/(RT \ln S)$ then $(dr/dt)_{r^*} = 0$. This is the so-called critical radius: if $r < r^*$ the particle dissolves, if $r > r^*$ the particle grows. It is common then to use $\rho = r/r^*$ as a dimensionless length in such problems (note that ρ is a function of time as r^* is). Therefore, in the PSD function $F(r,t) = A(r^*(t)).g(\rho)$, $g(\rho)$ “tails” down to zero because small particles are vanishing.

The average value $\langle r \rangle$ ($=r^*(t)$) evolves with time as

$$\langle r \rangle^\alpha = \langle r_0 \rangle^\alpha + Kt$$

α indicates the limit dynamics of the system: $\alpha = 2$ if reaction controlled and 3 if diffusion controlled.³

Nucleation

The classic homogeneous nucleation theory is based on the evaluation of the free energy of a transient cluster made of i monomers, that will act as a crystal seed of free energy ΔG_i . Above a threshold value, $d(\Delta G_i)/di < 0$ then the seed grows. The nucleation rate R is then the probability for a crystal to grow from monomers: $R = [M] A \exp(-\Delta G_i/RT)$.

I-1-2- Extension to UCNP polymorphs α and β phases

Haase and coworkers have carefully explored the case of the Ostwald ripening with 2 polymorphs of different stability. The key idea was to simulate the behavior of a population of kinetically unstable α phase nanoparticles in the presence of a small amount of β one. A time period was predicted during which the α -particles would undergo Ostwald ripening while β -particles keep growing when both phases are present as supersaturation is controlled mostly by the less stable, most soluble α -phase. During this growth stage, the number of β -particles is left unchanged and β -PSD experiences size focusing. When the mass transfer from α - to β -nanocrystals becomes dominant (i.e. when β -particles are big enough), the supersaturation drops bringing all α -particles to complete dissolution.

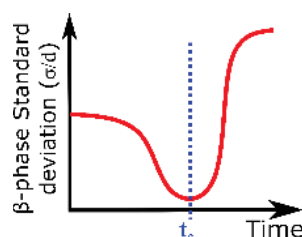


Figure 1. Nucleation and growth dynamics: Ostwald focusing

Once the α -phase has disappeared, Ostwald ripening takes place for the β -particles and PSD broadens. As a consequence, the narrowest β -phase PSD should therefore be found right after the α -phase has vanished.⁴ This mechanism is known as Ostwald focusing.

I.2 Chemical characteristics of NaREF₄

NaREF₄ precipitation considerations

NaREF₄ is highly insoluble (solubility product estimated at around 10^{-26} by the work of T. Soukka⁵), the precipitate is formed by a simple precipitation involving 3 components:



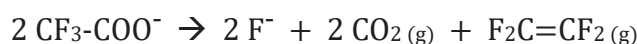
This chemical reaction can be run in different solvents, from water to oil. However small sizes are generally obtained in apolar solvents, as it is already well-known for QD (CdSe) and iron

oxide (Fe₃O₄) syntheses. As a result, small UCNPs are usually prepared in oleic acid:octadecene mixture, the former acting also as a NP stabilizer to control the crystal growth. For such a solvent mixture, the precursors commonly used are of three types:

- Rare-Earths are usually used as metallic soap RE(OA)₃ soluble in apolar solvent. It can be prepared and stored as a *premix*, or more usually prepared *in situ*. Such a soap is generally prepared from acetate or chloride precursors.
- Sodium cations can be introduced from start by using sodium oleate or by introducing NaOH in the OA:ODE mixture.
- Concerning the fluoride anions, two mains strategies have been developed:

-the direct delivery of ions using inorganic salts (NH₄F or NaF), or

-the introduction of a latent source of fluorure (trifluoroacetate TFA). The latter, coming from MOCVD (Metal Organic Chemical Vapor Deposition)⁶ approach, is based on TFA pyrolysis at temperature above 250°C, allowing the delivery of a burst of fluoride. However, TFA pyrolysis leads to gas formation, limiting the use of closed reactor devices such as microwave:



Compared to the thermal decomposition approach (Table 1), the thermal coprecipitation way appears as a more user-friendly strategy, despite the apparent poor control of nucleation. Thus, my work has focused on this latter.

Table 1. Comparison of pyrolysis and thermal coprecipitation pathways.

	Thermal decomposition (pyrolysis) ⁷	Thermal coprecipitation way ⁸
Fluoride source	TFA	NaF; NH ₄ F
Advantages	-Smaller NP size: 5-40 nm -better control of nucleation step	-easy to implement -size range: 10-40 nm
Inconvenients	-Toxic gaseous by-products (F ₂ C=CF ₂ ; COF ₂ ; HF) -pressure issue for closed reactors (MW)	- bigger object - poor control of nucleation

I.3 NaREF₄ polymorphs: $\alpha \rightarrow \beta$, an Ostwald's step rule

As described in the introduction chapter, NaREF₄ can appear in two polymorphs, the β -one being the only one interesting for upconversion. Experimentally, it has been noticed that when a substance can lead to different polymorphic phases, it crystallizes following a sequence process⁹: crystal phases appear successively in a rising thermodynamic stability order.

Thus, the challenge is to prepare pure β -phase. Therefore, the usual approach is based on heating for a sufficient time and at temperature high enough to ensure the complete α -to- β transformation. However, a prolonged reaction time leads to coarsening of the nanoparticle size: this is the Ostwald Ripening. The problem gets further complicated by the chemical reactivity of the various RE used.

Lanthanides and yttrium form the family of Rare Earth elements. Lanthanides, although very similar, have slight differences in their chemistry which were used since their discovery to distinguish two main RE groups: Light RE elements (LRE) from lanthanum to gadolinium and Heavy ones from gadolinium to lutetium (HRE). A third group, the “Middle rare-earth elements”, is sometimes used for metals around gadolinium. Although above lanthanum, yttrium presents similar chemical properties to the heavy lanthanides. This classification also translates in the making of NaREF₄.

Phase diagram

Phase diagrams of all possible NaF-REF₃ mixture were established by Thoma *et al.*¹⁰ in 1966. At low temperature (300°C), the defined phase is the hexagonal β -one. The α , cubic phase occurs only at high temperature and tolerates a larger range of NaF/REF₃ ratio. It is therefore expected that the less stable cubic phase should appear before the hexagonal one, according to the Ostwald rule of phases.⁹

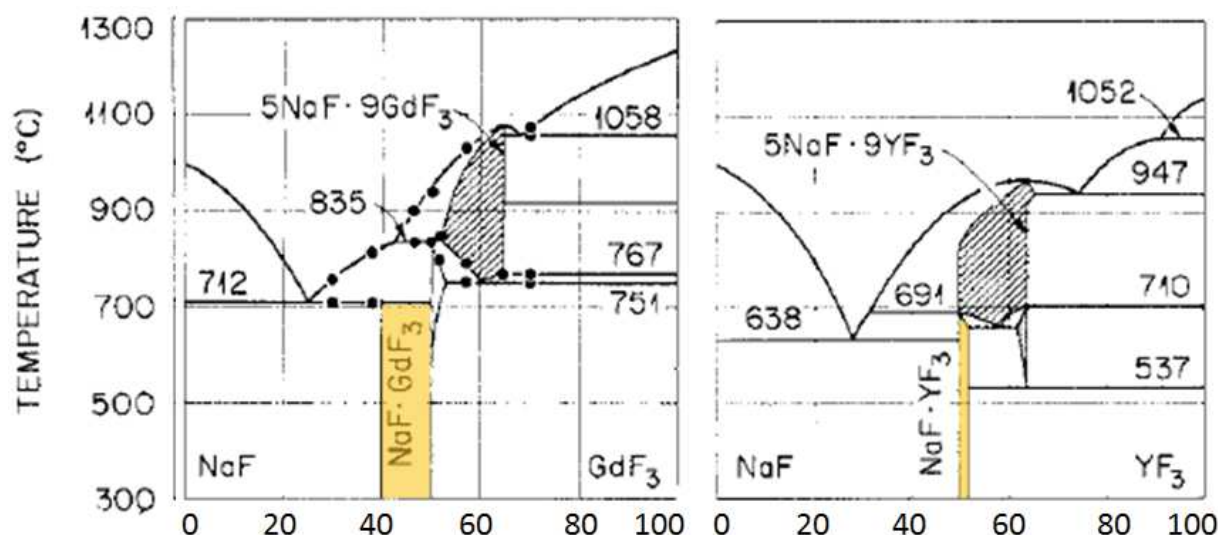


Figure 2. Phase diagrams of NaF-REF₃ for Gadolinium and Yttrium. Hatched domains are the cubic NaREF₄ phase. Hexagonal phase domains are highlighted in orange.

NaREF₄ cubic-to-hexagonal phase transformation

Over the twenty last years, investigations have compared the feasibility of the formation of the hexagonal phase at lower temperature (thermal coprecipitation, hydro/solvothermal or pyrolysis routes) according to the nature of the RE ions. In particular, the work by the team of Chun-Huan Yan¹¹ revealed some collective crystallization properties and trends for the hexagonal phase by thermal decomposition synthesis in Oleic Acid:Octadecene (OA:ODE) mixture:

Group I RE (Pr and Nd) have the particularity of forming RE₃F₆ as the transient phase, rather than cubic phase. The transformation to the thermodynamically stable hexagonal phase required strong conditions, with temperatures around 300-320°C. The two other groups show at high temperature a phase transition from the transient cubic phase to the hexagonal one. The main difference between them is the ability to achieve this phase transition.

Metals from Group II (from Sm to Tb) show an easy-going transition phase, that can be achieved in mild conditions, by heating only at 280°C.

However, for elements from the Group III (Y and Lanthanides from Dy to Lu) the access to the hexagonal phase is quite difficult, and requires stronger conditions (heating at 300-320°C). The following table summarizes these results.

Table 2. Trends for the hexagonal phase of the Rare Earth groups in the case of TFA-pyrolysis method.

	Group I	Group II	Group III
Rare-Earth elements	Pr and Nd	Sm, Eu, Gd, Tb	From Dy to Lu, and Y
Thermodynamically stable phase	β -NaREF ₄	β -NaREF ₄	β -NaREF ₄
Transient phase	REF ₃	α -NaREF ₄	α -NaREF ₄
Access to β -phase by TFA-pyrolysis method	difficult (300-320°C required)	Easy (mild conditions 280°C)	difficult (300-320°C required)

As a result, some strategies of doping group III matrix (such as NaYF₄) by another element from group II such as Gd (at least 30% Gd) were elaborated in order to promote the formation of hexagonal phase and/or to be able to perform the synthesis under mild conditions.¹²

I.4 Synthesis of small UCNPs

I-1-3- General procedure for UCNP preparation

Reference protocol

F. Wang *et al.* established a reference protocol for the preparation of small NaGdF₄⁸ for a thermal coprecipitation pathway, schematized, as below:

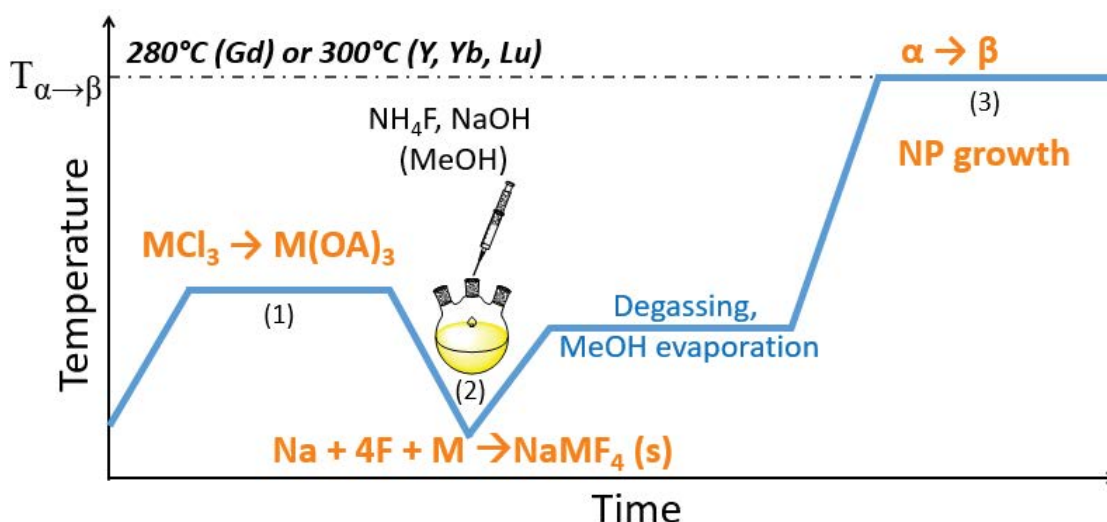


Figure 3. General Scheme of NaREF₄ thermal coprecipitation synthesis (in the oleic acid/octadecene mixture) showing the 3 main steps: (1) ligand exchange from Rare-Earth precursors (chloride) to oleates, (2) precipitation with sodium and fluoride, (3) high temperature annealing to achieve growth and phase transformation.

The process can be decomposed into 3 main steps: at first, there is ligand exchange between RE precursors and oleate to form at 160°C Rare-Earth oleate. Then at room temperature fluoride and sodium sources are introduced, and the precipitation occurs (except for trifluoroacetate source). Finally, after removing volatile compounds by degassing, a high temperature step is required to perform nanoparticle growth and phase transition to pure beta-phase. Therefore, it begs the question of the optimal duration of the step (3) to ensure complete $\alpha \rightarrow \beta$ transformation while keeping a controlled size.

Monitoring the $\alpha \rightarrow \beta$ transformation

As proposed by May's group, it is possible to monitor this transformation in real time, by recording the emission intensity *in situ*.¹³ However, this experiment is not easily set up, with regards to optics alignment and laser safety in common laboratory.

As a result, the most user-friendly but tedious approach is to analyze aliquots sampled during the process. The most complete example is coming from Resch-Genger's team¹⁴, with the comparison of size (TEM, SAXS), crystal phase and luminescence properties (emission, lifetimes, quantum yield).

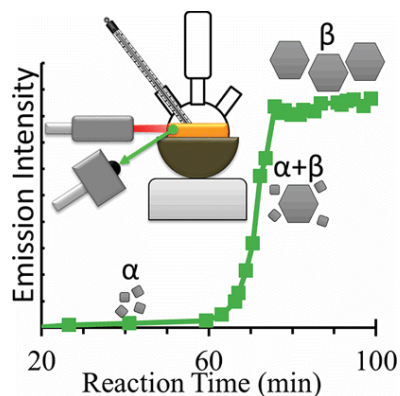


Figure 4. Experimental set up for real-time monitoring of UCP synthesis. Reproduced with permission from¹⁴.

I-1-4- Towards size reduction

Ostwald ripening in the presence of the two polymorphs has to be mastered to get a small size with a fine control of the dispersity. As described in the introduction, Ostwald ripening can be decomposed in two successive phases: at first the so-called Ostwald focusing when the less stable α -phase is disappearing while both polymorphs sizes are rising but with no modification of the dispersity of the β -one. Then, once no α phase is remaining, the size distribution of the β crystals is increasing and broadening during an Ostwald defocusing step. As a result, the optimal condition is to quench the reaction at the end of Ostwald focusing. If the number of β seeds was high enough, the average size will therefore be small.

Experimentally, in the reference protocol, every step seems to be of importance, but two key points can be stressed out:

- the nature of the RE has a strong impact: Gadolinium is known to favor easy transformation to the β -phase, and the resulting size are generally lower than with other matrices, in similar conditions;

- NaREF₄ nucleation is under kinetic control: it is a dynamic system, and there is some uncertainty on the starting moment of the reaction, that can lead for example to batch-to-batch reproducibility issues.

I-1-5- Reproducibility issue

Despite the attempt to standardize protocols for the preparation of UCNP⁸, it has been reported that one synthesis reproduced many times gives different results either regarding the size distribution or the photophysical properties, as highlighted by Mays's team¹³.

A radical solution was proposed by O. Wolfbeis' team: the production of UCNP at the litre scale.¹⁵ Thus, one batch can be characterized once, then sampled for several applications. Nevertheless, this strategy brings new scale-up issues such as reactor size, heating device, heating rate, precursors mixing, homogeneization of the reaction medium, volatile compound evaporation, etc ..., storage and aging.

I.5 Aim of the chapter

Since the UCNP research axis was introduced in the IMRCP laboratory simultaneously with the beginning of my PhD, my project was initiated from scratch. Concerning the nanoparticles synthesis two approaches had to be carried out simultaneously:

- 1) Production of high-quality UCNPs for super-resolution application:

On this first part the challenge was to prepare ultrasmall bright UCNP with a size competitive with QD (sub-10 nm). Therefore, starting from the most standard protocol on NaGdF_4 ⁸, we designed an original $\text{Na}(\text{Gd-Yb})\text{F}_4:\text{Tm}$ formulation with a high content of sensitizer (57% Yb) to increase the luminescence, as proposed by the work of Prasad¹⁶. By successive optimizations to enhance the control of Ostwald ripening, including the mixing procedure and the variations of heating strategies, we will describe how a size reduction from 10-15 nm to around 3 nm can be obtained.

- 2) As the preparation of ultrasmall objects is a time-consuming process, with a limited amount of matter produced, the second part focused on the simple preparation of large stock of bright UCNPs for further applications. These objects are dedicated for the first attempts of nanohybrid formation that will be described in chapter IV. Thus, NaYF_4 matrix was chosen as it is the most efficient for upconversion, in order to maximize the emission, to setup the nanohybrid parameters before using the less emissive ultrasmall ones.

In the present chapter, the validation of some key synthesis is assessed by fast comparison of luminescence spectra. However deeper analysis of the photophysical properties will be presented in the chapter III.

II From small to ultrasmall nanoparticles adapted for super-resolution

II.1 Small UCNP nanospheres (10-15 nm)

II.1.1 Core UCNP

We selected a quasi equimolar Yb-Gd composition to enhance the luminescence by increasing the nanoparticle cross-section at 980 nm. We first explored the protocol described by Wang *et al.* for the preparation of 15 nm Yb-Gd UCNPs of around 50 % Yb content.⁸ It illustrates the very standard “one-pot” approach, as described on figure 3: to the metal oleate, prepared from the chlorides (step 1), are added premixed sodium and fluorides sources (step 2). This protocol is later referred to as a “premix” protocol. The resulting mixture is then heated to high temperature (step 3) in order for crystallisation to proceed.

- During the ligand exchange (step 1), water was removed by argon flush. Some simple test during this steps indicated the evolution of HCl coming from RECl_3 precursors:

-test with AgNO_3 revealed the presence of chloride ($\text{AgNO}_3 + \text{Cl}^- \rightarrow \text{AgCl (s)} + \text{NO}_3^-$).

-pH paper revealed the presence of acidic compound in the fumes. However this point can be misleading. Indeed, the volume of the reaction mixture is lowered during the ligand exchange step if the argon flush is prolonged. This is due to azeotropic distillation of oleic acid and water. As a result, acidic compound revealed by pH paper can be HCl or oleic acid. No attempts were made to quantify the amount of HCl eliminated this way.

- Concerning the mixing (step 2), the strategy is to premix NaOH and NH_4F solution and introduce dropwise this mixture inside the reactor. However it should be noted that during this slow addition some white precipitate is observed in the $\{\text{NaOH}+\text{NH}_4\text{F}\}$ mixture. This precipitate byproduct is attributed to NaF formation. Over time the precipitate is evident bare eye: nanoobjects are thus very large.

- Our heating device is controlled by an electronic security preventing overshoot (that will be discussed on II-2 section). Thus, the heating rate gradually decreases when getting close to the setpoint temperature. We decided to record the “reaction time” only when the setpoint temperature was reached: For NaGdF₄ matrix it is 280°C.

When applied to our new composition, 10.1 ± 0.6 nm homogeneous monodisperse β -phase nanoparticles were obtained after 90-minute of heating at 280°C using a conventional

heating mantle. However, regular sampling during the 90 minutes plateau revealed before the end point a bimodal distribution, persisting almost throughout the reaction time, (figure 5 A, B). These two populations were identified by XRD and luminescence data as α (less than 6 nm) and β (10.1 ± 0.6 nm) particles, the first ones steadily disappearing, leaving only the latter at the end of the reaction time. While the small α -population experiences size coarsening before vanishing, the average size of the β -population did not drift much with time.

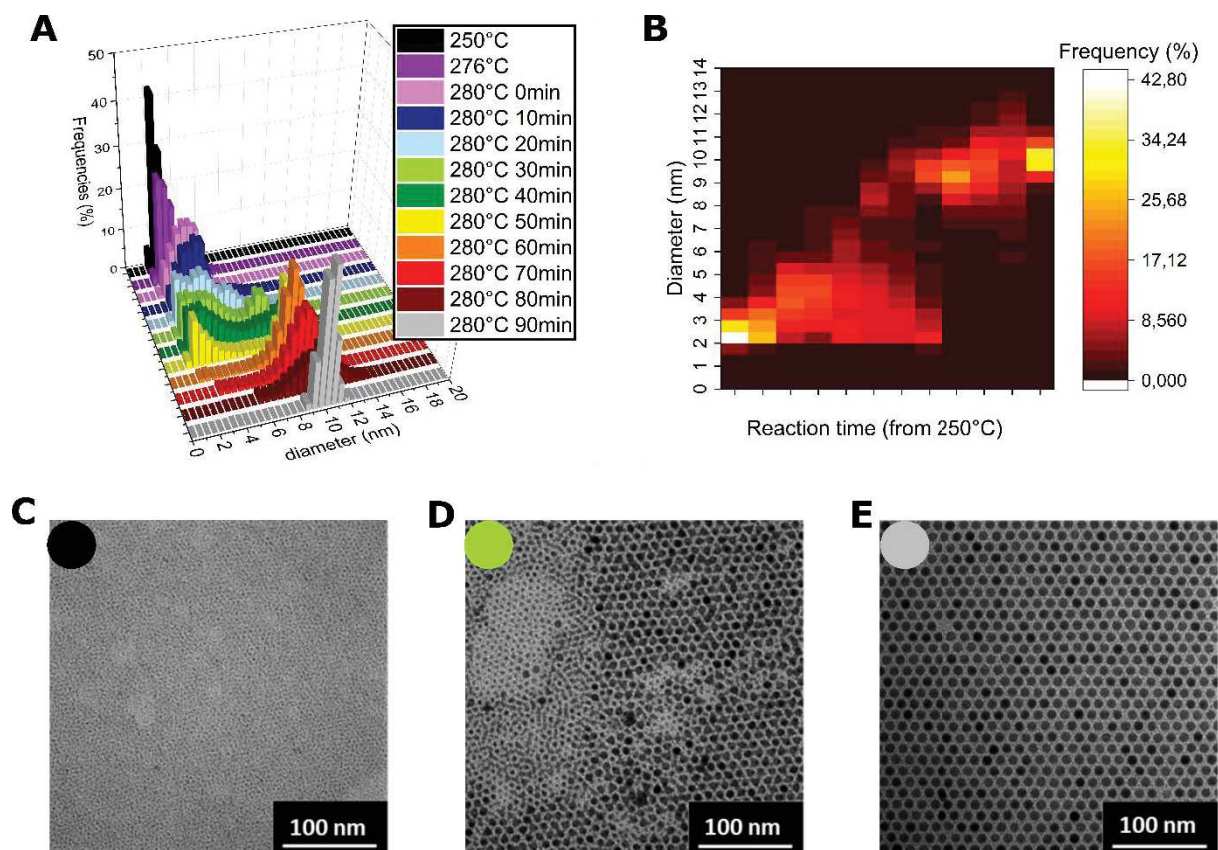


Figure 5. Core synthesis monitoring by analysis of TEM (Transmission Electron Microscopy) picture. A) and B) are 2 representations of the size distribution evolution with time. C-E are representative TEM images of the nanoparticles: when temperature reached 250°C (C), after 30 min at 280°C (D), and at the end point of the synthesis (E).

Complementary XRD results attested that the 1st population (C) was purely cubic, while the latter (E) was pure hexagonal phase.

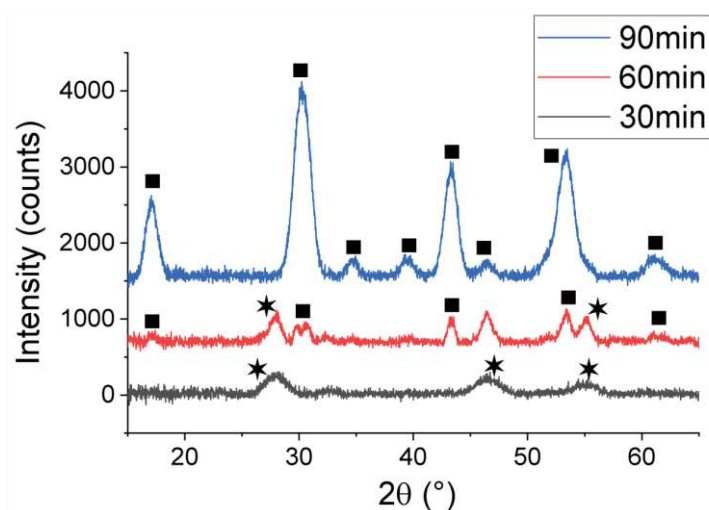


Figure 6. XRD analysis of samples taken at various times during the high temperature heating step at 280°C of the premix protocol with conventional heating mantle: 30 min (black), 60 min (red) or 90 min (blue). Black squares indicate hexagonal phase peaks, while the black stars refer to the cubic one. For the 60min reaction time (red line), peak at ca 48° can be attributed to overlapped peaks of the cubic and hexagonal phases.

As proposed by Stanley May and Mary Berry,¹³ luminescence monitoring was also considered (Figure 7): a clear increase of the 800 nm emission was observed over the reaction time, and especially after 50 minutes. Although not as sharp as expected, this coincides with the apparition of a predominant β -phase in the reaction mixture. Luminescence signals, though, are quite low, explaining the noisy blue and UV (respectively 474 and 361 nm) peak values.

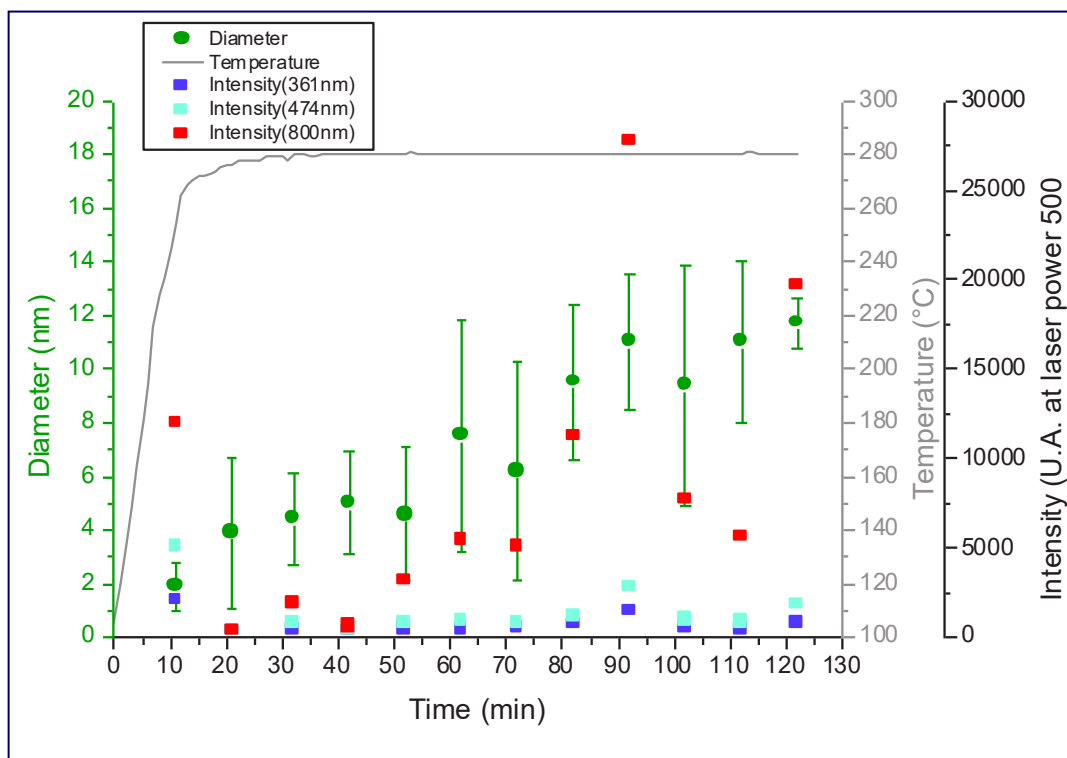


Figure 7. Evolution of average core diameter (green), and luminescence on 3 characteristic emission bands (red, cyan, and purple, respectively for 802 nm, 474 nm and 361 nm peaks).

Despite an apparent easy direct visual observation, luminescence monitoring can only give indications about qualitative variations of the photophysical properties: upconversion efficiency is increased when a certain amount β -UCNP is present in solution. For a precise quantitative analysis of the monitoring, XRD is the main tool as it is the only one giving the nature and proportion of the crystal phases. In addition, it provides a bulk measurement of the nanocrystals size using Rietveld refinement. TEM monitoring is mandatory only for the control of the Ostwald focusing as it will be more detailed later in the chapter. But the latter require to be coupled to XRD for crystal phase determination. Indeed, High-resolution TEM with electron diffraction is a time-consuming approach and can give crystal phase information, but only at the single nanoparticle scale, not on bulk.

These observations (morphological and photophysical) show that such a protocol could not yield the desired bright pure β -phase nanocrystals smaller than 10 nm. It is well established that a deficit of sodium in the solution mixture at the early stages of the precipitation favors the nucleation of α -phase nanocrystals.¹⁷ In the present case, significant precipitation of NaF resulting from the premixing of the NaOH and NH₄F methanolic solutions were observed during the introduction time. We suspected that this could impede the nucleation of the β -phase.

The overall luminescence of the core UCNP is weak. In order to increase the luminescence, we decided to grow an epitaxial undoped shell of NaYF₄ that would reduce surface quenching.

II.1.2 Core@shell UCNP

Synthesis pathway

As proposed by F. Wang *et al.*, cores can act as seeds under the thermal coprecipitation pathway to promote a shell epitaxial growth at their surface.⁸ Shell growth conditions differ from the core preparation only by the fact that core seeds are introduced as a cyclohexane suspension prior to {NaF+NaOH} addition. After the concomitant removal of cyclohexane and methanol, the synthesis is basically the same except for a shorter reaction time for the high temperature heating step (1h vs 1h30 for the core).

Shell effect on luminescence

Direct eye comparison of core and core@shell irradiated by the same laser revealed the success of the core@shell strategy to obtain brighter UCNP, as seen in the photograph in figure 8.

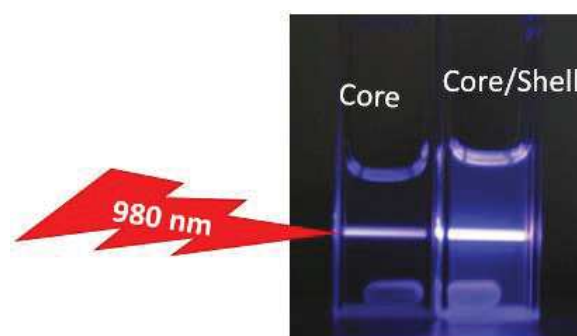


Figure 8. Comparison of core and core@shell brightness by direct observation under 58 W cm⁻² CW 976 nm laser. Laser beam passes through the core sample before reaching the core@shell suspension. Both samples are prepared at 5 mg/mL in cyclohexane.

Kinetic monitoring

As for the core synthesis, sampling during the shell growth was performed to monitor it by TEM and luminescence (figure 9). An increase of the luminescence is clearly observed. To our delight all emission band intensities (NIR, blue, UV), are increasing abruptly after around 50 min, following the size rise (figure 9). Our first explanation was that as the shell is gradually growing, surface quenching is progressively removed, leading to the apparent luminescence rise. Noticeably an experiment over much prolonged reaction time (2h instead of 1h) did not

lead to a luminescence plateau as it would be expected if NPs were totally insulated from the solvent. This discrepancy was not further explored.

Even more interesting is the TEM monitoring. Not surprisingly, early images (figure 10) show the presence of numerous smaller objects along with the core seeds. At the early stage (from 10 to 45 min) these small objects tend to form aggregates of apparent contrast close to the seeds, thus difficult to extract from the TEM images before treatment. This explains why NP sizes are smaller than seeds over the time period. After 45 min, size increases sharply, making the observed luminescence rise due to the shell growth. However, TEM images show the persistent presence of smaller objects; we interpreted these as “empty shells”: nano-objects made only of NaYF₄.

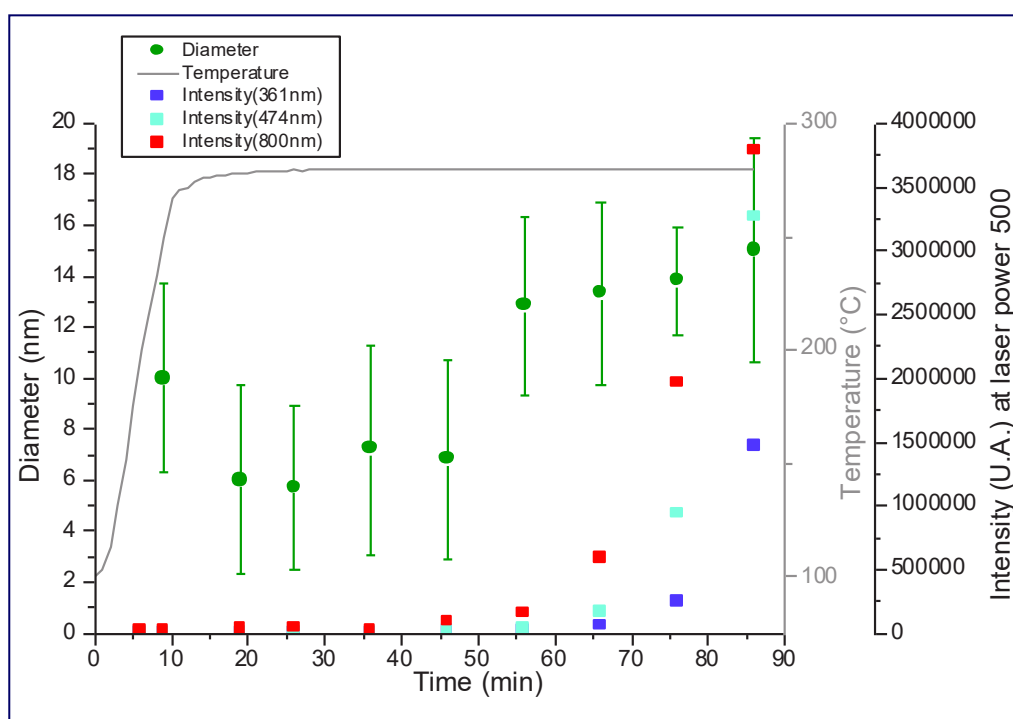


Figure 9. Evolution of core@shell average diameter (green) from TEM pictures analysis, and luminescence on 3 characteristic emission bands (red, cyan, and purple, respectively for 802 nm, 474 nm and 361 nm peaks).

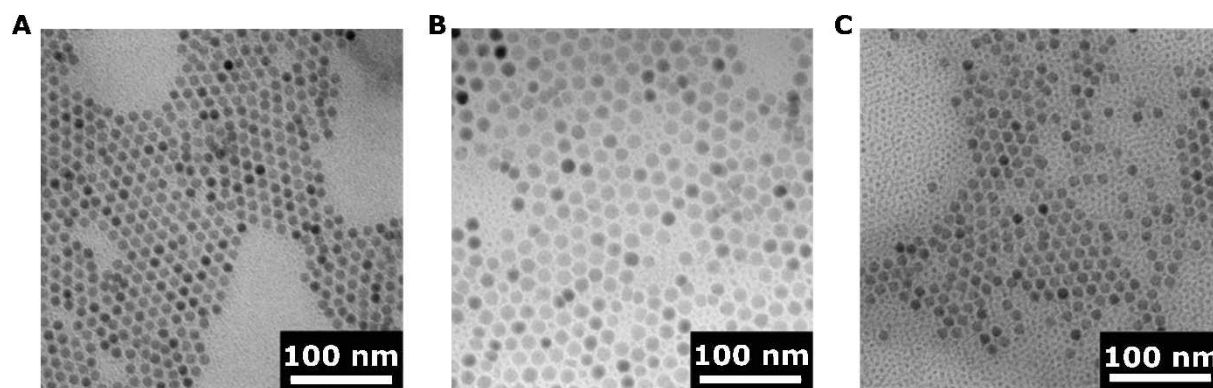


Figure 10. Evolution of UCNP during the shell growth. A) initial core nanoparticles. B) UCNP obtained after 30 min at 280°C. C) final « core@shell » after 60 min at 280°C.

Limitations

As revealed by electron microscopy pictures, the coexistence of “real core@shell” with bigger size than the former core, and smaller “empty shell-precursors based” nanoparticles can be attributed to the nucleation and growth of NaYF₄ crystals. Such hypothesis should require high-resolution TEM with EDX analysis on single object for confirmation. From this shape analysis, two hypotheses can be developed: either some part of the NaYF₄ nucleates and grows on its side (due or not to a stoichiometry excess), or the reaction time was too short to achieve the complete re-dissolution of the NaYF₄ matter to feed the complete shell growth. We repeated the experiment by doubling the reaction time but it led to similar results.

This inhomogeneity will be a problem for subsequent steps:

- for nanohybrid formation: encapsulation attempt (ex: in silica) will lead to the mixture of core@shell encapsulated and the coating of inactive NaYF₄ impurities;
- for photophysical characterization: no quantitative approach can be easily envisaged, as all the solution prepared in mg/mL of UCNP in solution are in fact a mixture of core@shell UCNP and undoped NaYF₄ impurities.

Such NaYF₄ impurities may be discarded by developing a purification process by density gradient centrifugation. But such protocol optimization is time-consuming, and only adapted to a small scale (few mg).

As a consequence, we decided to abandon this thermal coprecipitation approach for shell synthesis, as we cannot have an accurate control on the shell precursor nucleation and epitaxial growth.

II.1.3 Impact of our high sensitizer content

We have investigated the interest of our protocol as a function of Yb content addressing three issues: size, reproducibility and luminescence. As mentioned in the introduction chapter it has been commonly admitted in the literature that optimal sensitizer content is 20% Yb. According to the literature^{17,18}, group III RE matrix such as Yb leads to bigger object than group II (Gd). Therefore, we compared our original composition (42%Gd, 57%Yb, 1%Tm) to the “standard” one (20%Yb) to evaluate the impact on the growth of NP and on their optical properties.

Both compositions led to the formation of pure β -nanospheres. Nevertheless, our high Yb doping induced the formation of bigger objects, as revealed by TEM pictures and XRD (peaks broadening for 20%Yb due to smaller NP size).

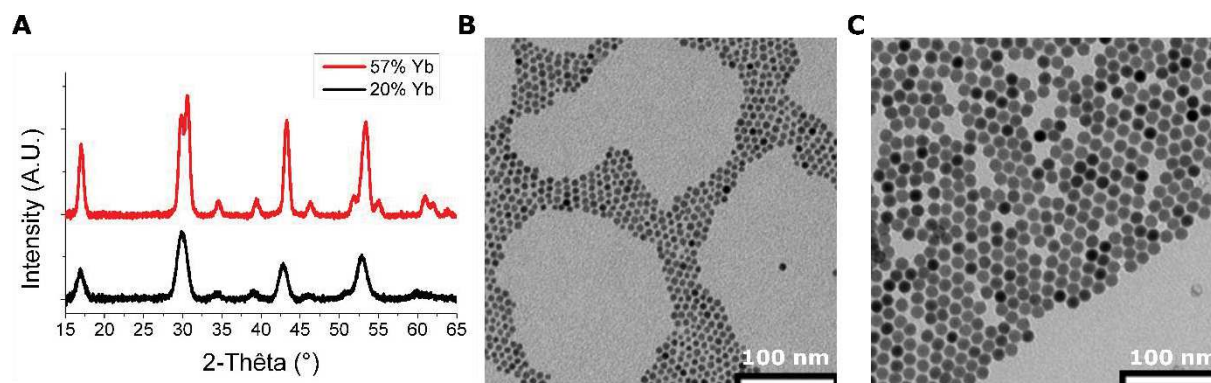


Figure 11. Comparison of small nanospheres with two Yb content (20% or 57%).

A) Diffractograms from powder XRD. B) and C) TEM pictures for respectively 20% and 57% Yb content.

Batch-to-batch size reproducibility is good for the standard 20% doped UCNPs, and yields particle of diameter of around 7.5 nm. However, our high doping led to a variable diameter between 10 (2 batch syntheses) and 15 nm (2 batch syntheses). The general observation that size increases with Yb content is in agreement with the literature, especially the work by Prasad team.¹⁶

Despite size variation, luminescence comparison was investigated between the 7.5 nm-sized 20%Yb-doped UCNPs and the 15 nm UCNPs with 57%Yb (figure 12).

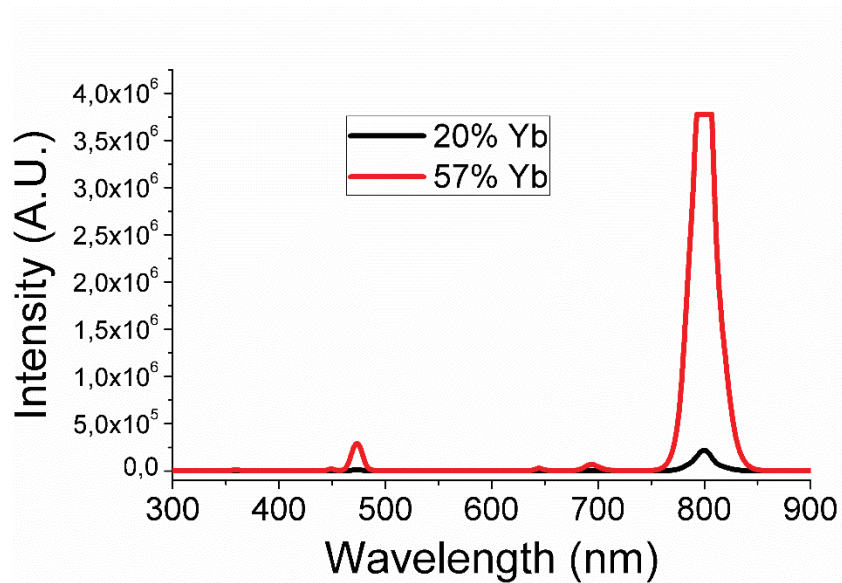


Figure 12. Comparison of luminescence intensity depending on the ytterbium content. Both samples were prepared at 5 mg/mL in cyclohexane and observed under 976 nm CW laser ($P=35\text{W cm}^{-2}$).

It is obvious that a gain of luminescence is observed at our high doping content, even if we have no clear evidence that this enhancement is due to the Yb content effect, size effect, or a combination of both. Nevertheless, this allowed us to validate our choice of high ytterbium doping composition.

II.1.4 Conclusion on small nanospheres

From these first preliminary investigations, we implemented a simple synthesis to produce small UCNP with an original Na(Gd_{42%}-Yb_{57%})F₄ matrix. By comparing with a lower but classical Yb content, we confirmed that our higher sensitizer doping leads to a better luminescence emission even if it limits the size reduction. We have demonstrated that the latter cannot be achieved by simple reaction time shortening.

Additionally reproducibility issues were stressed out with our composition, in agreement with May and coworkers.¹³

Shell growth *via* thermal coprecipitation was abandoned, due to a lack of control of the nucleation.

As a result, the remaining area of investigation in order to reach size reduction is the chemical engineering: either the precursors mixing or the high temperature heating step for the $\alpha \rightarrow \beta$ Ostwald's sequence.

II.2 Transposition of nanospheres synthesis from *premix* to *in situ* mixing approach

We started by the exploration of mixing variation of our above-described protocol. As the presence of NaF precipitate was evidenced, our goal was to prevent its formation during NaOH and NH₄F introduction. We expected a better sodium and fluoride availability, thus an increased number of nuclei generation, leading to a final smaller size.

In an interesting approach by Zhai *et al.*,¹⁹ it was reported that the size of β -NaYF₄-based UCNP could be halved by the simultaneous but separate introduction of NaOH and NH₄F to the OA:ODE solution of rare-earth precursors (hereafter referred to as “in situ” mixing).¹⁹ Differing only by this addition method from of the above-mentioned “*premix*” protocol,⁸ we decided to adapt it to our target formulation by coupling 2 syringe pumps containing respectively each precursors (sodium and fluoride).

Two core syntheses were performed from 2 different batches in order to check the reproducibility. Contrary to the precedent subsection, only 3 aliquots were sampled on key moments during heating at 280°C (either at 15 min, 30 min, and 90 min, or at 30 min, 60 min, and 90 min, figure 13).

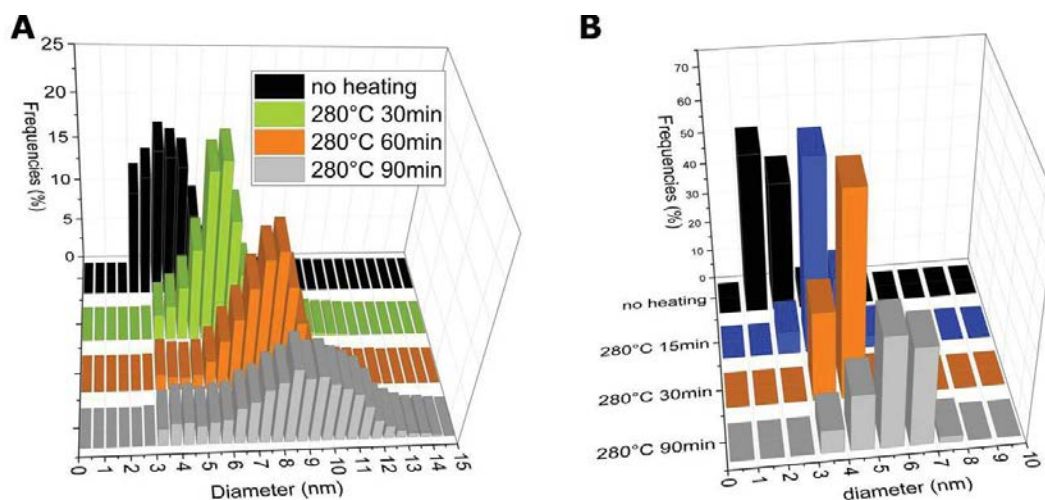


Figure 13. TEM monitoring of thermal coprecipitation synthesis via *in situ* mixing. A) and B) are respectively the result of 2 trials performed with 2 different batches of the same composition.

At first, a lack of reproducibility is clearly visible as both trials led to different size and dispersity. Nevertheless, in both cases, global size reduction is obvious compared to the size of 10-15 nm via *premix mixing* approach. The size broadening trend is also reproduced in the two trials (especially on figure 13 A), suggesting some Ostwald defocusing effect.

Although no spectacular size reduction was observed, the lack of distinct sub-populations tended to indicate that the “*in situ*” introduction process was compatible with our aim to prepare sub-10 nm β -UCNPs. Additionally, the automatization of addition rate, thanks to syringe pumps, prevents user-dependent reproducibility issue as it could be envisioned for premix with manual dropwise addition.

Once this new mixing approach was adopted, the last point was to question the high temperature heating step. The idea was to replace our heating mantle with an apparatus able to give a fast, sharp heating, with an accurate control of temperature. Therefore, we turned our attention to the transposition of this *in situ* mixing protocol with the so-called “conventional heating” to microwave-assisted heating to study its impact on the Ostwald focusing.

II.3 Towards sub-5 nm NP obtained via microwave synthesis

II.3.1 Reminder about UCNP and microwave synthesis

Principle of microwave heating

The interaction of MW (microwaves) with a material is usually described by two main mechanisms: dipole rotation and ionic conduction. Polar molecules are involved in dipolar polarization, while ions contribute to the latter.²⁰

The efficiency of MW absorption is the so-called loss-tangent ($\tan \delta$) which is the ratio between the dielectric constant describing the polarizability of molecules in the electric field (ϵ') and the dielectric loss (ϵ'') related to the microwave absorption. The higher $\tan \delta$, the more MW are absorbed. However, Beer's law then applies and the MW damping occurs over a thickness (skin effect) depending on $\tan \delta$ as well.

Microwave ovens

Two kinds of microwave oven can be distinguished according to the size of the resonating cavity coupled to the MW source (magnetron):

-multimode oven: such as domestic microwave ovens, they have a cavity larger than the MW wavelength. Several stationary modes match the cavity geometry and the energy is not evenly distributed spatially within the oven. The amount of energy effectively deposited within a sample is not known with accuracy. However, their large cavity enables the processing of reactors with a large volume.

-monomode oven: In order to know with precision how much energy is introduced into the reactor, another type of cavity has been developed, known as monomode oven. In this configuration the energy is localized at the center of the cavity. However, the cavity must have the size of the MW wavelength. Therefore, the adapted reactors have a limited capacity.

Thanks to the BLINK ANR project, the lab is equipped with a monomode reactor from Anton Paar. This apparatus can operate up to 300°C for 30 minutes, with a maximum pressure of 30 bars. Two different reactors can be used for different scales, respectively of 10 mL and 30 mL. These test-tube shaped reactors are capped by septum, allowing us to work under controlled atmosphere. In the present chapter, all the MW heating steps were performed in an argon atmosphere.

Microwave and chemistry

Currently, microwave (MW) oven reactor have become a common tool in chemistry laboratory. Two phenomena are expected:

- fast heating in organic reactions for time shortening, compared to standard heating devices. Trivial kinetic considerations states that chemical reactions are accelerated upon temperature increase. However fast heating also results in the reduction of side reactions. Heat generation is usually achieved by a proper solvent choice.
- or the so-called “microwave effect” that is based on specific MW-induced change of activation energy.

According to Arrhenius law, it has been empirically demonstrated that an organic chemical rate constant could be doubled by increasing the reaction temperature by 10°C. As a result, reaction time is halved. However, to the best of our knowledge, such a simple Arrhenius law consideration has not been applied to the case of nanoparticle synthesis, especially to a crystal phase transformation.

Expectations from microwave heating to UCNP synthesis

As for organic synthesis, increasing heating rate to high temperature with an accurate control of temperature has interested people involved in NP preparation. For inorganic crystals formation, such an apparatus has been mainly used as a substitute to the usual hydrothermal/solvothermal synthesis performed in stainless steel autoclave, in water or alcohol solvents. In the UCNP community, only a few pieces of work have investigated this area. As reported in the table 3, autoclave substitution approach usually leads to the preparation of big objects.

However since the seminal work of Thomas Nann²¹, synthesis in low absorbing “alkane-like mixture” solvent (OA:ODE) via “TFA pyrolysis approach” were developed to prepare ultrasmall objects, but only crystallized in the cubic phase. Even though not demonstrated experimentally, the explanation proposed is that trifluoroacetate is supposed to have a “high microwave extinction coefficient” thanks to its ionic character.²¹ Noticeably, nobody has tried to use usual fluoride sources other than TFA in OA:ODE. By continuity with our previous results, we decided to study the unexplored area (yellow case in the following table). The following points be addressed: feasibility of such high temperature heating in low-absorbing solvent, identification of the origin of microwave heating, and the possibility to reach sub-5 nm β -UCNPs.

Table 3. Overview of reported microwave syntheses of NaREF₄ as a function of the solvent and the fluoride source: NaF and/or NH₄HF₂ (blue), NH₄F (red), trifluoroacetate (green), or ionic liquid (brown). **Yellow case indicates the place we want to investigate with NH₄F.**

* represents phase mixture. ODE, OA, OM are respectively octadecene, oleic acid, oleylamine.

		tan δ ²⁰	Ultrasmall size (<10 nm)		Size >10 nm		
			α -phase	β -phase	α -phase	β -phase	other phases
high absorbing solvent tan δ >0.5	Ethylene glycol	1.350			16-200 nm NaYF ₄ ^{22,23} 40 nm NaGdF ₄ ²⁴	1-1,5 μ m NaYF ₄ ²² 45-65 nm NaGdF ₄ ^{24,25}	
	Ethylene glycol : water		8 nm NaYF ₄ ²⁶		35-45 nm NaYF ₄ * ²⁷ 75 nm NaYF ₄ ^{28,29}	35-45 nm NaYF ₄ * ²⁷ 0.2x0.4 μ m NaYF ₄ ²⁸	orthorhombic YF ₃ * ²⁷
	ethylene glycol: choline chloride					100-880 nm NaREF ₄ (RE=Gd; Y; or Yb) ³⁰	
	ethanol	0.941				2-3x0.3-0.4 μ m NaYF ₄ ³¹	
	Ethanol : acetic acid (: water)				25-32 nm NaYF ₄ ^{32,33}	107x83 nm NaGdF ₄ ³³ 26 nm NaYF ₄ ³⁴	tetragonal 2-4 μ m LiREF ₄ (RE=Y or Yb) ³³
medium-absorbing solvent 0.5>tan δ >0.1	Benzyl alcohol : water					15x30-100 nm NaYF ₄ ³⁵	
	Ionic liquid [bmim]PF ₆	0.185				80-300 nm NaYF ₄ ³⁶	
	Water	0.123			200 nm NaYF ₄ ³⁷ 9-30 nm M _{0.67} RE _{0.33} F _{2.33} ³⁸	μ m NaYF ₄ ^{37,39-41} 20-750 nm NaGdF ₄ ^{42,43}	
	oleic acid : alcohol : water		8-14 nm NaYF ₄ ⁴⁴		8-30 nm NaYF ₄ ⁴⁴⁻⁴⁶	20-120 nm NaGdF ₄ ⁴² 19-150 nm NaYF ₄ * ⁴⁶	
low-absorbing tan δ <0.1	“alkane-like” mixture (ODE, OA, OM, etc...)		6-10 nm NaYF ₄ ^{21,47,48}		13-26 nm NaYF ₄ ⁴⁷ 15-18 nm GdF ₃ and NaGdF ₄ ⁴⁹		tetragonal LiYF ₄ & Li _{0.8} Na _{0.2} YF ₄ ⁴⁷

II.3.2 Feasibility of MW heating in OA:ODE without TFA

We checked if the low absorbing OA:ODE mixture was compatible with microwave heating in order to reach 300°C by comparing with a heating mantle.

The first point was to tune the solvent composition to identify which component was responsible of the heating.

Solvent behavior

A striking feature of the studied system is the poor absorptivity of the reaction solvent. The dielectric properties of oleic acid and 1-octadecene solvents are not well described and their dielectric loss ($\tan \delta$) can be reasonably estimated to be less than 5×10^{-3} at 2.45 GHz.⁵⁰ However, it is possible to estimate which component is mostly responsible for MW heating efficiency using simple calorimetric considerations, by monitoring the temperature rise inside the oven under constant MW power irradiation. Blank experiments with solvents, pure or as a mixture, or the reaction mixture itself were undertaken. Figure 14 shows the temperature vs. time evolution when the oven applies the constant power of 100 W. The initial slope can be used to estimate P_{abs} , the power absorbed by the sample.⁵¹ In the vicinity of room temperature, one can consider the heating to be adiabatic. All things being equal (vials, stirring bars, etc.) the initial slope can be approximated as a function of the oleic acid mass fraction x according to the following equation:

$$P_{\text{abs}}(x) = A(x)P_0 = (C_0 + m[C_p^{\text{ODE}} + x(C_p^{\text{OA}} - C_p^{\text{ODE}})]) \frac{dT}{dt}$$

with P_0 the oven power, $A(x)$ the fraction of power effectively absorbed, C_0 the specific heat of the vessel, m the sample mass and C_p^i the massic specific heats of ODE and OA (1.6 J g^{-1} ⁵² and 2 J g^{-1} respectively).⁵³ As expected, it can be deduced that oleic acid is a better MW absorber than 1-octadecene. Noticeably, although relatively transparent to MW, the reaction mixture reached the 300°C set point within 5 minutes on a 5 mL scale using the “*as fast as possible*” (up to 850 W, figure 15) routine which is still much faster than with a conventional heating mantle. Beside the control of the nanoparticle growth, OA has here an important secondary role in the heat transfer capacity of the solvent.

It should be noted that UCNPs do not contribute significantly to the microwave heating, as the same slopes were obtained for the 43% OA composition with or without NP in the mixture.

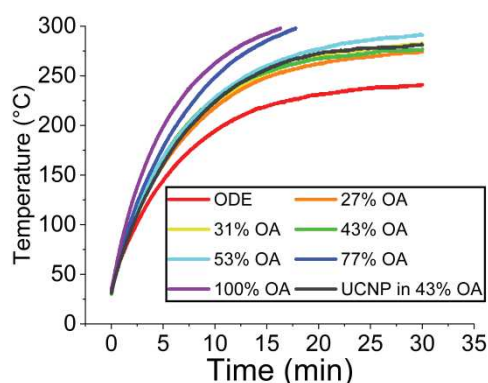


Figure 14. Comparison of microwave heating rates for different OA:ODE mixtures (%OA being mass percentage) under constant microwave irradiation ($P=100$ Watt).

Heating rate

Once identification of MW absorption in OA:ODE achieved, we turned our attention to the MW heating rate comparison with our heating mantle.

Using the MW heating, the target temperatures (ex: 300°C) were reached within 5 minutes using the “*as fast as possible*” instrument routine (figure 15), while a little more than 25 minutes were required for our heating mantle.

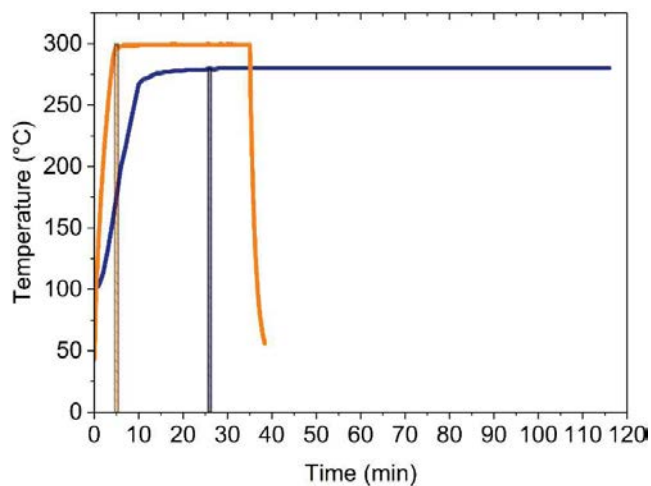


Figure 15. Heating profiles of high temperature heating step as a function of time monitored for conventional heating (dark blue curve) (Horst heating mantle and controller) and microwave heating (Monowave 300, Anton-Paar) experiment for the 300°C 30 min plateau (orange curve). Both orange and blue hatched rectangles indicate for the corresponding curves the end of the temperature rise (i.e. beginning of the plateau).

In usual UCNP protocol, only plateau duration is considered. Note for the heating mantle the heavy damping applied to avoid temperature overshoots. The cooling step was not monitored in the case of conventional heating. Practically it was achieved by just removing the heating mantle and letting the reactor cool down slowly with ambient air. Typically, it was empirically considered that a 20-30 min period was necessary to return to room temperature.

The temperature rise is sharper with microwave oven: Indeed, it is around 5 times faster to reach 300°C with microwave oven than 280°C with heating mantle.

The heating step (temperature rise + high temperature plateau) is shortened by 70% by replacing heating mantle with microwave oven, if we consider a 30 min plateau at 300°C which is the maximal duration of the microwave heating. Thus, important time shortening due to the sharp MW heating is expected if we find optimal microwave heating conditions to prepare the desired UCNPs.

II.3.3 Simple microwave heating: high temperature plateau

Optimization of the microwave heating

Based on our previous results, we investigated microwave heating to form homogeneous ultrasmall β -UCNP in the usual OA:ODE mixture (43% OA in mass percentage).

If the empirical Arrhenius law previously described is transposable to nanoparticle synthesis, high temperature plateau of 90 min at 280°C should result in 45 min at 290°C or 22.5 min at 300°C. Starting from this assumption, we investigated the optimization of the microwave heating thanks to the comparison of two parameters: at first temperature impact while fixing 30 min reaction time, then plateau duration for the best temperature conditions i.e. the so-called “reaction time” (figure 16).

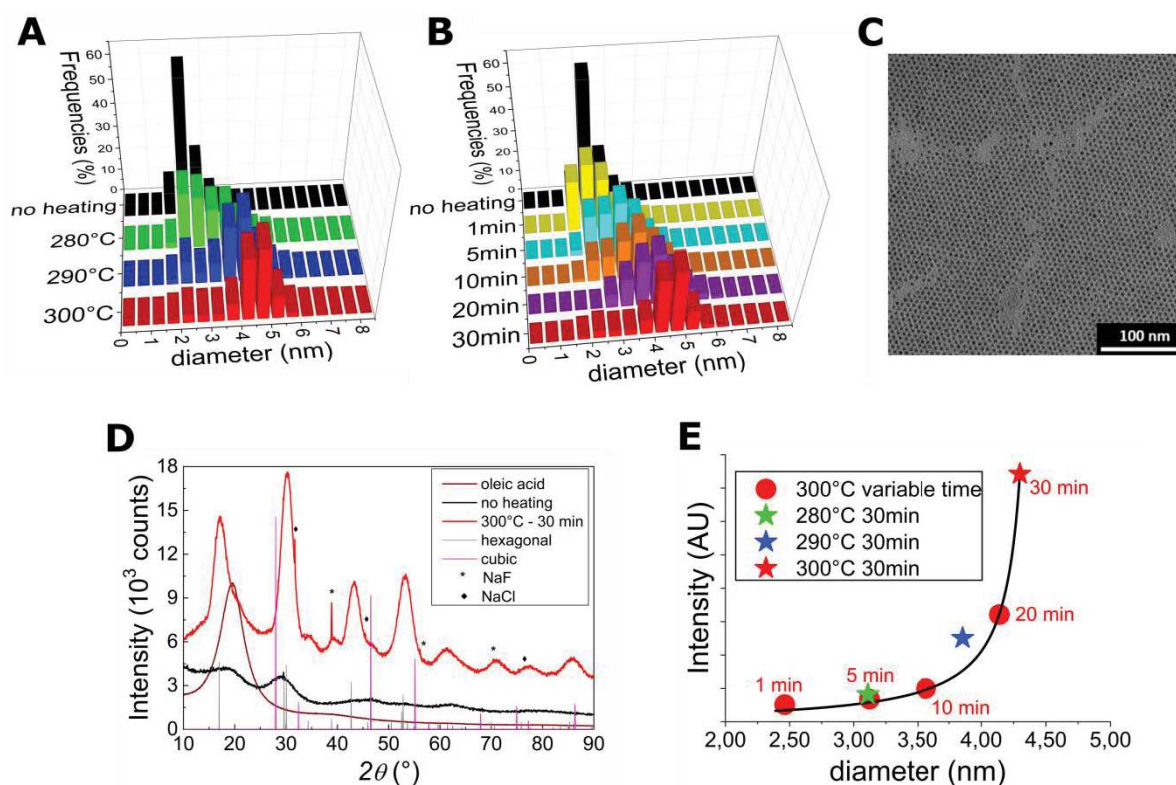


Figure 16. Characterizations of samples prepared by microwave-assisted thermal coprecipitation synthesis: A) Size distributions obtained from TEM pictures after 30 min of different temperature plateau. B) Size distributions obtained from TEM pictures after different plateau durations at 300°C. C) TEM picture for sample obtained by a plateau of 30 minutes at 300°C. D) XRD of a non-heated sample and a sample annealed at 300°C during 30 min. E) Luminescence intensity at 800 nm measured on unpurified crude material, as a function of the corresponding UCNPs sizes measured from TEM pictures – The black line is a guide for the eyes.

TEM examinations of the purified nanoparticles revealed no significant morphology changes for plateau temperatures lower than 280°C: particles remained almost as small as those in the initial precipitate (2.3 ± 0.3 nm). However, the size was found to increase at higher plateau temperature (figure 16A). Interestingly, the size distribution narrows down between 20 min (4.1 ± 0.8 nm) and 30 min (4.6 ± 0.5 nm) of heating at 300°C (figure. 16B).

As observed in figure 16C, after 30 min of heating at 300°C, highly homogenous sub-5 nm nanospheres were obtained. Note that this is the only condition that allows us to keep the

standard deviation within 10 %. As a result, 300°C 30°C seems to be the optimal condition to get sub-5 nm homogeneous NPs.

More information could be gained from XRD analyses of all the produced samples (figure 16D). As expected, the diffractograms could be interpreted as mixtures of cubic and hexagonal phases in various proportions. Keeping the reaction time constant (30 min), the increase of the temperature above 290°C led to the complete disappearance of the α -phase. More interestingly, at 300°C, the α -phase was found to be the major component at the early reaction stages but disappeared after as little as 20 minutes of heating (figure 17).

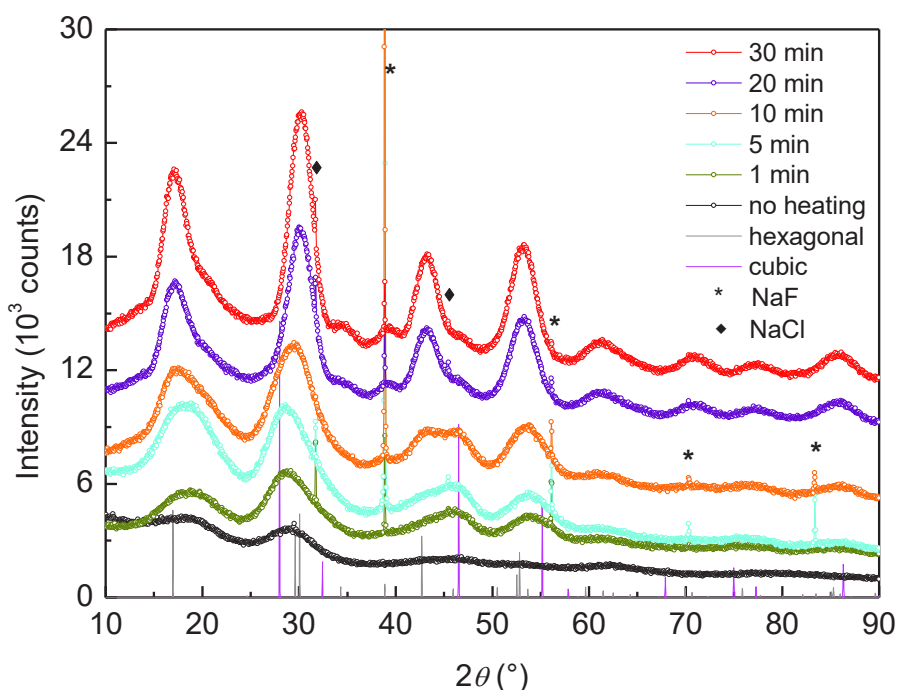


Figure 17. Experimental (symbols) powder XRD patterns of NaREF₄ synthesized at 300°C for various annealing durations: The theoretical patterns for the hexagonal (grey) and cubic (magenta) NaGdF₄ polymorphs are plotted as solid lines while the stars and diamonds indicate the visible peaks of NaF and NaCl, respectively. The broad humps or shoulders observed around 19° are attributed to the oleic acid used for the syntheses.

In parallel, a sharp rise of the emission intensity of the 800 nm thulium emission under 980 nm irradiation could also be observed for reaction times longer than 20 minutes. This α -to- β transition is thus analogous to what was observed for premixing conditions, but here it occurred between much smaller objects, in a similar way to the report by Zhai *et al.*¹⁹ Clearly, the

combination of *in situ* mixing and microwave-assisted heating at 300°C enabled us to prepare ultrasmall Na(Yb-Gd)F₄:Tm upconverting nanocrystals of an average size of 4.6 ± 0.5 nm within 30 minutes.

Impact of size reduction on luminescence

As already mentioned, a sharp rise for all thulium emissions is observed when the nanoparticle diameter is above *ca.* 4 nm (figure 16E). This threshold size is primarily associated to the α -population disappearance. However, as described in the introduction chapter, efficient surface quenching can impede emission for smaller β -nanoparticles. Indeed, Gargas *et al.* proposed the existence of a “dark layer” extending down to 1.8 to 2 nm below the surface.⁵⁴ Therefore, nanoparticles with a diameter smaller than *ca.* 3.6 nm would relax mostly through surface-induced non-radiative processes. Yet, the question remains about the “efficiency in depth” of this surface quenching.

Discussion on β -seeds

Considering that the α -population survives over 2/3 of the reaction time, the final Ostwald ripening of the β -nanocrystals happens on a very short time scale. It is therefore possible to approximate the proportion of β -seeds [8.8 % of NaREF₄ seeds, see below table 4] that should be present at the early stages of the synthesis such as at 1 minute, when all particle diameters are about 2 nm, to the number of particles observed after 30 minutes at 300°C. With such a small crystallite size, and small relative quantity, those β -particles are hardly visible on the XRD patterns measured at the early stage of annealing (figure 17). Complete transfer of the material stored as α -particles into the β -ones is compatible with the observed final sizes.

During the growth phase, the number of β -particles is frozen, and their size increase is solely due to the consumption of monomers that are produced by the redissolution of kinetically labile α -particles. If one considers that the Ostwald ripening has not started yet, the final number of β -nanoparticles is a good estimation of the number of initial β -nuclei. To estimate such a number, we first calculate the total volume of NaREF₄ that should be recovered after complete transformation (when all the material is now under the hexagonal phase). The average unit cell volume was calculated from the NaGdF₄ and NaYbF₄ unit cell volumes, neglecting the contribution of thulium.

Table 4. Data used for estimation of the number of β -seeds (sample “300°C -30min” figure 16-17)

Experimental parameters			Crystallographic data
ICP composition	Composition for calculation	Experimental data	
			JCPDS 00-027-0699 (NaGdF ₄) JCPDS 00-027-1427 (NaYbF ₄)
(%Gd) _{mol} =46.5%	(%Gd) _{mol} =47.06%	n _{RE} =1.983 mmol	$U_{NaGdF_4} = 113.02 \text{ \AA}^3$ (Z=1.5)
(%Yb) _{mol} =52.3%	(%Yb) _{mol} =52.94%	r _{TEM} = 22.5 Å	$U_{NaYbF_4} = 105.67 \text{ \AA}^3$ (Z=1.5)
(%Tm) _{mol} =1.14%			

$$U_{NaREF_4} = \Sigma[(\%RE_i)_{mol} \times U_{NaRE_iF_4}]$$

$$\approx [(\%Yb)_{mol} \times U_{NaYbF_4}] + [(\%Gd)_{mol} \times U_{NaGdF_4}] \quad (1)$$

$$V_{RE} = \frac{n_{RE} \times U_{NaREF_4} \times N_A}{Z} \quad (2)$$

The volume of one average nanoparticle can be obtained from TEM image analysis

$$V_{TEM} = \frac{4}{3} \pi r_{TEM}^3 \quad (3)$$

The number of seeds is therefore the ratio

$$N_{seeds} = \frac{V_{RE}}{V_{TEM}} \quad (4)$$

We can then hypothesize that seed particles were present but undistinguishable from the other α -particles at the early stages of the synthesis. TEM images after one minute of heating give an average diameter (i.e. $2 r_{seed}$) value of about 2 nm. Applying this value to the seeds leads to an average nucleus volume of:

$$V_{seed} = \frac{4}{3} \pi r_{seed}^3 \quad (5)$$

Knowing the unit cell of β -NaGdF₄ (U_{NaGdF_4}) and Z , the number of Gd per unit cell it is possible to compute the number of gadolinium ions inside a nucleus following:

$$N_{RE/seed} = \frac{V_{seed} \times Z}{U_{NaREF_4}} \quad (6)$$

The number of Gd³⁺ ions trapped into the seeds is then

$$N_{(RE)seeds} = N_{seeds} \times N_{RE/seed} \quad (7)$$

Thus, in moles:

$$n_{(RE)seeds} = \frac{N_{(RE)seeds}}{N_A} \quad (8)$$

Dividing this number of moles by the initial amount of RE used gives the **molar percentage** of the β -phase initially present when all particles are of *ca.* 2nm in diameter:

$$\% \beta = \frac{n_{(RE)seeds}}{n_{RE}} \approx \mathbf{8.8\%} \quad (9)$$

We can then calculate the **increase of radius** due to the complete transfer of the α -phase material onto the seeds by calculating the volume of β -NaREF₄ that can be produced by the remaining rare earths:

The number of moles of rare earth remaining in the α -nanoparticles phase is

$$n_{RE \alpha} = n_{RE} - n_{(RE)seeds} \quad (10)$$

And should produce the volume V_{excess} , if all this material is finally converted into β -NaREF₄:

$$V_{excess} = n_{RE \alpha} \times \frac{U_{NaREF_4} \times N_A}{Z} \quad (11)$$

This volume has to be spread-out over-all nuclei. Therefore, the volume growth of one nucleus is

$$V_{growth/seed} = \frac{V_{excess}}{N_{seeds}} \quad (12)$$

The final volume of a β -NaREF₄ nanoparticle is now:

$$V_{tot} = V_{growth/seed} + V_{seed} \quad (13)$$

Hence the estimated **final radius and diameter** are:

$$r = \sqrt[3]{\frac{V_{tot}}{\frac{4}{3}\pi}} \Leftrightarrow d \approx 4.5 \text{ nm} \quad (14)$$

These values are consistent with the experimental one.

Nanoparticle formation and Ostwald’s step rule

It is also worth mentioning that the evolution of the relative standard deviation ($\langle\sigma\rangle/d_m$) with time, becoming minimal when the α -population vanishes, is in agreement with the intrinsic focusing model developed for an α - β population interconversion by Voß *et al.*¹⁸

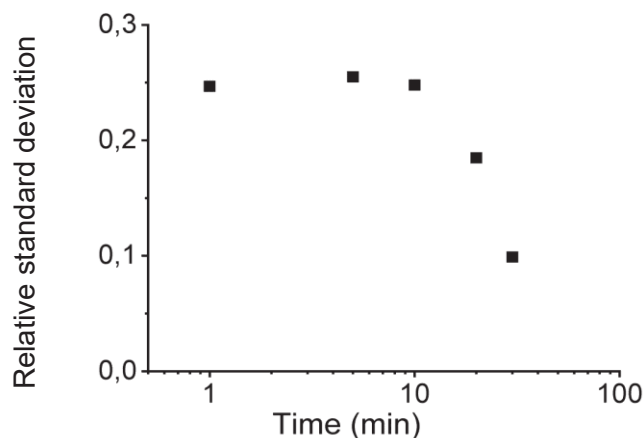


Figure 18. Evolution of the relative standard deviation ($\langle\sigma\rangle/d_m$) with time at 300°C.

No attempt was made to distinguish the two polymorphs as the two populations were found to be undistinguishable by TEM. Our experimental σ_d/d_m values are in agreement with the Voß *et al.* model.¹⁸ The β -population is expected to decrease abruptly when the α -population vanishes. Subsequent Ostwald ripening of the remaining β -population should then lead to an increase of the σ_d/d_m . In the present case, this would probably occur after 30 minutes.

Conclusion on simple microwave heating

Transposition to microwave heating was a success for the size reduction down to around 5 nm. Their luminescence properties (figure 16E) are in agreement with our supposed Arrhenius guide rule: indeed, the luminescence of the 290°C_30 min sample sits close to that of the 300°C_15 min sample. However additional points would be required to validate it completely. Moreover, our experimental data demonstrated Ostwald focusing mechanism in the nanoparticle synthesis.

Such small UCNP start to challenge the QD size range, but they are still bigger than blue-emitting QD. We therefore decided to modulate the microwave heating to expect an additional size drop.

II.3.4 Cycling temperature

II.3.4.1 Further decrease in size

Ostwald ripening theory has been developed for isothermal conditions. However, temperature changes during the crystal growth have a strong impact on the crystals shape and size. Thus, temperature cycling has been identified to cause crystals coarsening in various medium (from food processing to geochemistry⁵⁵), but has also been optimized to become a powerful tool to control the size and size distributions of micro-macrocrystals of proteins or pharmaceutical compounds. Several crystallization setup based on this principle have thus been proposed, such as non-isothermal Taylor vortex flow⁵⁶ or microwave.⁵⁷

Its grounds rely on the intuitive idea that warming up a suspension of microcrystals will induce the dissolution of the smallest one (*aka* the finest), while subsequent cooling allows the remaining ones to grow from the supersaturated solution⁵⁸. Yet, the mechanism is probably more complex as shown in a theoretical investigation recently disclosed for the diffusion-controlled growth of microcrystals under quasi-square temperature modulation. It was pointed out that Ostwald ripening can take place at both temperatures.⁵⁹ Depending on the extreme temperature plateau's duration, this can cause the PSD to recover its complete "LSW shape" (i.e. its tail) after being truncated by the fast redissolution phenomenon. Despite this PSD broadening, the recovery of the fine particles matters as these will feed the growth of the larger particles at the next cycle. Eventually, it was shown that globally, temperature cycling accelerates particle coarsening.

Although very efficient, temperature cycling is very scarcely used for the making of nanocrystals. Noticeably, a related approach has been developed for the preparation of up-converting nanoparticles: to induce the formation of a large number of nuclei of the β -phase, Li *et al*⁶⁰ have proposed to apply repeated very short temperature spikes to the reaction mixture, each spike supposedly generating a new bunch of nuclei.

This strategy is particularly well adapted to the use of a microwave oven as such an apparatus allows very fast and sharp temperatures changes. We have therefore implemented temperature cycling in order to reach sizes close to the luminescence limit. We will show how using a square-temperature profile and microwave oven enables us to determine the time when the

α -phase completely disappears. The luminescence properties of the obtained ultrasmall nanoparticles will then be discussed.

Methodology

Inspired by the work of Li *et al.*,⁶⁰ we explored cycling temperature by fixing constant durations of the high temperature plateau at (1 min) and of the low temperature plateau (5 min). Nevertheless, temperature range, number of cycles, and the eventual subsequent plateaus were explored (figure 19 & 20).

During steps (1) and (2), heating temperature to T_{\max} allows at least partial dissolution of the matter as described above. As a result, regarding figure B, monomer concentration in solution is increasing to the labile zone where nucleation can happen. Step (3) is a fast cooling process leading to the precipitation of NaREF₄: monomer concentration is quickly reduced to the metastable zone, but above the solubility curve. As a result, such cycle generates a burst of nuclei. By repeating this cycle many times, it is expected to remove quickly α -phases and promote the β -ones. We assumed that for at least the first cycle only nucleation occurs if the pulse is short enough. Subsequent pulses should induce growth during step (2).

Another expectation of such cycling temperature is the “proof-reading” behavior. As smaller particles are more soluble than bigger ones, size dispersity should be self-restricted.

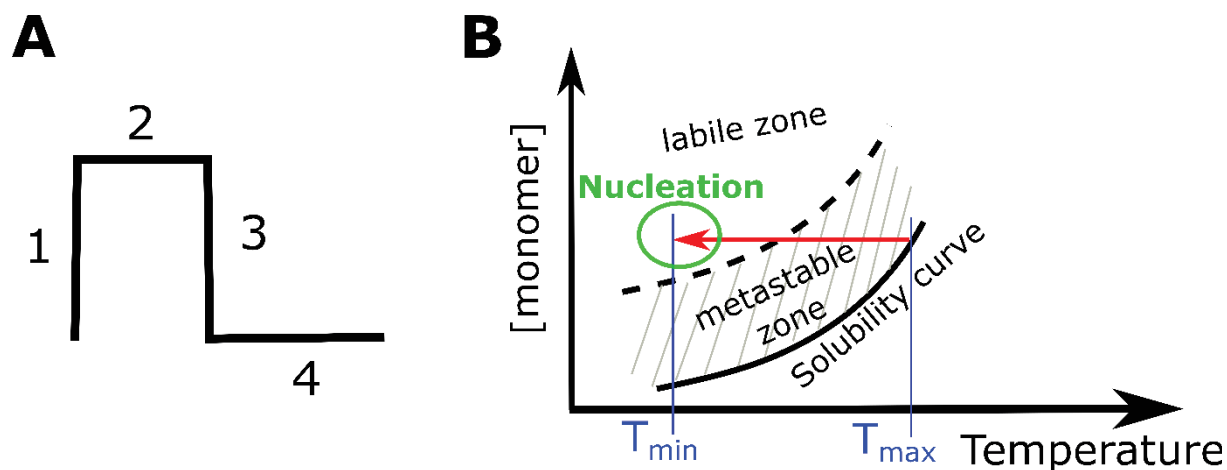


Figure 19. Principle of cycling temperature. A) Schematic representation of one cycle of the cycling temperature process. B) Temperature-dependent nucleation-growth model

By lack of time, no complete optimization by experimental plan was setup. Few series of conditions were tuned to quickly reach the following goal: reproducible synthesis of homogeneous UCNP with an average diameter of around 3 nm.

Cycling temperature “optimization”

Thanks to previous results on microwave heating plateau, we assume now that no homogeneous β -UCNP are formed at temperatures lower than 300°C. We set 300°C as a first approximation of T_{\max} (figure 19). On the same idea, at 280°C and cooler temperature no effect is expected. Hence the first attempts focus in this area, between 300°C and 260°C. As the only paper on UCNP dealing with temperature fluctuation (with conventional heating) assumed that pulses have to be followed by a plateau at lower temperature than the pulses,⁶⁰ we started by exploring the real impact of the plateau. On figure 20 A is compared the effect of additional plateau to two kinds of temperature ranges. It was observed that either plateau has dramatic size increase and broadening (for 265 to 300 °C or 265 to 285 °C temperature ranges followed by a plateau at 300°C) or no effect except extending the reaction time (265 to 285 °C then plateau at 275°C). Thus, plateau appears as a useless step. As a result, compared to this pioneer paper, we have directly a first improvement by shortening the overall reaction time.

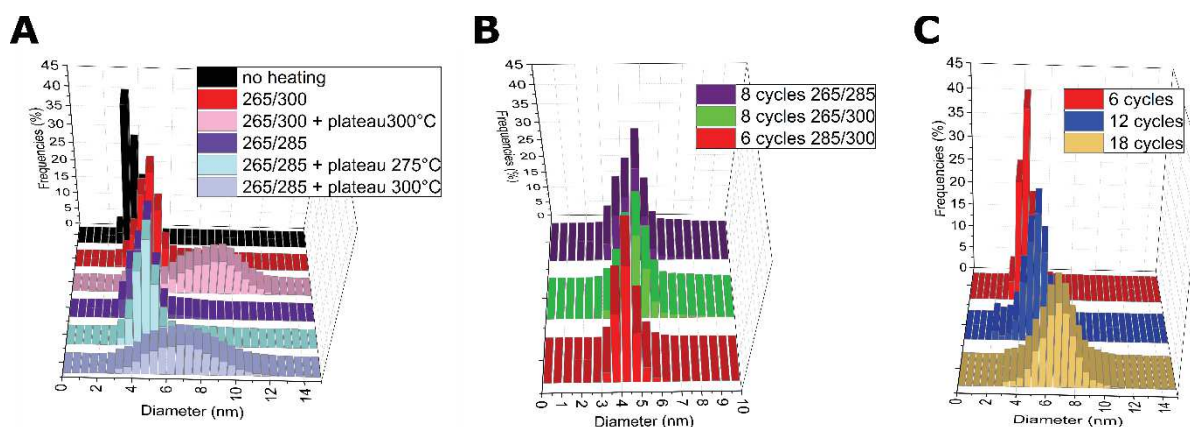


Figure 20. Optimization of cycling temperature in 3 steps. Investigation of the effect of: A) subsequent plateau, B) temperature range of oscillations, C) number of cycles.

Then temperature range was tuned (figure 20 B): it did not induce large variations between the 3 conditions (8 cycles between 265 and 285 or 265 and 300, or 6 cycles between 280-285 and 300°C). The latter was made for only 6 cycles as it was stopped by internal microwave security

due to exposure time at such high temperature. Nevertheless, for this condition, dispersity seems narrower.

Finally, figure 20 C addresses the impact of the number of cycles. As the microwave security is allowing only 6 cycles between 285 and 300°C, the heating sequence was repeated twice to get 12 cycles, or three times for 18 cycles. It is clearly identified that size increases and broadens after 6 cycles.

Therefore, the best condition was 6 cycles between 285 and 300°C. Additional experiments revealed similar result by replacing 285°C by 280°C.

Ostwald ripening control by cycling temperature

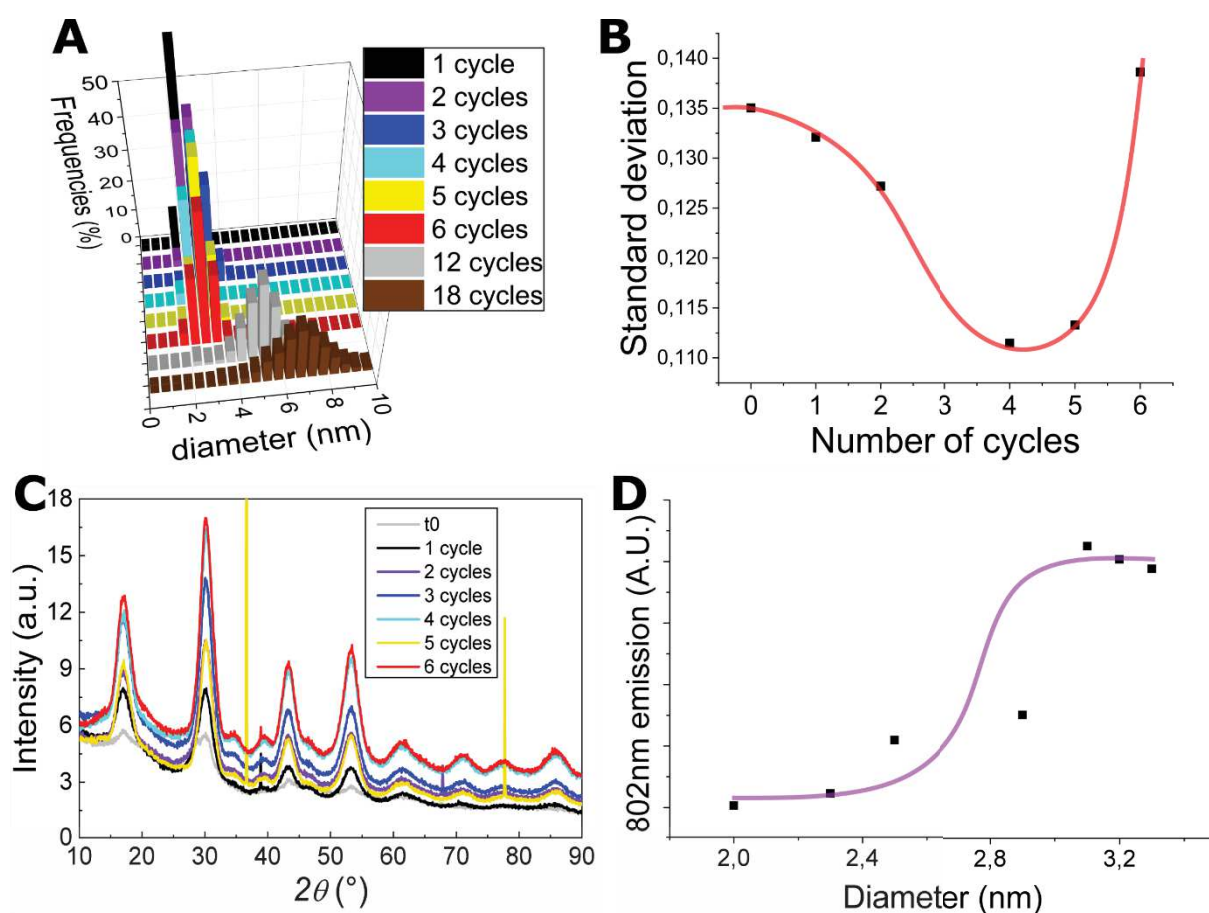


Figure 21. Monitoring of the cycling temperature inside 6 cycles: Size distribution compared to 12 and 18 cycles (A) and relative standard deviation σ/d (B) from TEM; XRD (C), and luminescence (D). On figure D, size of the object is following the number of cycles: from 2 nm for 0 cycles (no MW heating) to 3.3 nm for 6 cycles.

From TEM consideration (figure 21 A) one can observe an accurate size and dispersity control from the first 6 cycles while size increasing and broadening is revealed at 12 and 18 cycles, attesting the presence of Ostwald defocusing after 6 cycles.

Deeper analysis of the control of Ostwald focusing is addressed on figure 21 B by comparing the evolution of the standard deviation. Our experimental points are in agreement with the model proposed by Voss *et al.*¹⁸ Additionally, we can estimate that the cubic phase has disappeared between 4 and 5 cycles, according to the apparent position of the extremum. XRD monitoring (figure 21 C) is not easily analyzable without refinements as size peaks corresponding to the ultrasmall UCNPs are weak and broad. But after Sherrer-based model refinement (Table 5), it can be deduced that the cubic phase was in solution during the two first cycles. Nevertheless, no cubic phase was detected between 2 and 4 cycles. This is only due its low amount compared to XRD sensitivity and the size of the α -phase.

Concerning the luminescence monitoring (figure 21 D), as expected early small nanoparticles are lowly luminescent, while a sharp increase of luminescence is obtained after 4 and remains constant between 4 to 6 cycles. Such sudden appearance of luminescence matches with the disappearance of the cubic phase attested by the evolution of the standard deviation (figure 21 B). It should be noted that this can be attributed to a critical size of around 2.8 nm. This experimental critical size is of crucial importance, as the present data is the first reported experimental demonstration of such small size allowing upconversion phenomena. Up to now, critical sizes have been estimated by S. May *et al.* ($d_c > 5$ nm)⁶¹, or Gargas *et al.* ($d_c=3.6$ nm)⁵⁴ models based on extrapolation of Förster-based fitting model.

Table 5. Refinements on XRD monitored samples

Sample	Cell parameters (Å)	Apparent crystallite size (nm)	Corrected crystallite size (nm)	Relative proportion (%)
No heating		Non-refinable		
1 cycle	a = 5.992(1) c = 3.543(2)	3.4	4.5	87 (β)
	a = 5.541(6)	3.1	4.1	6 (NaF) 7 (α)
2 cycles	a = 5.9923(6) c = 3.5315(7)	3.9	5.2	98 (β)
	a ≈ 5.55	N.D.	N.D.	2 (α)
3 cycles	a = 5.9906(6) c = 3.5507(7)	3.5	4.7	100 (β)
4 cycles	a = 5.9841(5) c = 3.5468(6)	3.2	4.3	100 (β)
5 cycles	a = 5.9545(6) c = 3.5339(8)	2.7	3.6	100 (β)
6 cycles	a = 5.9790(5) c = 3.5433(6)	3.7	4.9	100 (β)

II.3.4.2 Ultrasmall Core Shell

There is previous evidence of a lack of control of shell growth via the thermal coprecipitation route. Additionally, for small-size core@shell, trifluoroacetate pyrolysis appears as a method of choice for the growth of a surface shielding layer. Therefore, we decided to move towards this way, following the work of Zhai *et al.*¹⁹

Shell growth by conventional heating

A first attempt of shell growth was performed with the heating mantle from cores of 3.2 nm in diameter. It was monitored by TEM analysis of sampled solution (figure 22).

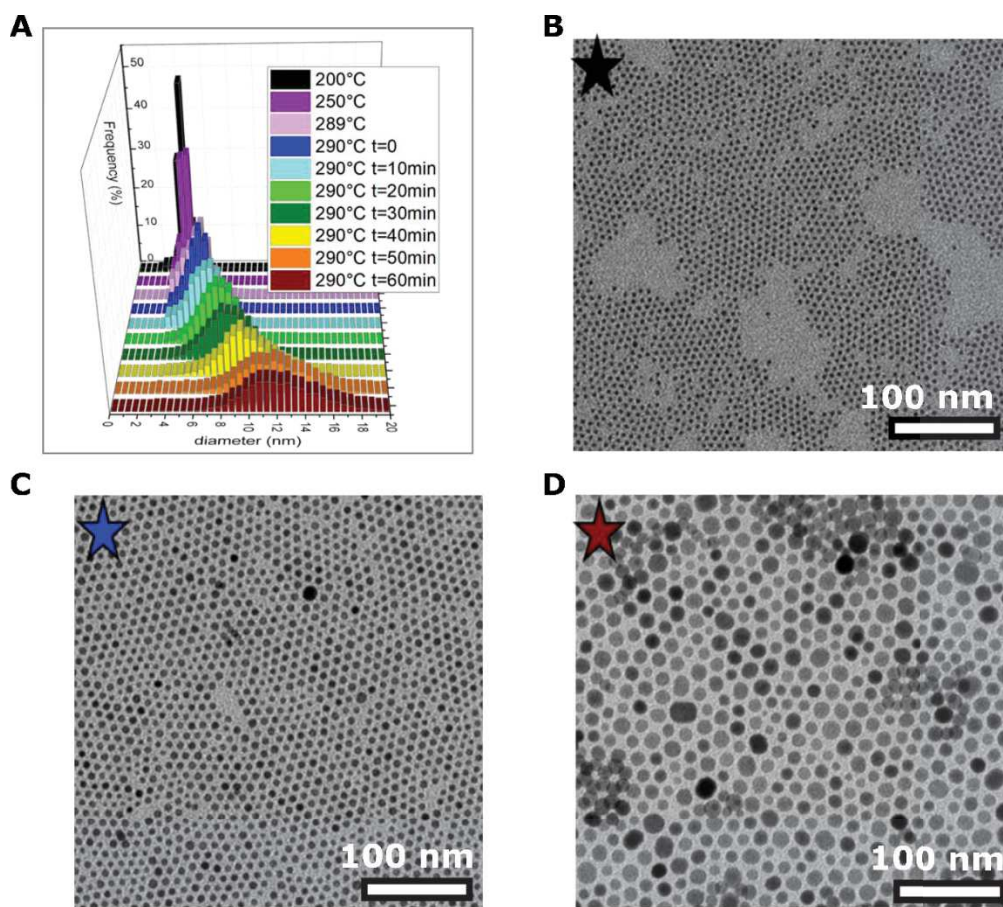


Figure 22. Kinetic monitoring of shell growth followed by TEM. A) Evolution of the size distribution with time. B, C, D are respectively initial core, UCNP at 290°C and final sample after 1h at 290°C.

Size increase and broadening occur with reaction time, suggesting Ostwald defocusing. It is clear that it is not optimized to limit size increase and dispersity. As a result, we turned toward microwave heating.

Shell growth by microwave heating, with a plateau

As the “Arrhenius acceleration” was a good option for core synthesis we decided to transpose such the previous heating step at 290°C for 1h to 30 minutes at 300°C in microwave reactor. As a control, a second condition with half of this time was also compared (figure 23).

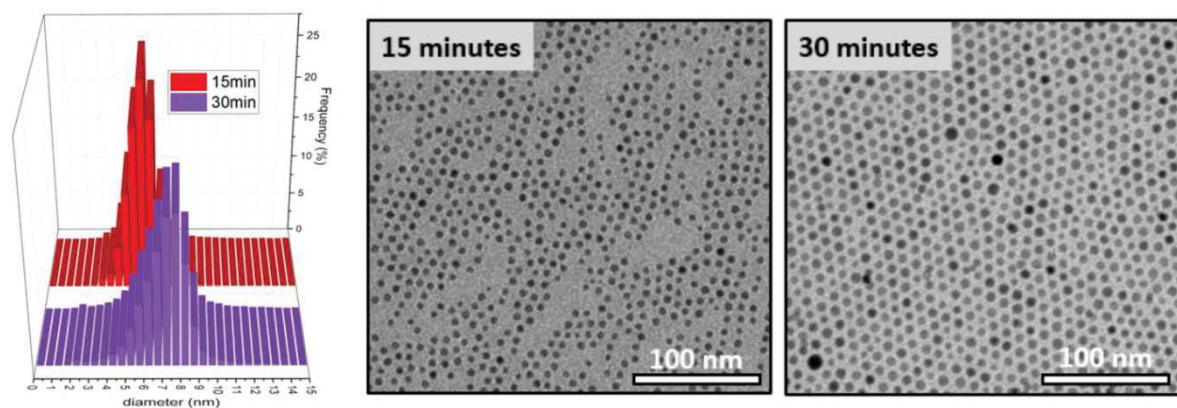


Figure 23. Comparison of Shell growth obtained via MW heating at 300°C during 15 min or 30 min.

Smaller size and narrower distribution are obtained by the transposition to microwave heating. After only 15 min, homogenous 5.7 ± 1.8 nm objects are obtained (compared to 7.3 ± 2.5 nm after 30 min). This appears to be our best condition. No further optimization of the shell growth was explored, as this positive result is good enough compared to our objectives which were to obtain an homogeneous core@shell UCNP of around 5-6 nm. Contrary to the core@shell attempt via thermal coprecipitation (section II.1.2), with this TFA-pyrolysis approach, only one homogeneous population is obtained.

Limitation of the shell growth protocol

The core size was 3.2 nm, corresponding to a sphere volume of 17.16 nm^3 . Because the amount of RE is identical for core and shell (2 mmol), a “perfect” core@shell should double this volume leading to an estimated size of 34.32 nm^3 . However, the prepared core@shell of 5.7 nm have a significantly larger volume (96.97 nm^3). The mechanism of core formation by temperature cycling assumes the partial dissolution of the UCNPs during the high temperature spikes at 300°C (6 times 1min). In the present shell growth protocol, the heating step at 300°C lasts for 15 min. Therefore, the observed larger volume of the core-shell nanoparticles could result from the partial redissolution of the ultrasmall core during their overexposition to such a high temperature. As a result, the “core@shell” architecture should be understood more like a “core + an intermixing of core and shell material”, in agreement with recent works⁶². High resolution microscopy (HRTEM) should be used to probe the exact local structure of the

supposed “core@shell” objects. As the present UCNP are extremely small, such investigation could be only performed with a synchrotron source.

II.3.4.3 Scope

Based on our pioneering well-controlled preparation of ultrasmall core and core@shell, we investigated the robustness of our protocol to variations such as doping content or reproducibility.

Impact of the doping content

Extension of the protocol to different compositions was evaluated by comparing the composition we have been describing (57%Yb) with the standard formulation (20%Yb) and a composition containing solely group III RE (99%Yb) under similar conditions. The desired hexagonal phase was obtained only for Yb contents of 20 and 57%. However, the cubic one is obtained with almost pure Yb matrix and bigger objects were obtained as demonstrated by the XRD (sharper peaks). TEM investigations were performed only on the two first batches. To our surprise, similar sizes were obtained with both composition which is in contradiction with the literature.¹⁶ Such a result will be particularly interesting considering photophysics, as the optical properties are strongly dependent on the doping concentration and the size. Therefore, with this robust protocol, direct comparison of the sensitizer content effect can be discussed. This will be discussed in the photophysics chapter.

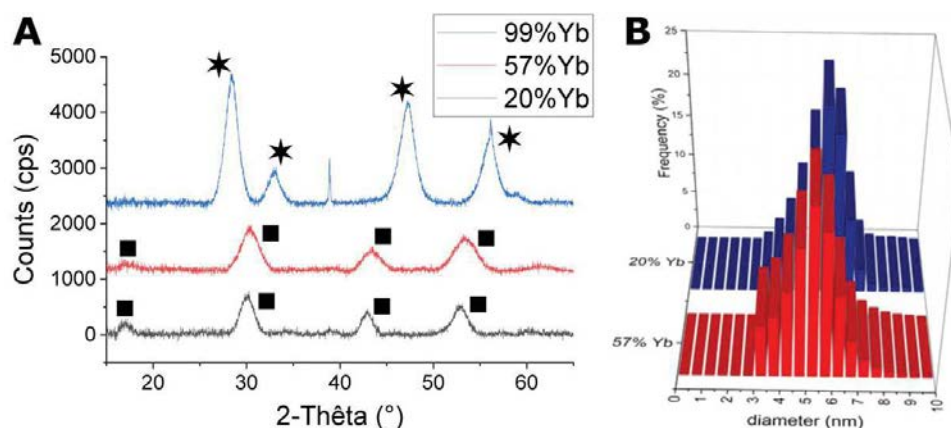


Figure 24. Impact of sensitizer content on crystal phase and size distribution. A) XRD obtained on ultrasmall core UCNP respectively doped at 20% (grey); 57% (red) or 99% Yb (blue). Squares indicate peaks from hexagonal phase, while the cubic ones are indicated by stars. B)

Size distributions obtained from analysis of TEM pictures for ultrasmall core@shell β -UCNP: respectively 20% Yb (dark blue) or 57% Yb (red).

Reproducibility

Over 6 batches, the size variation was found to be quite limited: core NP were always in the 2.5-3.5 nm range while core@shell had an average diameter in the 5-6 nm area.

One could here question the reliability of the heating process employed. Indeed, as the MW-reactor is limited to volumes from 2 to 20 mL, each UCNP batch (\approx 40 mL) had to be split into different fractions, each undergoing independent microwave heating. Then reaction mixtures were combined for purification and analysis. Thus, core and core@shell samples were respectively prepared by pooling 2 solutions of 20 mL and 3 solutions of 13-15 mL heated independently. Still, dispersity was found to not suffer from this methodology. As a result, it can be deduced that the “inter-batch variability” above-mentioned is not due to microwave-assisted heating but to an upstream step of the synthetic pathway. As far as reproducibility is concerned, this demonstrates the robustness of the microwave-assisted heating for ultrasmall nanoparticles synthesis.

II.3.5 Chemical characterization

In the whole manuscript, compositions are mainly given from theoretical value. If chemical yield was calculated, 2 sources of discrepancy between experiment and theory can be expected:

- overestimation of theoretical mass: Rare-Earth precursors used were of chemical formula $RECl_3 \cdot xH_2O$ (with $x=6$ for Gd and Yb; 7 for Tm). As a result, first error is coming from this incertitude on the amount of coordinated water molecules. Moreover, such Rare-Earth chlorides are hydroscopic and were not manipulated in a glove box, which could accentuate the error due to hydration uncertainty. Our calculations were based on the $RECl_3 \cdot xH_2O$ formula weight above-described.
- overestimation of the final UCNP mass produced: indeed NP are covered by a non-negligible organic corona of stabilizer (OA) increasing the formula weight. Additionally, the final product is not fully dried as it is deleterious for its further redissolution, thus a second error can come from solvent content.

II.3.5.1 Quantification of the surface coating

The organic corona was quantified thanks to thermogravimetry analysis (TGA) of partially dried UCNPs. A limited weight loss (<5%) at the low temperature is attributed to solvent evaporation. The subsequent loss up to 800°C is due to the oleate coating agent.

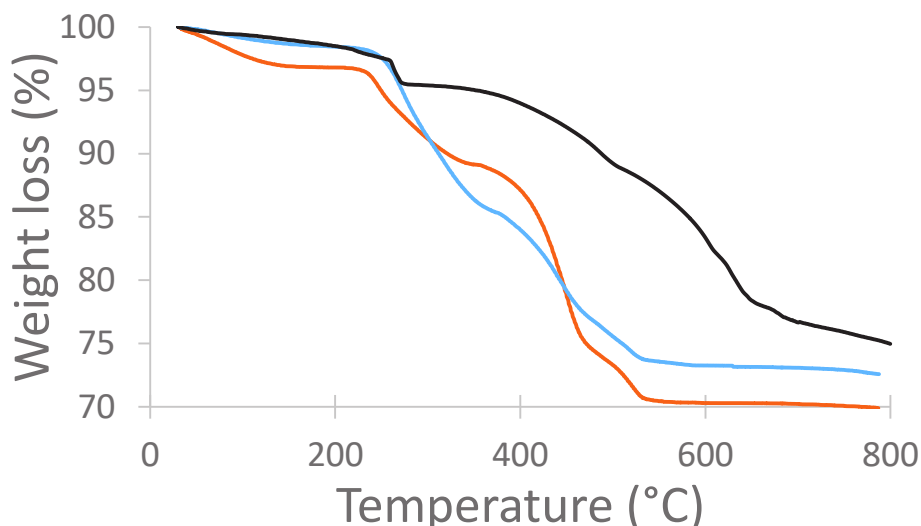


Figure 25. Comparative thermogravimetry analysis of different UCNP sizes: ultrasmall core (3nm, in red), ultrasmall core@shell (6 nm, in blue) and nanohexagons (40 nm, black)

Results are gathered in the following table (table 6). On ultrasmall UCNP, OA(+solvent) content can be approximated as 30% for both ultrasmall core and core@shell samples. On bigger object like nanohexagons (that will be described in the next section), OA coating content is surprisingly quite similar: indeed, the surface-to-volume ratio is moving from 1 to 0.15 between NPs with a diameter of respectively 6 and 40 nm, while OA content is only differing from 3% (Table 6). Therefore, for the whole manuscript, OA content will be approximated as 30% in weight of UCNP, for calculation of any kind of NPs between 2 and 40 nm.

Table 6. Result of thermogravimetry analysis on different kind of UCNP size

Percentage	% weight loss
Ultrasmall core (diameter \approx 3 nm)	30%
Ultrasmall core@shell (diameter \approx 5.5-6 nm)	28%
Nanohexagon (diameter \approx 35-40 nm)	25%

II.3.5.2 Quantification of the inorganic content

With the organic corona determined, our attention was turned on the RE mixture. As the singularity of our work was the choice of the matrix with a high Yb content (57% Yb, 42%Gd, 1%Tm), the remaining question was the validity of this claimed composition. It was investigated on batches of interest and was found to be reproducible. As an example, we will detail only the result for one ultrasmall core and its corresponding core@shell (figure 26).

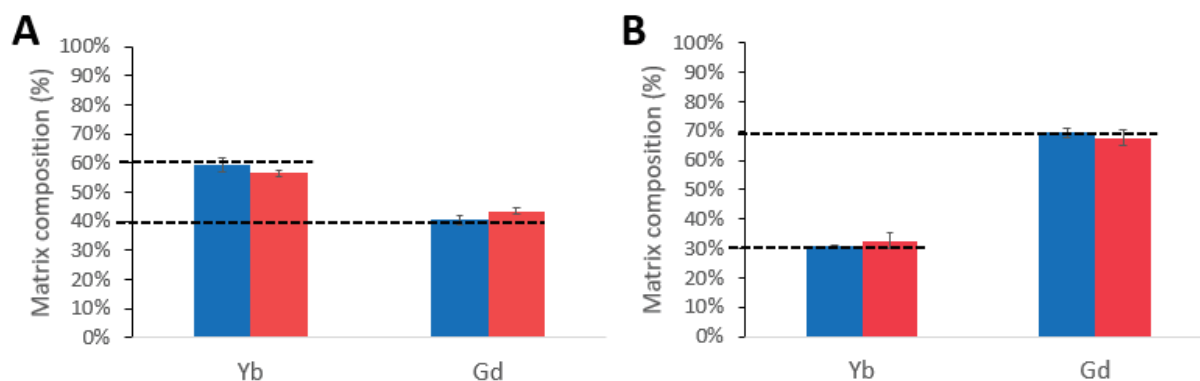


Figure 26. Determination of Gd-Yb content (percentage of moles) by two methods on ultrasmall $\text{Na}(\text{Gd-Yb})\text{F}_4:\text{Tm}$ “with 57% Yb”: ICP-OES measurement on bulk solution (in blue) and EDX measurements on single nanoparticles (in red) are compared to the theoretical composition (dashed line). A) ultrasmall core UCNPs ; B) ultrasmall core@shell UCNPs.

Two methods were used to assess the theoretical composition of UCNPs: one on bulk (ICP) and one on single nanoparticle scale (EDX).

ICP-OES is an analytical measurement on bulk. It is the method of choice for accurate absolute determination of metal concentration by comparing with standard solution. In our hands it was not used as an absolute determination of the moles of Rare-Earth, but only a relative comparison of RE content. As thulium reference was not available on time for analysis it was not quantified. For both techniques Yb and Gd content were compared, by neglecting Tm which represents $\approx 1\%$.

Analysis reported in Figure 26 revealed results in agreement with the theoretical composition calculated. We chose not to use it in routine as an absolute method due to sample preparation. After synthesis, UCNPs are partially dried before dissolution in volatile organic solvent (cyclohexane). This partial drying process was a key to enable dissolution.

However, it induces two errors on the declared concentration:

-error on UCNP mass as they are not fully dried

-error on the volume as cyclohexane is volatile at room temperature. Solutions were prepared in Toulouse, used for photophysical measurements, transferred to vials, shipped to Rennes and stored before preparation for ICP measurement. During each step, solvent evaporation could occur, leading to underestimation of the declared concentration.

ICP is a relative method by comparing peak intensity of well-calibrated standard to solution to be analyzed. But for accurate precise comparison, exact concentration in mg/mL of nanoparticle have to be known in order to have an accurate absolute quantification.

By comparing theoretical composition and ICP we can attest that our declared theoretical composition was accurate for both core and core@shell. However, there remains an uncertainty on the doping homogeneity within a batch. Hence, elemental analysis on single nanoparticle measurement was attempted by EDX. The latter requires high resolution-TEM. As it is a time-consuming experiment, we could not explore a large population of nanoparticles, but only 3 core nanoparticles and 7 core@shell. It confirms the trend, even at the single nanoparticle scale. As SAED revealed also the presence of few α -UCNP that were out of XRD sensitivity, it could also be interesting to compare the compositions between cubic and hexagonal phases.

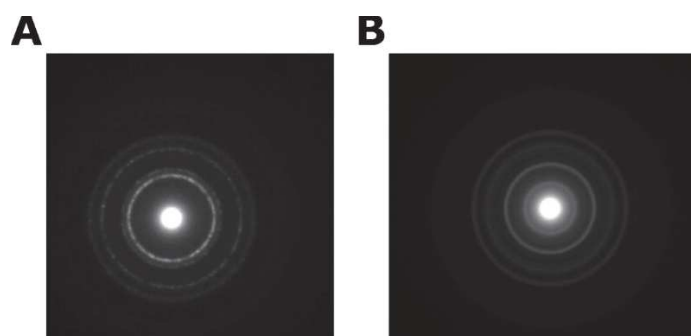


Figure 27. Selective Area Electron Diffraction (SAED) pattern obtained by HR-TEM on cubic (A) and hexagonal (B) phases

In conclusion, both analytical techniques validated the declared theoretical composition.

III Model particles for surface chemistry

As the preparation of small NP is a time-consuming process giving low yields (300-600 mg), we decided to prepare another kind of UCNPs following only 2 criteria:

- fast preparation of bright samples,
- large-scale synthesis.

These “easily prepared” NPs will be used as model particle for further explorations of nanohybrid design and photochemistry issues.

III.1 Fast preparation of UCNP on a small-scale batch

NaYF₄ UCNPs were prepared by transposing Zhang *et al.* protocol,⁶³ (45 mL, 2.3 mmol of Rare-Earth) which is a standard thermal coprecipitation synthesis based on the “premix” way, but with a different sensitizer content: 30% Yb. Compared to this protocol we used 1% Tm instead of 0.5, in order to keep the same Tm content as in the previous objects. This synthesis was also repeated with erbium (30% Yb, 2% Er).

Results

Such protocol led to the reproducible of 30-35 nm hexagons depending on batches: blue emitting and green emitting samples respectively doped by Tm (0,5%) or Er (2%).

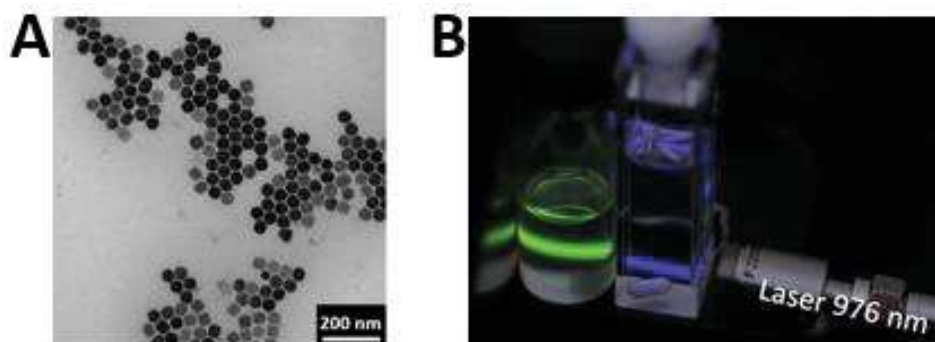


Figure 28. TEM Picture of NaYF₄:Yb(30%),Tm(0,5%) obtained by transmission electron microscopy. B) Luminescence of Tm-doped (blue color) and Er-doped (green color) hexagons under NIR CW laser (38 W cm⁻²), at 5 mg/mL in cyclohexane.

Limitations

Three critical points were revealed by these preliminary results: NaF precipitation, the evaporation a non-negligible amount of volatile compounds, and the control of the temperature of the heating setup.

Methanol is a convenient volatile solvent to solubilize sodium and fluoride precursors. However, along with the precursors addition the reaction mixture is almost doubled. So, it is not easy to define the chemical transformation during mixing as the concentrations are highly modified. Then, a volume of methanol has to be evaporated. Contrary to standard organic chemistry, such step is achieved by argon flush without using a proper distillation equipment, following the usual UCNP protocol⁸.

As NaYF₄ synthesis used to be reported with a plateau set a different temperature between 300-320°C, we decided to fix 310°C as the setpoint temperature, but starting the timer when 300°C is reached.

As a conclusion of small-scale synthesis, 600 mg of bright homogeneous 35 nm UCNP can be produced easily in less than ten hours.

III.2 Size reduction on UCNP hexagons scale-up issues

As stressed in the literature¹⁵ a great variability in the nanoparticles' properties (composition, size, photophysics...) can be experienced from batch to batch. Furthermore, a typical run (1 mmol of Rare Earth scale) yields around 600 mg amount of material quickly employed in further transformations. Therefore, a scale-up by a factor of 5 of the previous protocol was envisioned: from 21 mL (1 mmol of Rare-Earth) in 100 ml flask to 210 mL (10 mmol) in 500 mL round bottom-flask.

Three critical points were identified for scale-up purpose: the heating rate of the heating mantle used, the addition rate of precursors, and the evaporation rate of volatile compounds.

Scale up impact on addition rate

On small scale, NaOH and NH₄F are introduced with a large amount of methanol. On a larger scale (x5) it should be even worse. Knowing their low solubility in methanol (table 7), we are already close to the saturation in stock solutions.

Table 7. Solubilities in methanol

	solubility in methanol (g/mL)	Experimental stock solution concentration (g/mL)
NH ₄ F	0.036 (at 25°C) ⁶⁴	0.024
NaOH	0.391 (at 28°C) ⁶⁵	0.017

As we previously stressed out the beneficial use of double syringe pumps to prevent NaF formation we decided to implement it for this NaYF₄. Moreover, it is really convenient to automatize the addition of large amount of solution (2x 100 mL), the only limit being the syringe capacity. We expect to obtain smaller size than the 35 nm UCNPs previously prepared. Indeed, on a small scale, the modification of the protocol from *premix mixing* to *in situ mixing* should not have a big impact on the addition time (from 10 minutes to 45 minutes with syringe pumps). But with the scale-up, *in situ mixing* leads to a longer addition time of around 4h30. Stock solution storage become also an important parameter as the precursors' addition last now several hours. Due to the reactivity of fluoride on glass, usual glassware for NH₄F storage or addition had to be forsaken: vial and syringes made of plastic were used.

Scale up impact on volatile compounds evaporation

Solvents (water, methanol) evaporation is usually achieved, in reported UCNP's synthesis, by argon flush at high temperature (100°C). For water (used to introduce Rare-Earth precursors) it is not an issue as it represents only 0.5% of the reaction mixture. However, methanol represents half of the volume when introduced. Such huge volume brings another issue: uncertainty on the declared concentration and evaporation.

The uncertainty on concentration prevents the understanding in detail of the “primo-precipitation” when fluoride and sodium meet lanthanides. Indeed, along with the slow sodium and fluoride methanolic solutions addition (4 hours), the concentration is gradually lowered in the flask (to the half part). This brings questions in the comparison of the first droplets added to the last ones introduced: we cannot declare a real working concentration. An alternative should be the use of sodium oleate, limiting the use of methanol only for fluoride precursors. Nevertheless, as the reaction is under kinetic control, such variation may impact the nucleation and requires a new complete study.

Methanol evaporation is a major issue. Usual UCNP's protocol involves inert gas (argon, nitrogen) flush to remove it. As it was not critical on small scale (20-40 mL) we followed the same way. It is now a long process for such huge volume (200 mL of MeOH), with a non-negligible gas cost. A more adapted alternative would be the use of rotary vacuum evaporator, or a proper distillation setup.

Scale up impact on heating rate

The impact of scale-up on the heating rates during high temperature annealing was explored (figure 29). Setpoint temperature was 310°C but reaction time was 90 minutes from the moment 300°C was reached.

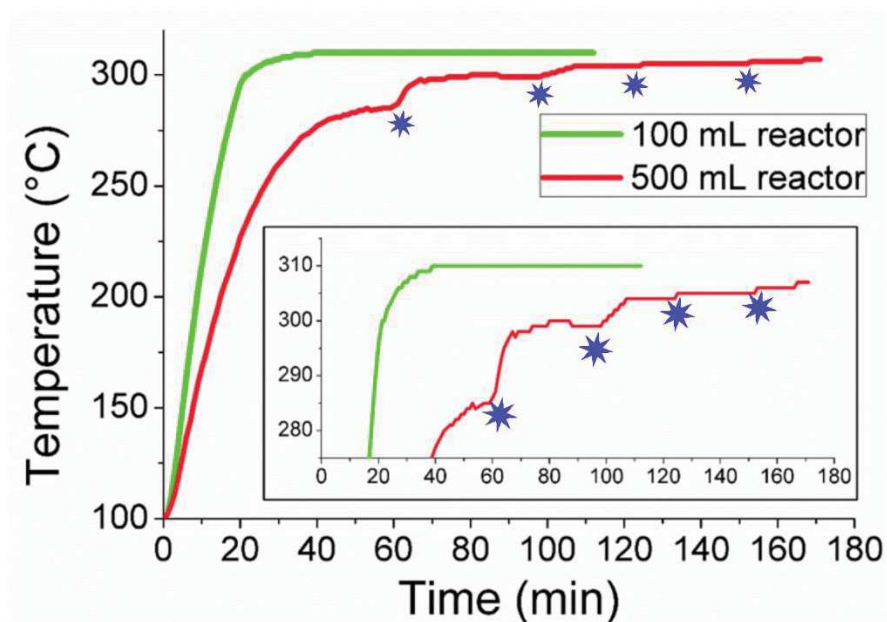


Figure 29. Heating rates comparison during the high temperature annealing step. For the 500mL reactor setpoint temperature was gradually increased after 40 min from 310 to 350°C in order to try to accelerate the heating, resulting in the successive slope failures. Blue stars indicate successive rise of temperature (max setpoint temperature was 350°C)

On the small reactor, 3 main steps can be identified: fast heating rate at early stage, then heating rate downturn close to the setpoint temperature, finally plateau at the setpoint temperature.

By scaling up the synthesis to the 500 mL reactor, a slower heating rate can be clearly observed. Moreover the 310°C setpoint temperature was never reach, but instead the temperature stayed

between 300 and 310°C, even if the setpoint temperature was fixed to higher value (350°C). This observation shows the limitation of the scale-up with our heating apparatus.

Results

Scale-ups have been performed for both kind of emitters: Er^{3+} or Tm^{3+} . Rare-Earth composition was 30% Yb for both kinds of samples, while the emitter content was 2% or 1% respectively for Er or Tm (figure 30).

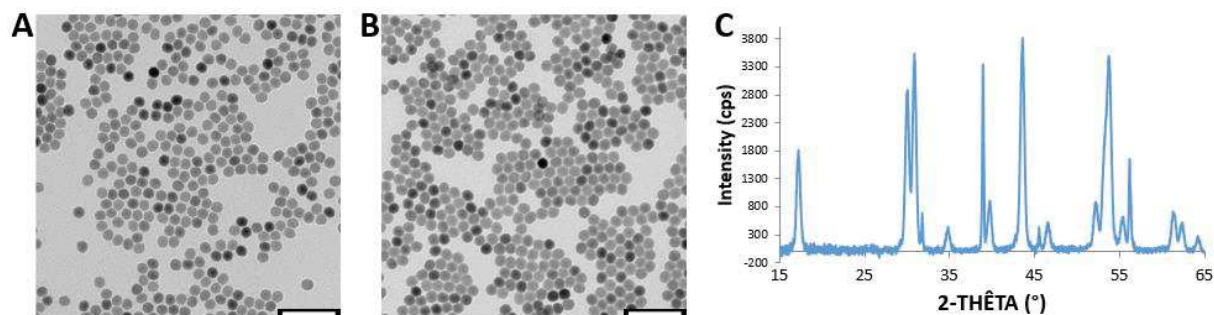


Figure 30. Characterization of nanohexagons prepared on large scale. A and B are respectively TEM pictures obtained for Tm-doped or Er-doped UCNP, (scale bar is 100 nm). C is a typical XRD obtained for both of them.

Results show a comparative size of around 20 nm (figure 30 & table 8), that is significantly smaller than the former preliminary protocol. All the batches were purely β -phase, as attested by XRD diffractograms.

Table 8. Comparison of hexagons size distributions fitted by a Gaussian model.

	Average diameter	FWHM
Er-Hexagon	37.0	4.0
Tm-Hexagon	35.9	3.7
Tm-doped nanohexagons	20.0	2.6
Er nanohexagons	21.8	1.3

Conclusion on the large-scale preparation of nanohexagons

As expected, the convenient automation of the addition of the sodium and fluoride precursors thanks to syringe pumps led to a NP downsizing. This spectacular size reduction was around 40%. We hypothesized that scale-up had no impact on it.

Despite the apparent brightness of the visible emission, the scale-up success (from 600 mg to 3 g of UCNP produced), such nanoparticles too large to fulfill our goal to have QD-competitive nanoparticle in term of size. However, they are perfectly adapted for preliminary photochemistry and nanohybrid formation attempts, as these batches are easily and fastly prepared, especially at the 3g scale.

Contrary to usual organic reactions, no chemical yield was calculated, as the weight of the produced UCNP could not be declared precisely. Indeed, a full drying process to get the precise mass of dry UCNPs is deleterious for further dissolution and storage, as dry UCNP could not be easily dissolved.

IV Conclusion on synthesis of ultrasmall UCNP

In the present chapter we highlighted the importance of the composition, the mixing strategy for the introduction of precursors and the heating apparatus in order to reach ultrasmall size of appropriate hexagonal phase. Concerning this new topic implemented in the lab, from scratch we finally acquired good understanding of a complex polymorphic mixture. Size reduction strategy was based on the coupled optimization of primo-precipitation and high temperature heating. The present work details the first trifluoroacetate-free microwave synthesis of β -phase sub-5nm core UCNPs in commonly used solvent mixture of oleic acid and octadecene. The first description of cycling temperature approach assisted by microwave reactor, and the empirical validation of Arrhenius law on UCNP synthesis open new perspectives for the synthesis of other nanomaterials. Additionally, our microwave-assisted cycling temperature is the first protocol allowing such size stability despite doping content variation (if Yb content is lowered than 57%).

However some other critical parameters remain to be explored:

- the use of water: RE precursors being chlorides, they are introduced in water. A small amount of water combined to a slow heating rate is required to prevent bumping issue from the alkane-like mixture during the $\text{RE}(\text{OA})_3$ ligand exchange. Moreover, it can eventually be a source of oxygen defect in the crystal, due to oxo-bridged lanthanides for example. An alternative should be the use of acetate precursors which are directly soluble without need of water. Besides, this water has then to be removed, this is done at 100°C under argon flush. This

“distillation” results in a drop of the alkane-like mixture amount, due to azeotrope between water and oleic acid. As a result, the solvent composition differs from the initial one.

- the use of methanol: A large amount of methanol is used for sodium and fluoride introduction. This large quantity of volatile solvent has then to be evaporated. Thus, at first the physicochemical properties change, considering the volume added, as a OA:ODE/MeOH 1/1 composition is reached after complete addition, and we have no idea how this impacts the nucleation. From a technical point of view, this methanol is removed by argon flush, which is particularly long especially in the scale-up approach and quite expensive regarding to the volume of inert gas used per synthesis. An alternative should be the use of sodium oleate as the sodium precursor, that will allow to half the MeOH volume, and/or the use of rotary evaporator or distillation apparatus for the volatile compound removal without loss of OA:ODE.

However, as UCNP formation is under kinetic control, each change in the protocol will impact the size. Thus, such alternatives described above will generate a complete re-investigation of the synthesis.

Nevertheless scale-up applications are still limited at the moment. Despite a first attempt on conventional heating to form nanoprisms, such approach is highly challenging for ultrasmall UCNP: our microwave reactor has a maximum capacity of 20 mL. Scale-up with our monomode apparatus can be envisioned only by parallel synthesis from a same starting batch. But such process opens questions about the global reaction time, and mainly the aging of the initial batch. The main limitation of time is the tedious preparation of reactor tubes with a time-consuming degassing step (around 1h per tube).

Large-scale application would require either to go for continuous flow monomode reactor, or high-scale multimode one.

The latter system is already existing at the litre scale. However, reactors for huge batches are not a solution, as a key factor for the cycling temperature was the fast cooling down. Turning to huge containers open the problem of thermal inertia inside the working reactor. As a result, the only viable alternative for large-scale syntheses should be based on a microfluidic continuous flow reactor. Such setup should be designed to present a number of loops inside the monomode cavity coinciding with the number of desired pulses at high temperature.

A large variety of nanoparticles was synthesized during this PhD project: 2 size ranges of hexagon-shaped UCNP, and various 2.5 to 15 nm-sized spheres. Once this UCNP library synthesized and chemically fully characterized, investigations on the photophysical properties

have to be performed, especially on the ultrasmall ones. Such details will be treated in the next chapter.

Table 9. Summary of UCNP library synthesis. Syntheses performed with heating mantle are labelled in blue, while pink ones were prepared with MW oven.

Batch name	Composition	Size (nm)	Amount (g)	Preparation time
	NaYF ₄ :Tm	35	0.6	1 day
	NaYF ₄ :Er	35	0.6	1 day
	NaYF ₄ :Tm	20	3	1.5 days
	NaYF ₄ :Er	20	3	1.5 days
	Na(Gd _{42%} -Yb _{57%})F ₄ :Tm	10	0.3	1 day
	Na(Gd _{42%} -Yb _{57%})F ₄ :Tm@NaYF ₄	15	0.6	2 days
	Na(Gd _{79%} -Yb _{20%})F ₄ :Tm	7.5	0.3	1 day
	Na(Gd _{42%} -Yb _{57%})F ₄ :Tm	15	0.3	1 day
	Na(Gd _{42%} -Yb _{57%})F ₄ :Tm	4.5	0.7	2 days
	Na(Gd _{79%} -Yb _{20%})F ₄ :Tm	2.5-3.5	0.7	2 days
	Na(Gd _{79%} -Yb _{20%})F ₄ :Tm@NaGdF ₄	5.5	1.4	1 week
	Na(Gd _{42%} -Yb _{57%})F ₄ :Tm	2.5-3.5	0.7	2 days
	Na(Gd _{42%} -Yb _{57%})F ₄ :Tm@NaGdF ₄	5.5	1.4	1 week
	Na(Gd _{42%} -Yb _{57%})F ₄ :Tm	3	3	1.5 week

V Experimental section

V.1 Materials

Rare Earth (RE) chloride hydrates, ammonium fluoride, oleic acid (OA) and 1-octadecene (ODE) were purchased from Alfa Aesar and used as received. All other organic solvents were of spectroscopic grade and used as received. Water used was deionized water ($\rho=18 \text{ M}\Omega \text{ cm}^{-1}$) obtained from Aquadem apparatus.

Powder XRD measurements of the dried samples were performed on a Bruker D8 Advance diffractometer working with monochromatized Cu K α 1 radiation ($\lambda = 1.5406 \text{ \AA}$). Transmission Electron Microscopy (TEM) was performed on a Hitachi HT-7700. TEM images were analyzed with ImageJ by using the free PSA (Particule Size Analyzer, version r12) macro. Size distributions were then fitted by Gauss function with OriginLab, the size in the following manuscript being the average size and corresponding standard deviation (xx nm \pm yy nm) of the Gaussian fit. The UCNP relative composition in the elements Gd, Yb and Tm was determined using Inductively Coupled Plasma Optical Emission Spectrometry ICP-OES (icap 7000 THERMO SCIENTIFIC).

Heating setups

Conventional heating steps were performed in 100 mL three-neck round-bottom flasks heated by high power heating mantle from Horst Company, placing the temperature probe directly in contact with the reaction mixture. Microwave heating was performed in monomode *Monowave 300* oven from Anton-Paar Company.

V.2 Synthesis

V.2.1 Synthesis of cores UCNPs

General procedure

Rare earth oleates^{8,19}

A solution of $\text{RECl}_3 \cdot x\text{H}_2\text{O}$ dissolved in 2 mL water was added to a mixture of OA:ODE and water was carefully distilled off. The cloudy mixture was then brought to 160°C under gentle argon flush until no solid material remained. During this final stage, it was possible to identify the evolution of HCl gas (pH paper and silver nitrate test). The pale yellow clear solution was then cooled down under argon and used without further analysis. The volumes of OA and ODE used were 12 mL and 18 mL for 1 mmol of RE⁸ for the standard “premix” protocol, and, 12 mL and 30 mL for 2 mmol of RE for the “in situ mixing”, respectively.¹⁹

Standard “premix” protocol.

According to Wang *et al.*,⁸ to the lanthanide oleate solution above prepared was added dropwise over 30 minutes a freshly prepared mixture of NaOH and NH_4F in MeOH, in order to reach a final 1:2.5:4 RE:Na:F ratio. Once the addition completed, the methanol was distilled off, first at 50°C for 45 minutes then at 100°C for degassing. Temperature was then risen up to 280°C (20°C min⁻¹) then maintained at this value for 90 minutes. Particles were isolated by precipitation in EtOH of combined crude mixtures, followed by centrifugation at 9000 rpm during 10 minutes. The pellet being re-dispersed in cyclohexane, the precipitation procedure was repeated twice. Particles were then redispersed in cyclohexane.

“In situ” mixing

According to Zhai *et al.*,¹⁹ two methanol solutions of sodium hydroxide (0.326 mM) and ammonium fluoride (0.5 mM) were simultaneously added with the help of two syringe pumps to a vigorously stirred solution of above-prepared metal oleate (47.6 μM) over 20 minutes (0.2-0.4 mL min⁻¹) in order to reach a final 1:2.5:4 RE:Na:F ratio. Methanol was gently evaporated before carefully degassing at 100°C the resulting mixture.

Reaction mixture was either heated up to 280°C for 90 minutes as in the standard “premix” protocol, or transferred by batches of 4 mL into argon-flushed MW reactors and then heated up in the MW oven (see main text). Particles were isolated as above.

Comparison of cores synthesis on 100 mL flask scale**Table 10.** Comparison of core synthesis

	Nanospheres				Nanohexagons
	10-15 nm	5-10 nm	4.6 nm	2-3.5 nm	20 nm
Matrix	Yb-Gd	Yb-Gd	Yb-Gd	Yb-Gd	Y
n(RE) mmol	2.85	2.00	2.00	2.00	2.33
%Yb	57	57	57	57	30
%Tm	1	1	1	1	1
n(Na)/n(RE)	2.85	2.5	2.5	2.5	4
n(F)/n(RE)	4	4	4	4	5.5
V(OA) mL	12	12	12	12	7
V(ODE) mL	18	30	30	30	38
{Na+F} mixing	Premix	<i>In situ</i>	<i>In situ</i>	<i>In situ</i>	Premix
Heating device	Heating mantle	Heating mantle	MW plateau	MW cycling temperatures	Heating mantle

Scale up to 500mL round-bottom flask scale

Similar protocol than for the 100 mL was followed. Scale-up of nanohexagons synthesis was achieved by multiplying all the volumes and number of moles by 5.

V.2.2 Synthesis of core@shell

Shell synthesis on small nanosphere

Similarly to the “Standard premix protocol” above-mentioned on core, gadolinium oleate was prepared. After cooling to room temperature, core NP dissolved in cyclohexane solution were introduced, followed by the *premix* addition of NaOH and NH₄F. Subsequent steps are identical than for the core, cyclohexane being removed with MeOH. Noticeably, the last high temperature heating step lasted for 1h for shell, instead of 1h30 for core.

Shell synthesis on ultrasmall UCNP¹⁹

On ultrasmall UCNP the process is the same, except that NaOH and NH₄F addition are replaced by the simple addition of CF₃COONa in MeOH.

Comparison of both shell growth protocols

Table 11 gathers the comparison of the protocols.

Table 11. Comparison of shell synthesis

	Small nanospheres	Ultrasmall NPs
Shell Matrix	Y	Gd
n(RE)shell/n(RE)core	1	1
Na precursors	NaOH	CF ₃ COONa
F precursor	NH ₄ F	CF ₃ COONa
n(Na)/n(RE)	2.5	2.5
n(F)/n(RE)	3.3	≥ 2.5
V(OA) mL	9	20
V(ODE) mL	21	20
{Na+F} mixing	Premix	<i>In situ</i>
Heating device	Heating mantle	MW plateau

V.2.3 Microwave heatings

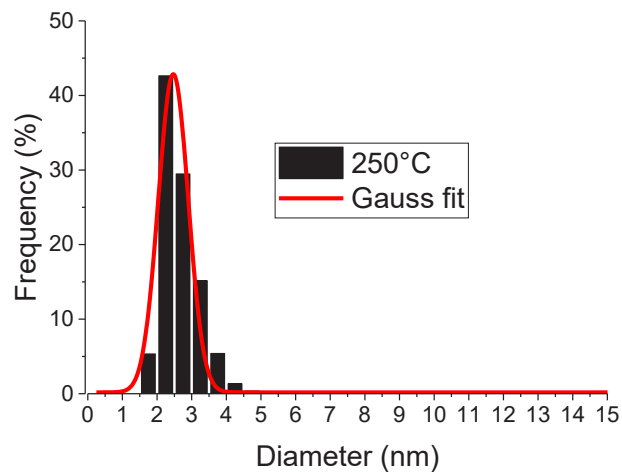
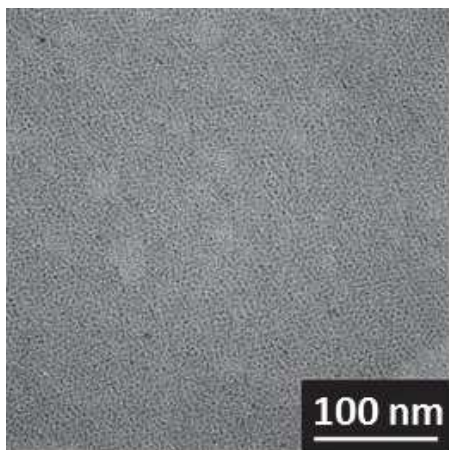
For core synthesis, 20 mL of degassed solution was transferred to G30 reactor tube from Anton Paar Company. As a result batch of around 40 mL required 2 parallel heating. G30 reactor was degassed prior to introduction of the solution: It was placed under vacuum during at least 1h by a small needle connected to a vacuum line. Then several argon/vacuum cycles were applied to prepare argon atmosphere. Degassed solution were transferred from the three-neck flask to the MW reactor tube with a glass syringe, then followed by new degassing in the tube. Reactor were there placed in the microwave oven.

For core@shell synthesis, following the same process solutions of only 15 mL were submitted to the parallel heating. Therefore, one batch required 3 parallel heating steps. 15mL was found empirically as the maximum capacity. With bigger volume (which is limited to 20mL) some leaking of the solution was observed after heating, probably due to higher gas release with bigger volume.

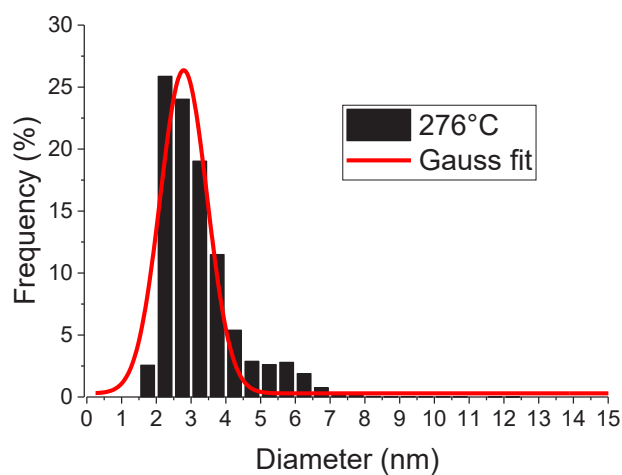
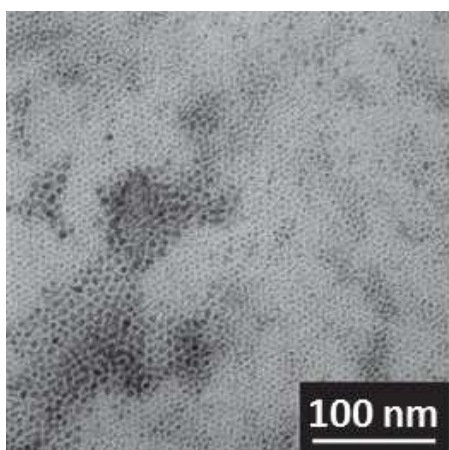
V.3 Characterization

V.3.1 Monitoring of the core synthesis, adapted from F. Wang *et al.*⁸: TEM images and image analysis (Image J treatment)

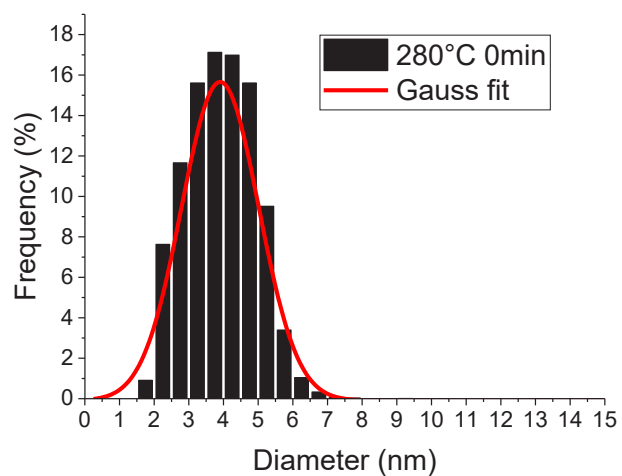
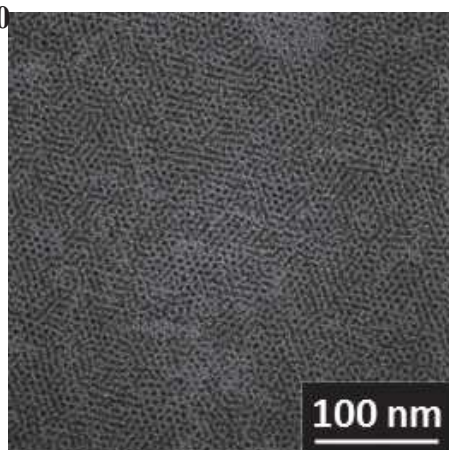
250°C



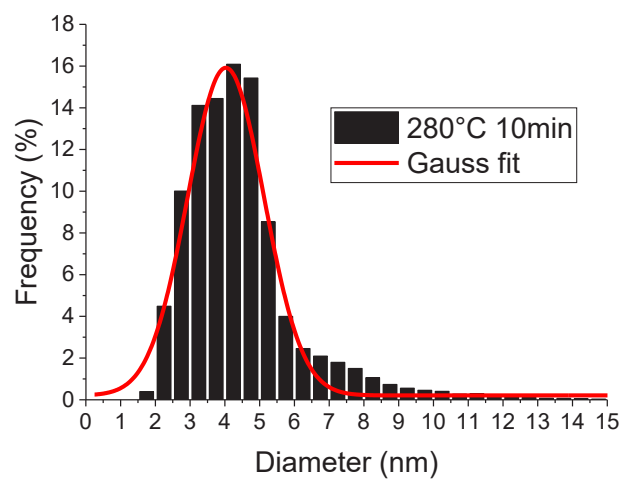
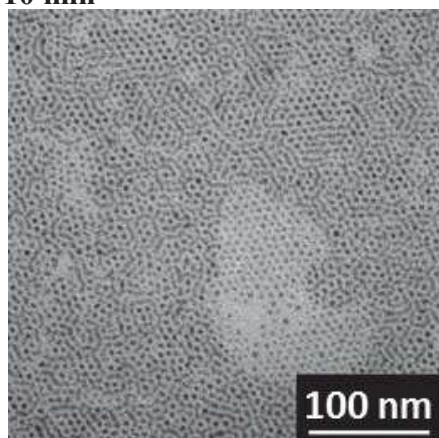
276°C



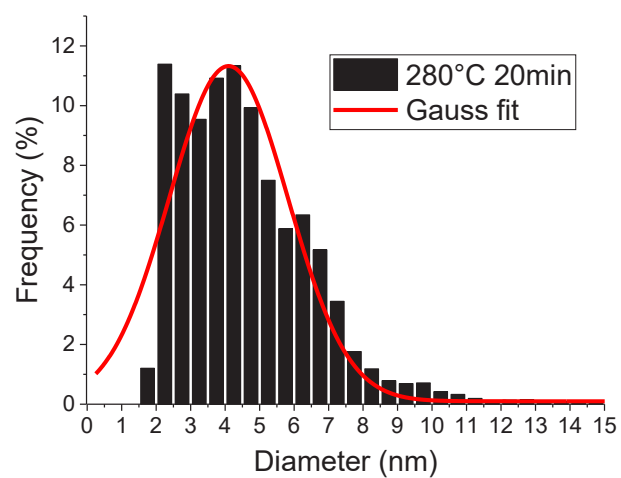
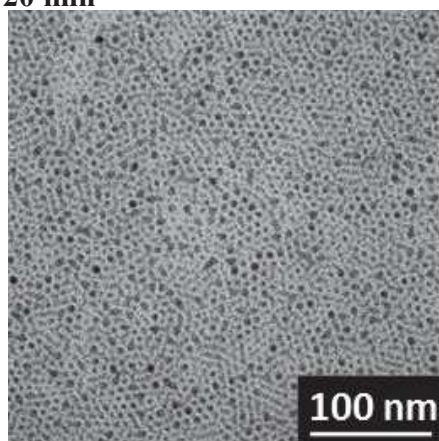
280°C t=0



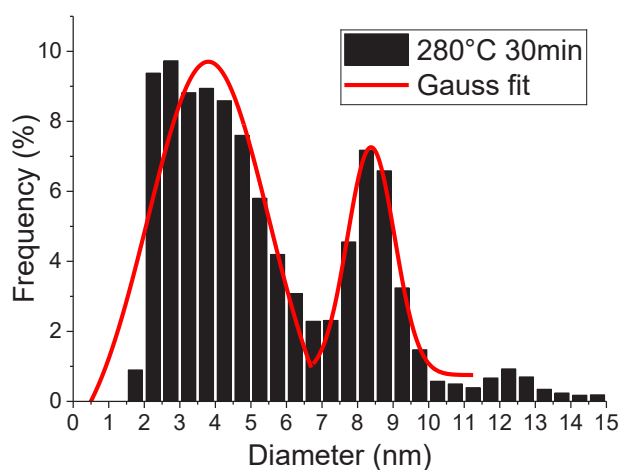
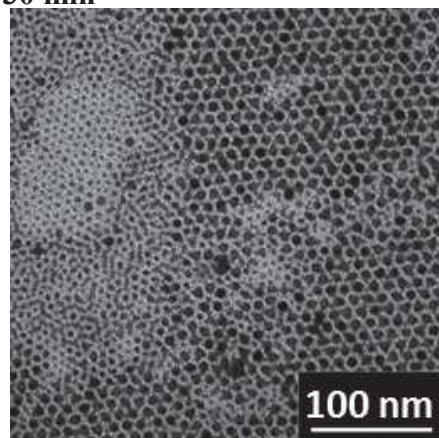
280°C t=10 min



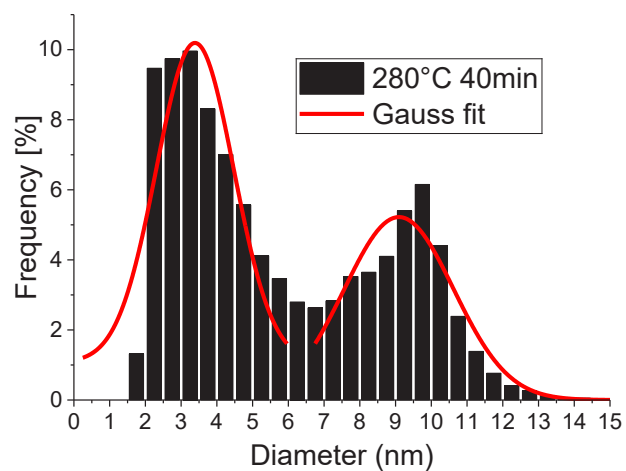
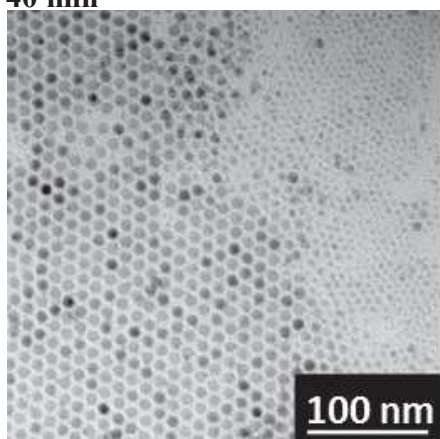
280°C t=20 min



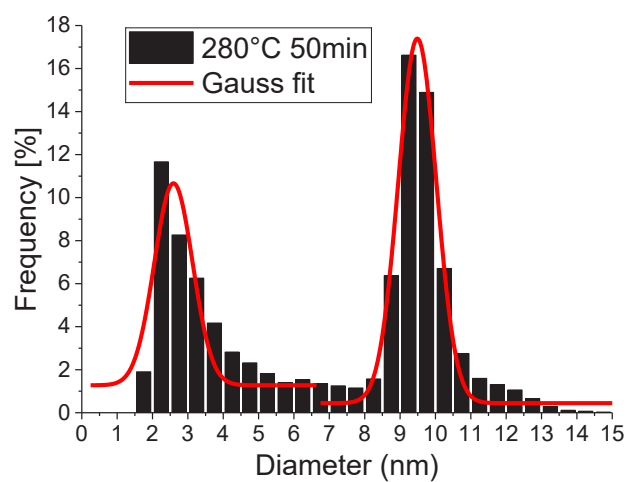
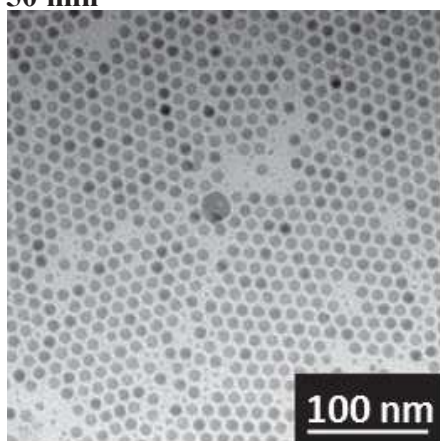
280°C t=30 min



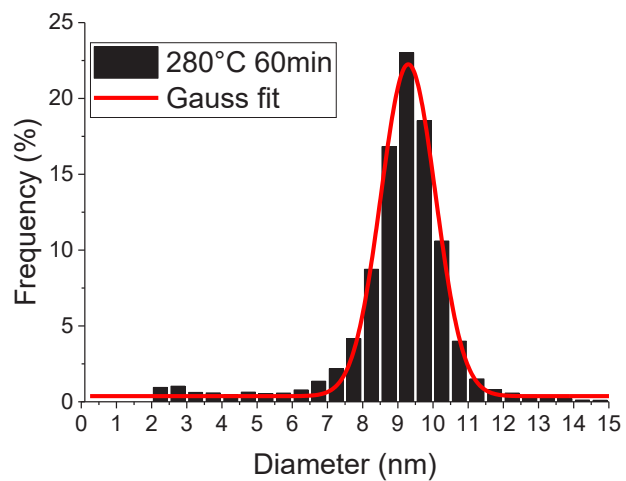
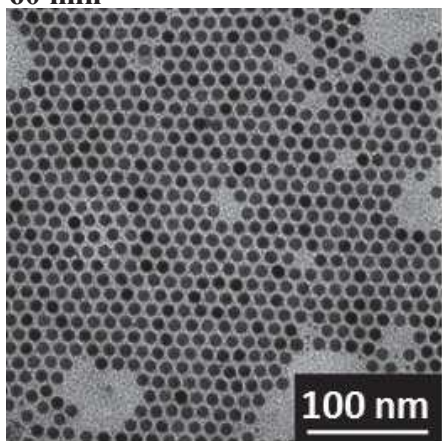
280°C t=40 min



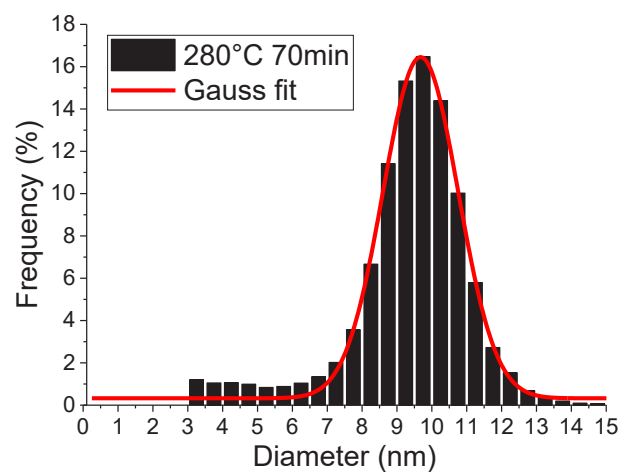
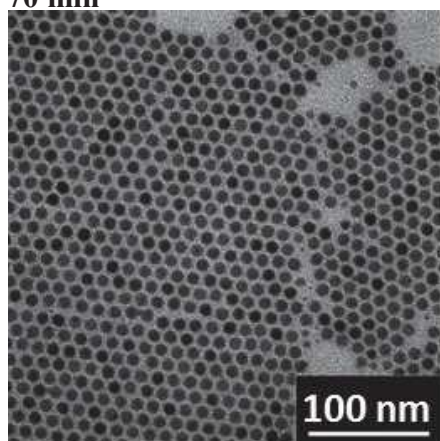
280°C t=50 min



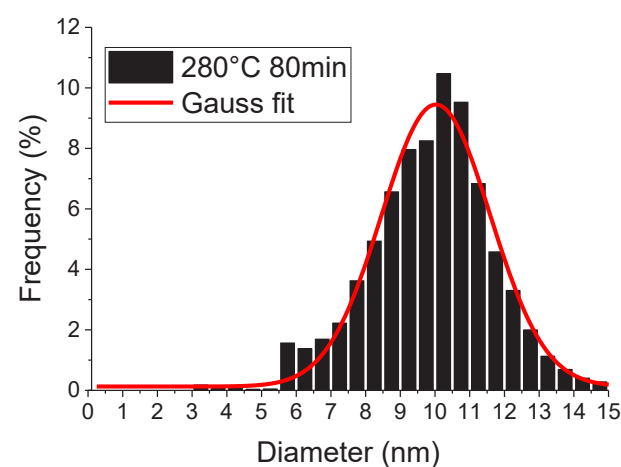
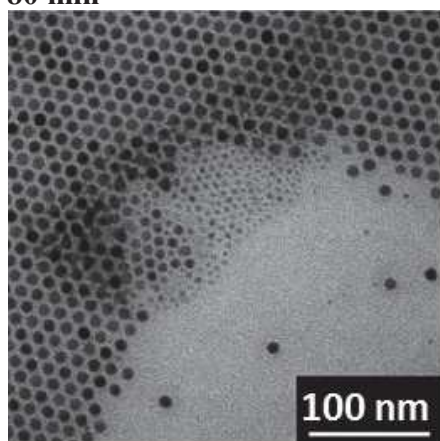
280°C t=60 min



280°C t=70 min



280°C t=80 min



280°C t=90 min

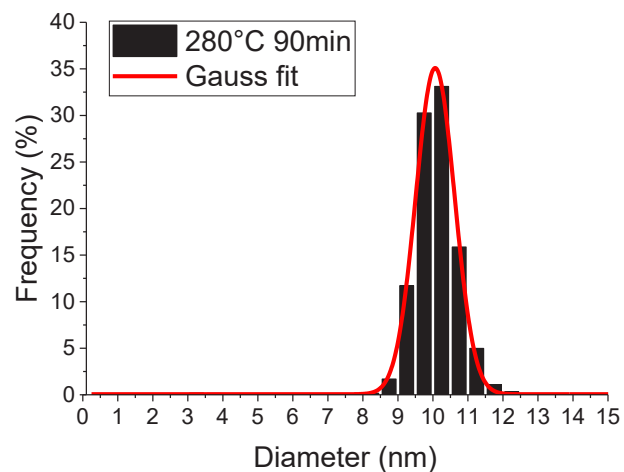
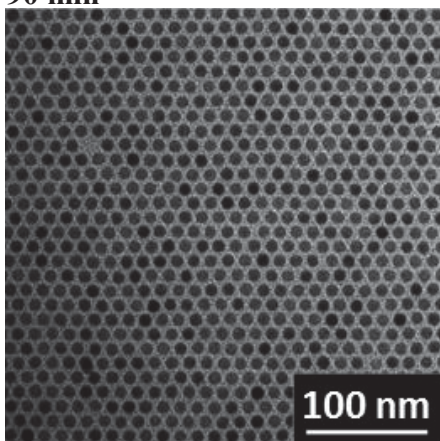


Figure 31. TEM monitoring of “premix” and conventional heating protocol

V.3.2 Luminescence monitoring of the shell growth

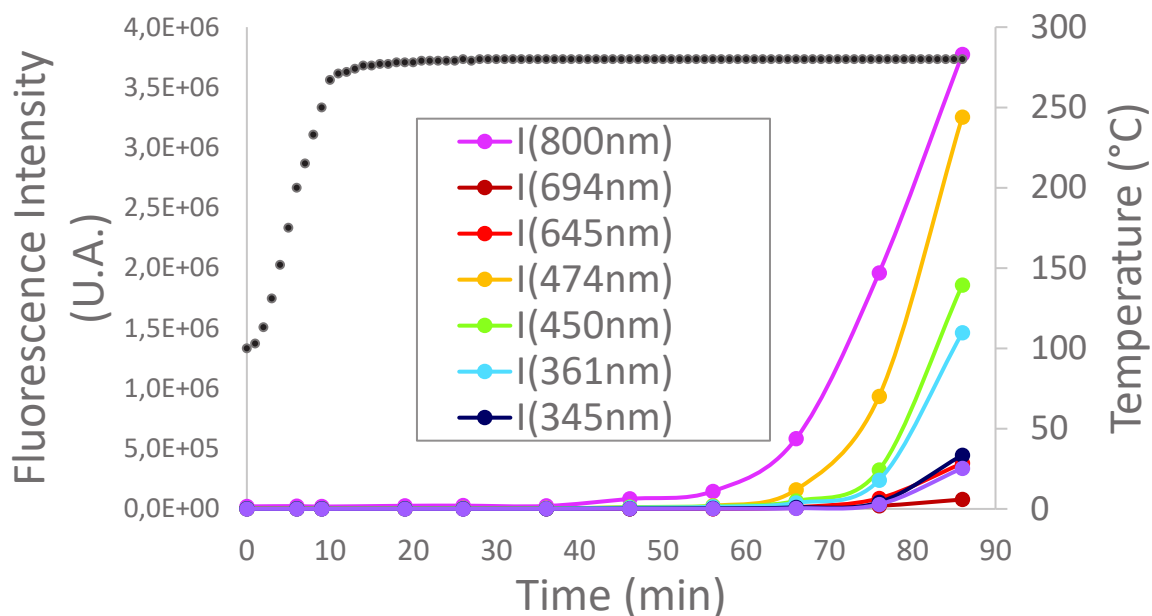


Figure 32. Monitoring of the shell growth for a 60 min plateau at 280°C (280°C (t=0) is reached at around 26 min.)

V.3.3 Luminescence monitoring of the shell growth with doubling of the reaction time.

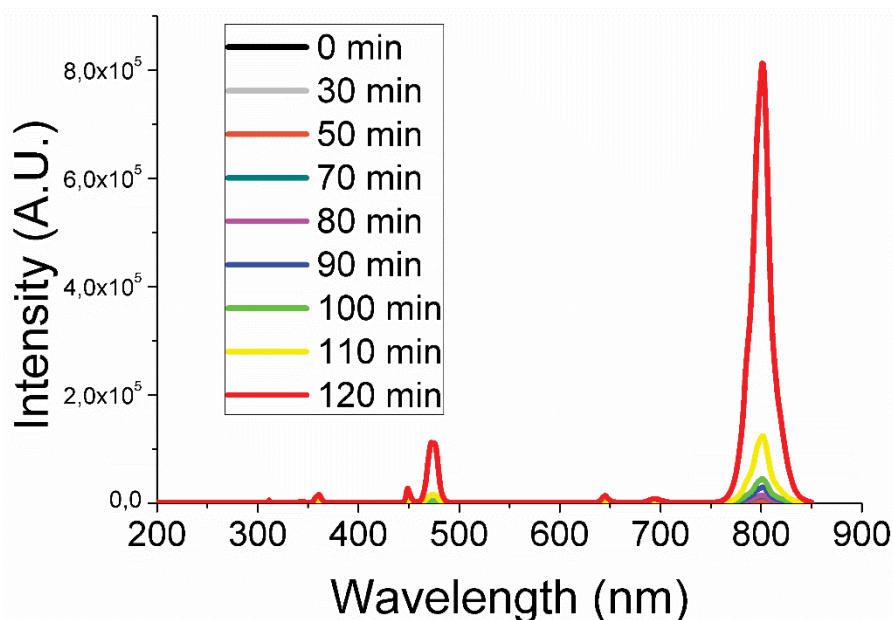


Figure 33. Monitoring of the shell growth for a 120 min plateau at 280°C. Only points of the plateau were monitored, compared to figure 32.

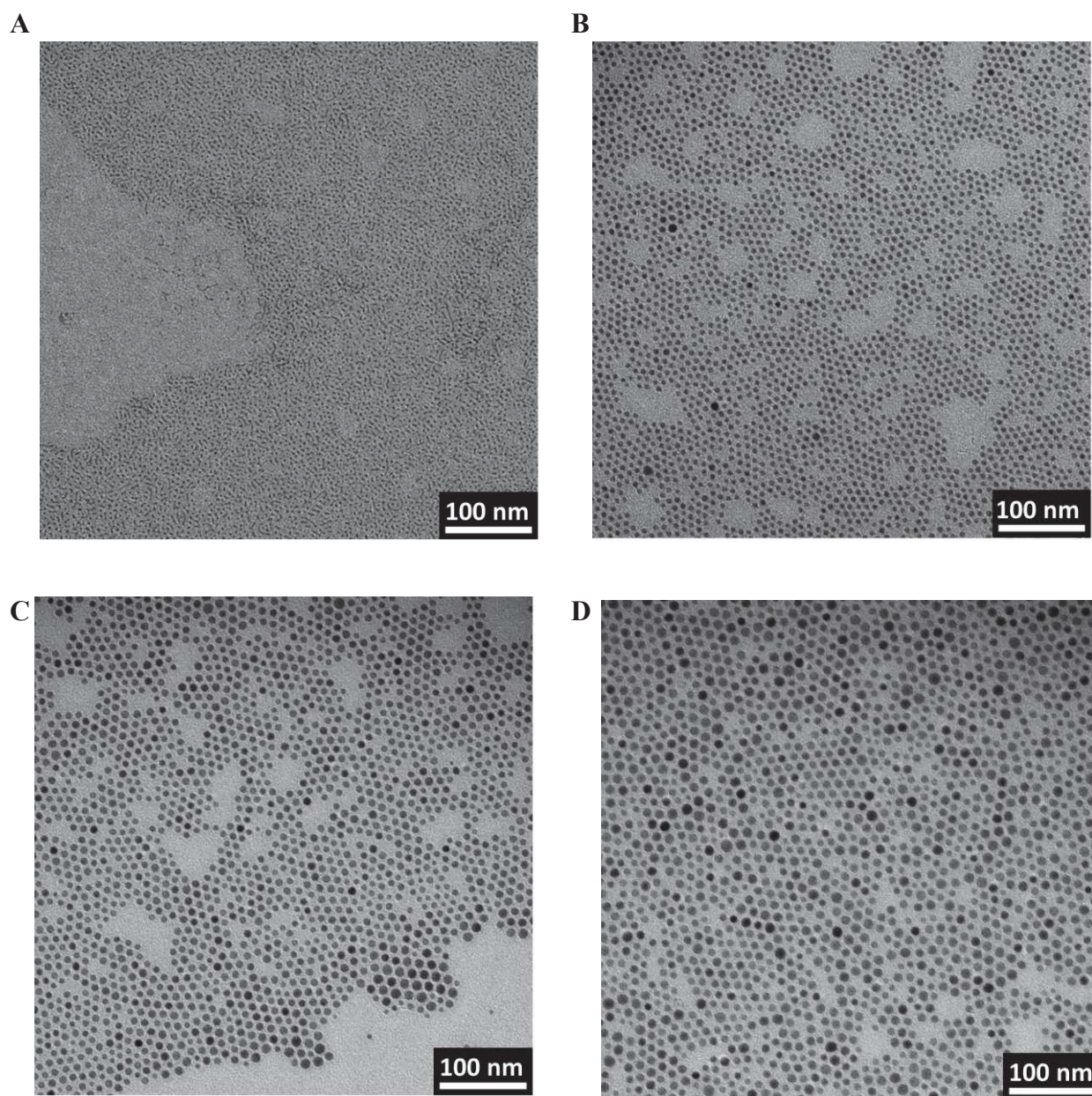
V.3.4 Combination of “in situ” introduction and conventional heating,¹⁹ trial#1

Figure 34. TEM pictures from sampling reaction mixture during conventional heating with “*in situ*” introduction trial#1: A) No heating. B) heating plateau 280°C 30 min. C) heating plateau 280°C 60 min. D) heating plateau 280°C 90 min.

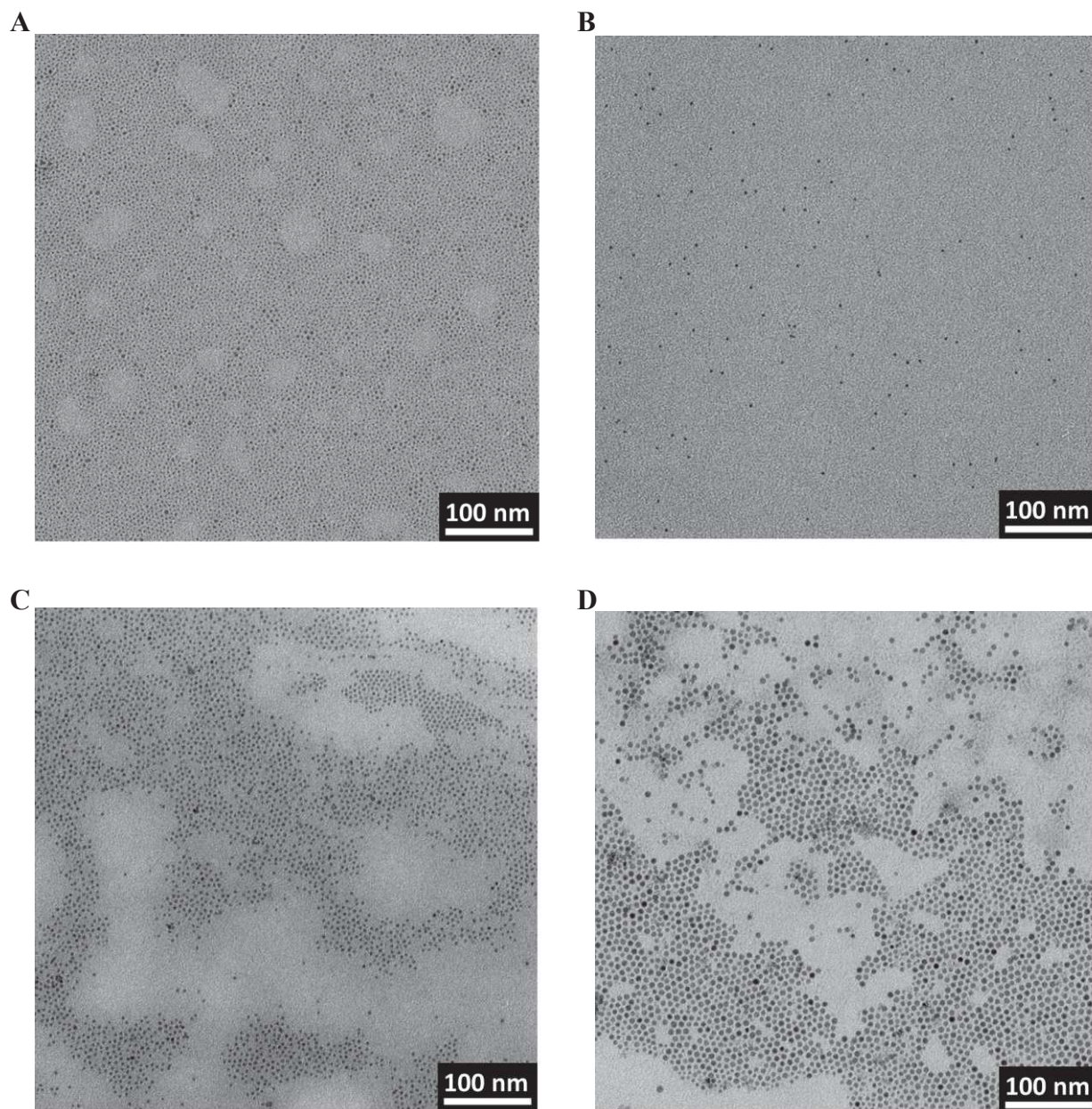
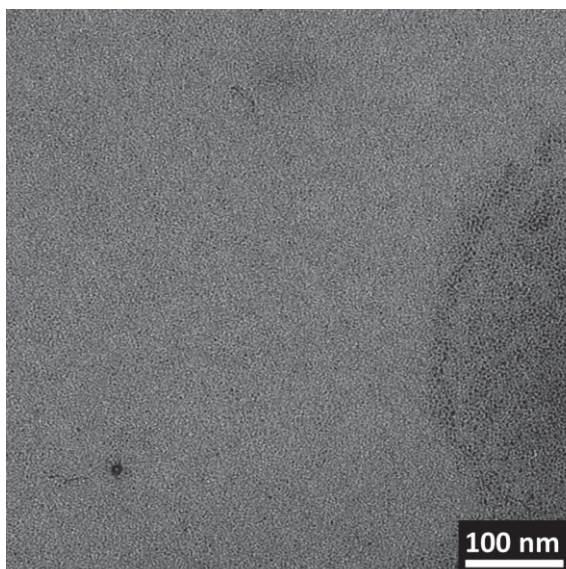
V.3.5 Kinetic analysis, combination of “*in situ*” introduction and conventional heating,¹⁹ trial#2

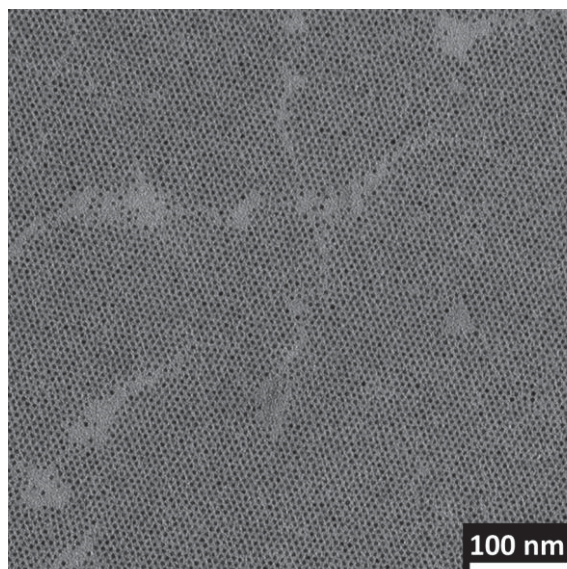
Figure 35. TEM pictures from sampling reaction mixture during conventional heating with “*in situ*” introduction trial#2: A) No heating. B) heating plateau 280°C 15 min. C) heating plateau 280°C 30 min. D) heating plateau 280°C 90 min.

V.3.6 Kinetic analysis, "in situ" mixing and 30 min microwave oven combination, variable temperature

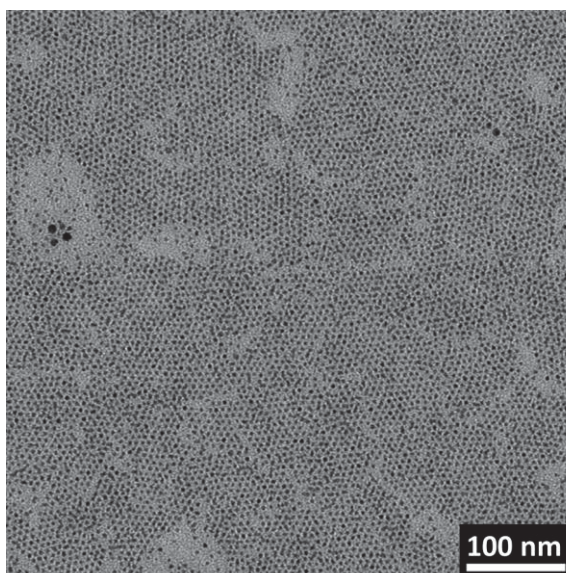
No heating



300°C 30min



290°C 30min



280°C 30min

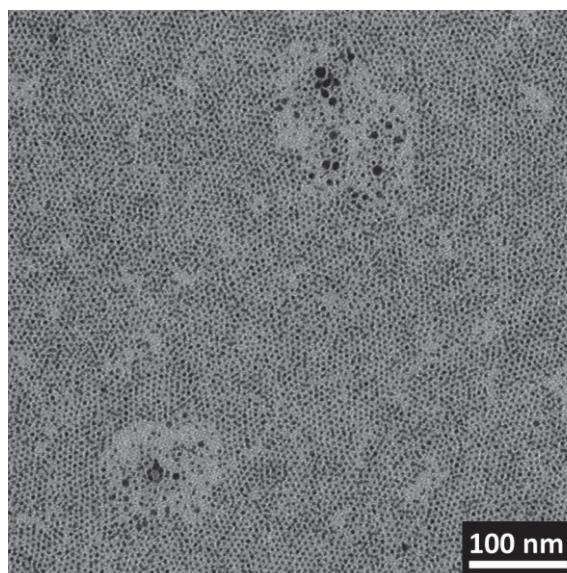
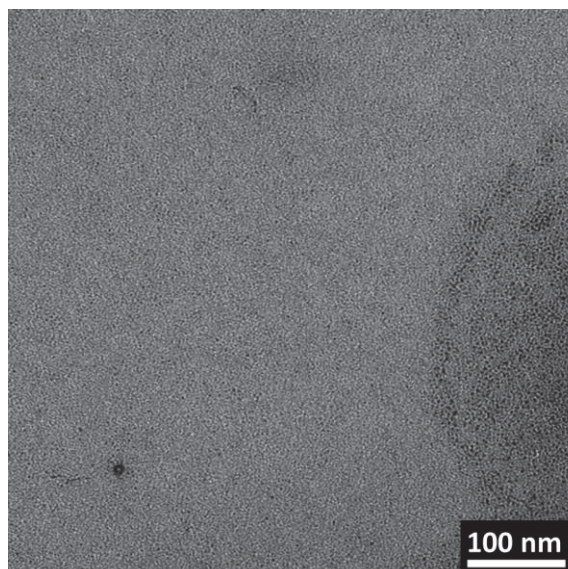


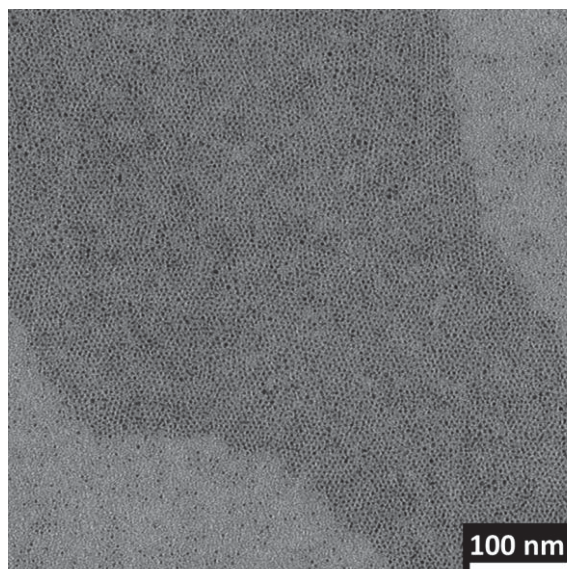
Figure 36. TEM pictures obtained at different temperature plateau of fixed duration (30 min) by using microwave heating and "in situ" mixing approach.

V.3.7 Kinetic analysis, "in situ" mixing and 300°C microwave oven combination, variable reaction time

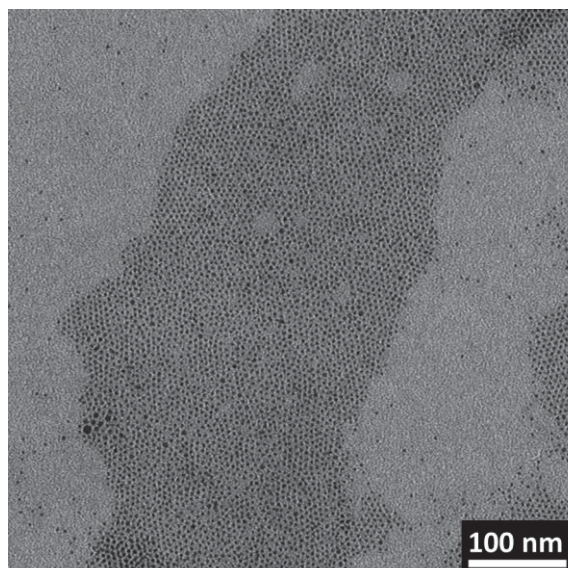
No heating



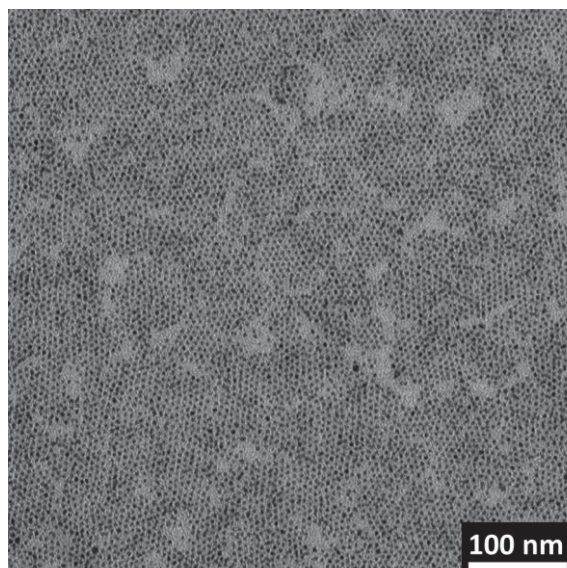
300°C 1min



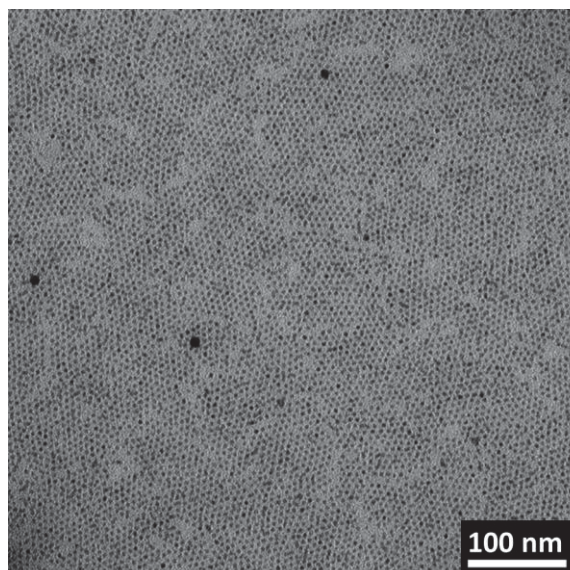
300°C 5min



300°C 10min



300°C 20min



300°C 30min

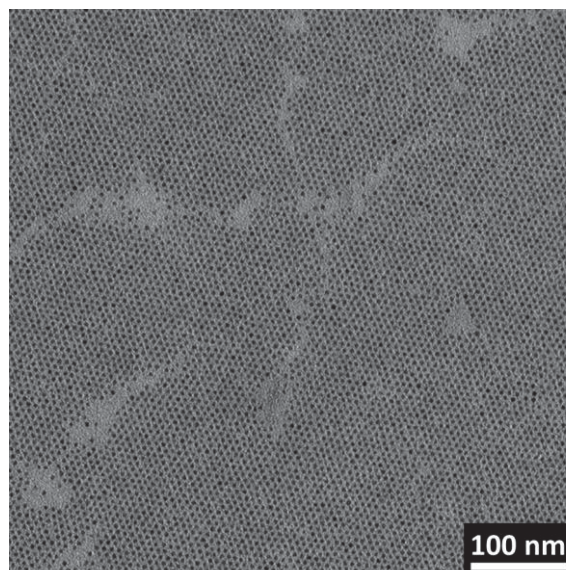


Figure 37. TEM pictures obtained after different reaction time at 300°C plateau by using microwave heating and “*in situ*” mixing approach.

V.3.8 Typical run for the “as-fast-as-possible” routine and 300°C plateau

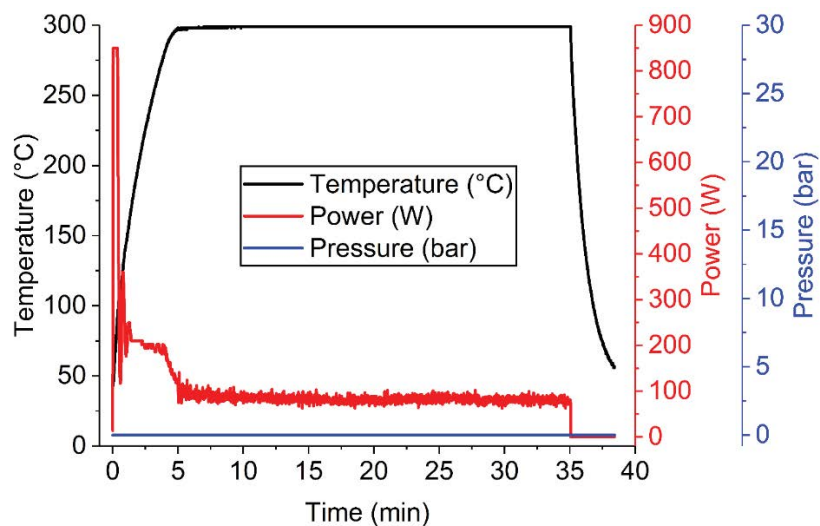


Figure 38. Typical heating profile performed with microwave oven (Monowave 300 Anton Paar) for a 30min plateau at 300°C: during all heating steps (temperature increase, plateau, cooling down), temperature, pressure, and magnetron power are monitored respectively in dark curve, blue curve and red curve.

V.3.9 Summary of the TEM analyses

Table 12. Summary of the TEM analyses

	TEM picture	diameter (nm)	Standard deviation		FWHM	
			(nm)	(%)	(nm)	(%)
« premix » + conventional heating (figure 31)	280°C t=90 min	10.3	0.56	5.6%	1.3	13.0%
“ <i>in situ</i> ” mixing + conventional heating (figure 34) trial#1	B	5.58	0.86	15.4%	2	35.8%
	C	7.43	1.13	15.2%	2.65	35.7%
	D	8.54	2.26	26.5%	5.31	62.2%
“ <i>In situ</i> ” mixing + conventional heating (figure 35) trial#2	A	1.95	0.51	26.2%	1.19	61.0%
	B	3.69	0.6	15.2%	1.32	35.8%
	C	4.2	0.51	12.1%	1.18	28.1%
	D	5.7	0.99	17.4%	2.32	40.7%
“ <i>in situ</i> ” mixing + microwave heating (figure 36)	no heating	2.32	0.3	12.9%	0.71	30.6%
	280°C 30min	2.94	0.85	28.9%	1.99	67.7%
	290°C 30min	4.08	0.53	13.0%	1.24	30.4%
	300°C 30min	4.55	0.45	9.9%	1.04	22.9%
“ <i>in situ</i> ” mixing + microwave heating (Ffigure 37)	300°C 1min	2.31	0.57	24.7%	1.33	57.6%
	300°C 5min	3.06	0.78	25.5%	1.84	60.1%
	300°C 10min	3.55	0.88	24.8%	2.06	58.0%
	300°C 20min	4.06	0.75	18.5%	1.75	43.1%

For each sample, TEM pictures were taken in a minimum of five different locations per grid (at the center of the grid, and at least one per quadrant). For each batch, the statistics were run on a minimum of 2k nanoparticles ensemble, using the PSA macro.

VI References

- 1 Baldan, A. Review progress in Ostwald ripening theories and their applications to nickel-base superalloys Part I: Ostwald ripening theories. *Journal of materials science* **37**, 2171-2202 (2002).
- 2 Talapin, D. V., Rogach, A. L., Haase, M. & Weller, H. Evolution of an ensemble of nanoparticles in a colloidal solution: theoretical study. *The Journal of Physical Chemistry B* **105**, 12278-12285 (2001).
- 3 Streitenberger, P. & Zöllner, D. The envelope of size distributions in Ostwald ripening and grain growth. *Acta Materialia* **88**, 334-345 (2015).
- 4 Sugimoto, T. Preparation of monodispersed colloidal particles. *Advances in Colloid and Interface Science* **28**, 65-108 (1987).
- 5 Lahtinen, S. *et al.* Disintegration of hexagonal NaYF₄: Yb³⁺, Er³⁺ upconverting nanoparticles in aqueous media: The role of fluoride in solubility equilibrium. *The Journal of Physical Chemistry C* **121**, 656-665 (2016).
- 6 Du, Y.-P., Zhang, Y.-W., Sun, L.-D. & Yan, C.-H. Luminescent monodisperse nanocrystals of lanthanide oxyfluorides synthesized from trifluoroacetate precursors in high-boiling solvents. *The Journal of Physical Chemistry C* **112**, 405-415 (2008).
- 7 Boyer, J.-C., Vetrone, F., Cuccia, L. A. & Capobianco, J. A. Synthesis of colloidal upconverting NaYF₄ nanocrystals doped with Er³⁺, Yb³⁺ and Tm³⁺, Yb³⁺ via thermal decomposition of lanthanide trifluoroacetate precursors. *Journal of the American Chemical Society* **128**, 7444-7445 (2006).
- 8 Wang, F., Deng, R. & Liu, X. Preparation of core-shell NaGdF₄ nanoparticles doped with luminescent lanthanide ions to be used as upconversion-based probes. *Nature Protocols* **9**, 1634-1644 (2014).
- 9 Van Santen, R. The Ostwald step rule. *The Journal of Physical Chemistry* **88**, 5768-5769 (1984).
- 10 Thoma, R., Insley, H. & Hebert, G. The sodium fluoride-lanthanide trifluoride systems. *Inorganic chemistry* **5**, 1222-1229 (1966).
- 11 Mai, H.-X. *et al.* High-Quality Sodium Rare-Earth Fluoride Nanocrystals: Controlled Synthesis and Optical Properties. *Journal of the American Chemical Society* **128**, 6426-6436 (2006).
- 12 Wang, F. *et al.* Simultaneous phase and size control of upconversion nanocrystals through lanthanide doping. *nature* **463**, 1061 (2010).
- 13 Suter, J. D., Pekas, N. J., Berry, M. T. & May, P. S. Real-time-monitoring of the synthesis of β-NaYF₄: 17% Yb, 3% Er nanocrystals using NIR-to-visible upconversion luminescence. *The Journal of Physical Chemistry C* **118**, 13238-13247 (2014).
- 14 Radunz, S. *et al.* Evolution of Size and Optical Properties of Upconverting Nanoparticles during High-Temperature Synthesis. *The Journal of Physical Chemistry C* **122**, 28958-28967 (2018).
- 15 Wilhelm, S. *et al.* Water dispersible upconverting nanoparticles: effects of surface modification on their luminescence and colloidal stability. *Nanoscale* **7**, 1403-1410 (2015).
- 16 Damasco, J. A. *et al.* Size-Tunable and Monodisperse Tm³⁺/Gd³⁺-Doped Hexagonal NaYbF₄ Nanoparticles with Engineered Efficient Near Infrared-to-Near Infrared

- Upconversion for In Vivo Imaging. *ACS Applied Materials & Interfaces* **6**, 13884-13893 (2014).
- 17 Rinkel, T., Nordmann, J., Raj, A. N. & Haase, M. Ostwald-ripening and particle size focussing of sub-10 nm NaYF₄ upconversion nanocrystals. *Nanoscale* **6**, 14523-14530 (2014).
- 18 Voss, B. & Haase, M. Intrinsic Focusing of the Particle Size Distribution in Colloids Containing Nanocrystals of Two Different Crystal Phases. *ACS Nano* **7**, 11242-11254, (2013).
- 19 Zhai, X. *et al.* A Simple Strategy for the Controlled Synthesis of Ultrasmall Hexagonal-Phase NaYF₄: Yb, Er Upconversion Nanocrystals. *ChemPhotoChem* **1**, 369-375 (2017).
- 20 Baghbanzadeh, M., Carbone, L., Cozzoli, P. D. & Kappe, C. O. Microwave-assisted synthesis of colloidal inorganic nanocrystals. *Angewandte Chemie International Edition* **50**, 11312-11359 (2011).
- 21 Wang, H.-Q. & Nann, T. Monodisperse upconverting nanocrystals by microwave-assisted synthesis. *Acs Nano* **3**, 3804-3808 (2009).
- 22 Niu, N. *et al.* Rapid microwave reflux process for the synthesis of pure hexagonal NaYF₄: Yb³⁺, Ln³⁺, Bi³⁺(Ln³⁺= Er³⁺, Tm³⁺, Ho³⁺) and its enhanced UC luminescence. *Journal of Materials chemistry* **22**, 21613-21623 (2012).
- 23 Li, F. *et al.* Aqueous phase synthesis of upconversion nanocrystals through layer-by-layer epitaxial growth for in vivo X-ray computed tomography. *Nanoscale* **5**, 6950-6959 (2013).
- 24 Li, F. *et al.* Hydrophilic, upconverting, multicolor, lanthanide-doped NaGdF₄ nanocrystals as potential multifunctional bioprobes. *Chemistry–A European Journal* **18**, 11641-11646 (2012).
- 25 Yu, S., Wang, Z., Cao, R. & Meng, L. Microwave-assisted synthesis of water-disperse and biocompatible NaGdF₄: Yb, Ln@ NaGdF₄ nanocrystals for UCL/CT/MR multimodal imaging. *Journal of Fluorine Chemistry* **200**, 77-83 (2017).
- 26 Hazra, C., Adusumalli, V. N. & Mahalingam, V. 3, 5-Dinitrobenzoic acid-capped upconverting nanocrystals for the selective detection of melamine. *ACS applied materials & interfaces* **6**, 7833-7839 (2014).
- 27 Wu, W. *et al.* NIR-Light-Induced Deformation of Cross-Linked Liquid-Crystal Polymers Using Upconversion Nanophosphors. *Journal of the American Chemical Society* **133**, 15810-15813 (2011).
- 28 Tong, L. *et al.* Comparative study on upconversion luminescence and temperature sensing of α - and β -NaYF₄: Yb³⁺/Er³⁺ nano-/micro-crystals derived from a microwave-assisted hydrothermal route. *Journal of Luminescence* **167**, 386-390 (2015).
- 29 Tong, L. *et al.* Anomalous Temperature-Dependent Upconversion Luminescence of α -NaYF₄: Yb³⁺/Er³⁺ Nanocrystals Synthesized by a Microwave-Assisted Hydrothermal Method. *Journal of nanoscience and nanotechnology* **16**, 816-821 (2016).
- 30 Furman, B. R., Gutierrez, R. D. & Baker, C. K. Ionothermal Synthesis of Lanthanide Tetrafluoride Nanoparticles Using Deep Eutectic Solvents. *MRS Online Proceedings Library Archive* **1804**, 25-30 (2015).
- 31 Ding, M., Lu, C., Ni, Y. & Xu, Z. Rapid microwave-assisted flux growth of pure β -NaYF₄: Yb³⁺, Ln³⁺ (Ln= Er, Tm, Ho) microrods with multicolor upconversion luminescence. *Chemical Engineering Journal* **241**, 477-484 (2014).

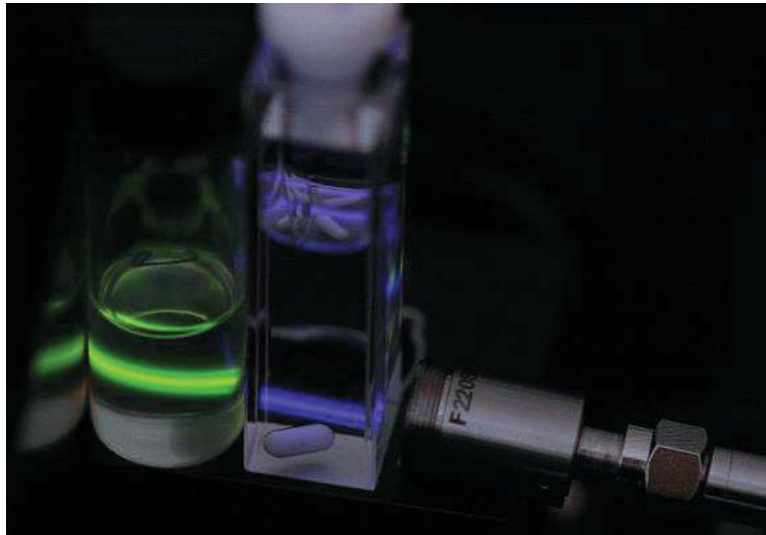
- 32 Reddy, K. L., Prabhakar, N., Arppe, R., Rosenholm, J. M. & Krishnan, V. Microwave-assisted one-step synthesis of acetate-capped NaYF₄: Yb/Er upconversion nanocrystals and their application in bioimaging. *Journal of materials science* **52**, 5738-5750 (2017).
- 33 Panov, N., Marin, R. & Hemmer, E. Microwave-Assisted Solvothermal Synthesis of Upconverting and Downshifting Rare-Earth-Doped LiYF₄ Microparticles. *Inorganic chemistry* **57**, 14920-14929 (2018).
- 34 Reddy, K. L. *et al.* Amine-functionalized, porous silica-coated NaYF₄: Yb/Er upconversion nanophosphors for efficient delivery of doxorubicin and curcumin. *Materials Science and Engineering: C* **96**, 86-95 (2019).
- 35 Guzzetta, F., Roig, A. & Julián-López, B. Ultrafast Synthesis and Coating of High-Quality β-NaYF₄: Yb³⁺, Ln³⁺ Short Nanorods. *The journal of physical chemistry letters* **8**, 5730-5735 (2017).
- 36 Chen, C. *et al.* Ionic liquid-based route to spherical NaYF₄ nanoclusters with the assistance of microwave radiation and their multicolor upconversion luminescence. *Langmuir* **26**, 8797-8803 (2010).
- 37 Som, S., Das, S., Yang, C.-Y. & Lu, C.-H. Enhanced upconversion of NaYF₄: Er³⁺/Yb³⁺ phosphors prepared via the rapid microwave-assisted hydrothermal route at low temperature: phase and morphology control. *Optics letters* **41**, 464-467 (2016).
- 38 Grzyb, T. & Przybylska, D. Formation Mechanism, Structural, and Upconversion Properties of Alkaline Rare-Earth Fluoride Nanocrystals Doped With Yb³⁺/Er³⁺ Ions. *Inorganic chemistry* **57**, 6410-6420 (2018).
- 39 Chen, X. *et al.* Microwave hydrothermal synthesis and upconversion properties of NaYF₄: Yb³⁺, Tm³⁺ with microtube morphology. *Materials letters* **63**, 1023-1026 (2009).
- 40 Wawrzynczyk, D., Piatkowski, D., Mackowski, S., Samoc, M. & Nyk, M. Microwave-assisted synthesis and single particle spectroscopy of infrared down-and visible up-conversion in Er³⁺ and Yb³⁺ co-doped fluoride nanowires. *Journal of Materials Chemistry C* **3**, 5332-5338 (2015).
- 41 Tong, L. *et al.* Microwave-assisted hydrothermal synthesis, temperature quenching and laser-induced heating effect of hexagonal microplate β-NaYF₄: Er³⁺/Yb³⁺ microcrystals under 1550 nm laser irradiation. *Sensors and Actuators B: Chemical* **246**, 175-180 (2017).
- 42 Wang, D. *et al.* Rapid microwave-enhanced hydrothermal synthesis and shape evolution of uniform NaGdF₄: Yb, Er (Tm/Ho) nanocrystals with upconversion and paramagnetic properties. *Nanotechnology* **23**, 225705 (2012).
- 43 Yang, C. *et al.* Microwave heating synthesis and visible upconversion luminescence of NaGdF₄: Yb, Er/reduced graphene oxide nanocomposites. *Journal of Materials Science: Materials in Electronics* **27**, 11720-11725 (2016).
- 44 Chen, Z. *et al.* Versatile synthesis strategy for carboxylic acid– functionalized upconverting nanophosphors as biological labels. *Journal of the American Chemical Society* **130**, 3023-3029 (2008).
- 45 Bednarkiewicz, A., Nyk, M., Samoc, M. & Streck, W. Up-conversion FRET from Er³⁺/Yb³⁺: NaYF₄ nanophosphor to CdSe quantum dots. *The Journal of Physical Chemistry C* **114**, 17535-17541 (2010).
- 46 Palo, E. *et al.* Up-conversion luminescence of the NaYF₄: Yb³⁺, Er³⁺ nanomaterials prepared with the solvothermal synthesis. *Optical Materials* **59**, 49-54 (2016).

- 47 Wang, H.-Q., Tilley, R. D. & Nann, T. Size and shape evolution of upconverting nanoparticles using microwave assisted synthesis. *CrystEngComm* **12**, 1993-1996 (2010).
- 48 Quintanilla, M., Ren, F., Ma, D. & Vetrone, F. Light management in upconverting nanoparticles: ultrasmall core/shell architectures to tune the emission color. *ACS Photonics* **1**, 662-669 (2014).
- 49 Wang, H. & Nann, T. Monodisperse upconversion GdF₃: Yb, Er rhombi by microwave-assisted synthesis. *Nanoscale research letters* **6**, 267 (2011).
- 50 Fannin, P. C., Marin, C. N., Malaescu, I. & Stefu, N. Microwave dielectric properties of magnetite colloidal particles in magnetic fluids. *Journal of Physics: Condensed Matter* **19**, 036104 (2007).
- 51 Washington Ii, A. L. & Strouse, G. F. Microwave Synthesis of CdSe and CdTe Nanocrystals in Nonabsorbing Alkanes. *Journal of the American Chemical Society* **130**, 8916-8922 (2008).
- 52 TRC Thermodynamic Tables-Hydrocarbon, T. T. A. M. U. S., College Station, TX & 77843-3124.
- 53 Cedeño, F. O., Prieto, M. M. & Xiberta, J. Measurements and Estimate of Heat Capacity for Some Pure Fatty Acids and Their Binary and Ternary Mixtures. *Journal of Chemical & Engineering Data* **45**, 64-69 (2000).
- 54 Gargas, D. J. *et al.* Engineering bright sub-10-nm upconverting nanocrystals for single-molecule imaging. *Nat Nano* **9**, 300-305 (2014).
- 55 Erdmann, M. & Koepke, J. Experimental temperature cycling as a powerful tool to enlarge melt pools and crystals at magma storage conditions. *American Mineralogist* **101**, 960-969 (2016).
- 56 Wu, Z., Seok, S., Kim, D. H. & Kim, W.-S. Control of Crystal Size Distribution using Non-Isothermal Taylor Vortex Flow. *Crystal Growth & Design* **15**, 5675-5684 (2015).
- 57 Kacker, R. *et al.* Microwave Assisted Direct Nucleation Control for Batch Crystallization: Crystal Size Control with Reduced Batch Time. *Crystal Growth & Design* **16**, 440-446 (2016).
- 58 Wu, Z., Yang, S. & Wu, W. Application of temperature cycling for crystal quality control during crystallization. *CrystEngComm* **18**, 2222-2238 (2016).
- 59 van Westen, T. & Groot, R. D. Effect of Temperature Cycling on Ostwald Ripening. *Crystal growth & design* **18**, 4952-4962 (2018).
- 60 Li, D., Lai, W.-Y., Shao, Q. & Huang, W. Facile synthesis of ultrasmall hexagonal NaYF₄: Yb³⁺, Er³⁺ upconversion nanocrystals through temperature oscillation. *Inorganic Chemistry Frontiers* **4**, 1211-1214 (2017).
- 61 Hossan, M. Y. *et al.* Explaining the Nanoscale Effect in the Upconversion Dynamics of β-NaYF₄:Yb³⁺, Er³⁺ Core and Core–Shell Nanocrystals. *The Journal of Physical Chemistry C* **121**, 16592-16606 (2017).
- 62 Hudry, D. *et al.* Direct evidence of significant cation intermixing in upconverting core@shell nanocrystals: Toward a new crystallochemical model. *Chemistry of Materials* **29**, 9238-9246 (2017).
- 63 Li, Z. & Zhang, Y. An efficient and user-friendly method for the synthesis of hexagonal-phase NaYF₄: Yb, Er/Tm nanocrystals with controllable shape and upconversion fluorescence. *Nanotechnology* **19**, 345606 (2008).

- 64 Kiper, R. A. Properties of substance: ammonium fluoride. <http://chemister.ru/Database/properties-en.php?dbid=1&id=370>, accessed on 30/01/2019 (s.d.).
- 65 Kiper, R. A. Properties of substance: sodium hydroxide. <http://chemister.ru/Database/properties-en.php?dbid=1&id=758>, accessed on 30/01/2019 (s.d.).

Chapter III

Upconverting nanolamps



“La musique est l’arithmétique du son, comme l’optique est la géométrie de la lumière” (Claude Debussy)

“Pour atteindre la vérité, il faut une fois dans la vie se défaire de toutes les opinions qu’on a reçues, et reconstruire de nouveau tout le système de ses connaissances” (René Descartes)

Contents

I	Introduction.....	151
I.1	Non-linear behaviour	151
I.2	Theoretical models	151
I.3	Aim of the chapter	155
II	Photophysical properties of UCNP	158
II.1	Absorption	158
II.1.1	Absorbance in solution.....	158
II.1.2	Reflectance/transmittance on powder	162
II.2	Emission	163
II.2.1	Experimental considerations	163
II.2.2	Comparative study of UCNPs under steady–state conditions.....	167
II.2.3	Exploration of Tm-based UCNP’s nonlinear behavior	176
III	Quantitative photophysics of the ultrasmall UCNPs.....	183
III.1	Identity card of ultrasmall UCNP nanolamp	184
III.1.1	Steady state.....	184
III.1.2	Time-resolved emission	185
III.1.3	Quantum yield – efficiency	202
IV	Towards our own kinetic model.....	204
IV.1	Description of the model	204
IV.2	Mathematical expression of the model.....	205
IV.3	Data mining of rate constant.....	207
IV.4	Preliminary results.....	209
V	Conclusion	212
VI	Experimental section	214

VII References 221

I Introduction

The main parametrization of a nanolamp relies on knowing the efficiency of the light emissions. Classically, this is achieved with two quantifiers: quantum yields and lifetimes. In order to know whether such descriptors apply to UCNPs and their ultrasmall versions, we have initiated a detailed photophysical study of a library of nanoparticles. Before exposing our results, a brief introduction to the photophysics of upconversion is necessary.

I.1 Non-linear behaviour

One of the most characteristic property of UCNP emissions is the non-linear behavior of the emission intensities with the excitation power I_0 . It is commonly written as

$$I_{em}^\lambda \propto (I_0)^p \quad (1)$$

It is common to analyze the data using log-log plot, since one expects:

$$\log(I_{em}^\lambda) = p \log I_0 + b \quad (2)$$

Indeed, for a range of powers, a linear correlation is usually observed.

By analogy with NLO, it would be tempting to correlate the exponent p to the number of 980nm-photon used to populate the emitting level. The following will show that such a hypothesis is not valid.

I.2 Theoretical models

To understand the “exponent issue”, it is important to remind the complex energy redistribution network leading to the energy emission. Beside the classic monomolecular processes (radiative and non-radiative decays), key kinetic features are bound to the bimolecular processes, ensuring the upconversion and the transport of the energy.

Depopulation pathway of sensitizer (Yb)

Contrary to the emitter, the behaviour of the sensitizer is easy to understand: it is similar to standard luminophores, such as an organic dye for example, as it has only one excited state. The emission from the ytterbium ions is not expected to be power-dependent. Beside the spontaneous first order processes (radiative and non-radiative relaxations), the Yb excited state (Yb*) within UCNPs can disappear via the so-called “energy migration” toward the surface. This elementary step can be written as:



Rate constant models are resonant-like and depends on the inter ions distance within the crystal (i.e. the ytterbium concentration).

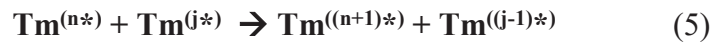
Depopulation pathway of emitter (Tm)

As the optimal concentration of Tm emitters has been adopted as 0.5-1%, [Tm]-dependent effect can be neglected. However, the multiple excited states can suffer from back transfer, mainly to sensitizer, or to other Tm excited states. For simplicity we will represent only the cross relaxation to Yb which is [Yb]-dependent :



Thus, high doping content (Yb or Tm) can increase the depopulation of the Tm excited states.

In addition to these processes, many possible cross-relaxations can happen. They can be schematized according to the following general bimolecular process:



These are mainly controlled by the (Tm-Tm) distance.

Complete models

As summarized by M. Kraft *et al.*, several propositions of kinetic pathways have been proposed in the literature.¹

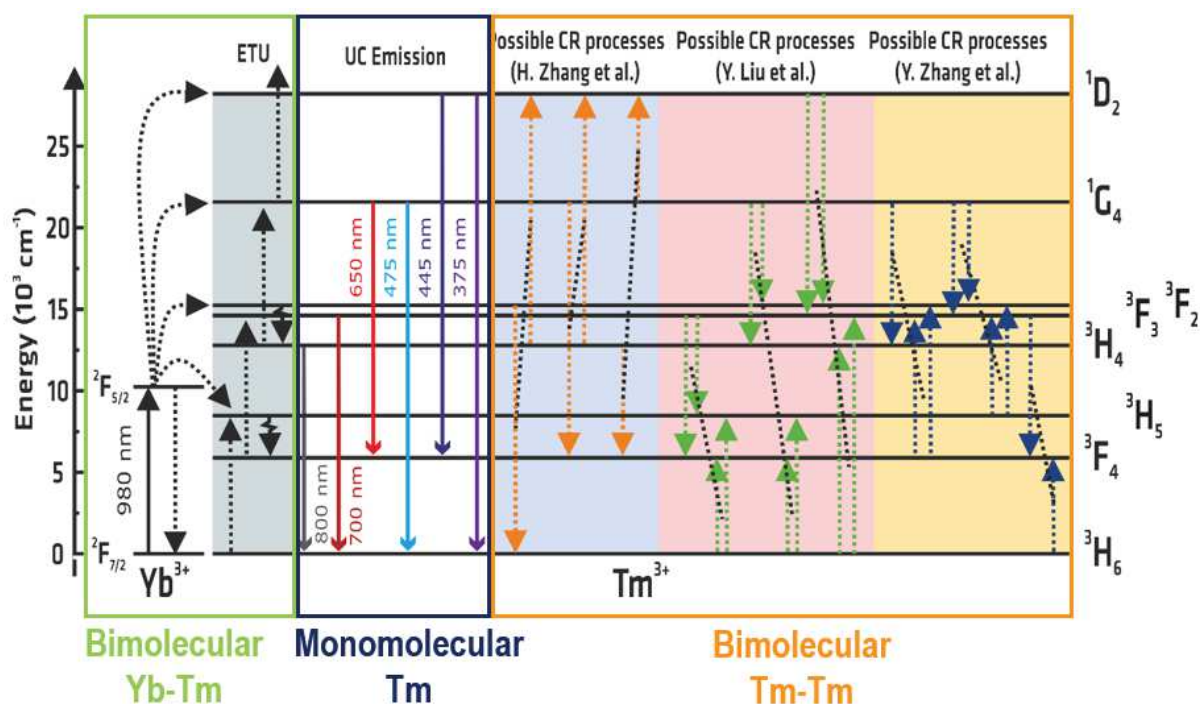


Figure 1. Energy level diagram of Yb^{3+} , Tm^{3+} codoped UCNP particles. The Yb-to-surface energy migration path is not mentioned for clarity. The black short dotted lines represent the ETU steps, the orange short dotted lines the CR processes and the zig-zag lines MPR processes. The possible CR processes according to H. Zhang *et al.*,² Y. Liu *et al.*³ and Y. Zhang *et al.*⁴ are respectively highlighted with blue, red and yellow background colours. ETU: energy transfer upconversion; CR: cross-relaxation; MPR: multiphonon-relaxation. Reproduced from ¹.

Beside the “standard” processes evoked in the Introduction (Chapter 1, section II-2) and describing the global ETU phenomenon, the Tm-Tm bimolecular cross-relaxations were added. The number and associated levels differ from authors to authors

Stationary state experiments: simple, three Tm-levels kinetic model.

In the absence of emitter-emitter cross relaxation, a simple model to explain the observed dependence of the luminescence as a function of the excitation intensity (power) was developed by the team of S. Andersson-Engels in 2013.⁵ Using the general formalism commonly encountered in laser material science, this model is the translation into kinetic equations of the ETU mechanism involving ytterbium and an emitter. It is a “2+3” level system with two levels describing the ytterbium ground state Yb and excited state Yb^* , and three levels for the emitter (ground state 0 and two excited states 1 and 2). Kinetic parameters are given in

figure 2. The emission is associated to the radiative lifetime τ_{rad} for level 1 (it is of course a part of the lifetime τ_2 of the excited state 1).

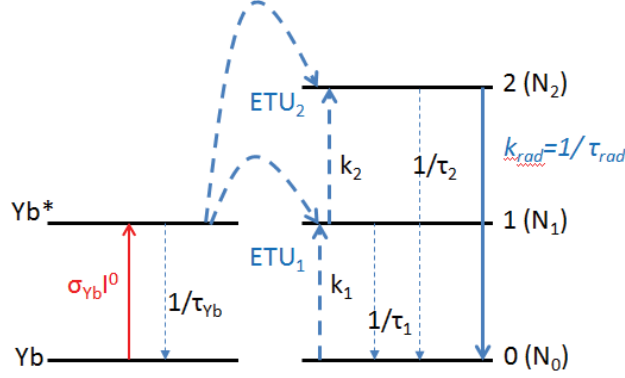


Figure 2. Kinetic scheme used by S. Andersson-Engels for the ETU mechanism

In order to give simple analytical expressions, several simplifying assumptions are made:

- Concentrations of excited states are always negligible compared to ground states
- ETU processes from Yb*-to-Yb are negligible compared to Yb* spontaneous decay
- Photo-stationary state is reached

The system of equations driving the populations of each excited state becomes:

$$\left\{ \begin{array}{l} \frac{d[Yb^*]}{dt} = \sigma_{Yb} I_0 [Yb] - \frac{1}{\tau_{Yb}} [Yb^*] - (k_0 N_0 [Yb^*] + k_0 N_1 [Yb^*]) \\ \quad \approx \sigma_{Yb} I_0 [Yb] - \frac{1}{\tau_{Yb}} [Yb^*] = 0 \\ \frac{d[N_1]}{dt} = k_0 N_0 [Yb^*] - k_0 N_1 [Yb^*] - \frac{1}{\tau_1} N_1 = 0 \\ \frac{d[N_2]}{dt} = k_1 N_1 [Yb^*] - \frac{1}{\tau_2} N_2 = 0 \end{array} \right. \quad (6)$$

Remarking that the emission rate is $I_{em} = \frac{N_2}{\tau_{rad}}$, simple calculations give the following dependence of the exponent (p) of the log-log plot slope with the power I_0 :

$$p = \frac{d \log I_{em}}{d \log I_0} = 1 + \frac{1}{1 + k_1 \tau_2 \tau_{Yb} [Yb] \sigma_{Yb} I_0} \quad (7)$$

At low power (I_0), p is close to 2, at higher power p is closer to 1.

Upconversion quantum yield being defined as: $\eta = \frac{I_{em}}{I_0^{abs}} = \frac{I_{em}}{\sigma_{Yb} I_0 [Yb]}$, it becomes:

$$\eta = \frac{\eta_s \frac{I_0}{I_0^B}}{1 + \frac{I_0}{I_0^B}} \quad (8)$$

Two key parameters are thus defined:

- the balancing power $I_0^B = \frac{1}{(k_1 \tau_2 \tau_{Yb} [Yb] \sigma_{Yb})}$ and
- the maximum quantum yield $\eta_s = k_0 N_0 [Yb *] \frac{\tau_{Yb} \tau_2}{\tau_{rad}}$.

When the power reaches the balancing power I_0^B , the quantum yield is at the half of the maximum available η_s : this pivotal power completely determines the photophysics of the UCNPs. The same authors have extended this modeling to more complex systems.

This model reproduces the apparent curvature of the log-log plot, stressing out the impact of the kinetic network on the emission. However, although very straightforward, it suffers from limitations: the hypotheses are very strong and the numbers of levels and processes are limited as an analytical expression of the system response is sought. More complex models have been developed without assumptions, including all levels.⁶

I.3 Aim of the chapter

The synthesis (chapter 2) has shown that it is irrelevant to try and reproduce exactly a defined size and composition (as it would be for organic compounds), therefore each batch had to be considered independently. The following list gathers all the samples examined for their photophysical properties. Furthermore, it is possible to envision different techniques and setups to achieve this goal. Beside the equipment available at IMRCP, other instruments have been used (table 1) thanks to collaborations established over the duration of my PhD. In the following, we will summarize the results obtained using different setups among 3 laboratories. I performed experiments myself at IMRCP and BAM (under the guidance of Dr Ute Resch-Genger), while the ones made at LASIR were conducted by Drs Aude Bouchet and Michel Sliwa.

Table 1. Summary of samples presented in this chapter. Analyses marked with “X” were carried out. Sizes are average diameters. (BA1 & BA4), (BA2 & BA5), (BA3 & BA7), (BA 11 & BA12), (BA13 & BA14), (BA15 & BA16) are respective pairs of core and core@shell originating from the same core.

Shape	Sample	Batch code	Steady-state IMRCP	Steady-state Time-resolved BAM	Integrating sphere BAM	Time-resolved LASIR
Ultrasmall spheres	Core 2.5 nm 20%Yb	BA1	X	X	X	X
	Core 2.8 nm 57%Yb	BA2	X	X	X	X
	Core 3.2 nm 57%Yb	BA3	X			X
	Core@shell 5.5 nm 20%Yb	BA4	X			X
	Core@shell 5.5 nm 57%Yb	BA5	X			X
	Core@shell 5.7 nm 20%Yb	BA6	X	X	X	X
	Core@shell 5.7 nm 57%Yb	BA7	X	X	X	X
	Core@shell 5.5 nm 57%Yb	BA17	X			X
Small spheres	Core 7.5 nm 20%Yb	BA8	X	X	X	X
	Core 7.5 nm 20%Yb	BA9	X			X
	Core 15 nm 57%Yb	BA10	X			X
	Core 10 nm 57%Yb	BA11	X			
	Core@shell 15 nm 57%Yb	BA12	X			
	Core 10 nm 57%Yb	BA13	X			
	Core@shell 15 nm 57%Yb	BA14	X			X
	Core 9.3 nm 57%Yb	BA15	X			
	Core@shell 10.2 nm 57%Yb	BA16	X			

The selected samples were chosen to explore the effect of the size, doping effect, and shell on the overall luminescence. At first, as the full chemical and the corresponding photophysical characterizations are time-consuming, a straightforward protocol was established at IMRCP in order to rapidly obtain emission spectra by maximizing the detection of each different sample. Therefore, the limit of this approach is the lack of calibration, as acquisition parameters were not identical. These issues were then taken into account during my internship at the BAM. There, the extensive knowledge of the upconversion phenomenon has led to a standardized and

calibrated routine previously put in place, and I was able to work under more comparable excitation conditions than at IMRCP (laser power density in the 1-125 W cm⁻² range). Additionally, time-resolved experiments at BAM were performed by using the same laser as for steady-state studies. A signal generator was used to trigger long excitation pulses (500 μs). Meanwhile, collaborators at LASIR have achieved a complementary study by investigating UCNP behavior under higher laser power (kW-GW) with very short pulses of 5 ns, either isolated to record luminescence rise and decay or grouped by trains to simulate square pulsed excitation.

II Photophysical properties of UCNP

We started to look at the optical properties of UCNP by investigating the “entrance” of the ETU (i.e. the Yb absorption) and its result (the up-converted Tm emissions).

II.1 Absorption

It is notorious that UCNPs display a very weak electronic absorption due to the poor RE cross section and also to the colloid nature of the material (high scattering and limited colloidal stability at high concentrations). Nevertheless, we attempted to record absorption spectra was in dispersed suspensions or in the solid state.

II.1.1 Absorbance in solution

Usual UV-visible spectrophotometers suffer a drop of detector sensitivity above 800 nm therefore the recording of a complete UV-vis-NIR spectrum requires a dedicated instrument.

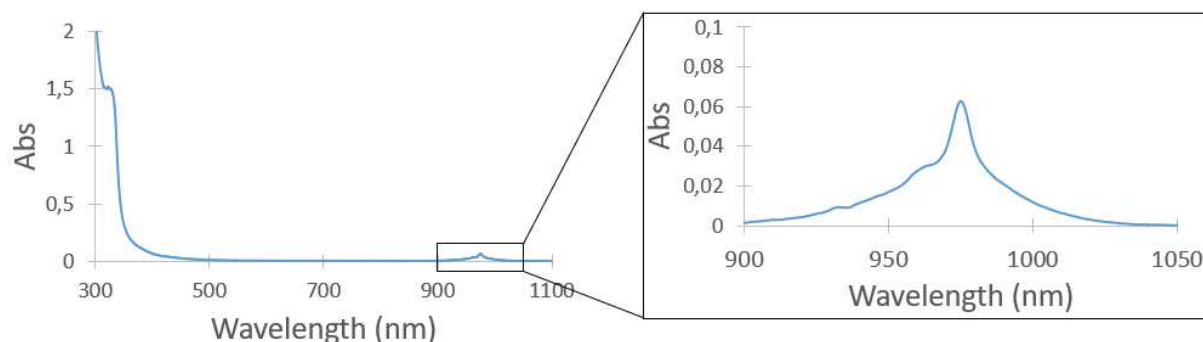


Figure 3. UV-vis-NIR absorbance spectrum of BA5 sample at 50 mg/mL in cyclohexane.

The typical spectrum presented in figure 3 shows the expected features of nanoobjects containing Yb; scattering dominates the response in the visible range (300 nm down to 500 nm). The absorption of ytterbium generates in all recorded spectra a large band centered at 976 nm. This broad band is the convolution of the different transitions within the 4f Stark sub-levels of Yb.

As expected, despite the extremely high declared concentration of 50 mg/mL, maximum absorbances at 976 nm, A_{\max} were extremely low, ranging from 0.01 to 0.1. Table 2 gathers the absorbance of all the samples to be studied. Ultrasmall core and core@shell prepared in the same conditions (50 mg/mL of UCNP@OA) differ in absorbance by only a factor of around 3.

It matches with the difference of Yb content (respectively 20 and 57%) as expected following Beer-Lambert's law.

Table 2. Absorbance measurements of ultrasmall UCNPs in cyclohexane solution at 976 nm. BA4 and BA5 are respectively core@shell of BA1 and BA2 cores.

	BA1	BA2	BA4	BA5	BA8
A_{\max}	0.036	0.109	0.018	0.063	0.059

However, at such a concentration, some part of the nanoparticles sedimented. A simple experiment (figure 4) of absorbance spectra comparison of BA2 before and after manual stirring highlighted the decantation phenomenon. Starting from $A_{\max}=0.1099$ at 976 nm for a solution left at rest, this value was multiplied by 3 ($A_{\max}=0.3276$, red curve) when measured a few seconds after vigorous agitation. Monitoring when left at rest shows that the absorbance is already back to 0.1319 (yellow curve) after 1h30, and to the initial point after at least 3h (dark blue curve). This absorbance no longer varies after 2 or 5 days, indicating the “saturated” character of the solution. Similar behavior was observed for the different batches. Therefore, the apparent factor of 3 above-mentioned seems to indicate that the batches BA1 and 2 or BA4 and 5 seem to have similar colloidal stability.

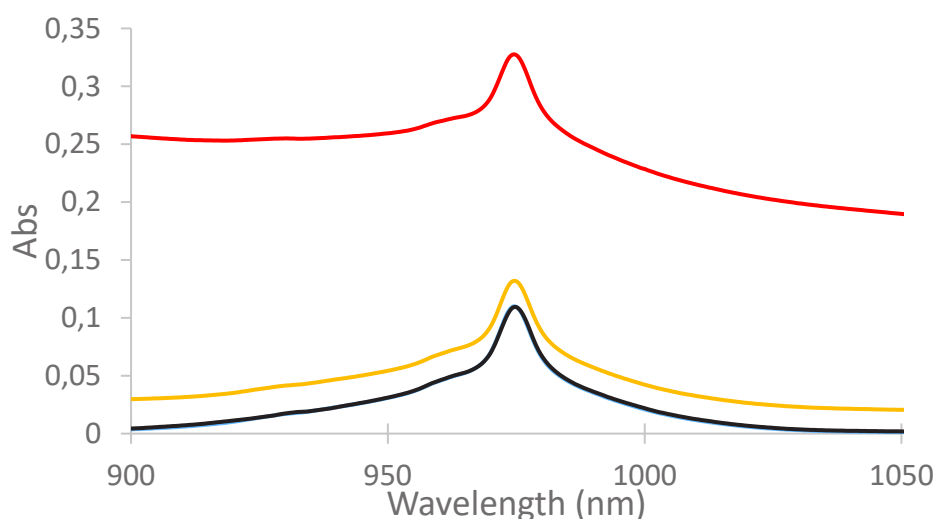


Figure 4. Evolution of A_{\max} on BA2 after agitation. Light blue and dark blue overlapped curves are Abs spectra measured before agitation and since 3h after agitation. Red and yellow ones were respectively acquired a few seconds and 1h30 after agitation.

In the following, all the experiments were run on “rested” colloidal suspensions. The ytterbium absorbance was then used to estimate the amount of NPs in solution (supernatant) or decanted (pellet), knowing the chemical parameters (table 3) of the UCNPs stock solutions (in mg/mL) and using $\epsilon_{976\text{nm}}(\text{Yb}) = 3.1 \text{ L mol}^{-1} \text{ cm}^{-1}$,⁷ as reported in table 4.

Table 3. Chemical parameters of the nanoparticles of different compositions. BA4 and BA5 are respectively core@shell of BA1 and BA2 cores.

	BA1	BA2	BA4	BA5	BA8
$d_{\text{TEM}} (\text{\AA})$	24	28	55	55	75
%Yb	20.29	57.48	10.15	28.74	20.00
%Gd	78.68	41.5	89.34	70.75	79.00
%Tm	1.03	1.02	0.51	0.51	1.00
$M_{\text{NaREF4}} (\text{g/mol})$	259.57	265.44	257.08	258.55	259.52
$U_{\text{NaREF4}} (\text{\AA}^3)$	111.513	108.752	112.270	110.897	111.535
Z	1.5	1.5	1.5	1.5	1.5
RE/NP	97.4	158.5	1163.9	1178.3	2970.7
Yb/NP	20.0	92.1	118.7	340.4	600.1
Tm/NP	1.0	1.6	6.0	6.0	29.7
$[\text{UCNP@OA}]_{\text{theo}}$ (mg/mL)	50.036	49.986	50.038	49.926	50.000
OA content	30%	30%	30%	30%	30%
$[\text{UCNP}]_{\text{theo}}$ (mg/mL)	35.025	34.990	35.027	34.948	35.000

Noticeably, among the samples, the average concentration of inorganic matter in suspension was found to be around 10 mg/mL, corresponding to 15 mg/mL of UCNPs, taking into account the amount of oleic acid per particle. In other words, in our attempt to use a 50 mg/mL concentration, only 30% of the weighted particles remain in solution without agitation. These calculations are in agreement with the absorbance measurements on BA2 previously described:

the discrepancy between agitated ($A_{\max}=0.3276$) and calm solution ($A_{\max}=0.1099$) represents 33%.

This value seemed to be the solubility limit for of UCNPs in this range of size. However, sample BA8 was found to be much more soluble. This difference can be explained by the variation of NP drying, as discussed in chapter 2 for redissolution issues. Indeed, BA8 batch was the last one to be prepared and probably not as dried as the other ones.

Table 4. Estimation of the concentration in suspension

	BA1	BA2	BA4	BA5	BA8
$[\text{Yb}]_{\text{suspension}}$ (mol/L)	0.0116	0.0352	0.0058	0.0203	0.0190
$n(\text{NP})/\text{L}$ (mmol/L)	$5.82 \cdot 10^{-4}$	$3.82 \cdot 10^{-4}$	$4.89 \cdot 10^{-5}$	$5.97 \cdot 10^{-5}$	$3.17 \cdot 10^{-5}$
$m(\text{NP})/\text{L}$ (mg/mL)	0.1510	0.1014	0.0125	0.0154	0.0082
$m(\text{NaREF}_4@OA)/\text{L}$ (mg/mL)	14.86	16.24	14.71	18.28	24.70
$[\text{NaREF}_4]_{\text{suspension}}$ (mg/mL)	10.40	11.37	10.30	12.80	17.29
$[\text{NaREF}_4]_{\text{settled}}$ (mg/mL)	24.63	23.62	24.73	22.15	17.71
%NP in suspension	30%	32%	29%	37%	49%

On the instrument used, the spectral window is truncated after 1000 nm. To get more insight on the IR absorption we moved to reflectance measurements on dry powders.

II.1.2 Reflectance/transmittance on powder

All spectra (figure 5) are characterized by a poorly defined visible range section, and absorptions in the IR range could be clearly observed only for the “core” nanoparticles. These latter transitions were assigned according to literature data (Table 5). Thus, Yb absorption is centered at around 975 nm, while Tm ground state (3H_6) absorptions to 3H_5 and 3F_4 , give bands at respectively 1210 and 1725 nm. Some Tm excited states absorptions (from 3F_4 and 3H_5) occurring in the SWIR area (1000-2500 nm) (table 5) could be detected as well.

For core@shell nanoparticles (BA4 and BA5), these transitions were undetectable. This was attributed to the dilution of the IR-active Ln^{3+} in such architectures.

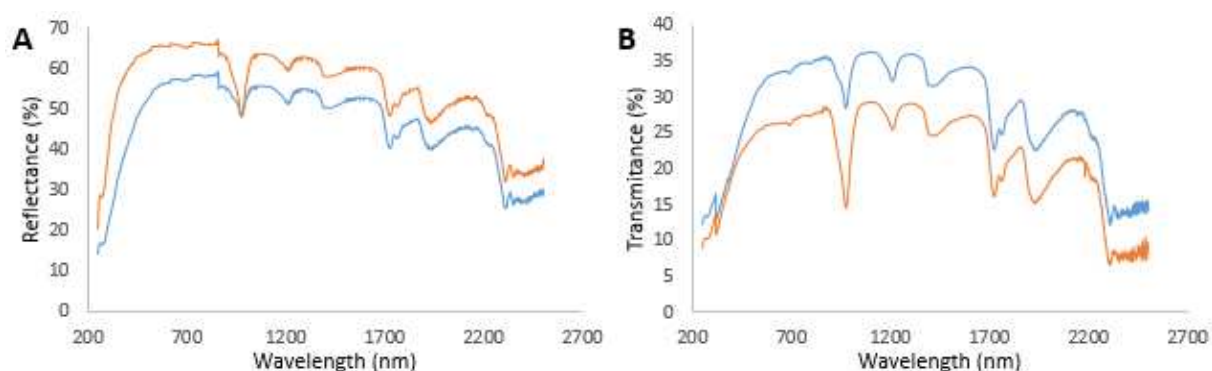


Figure 5. Reflectance (A) and Transmittance (B) measurement on powder for ultrasmall core@shell UCNPs with respective BA1 (blue) or BA2 (orange).

Table 5. Ln^{3+} absorption bands revealed by transmittance and reflectance measurements performed on powders of ultrasmall core 1%Tm-doped Na(Gd-Yb)F₄ with 20% (BA1) or 57% Yb (BA2).

Peak (nm)	Absorption assignation
975	$^2F_{7/2} \rightarrow ^2F_{5/2}$ (Yb ground state)
1210	$^3H_6 \rightarrow ^3H_5$ (Tm ground state)
1400-1424	$^3F_4 \rightarrow ^3H_4$ (Tm 1 st excited state)
1725	$^3H_6 \rightarrow ^3F_4$ (Tm ground state)
2307	$^3H_5 \rightarrow ^3H_4$ (Tm 2 nd excited state)

The broad band centered at 1935 nm is probably due to the organic oleate coating layer.

Unfortunately, we could not get enough resolution to have details over the NIR -visible range, where the Tm absorptions bands to higher excited states should be found. This was disappointing as these transitions mirror the UCNPs emissions: their observation would be of importance to parametrize the radiative rate constants according to the Judd-Ofelt theory. The lack of such emissions was attributed to a strong scattering at the surface of the powder sample, due to an inhomogeneous flat surface layer, and also to the low amount of sample. Eventually, a drop of sensitivity of the spectrophotometer in the UV part prevented an accurate analysis of the Gd³⁺ absorption (312 nm expected).

II.2 Emission

II.2.1 Experimental considerations

II.2.1.1 Setup from IMRCP

Fluorimeter scheme

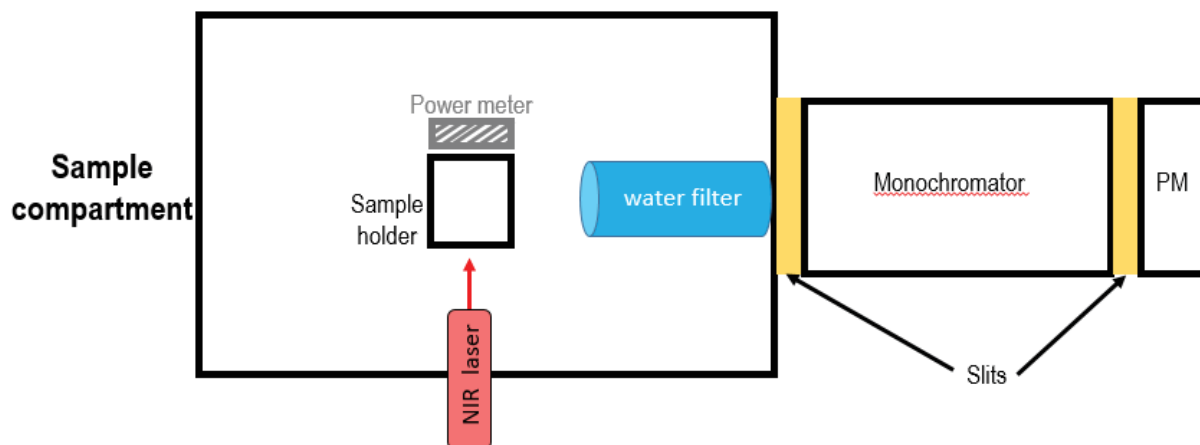


Figure 6. Home-modified standard fluorimeter.

A standard fluorimeter was modified in order to be used as a control instrument for routine measurements (figure 6). As a source, we used a fibered CW 980 nm multimode laser (MDL-H 980nm, Acal BFi/Changchun Industry) of a power range spanning from 0 to 35.4 W cm⁻². The beam was collimated before crossing the cuvette. We further upgraded the instrument by inserting a power-meter probe in front of the laser beam directly behind the quartz cell. This

allowed us to have an estimation of the laser power (P) in realistic conditions, and for UCNPs suspensions, the transmitted power P_0 was used to standardize the suspensions as, in section II.1.1, according to:

$$\text{Absorbance} = \log\left(\frac{P_0}{P}\right) = \log\left(\frac{P_{\text{cyclohexane}}}{P_{\text{sample in cyclohexane}}}\right)$$

On the detection side, a water filter was introduced in front of the PM to eliminate the scattered 980nm light.

II.2.1.2 Setups from BAM

Steady state & Time-resolved measurements

Steady state measurements and Time-resolved measurements were acquired by using a standard fluorimeter FLS 980 from Edinburgh instruments equipped with a 976 nm laser. Laser power and beam were calibrated, giving power densities up to 124.4 W cm^{-2} . Measurements were performed with a fluorimeter bandpass of 10 nm.

The same laser used for steady-state studies was employed for time resolved measurements thanks to the addition of a signal generator to trigger long excitation pulses of $400 \mu\text{s}$. Under such conditions, the luminescence rises during the pulse (figure 7). It can be assimilated to the filling of the excited levels to photostationary point (PSS), comparably with usual photochemical process.

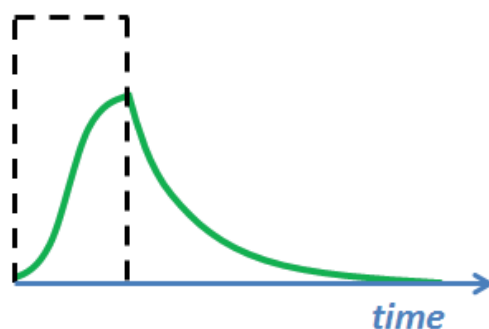


Figure 7. Typical result of lifetime measurement at BAM

Fluorimeter detection curve was recalibrated prior to my internship at the BAM, allowing us to obtain well-standardized measurements.

Integrating sphere

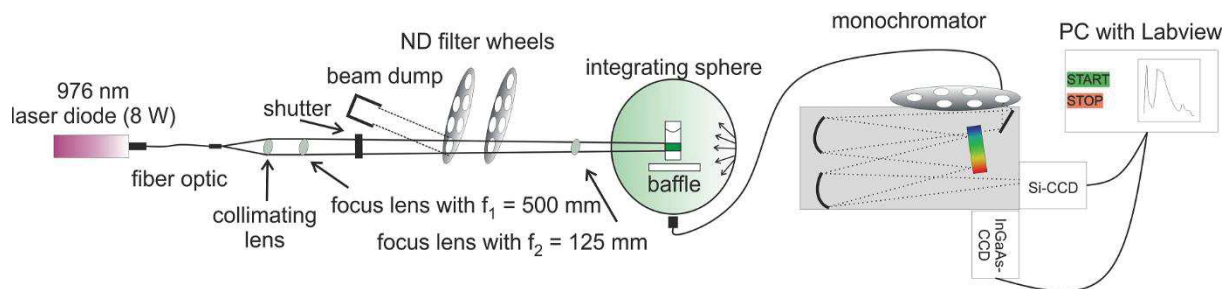


Figure 8. Schematic presentation of the custom-built integrating sphere setup. The setup could be either operated with the focusing lens with a focal distance of 500 mm, or with the lens with a focal distance of 125 mm. Reproduced from ¹.

The benefits of the BAM custom-built setup dedicated to the UCNPs luminescence measurements stems from the use of an integrating sphere (figure 8).⁸ The excitation channel consists of a 976 nm laser diode, collimating and focusing optics, a shutter that can block the excitation light, filter wheels with neutral density (ND) filters, used to attenuate the excitation light without affecting its stability, and a beam dump that collects the reflected light from the filter wheels. Furthermore, to excite the UCNPs, two beam shapes are available: the initial Gaussian beam profile with an average power spanning from 2.5 to 3,400 W cm⁻² that can be converted into a top-hat one (from 0.25 to 410 W cm⁻²), simply by choosing the appropriate focusing lens (focal distance of 500 or 125 mm). The setup was recently upgraded during the PhD of M. Kraft.¹ The detection channel has been extended with an additional indium-gallium-arsenide (InGaAs) charge-coupled device (CCD), and with a new integrating sphere (diameter of *ca.* 11 cm, coated with high reflectivity hydrophobic Spectralon – 99 % from 400 to 1,500 nm; equipped with six ports), allowing to cover the NIR emission of UCNPs up to 1,550 nm. The integrating sphere contains the sample holder, and baffles to protect the optical fibre from direct illumination. The detection channel consists of the optical fibre, the monochromator (Andor 303i) with a filter wheel at the front and the two Peltier-cooled CCDs (T = 188 K; silicon (Si)-CCD: iDus Si DU4230_DD, Andor Technology PLC; CCD line, 1024×256 pixel, pixel sizes of 26×26 μm; InGaAs-CCD: iDus InGaAs DU491A, Andor Technology PLC; CCD line, 1024×1 pixel, pixel sizes of 25×500 μm). The whole system is controlled and operated via a custom-built software that was programmed with LabView. My work was performed only with the top-hat beam profile.

II.2.1.3 Setups from LASIR

Partners at LASIR ussed a flash photolysis set-up based on the use of a linearly polarized pulsed 976 nm laser (5ns, 4mJ, beam size 10mm) obtained by a 10-Hz Nd:YAG laser coupled to an OPO (Continuum Panther EXOPO pumped by a Surelite II). The excitation light was focused ($\approx 500 \mu\text{m}$) into a 1 cm x 2 mm spectroscopic cell (Thorlabs). The emission light was collected by a 100 mm lens, dispersed by a monochromator (bandpass 12 nm) (Horiba Jobin-Yvon, iHR320) and analyzed with a photomultiplier (R1477-06, Hamamatsu) coupled to a digital oscilloscope (LeCroy 454, 500 Mhz). The output of the PMT was multiplied by a resistance of 5 kOhms that leads to an IRF of 0.5 microsecond. The experiment was repeated for different wavelengths of the monochromator and accumulated 64 times (each acquisition separated by 1 second). Time windows range studied was from 0 to 2 ms with 10000 points (0.2 microsecond/ point).

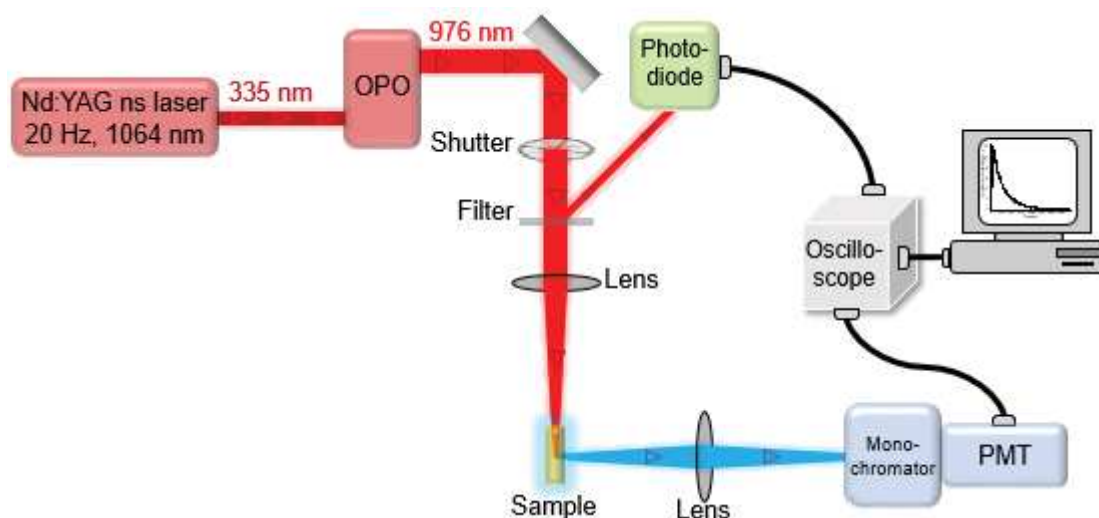


Figure 9. Schematic representation of the setup developed at LASIR

Thus, compared to the typical lanthanide lifetimes, the pulse shape (single 5 ns pulse) is akin to a Dirac function at $t=0$ s (figure 10). Rises are occurring after the end of the excitation pulse.

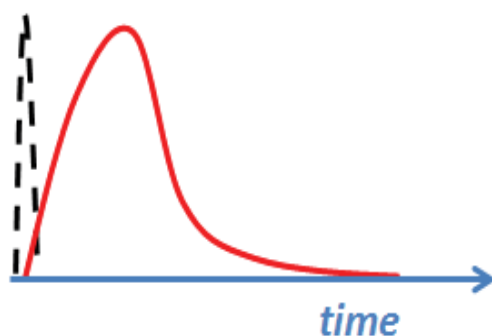


Figure 10. Typical result of lifetime measurement in LASIR. In black, the laser pulse. In red the emission rise and decay.

II.2.2 Comparative study of UCNPs under steady-state conditions

This first study was achieved on the IMRCP modified fluorimeter. The various analyses of samples were acquired with different configurations, in particular the slits of the monochromators were varied. Therefore, they will be presented by groups of experiments recorded in similar conditions.

II.2.2.1 Steady-state comparison of nanospheres

Chemical parameters

From the previous chapter, a library of core and core-shell $\text{Na}(\text{Gd-Yb})\text{F}_4:\text{Tm}$ nanoparticles was available, comprising large objects and ultrasmall spheres (diameters of respectively 7.5–15 nm or 2–6 nm). Table 6 gathers the first group of samples compared by using both slit apertures of 6 nm.

Table 6. Chemical parameters of the studied nanoparticles.

	BA3	BA6	BA9	BA10
diameter (Å)	32	57	75	150
%Yb	57.63	28.71	19.78	58.02
%Gd	41.39	70.79	79.28	40.93
%Tm	0.98	0.51	0.94	1.05
U_{NaREF4} (Å ³)	108.860	111.001	112.832	109.853
Z	1.5	1.5	1.5	1.5
Yb/NP	136.2	376.2	580.9	14*10³
Tm/NP	2.3	6.6	27.6	253.4
Surface/Volume	0.188	0.105	0.080	0.040

Comparison of such a range of UCNP is difficult as several key points can impact the observed luminescence. A preliminary question is: how to best manage the apparent energy absorption? As previously explained (section II.1.1), the ytterbium concentration, and consequently, a nanoparticle concentration (in mg/mL) can be assessed by monitoring the absorption of the studied sample at 980 nm. A standard power of $P_0=1.6269$ W (after a cyclohexane cuvette) was used for the Beer-Lambert law. Results are gathered in Table 7.

Table 7. Estimation of the number of UCNP. ($P_0=1.6269$ W)

	BA3	BA6	BA9	BA10
P (W)	1.4366	1.3543	1.4769	1.4244
Abs=log(P_0/P)	0.05402	0.07966	0.04202	0.05773
[Yb] (mmol/L)	17.42	25.70	13.55	18.62
N(Yb)	$2.6*10^{19}$	$3.9*10^{19}$	$2.0*10^{19}$	$2.8*10^{19}$
N(RE/NP)	236	1310	2937	24130
N(NP)/L	$1.93*10^{17}$	$1.03*10^{17}$	$3.51*10^{16}$	$2.00*10^{15}$
[NP] mg/L	33.95	17.82	6.05	0.35

Recording conditions

As discussed in the absorption section (II.1.1, fig 3), the scattering was found to be important in the high energy spectral range. To limit such diffusion issues, nanoparticle concentrations were fixed at 5 mg/mL for all the studied samples.

A crucial point is then: How to perform accurate comparison of batches displaying very different brightnesses?

The main issue was the huge gap in intensity between the strong 802 nm emission (despite the drop of sensitivity of the detector) and all the other higher energy emissions bands. Consequently, slit apertures were adjusted for each batch in order to maximize the intensity at 802 nm up to 1 million counts per seconds, keeping the detector response in its linear regime. For batch-to-batch comparison purposes, a compromise had to be found, with conditions giving almost no signal for the batch showing the weakest emission (BA3) and a non-analyzable 802 nm peak (i.e. beyond the PM linearity threshold) for the brightest one, BA10 (figure 11).

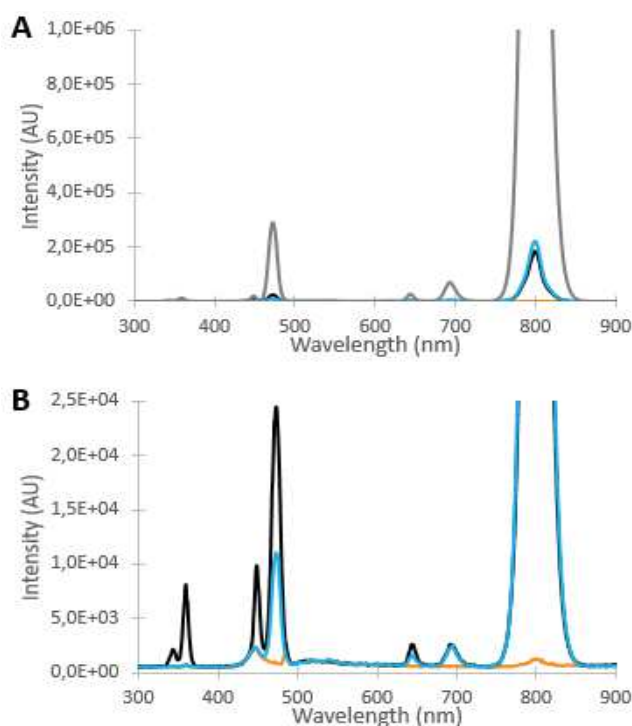


Figure 11. Comparison of NPs luminescence recorded in similar conditions: solutions at 5 mg/mL in cyclohexane, under CW 976 nm laser excitation at 35.39 W cm^{-2} with identical fluorimeter slits configuration: BA10 (grey curve), BA9 (cyan), BA6 (black) and BA3 (orange). A) full spectra. B) Zoom-in to reveal UV and visible emission peaks.

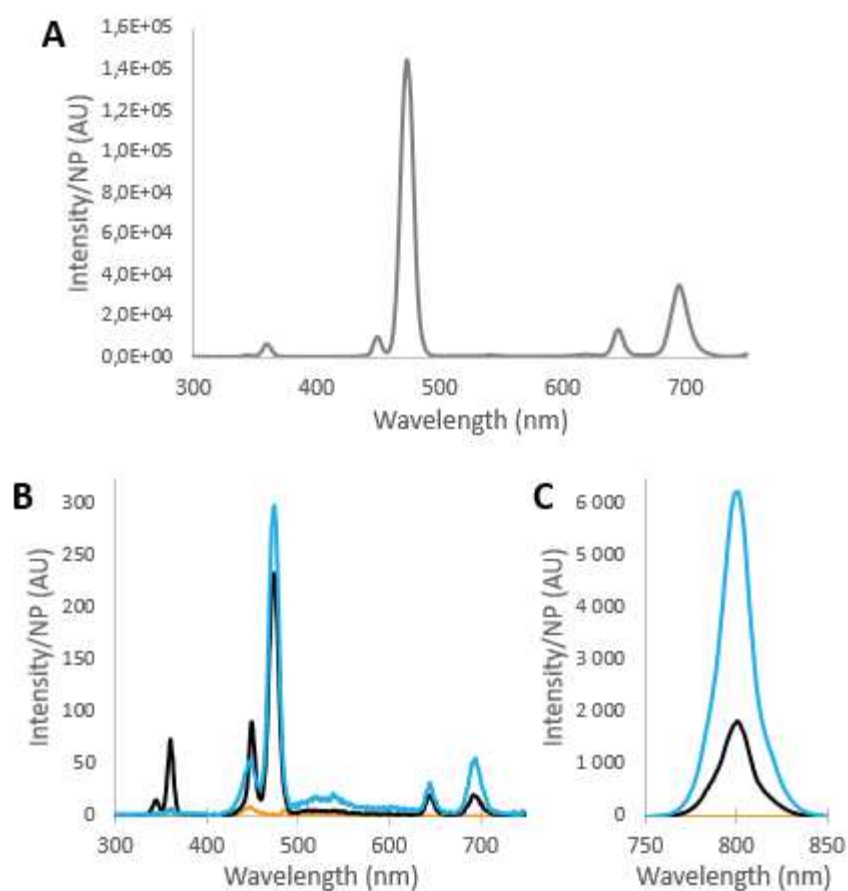


Figure 12. Comparison of NPs luminescence normalized by the number of nanoparticles per sample estimated from absorbance measurement, under CW 976 nm laser excitation at 35.39 W cm^{-2} . A) Luminescence spectra of BA10 (grey curve). B) and C) are overlaid spectra of resp. the UV-vis part and the NIR (800nm) part of BA9 (cyan), BA6 (black) and BA3 (orange).

Comparison of BA3 and BA10 highlights the effects of size reduction on UCNP with similar composition (57% Yb, 1% Tm) but with diameter of 3.2 nm and 15 nm respectively (figure 12). Indeed, BA3 (3.2 nm) has almost no signal in these recording conditions while BA10 (15 nm) exhibit very intense emission. Such discrepancy (≈ 5 orders of magnitude) can have two origins for ultrasmall core samples:

- the very different amounts of active ions per particle: 2 orders of magnitude separate these two samples for both absorbing (Yb) and emitting (Tm) centers (table 7).
- the large change of surface to volume ratio (4.7 factor) that should lead to an increase of the surface quenching for ultrasmall nanoparticles compared to larger ones.

Noticeably, the ultrasmall core@shell of 5.7 nm (BA6) shows upconversion emissions which are almost as intense as the emission of the 7.5 nm core (BA9). The shell limits at least partially the energy loss via the surface, compared to the core. Despite its uncertain composition as mentioned in Chapter 2, it behaves here as a simple undoped barrier.

The cumulative effect of size and Yb composition is exemplified on the pair BA9 and BA10. The latter (larger and with a higher [Yb]) was found to be vastly more luminescent, with all the emission peaks at least 2 orders of magnitude higher in intensity. Surprisingly, except for the emission band at 450 nm and the noisy 500-630 nm area, it appears that these spectra are proportional by a factor 20 (figure 13), but no interpretation was found to this result.

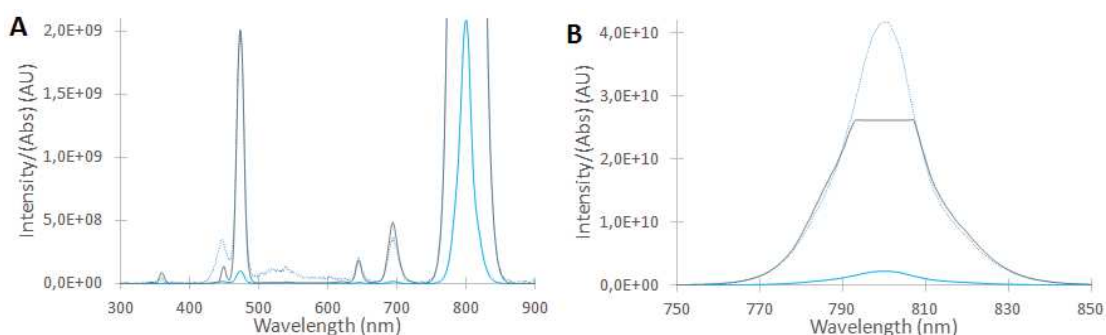


Figure 13. Comparison of small nanosphere luminescence normalized by their sensitizer content: with 20% (BA9, cyan) or 57% Yb (BA10, grey), under CW 976 nm laser excitation at 35.39 W cm^{-2} . Light blue dashed-line is the cyan curve multiplied by a 20 factor along the spectra. A) full spectra. B) Zoom-in on 802 nm peak.

It appears difficult to choose between normalization by the number of nanoparticles or by the total ytterbium content for batch-to-batch comparison.

Therefore, we turned our attention to ultrasmall nanoparticles, as they were the only group of samples whose size was not affected by the sensitizer content.

II.2.2.2 Size effect, evidence of a critical size

Monitoring of the ultrasmall core synthesis by cycling temperature can have a second utility: the regular sampling generates a convenient library to explore the effect of the size on the luminescence (figure 14). Despite very weak signals, two main bands can be detected at 800 nm and 475 nm. As exposed in the chapter II, luminescence of both emissions is slightly rising with the size from 2 to around 2.9 nm. Then a sharp increase of upconversion between 3 and 3.1 nm stresses is observed. Afterward, the luminescence intensity remains constant while the size increases from 3.1 to 3.4 nm. This abrupt change in the luminescence properties is reminiscent of the interpretation proposed by Gargas *et al.*⁹ as evoked in the introduction chapter. In their model, the surface quenching extends below the surface and significantly quenches all the emitters of this zone. Therefore, the luminescence is expected to rise only if the particle's diameter is big enough. For comparison purposes, the authors have defined a “volumic emission”, $I_{em}/V_{NP}(r)$, for each size of particles. Setting this ratio to unity for the large, “unquenched” nanoparticles ($r \approx 100$ nm) and considering that the observed emission for any NPs was coming from the fraction of the particle made of a similar “unquenched” material, led the authors to estimate the thickness of a “dark layer”: particles below the critical size of 3.4 nm diameter were declared to have negligible emission. Unfortunately, the range of sizes explored was above this critical size. In our study, the observed threshold at around 3 – 3.1 nm sits in the range of size of the very small crystals we have prepared. To our knowledge, this represents the first experimental study confirming the existence of such a critical size.

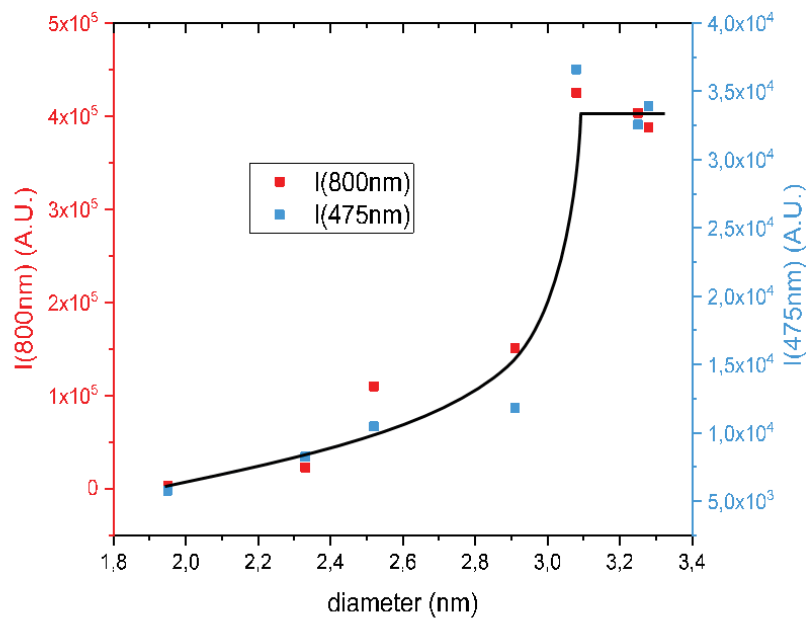


Figure 14. Evolution of photophysical properties along the size growth of ultrasmall cores. Luminescence intensity was measured on 5 mg/mL cyclohexane solution irradiated at 35.39 W cm⁻². Black curve is a guideline for the eye.

II.2.2.3 Doping effect on ultrasmall UCNP

Quantitative comparisons of the Yb effect were done for the brightest samples available: two core@shell of 5.7 nm, respectively with a core composition of 20% Yb (BA7) and 57% Yb (BA6) (figure 13). As the sizes (and shell) are identical, we can now clearly identify the effect of the Yb doping without any surface effect consideration.

Spectra of figure 15 reveals that a higher sensitizer content leads to a luminescence increase of each emission bands. This rise, by a factor of around 2.8, correlates nicely with the ratio of Yb content (57% vs 20%) and was therefore interpreted as a better light collecting efficiency (antenna effect).

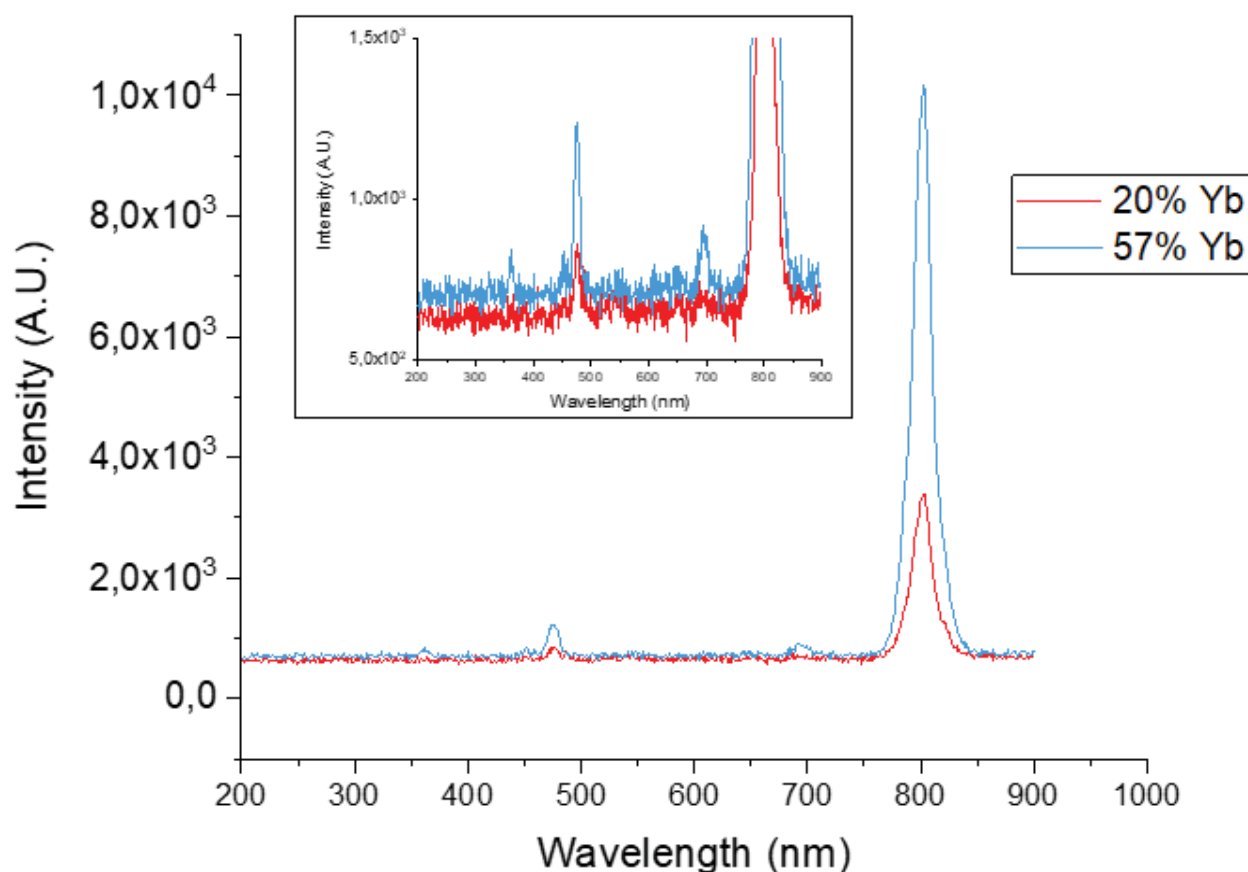


Figure 15. Comparison of ultrasmall core@shell with 20% (BA7) or 57% Yb (BA6) content in core, both prepared at 5 mg/mL in cyclohexane, under 976 nm CW laser at 35.39 W cm⁻².

II.2.2.4 Shell effect on small UCNP

As revealed by the picture (chapter II, figure 8), a huge enhancement of the photophysical properties after shell growth could be clearly seen by direct eye observation when Na(Gd-Yb)F₄ NP core of 10 nm (BA11) was compared to its core@shell analogue of 15 nm (BA12). The recording of a luminescence spectrum (figure 16) shows that this qualitative observation is a gain of around 3 orders of magnitude of upconversion efficiency.

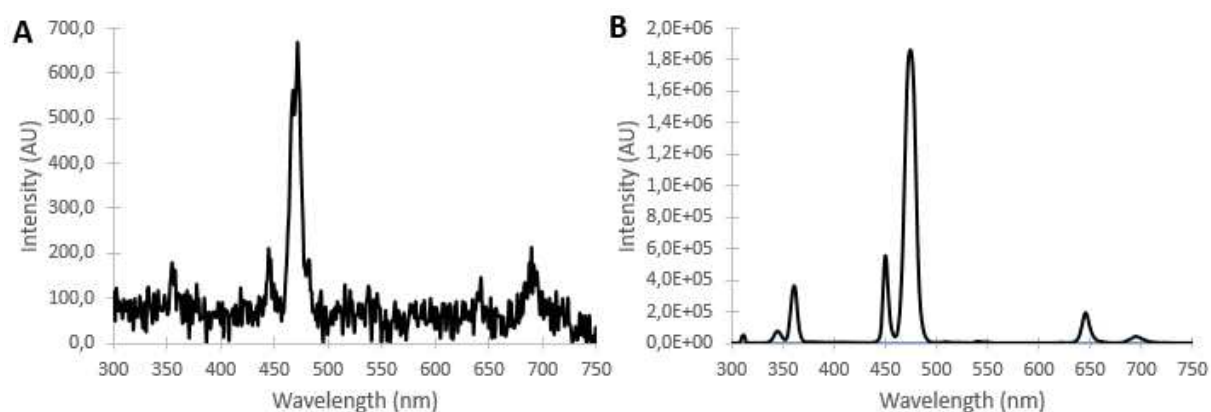


Figure 16. Comparison of core BA11 (A) and its corresponding core@shell BA12 (B) at 5 mg/mL in cyclohexane, under 976 nm CW laser at 22.66 W cm⁻².

II.2.3 Exploration of Tm-based UCNP's nonlinear behavior

The power-dependency of our synthesized UCNPs was assessed by recording the complete emission spectra at different power laser density. Then the maximum intensity of each peak was plotted against the laser intensity in a log-log lot as previously explained. In order to focus on the measurement of the slope we have privileged to optimize the signal intensity and reset the recording parameter (*inter alia* the detection slits) for each sample. This unfortunately precludes any comparison from sample to sample, beside the slopes of the log-log plots. The non-linear behavior of the UCNPs was explored according to two different criteria: the influence of the shell, and the impact of the laser source. While figure 17A is a simple overlap of power-dependent spectra, Fig 17B shows the typical representation of the nonlinear behavior.

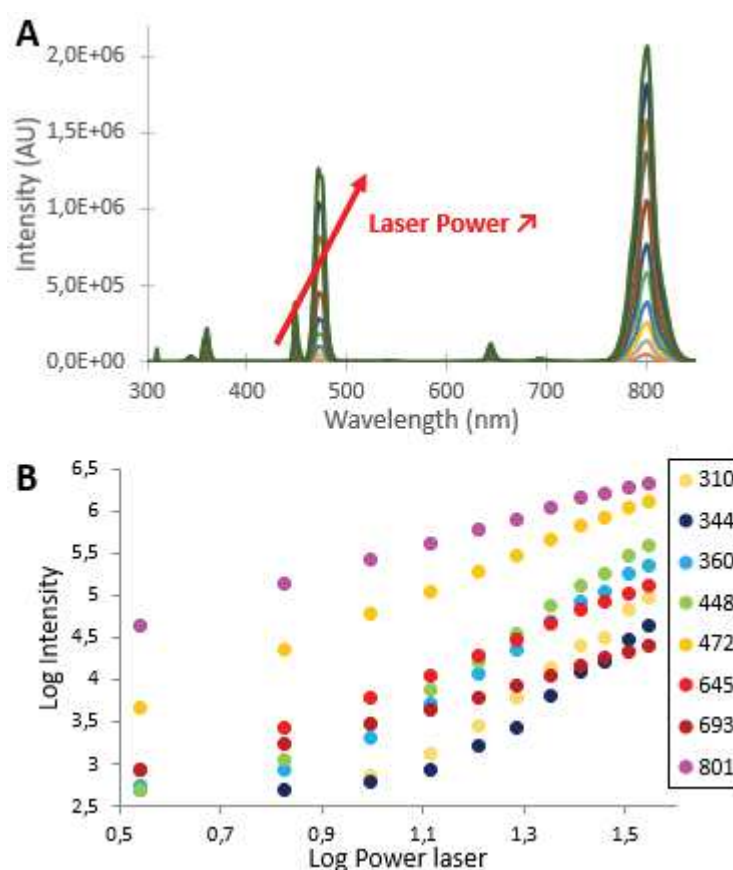


Figure 17. Power dependent optical properties of BA12 at 5 mg/mL in cyclohexane. A) Overlap of emission spectra. B) Log-log plot of the emission bands power-dependency.

Contrarily to the predicted behavior in the power range explored, the global shape is a slightly deformed straight line with curvature convexity varying according to the emission monitored:

while low energy, intense emission shows the expected behavior (negative convexity at high power, the high energy one shows the reverse (positive convexity at low power) especially for the poorly luminescent batches. Therefore, we decided to compare a linear fit to a 2nd order polynomial one (table 8).

Table 8. Comparison of linear and polynomial fit of the log-log plot of BA12. Emission bands with comparable behavior are labelled by color.

Peak (nm)	Linear fit		2 nd order polynom	
	Slope	R ²	Slope	R ²
802	1.69	0.9992	1.6-1.7	0.9993
697	1.5	0.9879	1.2-2.1	0.9996
647	2.24	0.9942	1.9-2.8	0.9988
475	2.48	0.9995	2.4-2.6	0.9996
452	3.25	0.9928	2.2-5.1	0.9972
362	3.85	0.9978	1.9-5.1	0.9949
346	4.35	0.9952	0.5-5.3	0.9932
312	4.5	0.9942	0.8-5.8	0.9953

Whichever the type of fit chosen, the apparent exponents can be classified in four groups: around 1.5 (green), 2.5 (orange) 3.2 (blue) and 4.3 (white). Clearly the values are not equal to the number of photons necessary to excite the emitting level. A simple calculation shows that on average half of the 980 nm photon energy is used for the upconversion process whatever the emission band which is considered (table 9).

Table 9. Energy balance of the upconversion process. Slope of linear fit was used for calculation. $E(\text{eV})$ was calculated from $E(\text{eV}) = \frac{1240}{\lambda}$, with λ expressed in nm.

λ (nm)	346	362	452	475	647	697	802	980 (exc)
E (eV)	3.57	3.43	2.74	2.61	1.91	1.78	1.54	1.27
E/E(980)	2.83	2.71	2.17	2.06	1.51	1.41	1.22	
slope * E	5.50	4.87	4.11	3.14	2.83	1.90	2.14	
%E(980)used	51%	56%	53%	66%	53%	74%	57%	

However, the observed grouping is in agreement with the Dieke diagram (figure 18) indicating the origin of the radiative transition: 802 and 697 nm are coming from $^3F_{2,3}$ level while 647 and 475 nm peaks result from radiative desexcitation of 1G_4 . The third one (452 nm and 362 nm), originate from 1D_2 excited state.

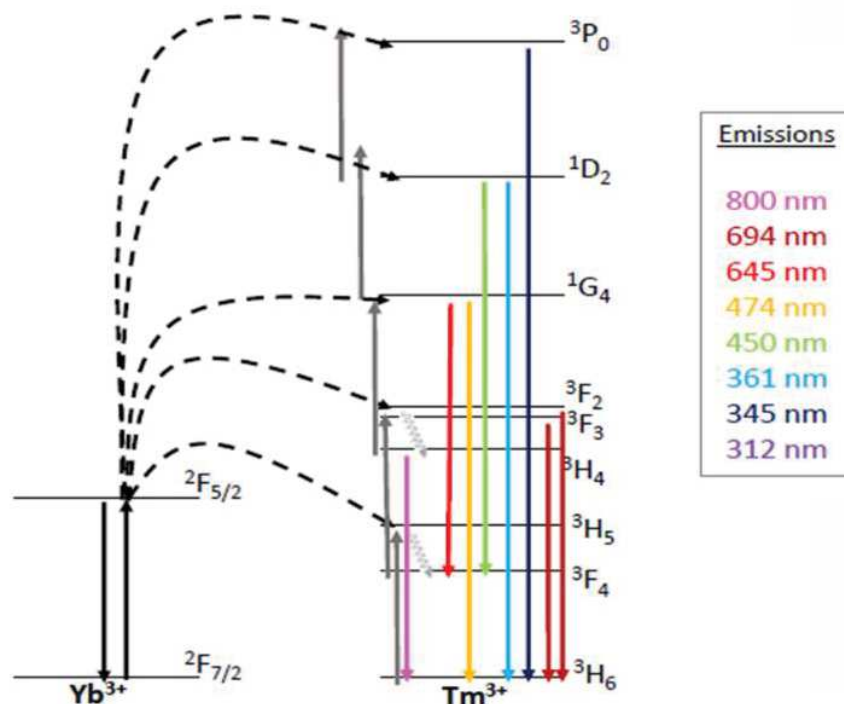


Figure 18. Dieke diagram completed with the representation of ETU scheme for a Tm-based UCNP. Dark grey arrows represent the equivalent of energy transfer from one single NIR photon (980 nm) absorption. “Oscillating” light grey arrows are non-radiative relaxations. Dash line arrows are energy transfer between sensitizer and different energy level of thulium emitter.

From this initial observation we compared the log-log plot of various types of NPs according two different criteria: the influence of the shell, and the impact of the laser source. For clarity purpose, the behavior of only the 802 and 475 nm emission bands will be presented.

II.2.3.1 Shell effect

Two batches prepared following *premix* way and conventional heating were used for core and core@shell comparison (figure 19).

Remarkably, for the two samples, the linear parts of the 475 nm have quasi identical slopes, as highlighted by the blue guideline (the situation is almost the same for the 800 nm one.)

Thus, UCNP's non-linear behavior seems not to be affected by the surface, as the exponents are conserved. The efficiency of the surface quenching can be responsible for the delayed rise in the 475 emission.

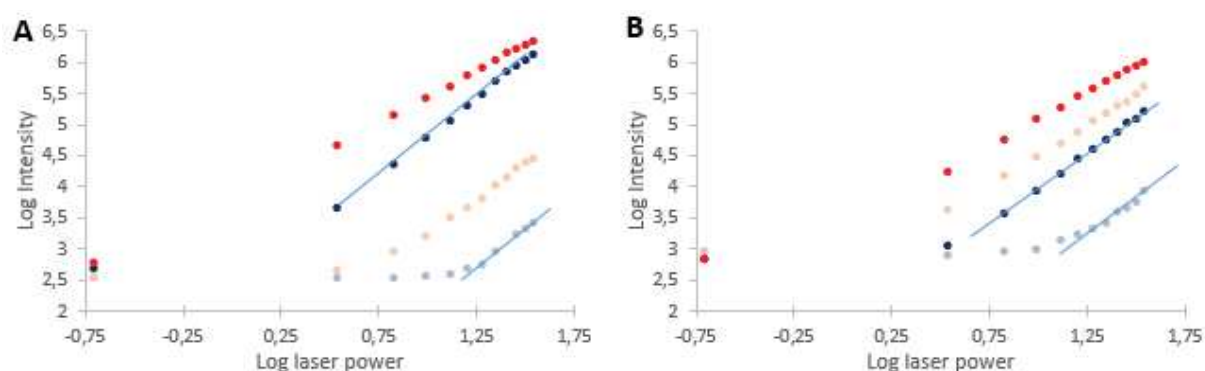


Figure 19. Comparison of two batches of core and their corresponding core@shell Na(Gd-Yb)F₄:Tm@NaYF₄ prepared following *premix* way and conventional heating. Light and dark red are respectively 802 nm peak of core and core@shell, light blue and dark blue are the equivalent for 475 nm emission band. A) core BA11 and its corresponding core@shell BA12. B) core BA13 and its corresponding core@shell BA14. Blue lines are guideline for the eye, showing a similar slope on 475 nm emission peak.

II.2.3.2 Excitation source effect

We then addressed the question of the excitation source (figure 20). We compared the use of two lasers: a monomode and a multimode one. Monomode lasers are more focused than multimode ones, therefore enabling higher energy densities favorable to non-linear phenomena. The monomode laser beam employed (ThorLab 976 nm, 1 W) delivers a gaussian beam ($r(1/e)^2=0.07$ mm) narrower than the multimode one (MDL-H 980 nm, Acal BFi/Changchun Industry, 3-5 W, beam radius: 0.175 mm).

Luminescence spectra were measured on one batch of core (BA15) and its corresponding core@shell BA16 (figure 20).

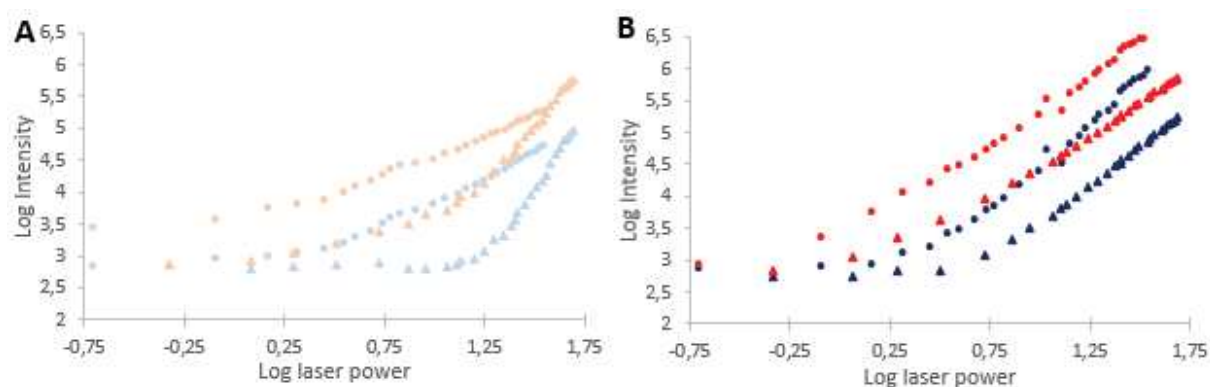


Figure 20. Comparison of the impact of the excitation source on log-log plot. A) core BA15 and B) Core@shell BA16. Red and blue colors are respectively for the 802 nm and 475 nm emission bands. Experimental points obtained with the multimode laser are represented by circles while triangles are from the monomode one.

In the case of cores (figure 20A), the observed behavior is markedly different. Indeed, UCNP emissions under multimode irradiation show a steady and weak increase. On the other hand, the use of a monomode excitation leads to a delayed sharp exponent. This unexpected result is of importance, as it can explain the problem of reproducibility measurement among laboratories. These differences are considerably smoothed for the core@shell samples (figure 20B): no significant differences were observed and all emission tends to rise steadily as for the core NPs under multimode excitation. The slight difference in absolute intensities between multimode (35.39 W cm^{-2} , discs) and monomode (58 W cm^{-2} , triangles) lasers was attributed to the differences of the beams' diameters. As our monomode laser has a smaller beam section than the multimode one, it deposits more energy than the multimode one but on a lower amount of NP.

The impact of the type of excitation laser can be used to alter the emission spectrum: the power of the monomode laser affects the overall luminescence intensity, but also the emission bands ratio (fig 21), in particular between the two “blue emission” bands (450 and 475 nm) which are of interest for our application (see chapter IV). At low power, the 475 nm is the main emission,

while at higher power, the 450nm one becomes predominant thanks to a higher exponent. From this highly sensitivity, emission band ratio between 450 and 475 can be manipulated simply by laser power tuning.

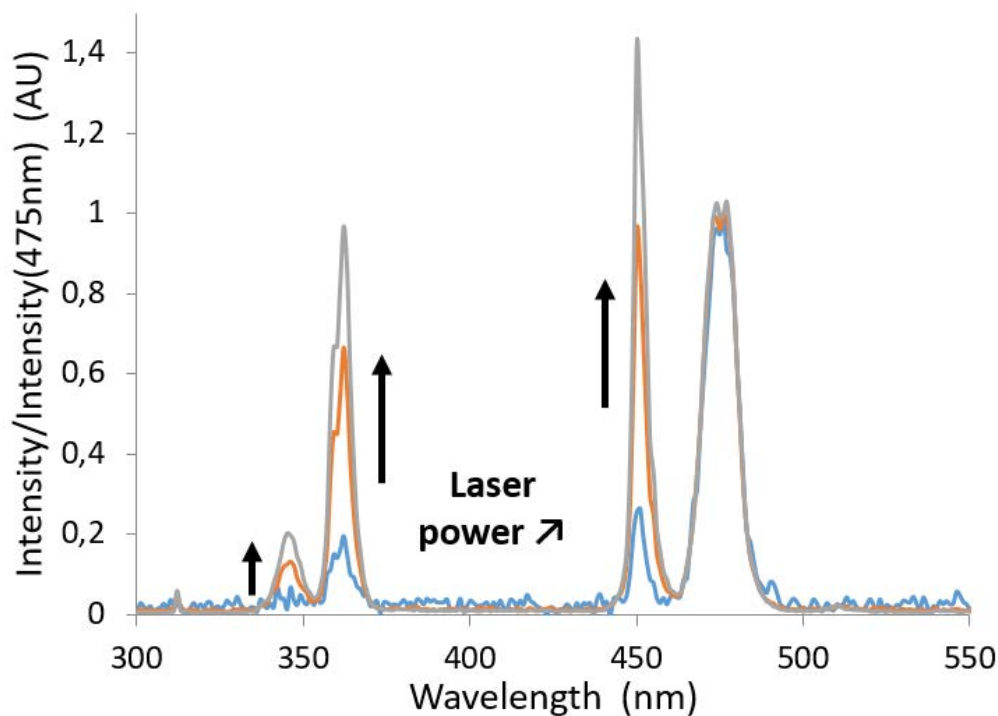


Figure 21. Comparison of the emission spectra of BA15 under CW 976 nm monomode laser at different laser powers, respectively 28.19 (blue); 40.35 (orange); and 50.02 W cm⁻² (grey). Intensity is normalized by the intensity at 475 nm of each sample.

The present data show that even one sample can give different signals depending on the CW laser. Thus, it opens questions of standardization of the photophysical measurements. A solution should be the use of a well-defined UCNP standard to standardize the analysis.

II.2.3.3 Conclusion on log-log plot

Gathering the measurement of log-log plots among the different samples helped us to distinguish some particular behaviors. Indeed, 3 main groups of peaks stand out, with similar exponent behavior (shape and slope factor):

- 450 nm and 361 nm (and 344 nm)
- 474 nm and 645 nm
- 800 nm and 694 nm

By referring to the Dieke diagram, we can see that emission bands of similar exponent come from the same excited state (figure 22).

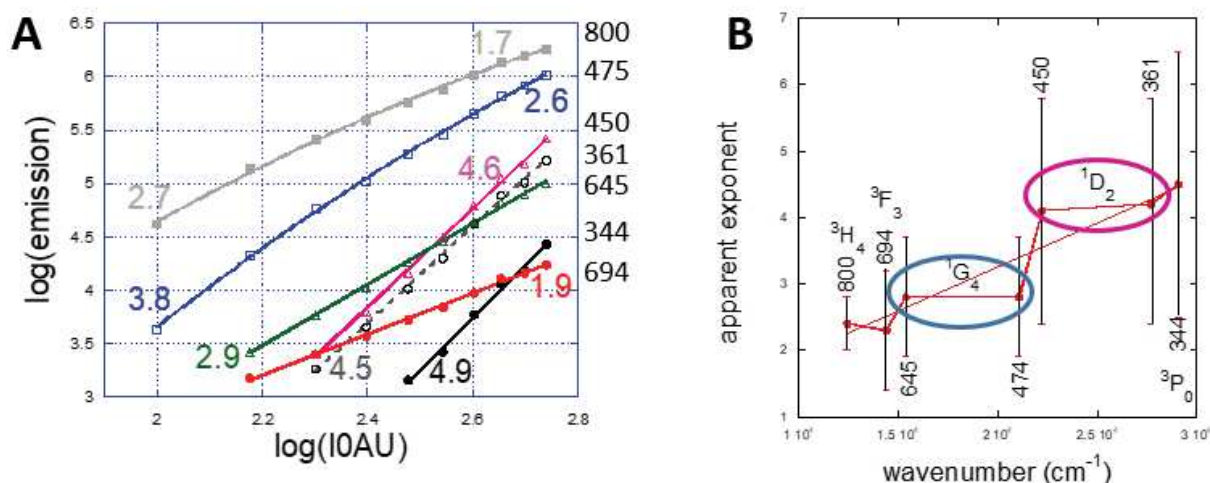


Figure 22. A: Comparison of the average exponents for the samples above described in the chapter. B: Correlation between exponent and excited state level energy.

Eventually, samples could be classified as described below (table 10):

Table 10. Classification of UCNPs batch exponents, as a function of their composition

	%Yb	%Tm	Matrix core	shell	800 nm exponent	475 nm exponent
BA11	57.38	1.02	Gd	-	2.25	2.30
BA15	57.35	0.99	Gd	-	2.25	2.30
BA12	57.38	1.02	Gd	100%Y	2.3	3.15
BA14	57.28	1.18	Gd	100%Y	2.3	3.15
BA6	57	1	Gd	100%Gd	2.32	2.80
BA17	57	1	Gd	100%Gd	2.32	2.80
BA16	57.35	0.99	Gd	100%Gd	2.40	2.70
BA7	20	1	Gd	100%Gd	2.85	

Independently of their size, sub-10 nm cores have similar behavior. Core@shell of all sizes are rather similar: all of them have an exponent of 2.3-2.4 for the NIR emission. However, the nature of the shell (Y or Gd) has an impact on the 475 nm: lower slope is obtained with Gd. This last point is in agreement with NaYF₄ known as a more efficient shielding layer.¹⁰ Eventually the restriction of the log-log plot to only the linear domain as commonly seen in the literature can be questioned. Comparison with realistic numerical models might be a solution.

III Quantitative photophysics of the ultrasmall UCNPs

In the up-coming section we focus on the exploration of the photophysics of the very small nanoparticles prepared in chapter 2 and already presented in the “Absorption” section: BA1, BA2, BA4, BA5, BA8, whose chemical parameters were presented in Table 1. As explained previously, the modified fluorimeter of IMRCP is insufficient to analyze quantitatively extremely weak signals. We therefore moved to the dedicated equipment available at BAM and LASIR as introduced earlier (section II.2.1). To record the data, a “50 mg/mL” concentration was used for all the measurements. However, one has to remember that some of the particles tend to settle down.

III.1 Identity card of ultrasmall UCNP nanolamp

III.1.1 Steady state

Emission spectra

These spectra were collected at the BAM in Berlin. As expected, and despite potential sedimentation, cores-shell samples were found to be qualitatively brighter than the cores only. An example is shown in figure 23, comparing the 57% core (BA2) and Core-shell (BA5) sample. The important point is that because of higher laser energy density (124.4 W cm^{-2} instead of 58.4 W cm^{-2} or 30 W cm^{-2} at IMRCP), all lines can be observed even for weakly luminescent samples.

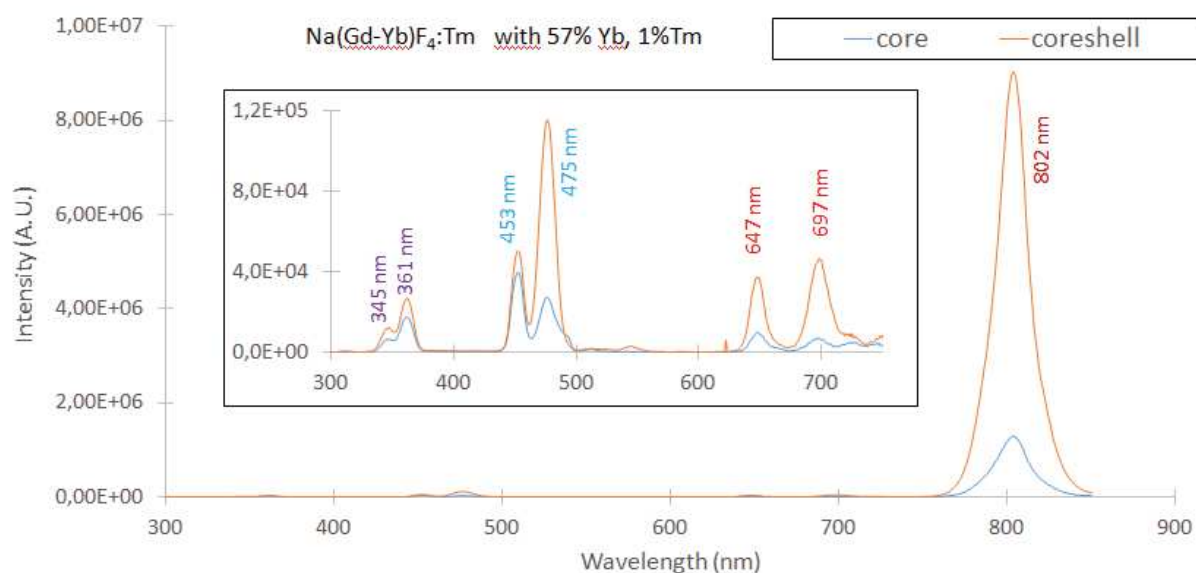


Figure 23. Comparative emission spectra of BA2 and BA5 under 976 nm CW laser at 124.4 W cm^{-2} .

In the following, sedimentation issue will not affect the observed results. If necessary, ytterbium absorption will be used to calibrate the suspension as in sections II.1.1 and II.2.2.1.

Energy breakdown analysis

Area under the peaks of emission spectra were integrated and multiplied by the energy (in eV) of the corresponding emission band wavelength to show the energetic proportion of each emission band, as summarized in the table 11.

Table 11. Energy breakdown of ultrasmall UCNP under 976 nm CW laser at 124.4 W cm⁻².

	BA1		BA2		BA8		BA4		BA5	
	area	%eV	area	%eV	area	%eV	area	%eV	area	%eV
347	2,38E-03	0,50%	1,97E-03	0,42%	0	0,00%	7,14E-04	0,16%	5,60E-04	0,13%
362	4,76E-03	0,96%	6,31E-03	1,31%	2,30E-04	0,05%	1,12E-03	0,24%	1,42E-03	0,31%
453	1,38E-02	2,22%	1,37E-02	2,27%	5,47E-04	0,10%	2,33E-03	0,40%	2,45E-03	0,42%
476	2,75E-02	4,22%	1,35E-02	2,13%	1,79E-03	0,30%	1,15E-02	1,86%	7,46E-03	1,23%
511	4,84E-04	0,07%	1,91E-04	0,03%	0	0,00%	1,05E-05	0,00%	0	0,00%
648	8,06E-03	0,91%	4,08E-03	0,47%	6,54E-04	0,08%	3,53E-03	0,42%	2,22E-03	0,27%
697	1,89E-03	0,20%	2,13E-03	0,23%	2,55E-03	0,29%	6,54E-03	0,73%	3,02E-03	0,34%
804	1	90,91%	1	93,14%	1	99,18%	1	96,19%	1	97,31%

The Branching Ratio (BR) can be calculated from the percentage of area under the peaks of emission coming from the same excited state, as evoked in the introduction chapter. In the present case, two BR could be compared among samples: BR(¹G₄) and BR(¹D₂) as shown in table 12.

Table 12. Comparative Branching Ratio (BR) extracted from emission spectra under 976 nm CW laser at 124.4 W cm⁻².

	BR(¹ G ₄)		BR(¹ D ₂)	
	%(476 nm)	%(648 nm)	%(362 nm)	%(453 nm)
BA1	77.3	22.7	25.7	74.3
BA2	76.8	23.2	31.5	68.5
BA8	73.2	26.8	29.6	70.4
BA4	76.4	23.6	32.5	67.5
BA5	77.0	23.0	36.7	63.3

Among the samples studied, it appears that globally the Branching Ratio evolves in the same way: for each excited level, there is no inversion of the balance between the two emissions i.e. 476 nm is the main radiative relaxation path of ¹G₄ (73-78%) while it is 453 nm for ¹D₂ (63-75%).

III.1.2 Time-resolved emission

III.1.2.1 Design of experiments

Two different set-ups were tested for the measurements of the time-dependent luminescence data. Our aim was to check the influence of the pulse shape and intensity on the dynamics of each emission lines.

Classically, time-dependent emissions monitor the first-order disappearance of an excited state, thus are characterized by lifetimes. Only relative amplitudes are considered as pertinent parameters, so the data acquisition favors the signal-to-noise ratio, typically by fixing a limited number of counts as a stop condition. The consequence is that duration of a measurement is signal-dependent: bright emissions are analyzed within 5 min while weak ones can take hours. Subsequent data treatment consists generally in fitting the experimental decays with a multi-exponential function.¹¹

From the Dieke diagram it is clear that the energy redistribution dynamics, presenting several bimolecular processes, will give rise to luminescence kinetics that should be sensitive to acquisition conditions, and should differ for each studied line. Therefore, the validity of the standard approach can be questioned. In particular, it becomes important to collect all the lines' traces under identical recording conditions.

During my stay at the BAM, I explored the two different approaches:

- measurements with a constant amount of 4k counts,
- or with an identical acquisition time (15 min).

Noticeably, the second type of recording, which was found to be very uncommon in the literature, was motivated by the desire to implement and feed a kinetic modeling of the upconversion phenomenon.

Since the Yb plays the role of antenna, we also paid special attention to the recording of a signal originating from its excited state.¹² Ytterbium has broad emission due to the splitting of the Stark levels, peaking at 1030nm, beyond the detection limit of the fluorimeter, However, this emission tails up to 940nm. Despite close vicinity with the excitation laser (980 nm) and the large slits aperture (10 nm), meaningful signal could be collected at this wavelength to monitor this excited state.

III.1.2.2 Lifetimes measurement with BAM setup

Lifetime acquisition in “standard conditions”: example of BA5

At first, decays were acquired by fixing a number of 4000 counts as the stop-limit of the lifetime measurements. As mentioned previously, the very large intensity range between strong

and weak emission transpires into the acquisition times. Thus, for a laser power of 115.5 W cm^{-2} , the recording of the 940 nm decay took 2 min, while 15 min were required for 476 nm emission. More spectacular was the low emissive 345 nm band, requiring more than 12 hours! Similarly, diminishing the excitation power led to an increase of the acquisition time. Thus, for a laser power of 76.4 W cm^{-2} , the 476 nm decay required 45 min.

With such conditions, all the emissions reach the same maximal intensity in arbitrary units and the decay traces are then subjected to multiexponential fit. In our case, data treatment routine was performed using a dedicated biexponential-based software delivered from the fluorometer manufacturing company.

Typical result of decays obtained are gathered in figure 24.

As evidence by the partial mismatch between experimental points and fit curve, coupled to the poor quality of the residuals, this multiexponential approach does not seem ideal.

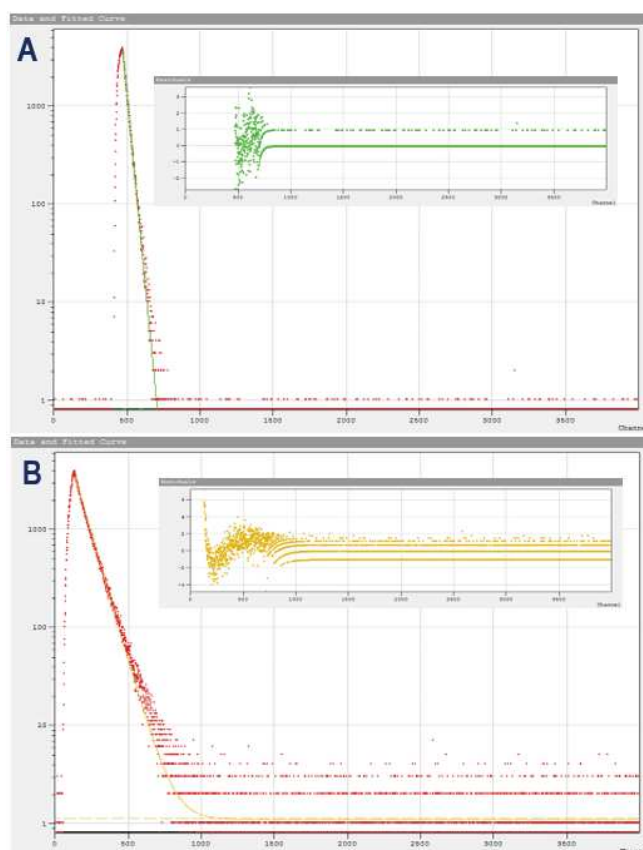


Figure 24. Typical fit routine of decay at BAM. Insets are residuals obtained with the fit. Decays represented in the figure were obtained under 976 nm CW laser at 115.5 W cm^{-2} . A) 940 nm decay. B) 475 nm decay.

By applying this measurement routine, several lifetimes were measured. They are gathered in table 13. Surprisingly, except for 940 nm (Yb), core BA1 and BA2 seem to have longer lifetimes than core@shell BA5. From this first experimental database supposedly obtained in “ideal conditions” with the 4000 counts approach, we started then to modify the acquisition parameters in order to progress towards a description of the kinetic network.

Table 13. Summary of lifetimes (in μs) obtained in the “4000 counts” approach

	BA1	BA2	BA5
940 nm	11.7	7.3	13.9
802 nm	1680 (80%) & 165 (20%)	727 (85%) & 97 (15%)	424 (13%) & 98 (87%)
475 nm	934	617	515 (69%) & 290 (31%)
452 nm	681	321	
362 nm	791		216

Lifetime acquisition in “kinetic conditions”: example of BA5

In order to be able to compare simultaneously the instantaneous radiative relaxation of all the states involved, the amplitude of all emissions had to be recorded under similar conditions. This precluded the previous approach (i.e. “the 4k counts” in BAM routine).

Consequently, we arbitrarily fixed the acquisition time at 15 min. In order to accumulate enough signal, measurements were performed with different temporal step (i.e. the number of channels): small step (1 μs) was required for sharp decays such as 940 nm, while acquisition was done with 4 μs for low emissive bands such as 452 and 362 nm that have longer lifetimes. These data were then fitted using a multiexponential function, providing lifetimes.

The comparison of the absolute amplitudes required the same time scale. Therefore, the binning was converted to a 4 μs step, common to all the measurements. Then, these rescaled data were corrected by the specific wavelength-dependent detection calibration curve of the PM. Therefore, the comparison of the amplitudes between the different emission bands and sample was now quantitative. BA5 is presented as an illustration in figure 25.

The 940 nm emission was found to be very intense and followed remarkably the laser profile (980nm). This was somewhat expected as this emission is the ytterbium's one. On the opposite, all the other lines, originating from thulium, presented a steady rise during the excitation pulse. This is a characteristic of the ETU process. In terms of relative intensities, the 802 nm was found to be very intense and 476 nm and the two red emissions (647 and 697nm) as well. However, 452 nm and UV bands are weak and will be challenging to observe while decreasing laser power.

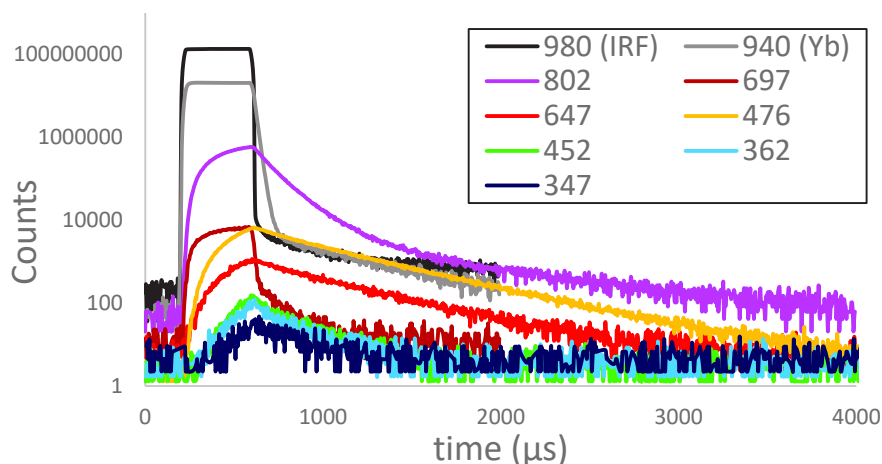


Figure 25. Emission bands decays recorded under 976 nm CW laser at 124.4 W cm^{-2} .

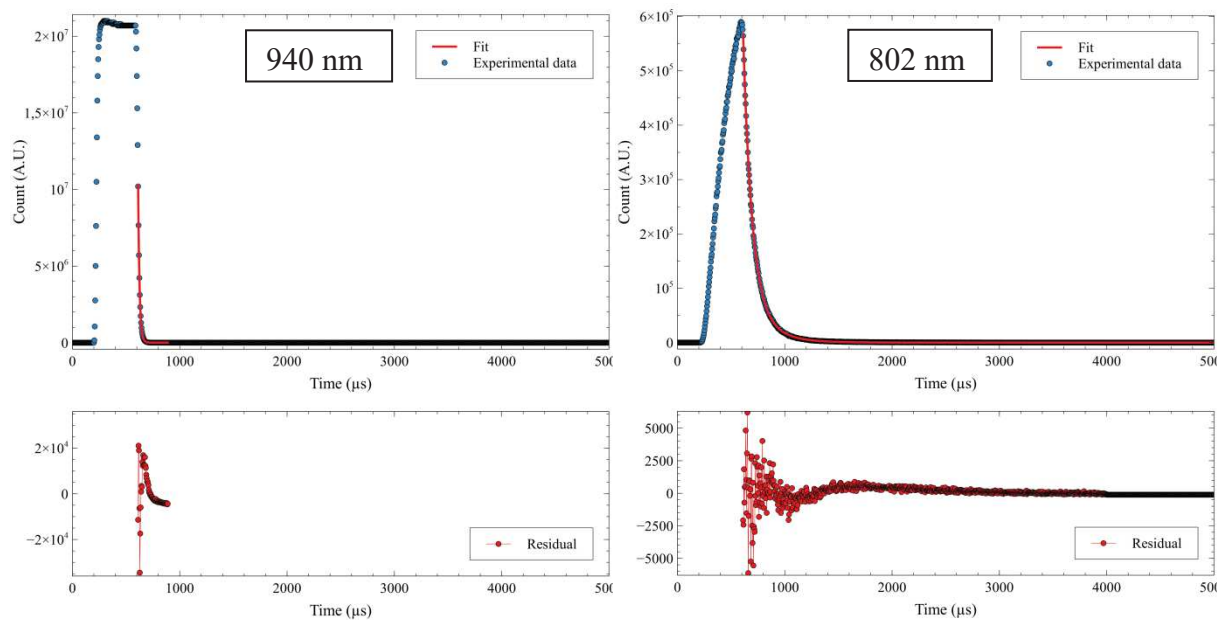
Data treatment routine: example of BA5

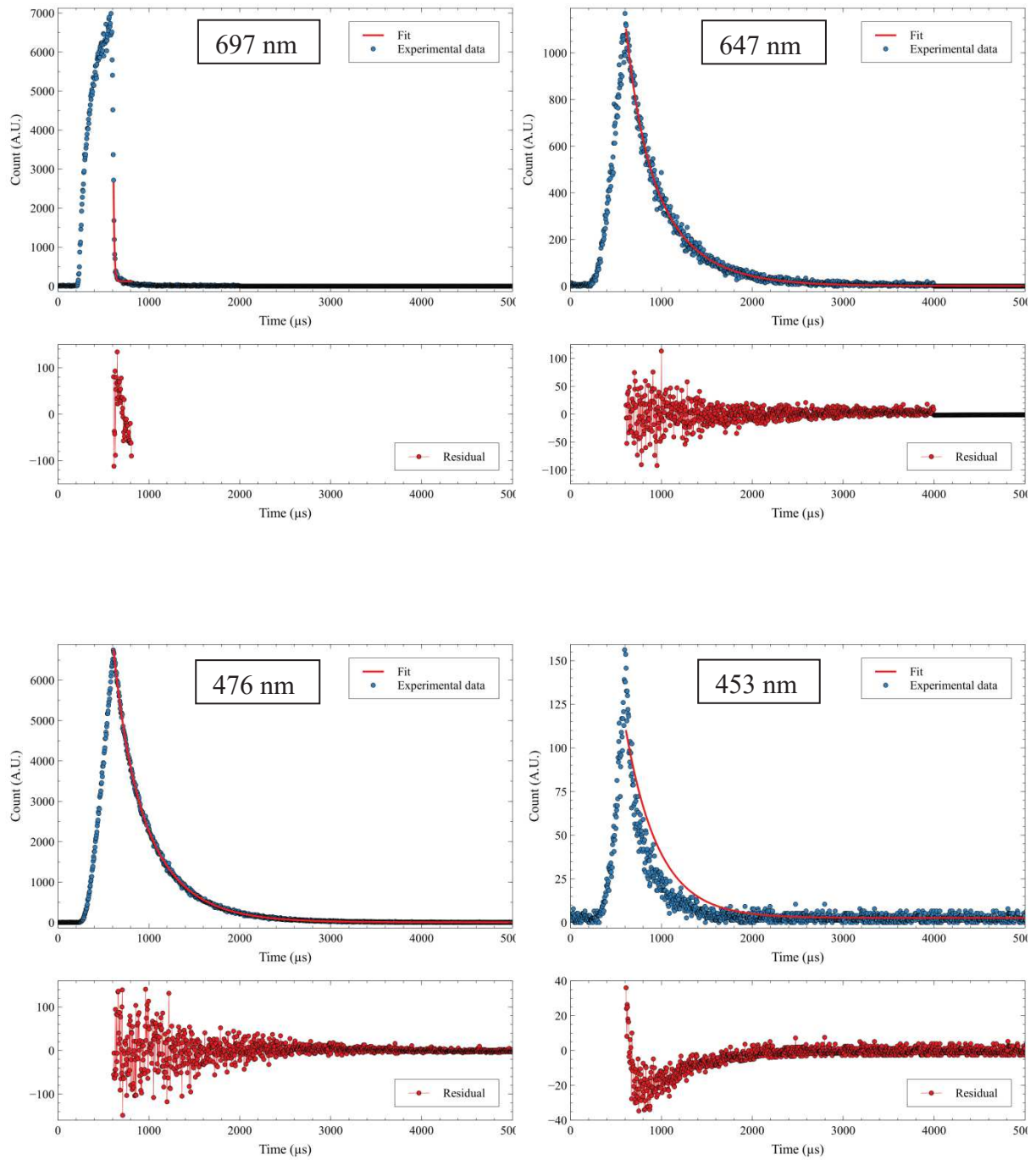
Fit of the decay traces were made on Origin software with mono or biexponential model. Due to overlap of the large laser pulse (IRF, $400 \mu\text{s}$ pulse) with the rise, the latter could not be exploited. Results of multiexponential decaying functions are gathered in table 14, residuals of the fits are in figure 26. As expected, regarding to their shape, most of the decays could be fitted by biexponential function. The main difficulty for the fit comes from the noisy signal obtained with such a short time of experiment (900 s). On unmodified raw data, the lack of signal cannot

be fitted by biexponential function despite the clear multiexponential observable. Thus, the rebinning normalization for quantitative comparison of the shape was crucial for the treatment. This artificially increased the signal-to-noise ratio, leading thus to a better quality of the fits. However, figure 26 shows that this treatment is still not optimal and.

Table 14. Results of linear fits by mono- or bi-exponential decaying function for BA5 (lifetime, error bar, and R^2).

$\lambda(\text{nm})$	$\tau_1 (\mu\text{s})$	$\tau_2 (\mu\text{s})$	R^2
940	13.54 ± 0.02	-	0.99998
802	81.1 ± 0.3	207 ± 3	0.99988
697	9.8 ± 0.4	-	0.98445
647	178 ± 12	486 ± 10	0.99504
476	163 ± 4	449 ± 3	0.99957
453	16.6 ± 1	363 ± 8	0.79974
362	48 ± 5	264 ± 12	0.9054
347	32 ± 32	246 ± 20	0.51313





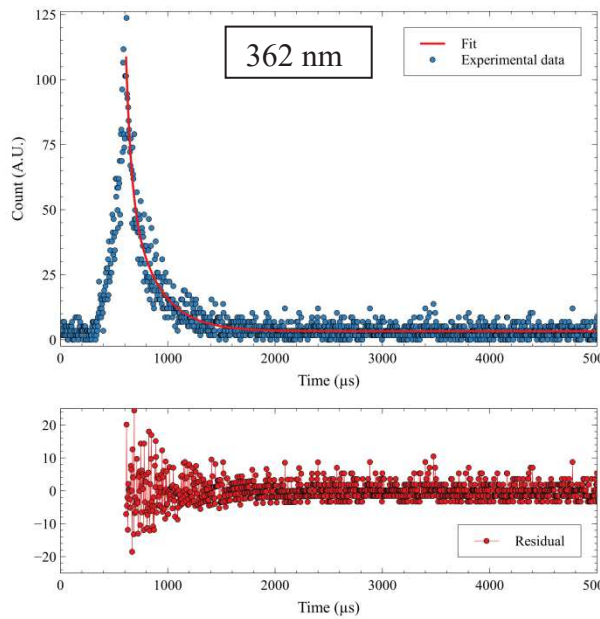


Figure 26. Experimental fit by multiexponential fit presented in table 14 (for BA5 at 124.4 W cm⁻²). Fit were obtained from biexponential decay function except for 940 nm and 697 nm. For these last two, the fit did not converge as a biexponential function but only with a monoexponential one. Blue points are experimental data, red ones are obtained by fit (fit curve and residual)

Comparison of ultrasmall samples at power constant

Once adopted a routine of measurement and data treatment, we could then start to compare ultrasmall batches at the same laser power (figure 27).

Generally, the same behavior in term of amplitudes order can be found in each batch. 940 nm is higher than 802 nm. Then are following in order of decreasing amplitude: 476 nm > 697 nm and 647 nm > 452 nm > UV.

However, two unexpected facts can be observed:

- Core seems to have longer lifetimes, especially for 20% Yb content
- Batches at 20% Yb show unexpected negative convexity, in particular on core 20% Yb

We were unable to explain these two points.

Measured lifetimes are gathered in the table 16.

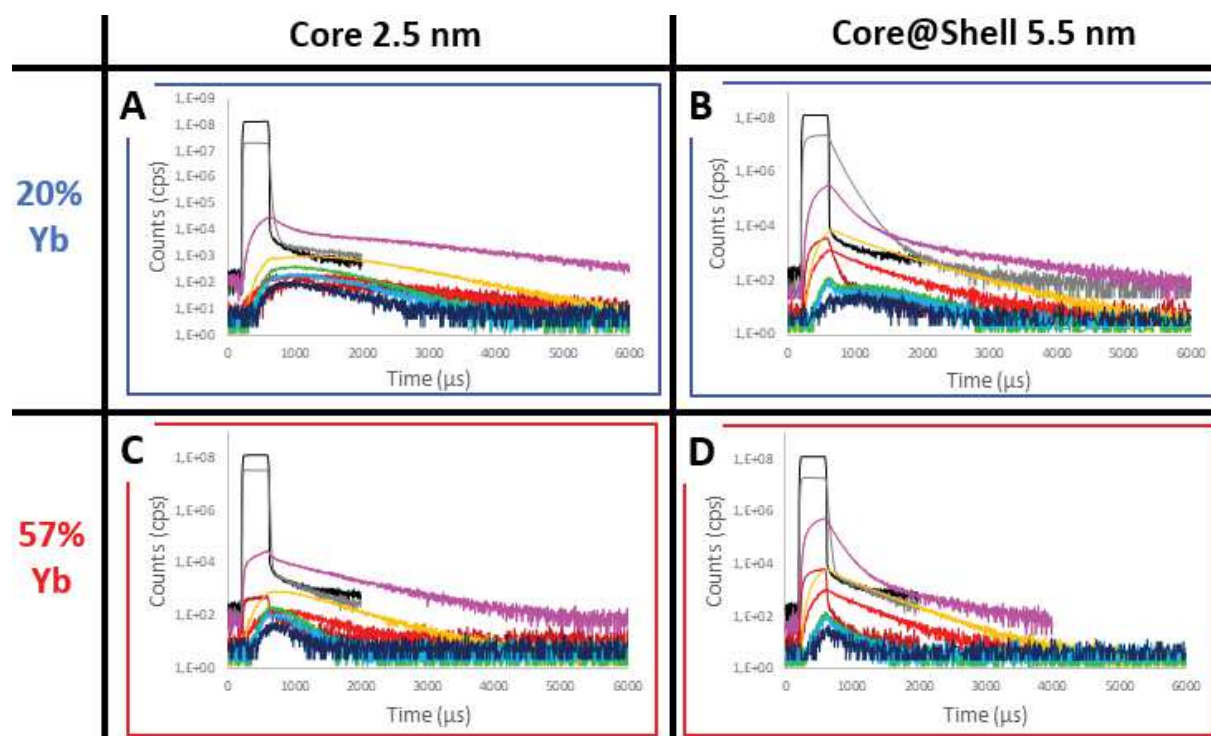


Figure 27. Comparison of luminescence decays for ultrasmall core and core@shell at both Yb composition (20% or 57% Yb) recorded over 15min. A) core 2.4 nm with 20%Yb. B) core 2.8 nm with 57%Yb. C) core@shell 5.5 nm with 20%Yb. D) core@shell 5.5 nm with 57%Yb. Black curve is IRF (laser 976 nm at 124.4 W cm^{-2}). Other curves are luminescence decays of Ytterbium at 940 nm (grey), and decays of the respective Tm emissions: 802 nm (pink), 697 nm (dark red), 647 nm (red), 476 nm (yellow), 452 nm (green), 362 nm (light blue), and 347 nm (dark blue).

Table 16. Comparison of ultrasmall UCNPs emission decays (in μs)

$\lambda(\text{nm})$	BA1	BA2	BA4	BA5	BA8
940	No convergence	No convergence	81	13.54	No convergence
802	No convergence	No convergence	151 & 1368	81 & 207	No convergence
697	177 & 1975	56	149 & 26	10	138 & 376
647	3189	299	309 & 742	178 & 486	36
476	1354	796	444 & 1300	163 & 449	138 & 742
453	1251	801	999	17 & 363	165 & 507
362	1117	362	1050	48 & 264	69 & 331

Noticeably, the shape of some emissions' decays revealed strong similarities reflected in the results of the fit. The same group behavior as already seen in stationary state experiments (in section II.2.3.3) was confirmed:

-476 and 697 nm

-454 and 362 nm

-347 nm emission behaves quite similarly to the 454-362 nm group.

- Concerning the Yb emission at 940 nm, decays are shorter
 - for core than core@shell,
 - for 57% Yb than 20%

Increasing the size of the core (BA8 vs. BA1) also leads to longer lifetime.

- Concerning the Tm emission:
 - lifetimes are longer with 20% Yb content than with 57%
 - cores have longer lifetimes than core@shell,

One exception to this last conclusion concerns the batch BA2 (Core, 57% Yb) for which the 802 nm emission lifetime is 2.5 larger than for a 20% Yb particle of similar size (batch BA1).

The effect of the ytterbium content on the thulium emissions can be rationalized in terms of “concentration quenching” (section III-1-2): the more ytterbium, the faster the transfer to the surface, thus the more energy is dissipated through this process. Back transfers from Tm excited states to ytterbium are also more probable.

The most intriguing result is the effect of the shell on the Tm-emissions compared to core nanoparticles. Indeed, addition of a shell was expected to suppress the surface quenching and an increase of the lifetime was foreseen. The exact opposite was observed. We have not found any explanation to this counter-intuitive result.

Power-dependent behavior: example of BA5

As an illustration, only results obtained for BA5 batch will be presented in figure 28.

The objective was now to evaluate the sensitivity of the recorded lifetimes to the excitation power $\tau(P_0)$.

Power-dependent measurements were difficult to perform due to the very large difference in noise between all the emission bands. Data could be accumulated mainly on 940, 802 and 476 nm. The other emissions gave noisy signal at lower laser power.

For one emission wavelength, decays were found to have similar features over the 3 – 124 W cm^{-2} power range explored, implying lifetimes to be power-independent. Similar results were found for all the other batches (cf experimental section).

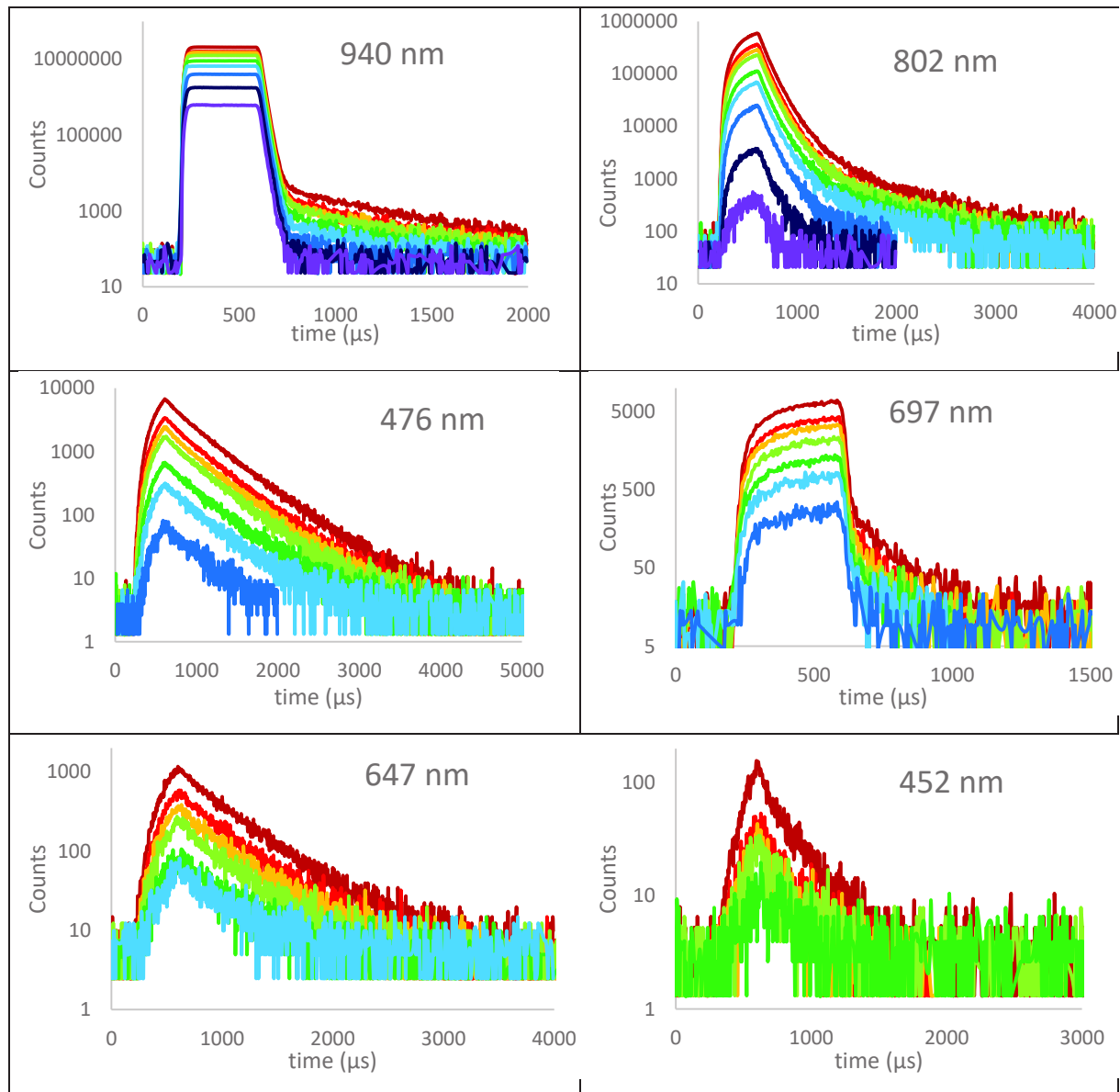


Figure 28. Power-dependent measurements of BA5. Power laser is decreasing following rainbow colors from dark red to purple (respectively 124.4; 98.53; 83.09; 64.91; 43.55; 33.90; 22.64; 10.02 and 3.33 W cm⁻²).

As the data have been acquired in a quantitative way, we can also use them to explore the non-linear behavior. Hypothesizing that at the end of the pulse the concentrations have reached their steady-state values, the emissions' intensities at this very moment are stacked as for stationary

state experiments. Plotting these intensities as a function of the power in a log-log plot give a similar graph as in section II.2.3 (figure 29).

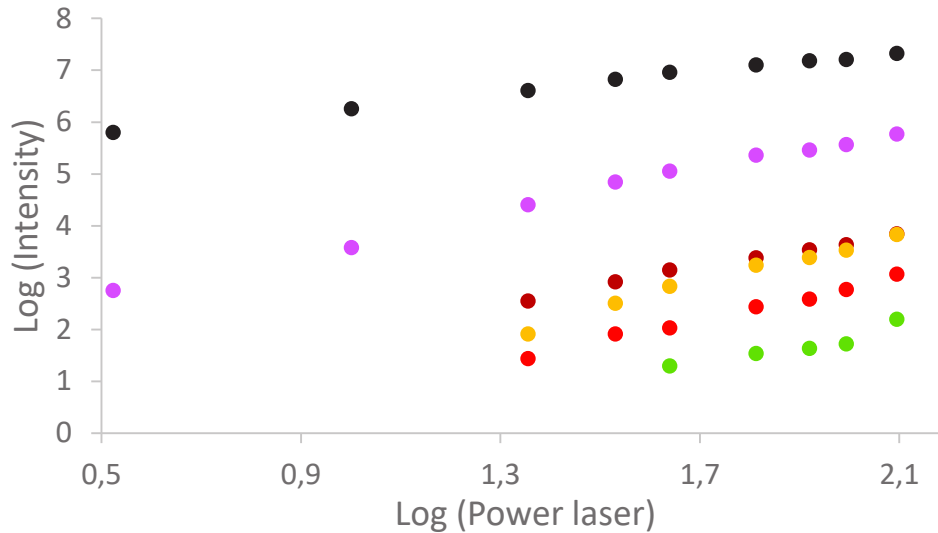


Figure 29. Typical log-log plot extracted from power-dependent lifetimes of BA5. The different emission band detectable are overlapped: 940 nm (black), 802 nm (pink), 697 nm (dark red), 647 nm (light red), 476 nm (yellow) and 452 nm (green).

Among the five samples, experimental points seem to be well aligned, without significant curvature. Hence, the exponents were directly obtained from the slope of linear fits. Results are gathered in the following table 17:

Table 17. Exponent obtained from power-dependent lifetimes

	BA2		BA1		BA5		BA4		BA8	
	slope	R ²	slope	R ²	slope	R ²	slope	R ²	slope	R ²
940	1.71	0.9037	1.24	0.9612	0.98	0.9961	0.96	0.9995	0.61	0.9538
802	2.33	0.9267	2.48	0.9867	1.99	0.9932	1.90	0.9999	1.44	0.9945
697					1.67	0.9912	1.91	0.9971	1.14	0.9845
647			2.29	1	2.09	0.9914	2.44	0.9786	1.33	0.9818
476			2.34	0.9765	2.47	0.9853	2.67	0.9999	1.94	0.9987
450	4.32	0.8912			1.03	0.9981	2.66	0.993	2.26	0.9913

As expected, the analysis of the exponents revealed the grouping of some emission lines: 802 nm with 607 nm (green boxes) and 647 nm with 476 nm lines (orange boxes). More interestingly, the slopes were also consistent with the previously recorded one. The observed trends are: for the 802 nm and 607 nm lines, a slope slightly lower than 2 instead of *ca* 1.5, section II-2-3; for the 647 nm and 476 nm lines, a slope about of 2.5 instead of *ca* 2.3, section II-2-3. Surprisingly, the BA8 batch consisting of larger core particles was found to not follow this classification: all exponents being lower than for the other batches. No explanation was found for this feature.

Conclusion on BAM setup

This first series of lifetimes measurement was successful. We could record data in a kinetic mode for a large amount of emission bands and at different power on samples varying in composition, size and architecture.

Thus, for the batches under scrutiny, the conclusions are:

- apparent lifetimes seemed grouped in a similar way as the exponents in the steady state measurements.
- lifetimes are longer for the standard 20% Yb composition than for the 57% one.
- core@shell NPs seem to have as yet unexplained shorter lifetime than the corresponding cores.

The only limitation found was the poor signal-to-noise for the weak emissions, precluding the extraction of quantitative information for the levels concerned. Additionally, with this shape of excitation profile, closer to a chopped illumination, we cannot extract easily some information on the “rise” part.

Thus, subsequent measurements were performed in different conditions at LASIR.

III.1.2.3 Lifetimes measurement with LASIR setup

New fitting approach

In the LASIR setup, the very short excitation pulses deliver a power several orders of magnitude than the BAM excitation laser. This generates “instantly” a limited but large amount of Yb* that will further feed the Tm emissions. Therefore, rise and decays of all Tm-based signals are well separated from the excitation pulse. Compared to the Berlin setup, the main differences come from the PM whose sensitivity drops above 600 nm: the 800 nm line will then be apparently weaker, and no Yb emission can be recorded. Consequently, no quantitative amplitude analysis has been attempted yet.

From the previously encountered fitting issue, another approach was employed to sort the kinetic traces. It is based on the measurement of their luminescence averaged lifetime:

$$\langle \tau \rangle \equiv \frac{\int_0^{\infty} t \cdot I(t) dt}{\int_0^{\infty} I(t) dt}$$

Effect of the power: case of BA5

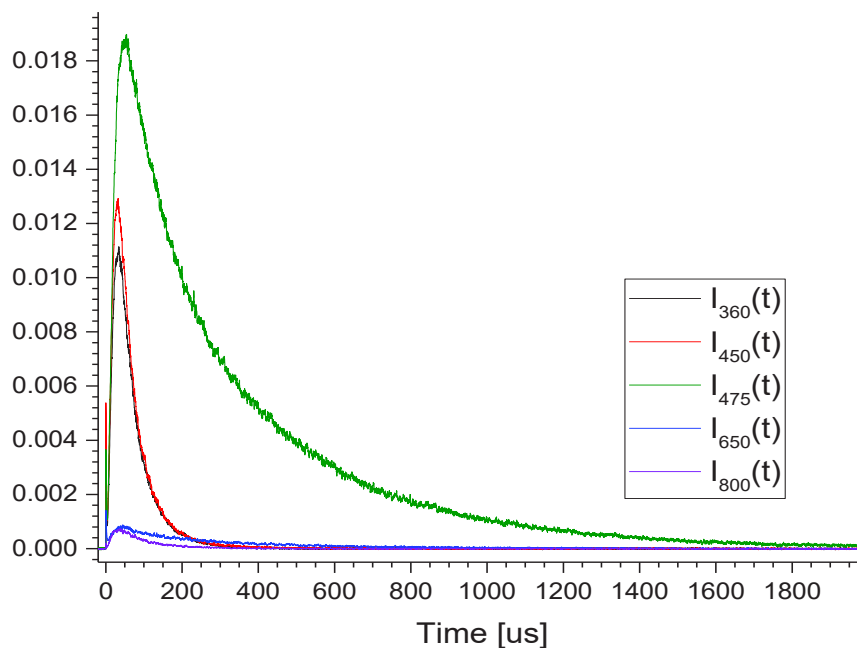


Figure 30. Typical kinetic traces recorded in Lille showing the rise and decay of each emissions (BA5 batch) (NB: the 5ns excitation pulse is merged with the intensity axis).

Results of the fit for different powers are gathered in the table 18. Here again, the averaged lifetimes could be gathered by groups, in particular the pair (475 nm, 650 nm).

Table 18. Luminescence averaged lifetimes (μs) of power-dependent decays fit of BA5 sample (laser power in MegaWatt (MW))

	255 MW	132 MW	63.2 MW	32.6 MW
360 nm	72.0	67.1	61.0	59.5
450 nm	71.6	68.2	55.2	63.7
475 nm	354.0	362.7	384.2	250.4
650 nm	321.5	297.5	177.3	-
800 nm	93.9	90.5	68.8	-

Lifetimes were found to be power independent, except for the 650 nm that is increasing with the power. To investigate the effect of batch-to-batch variations, we only focused on the three emission lines: NIR (800 nm), and blue emissions (475 and 450 nm). Main conclusions were (table 19) (i): whatever the architecture (core or core@shell), an increase of ytterbium concentration leads to the decrease of lifetime of all the Tm emissions, and (ii): the introduction of a shell leads to an increase of the lifetime as evidenced by the comparison of core nanoparticles with core@shell ones of similar Yb content (BA1 vs BA4, 20%Yb or BA2 vs BA5 57%Yb).

Table 19. Comparison of batch variation effect on photophysics of ultrasmall UCNP at 255 MW. Samples made of 57% Yb in core are written in brown. Blue one have 20%. Yellow lines indicate Core@shell.

	800 nm	475 nm	450 nm
BA2	25.2	76.2	24.5
BA1	68.6	158.5	115.7
BA5	93.9	354.0	71.6
BA4	187.4	510.6	158.3

Compared to what was observed on the BAM setup:

- The independence of the lifetimes with the excitation power, with the exception of only one line (650 nm), is remarkable in view of the very high powers available at the LASIR.
- The ytterbium effect can be considered as a general property since the same trend is observed for both setups and can be interpreted as the manifestation of the concentration quenching effect.
- Remarkably the effect of the shell gives opposite results, depending on the setup used.
- In general, lifetime determinations at the BAM were more difficult due to the quality of some of the data. The use of more intense laser square pulses would certainly help to record decay traces with a better signal-to-noise ratio, even for the less efficient transitions. This could be achieved at LASIR by grouping the ns-pulses in trains of various durations.

III.1.3 Quantum yield – efficiency

Final point was to evaluate the efficiency of the UCNPs. It was made at BAM with a dedicated setup allowing power-dependent measurement with an integrating sphere.

A measurement consists of the recording of the power-dependent quantum yield by browsing back and forth a series of laser power. For statistical accuracy, each measurement was triplicated (figure 31). Absorbance was checked to remain constant throughout the experiment.

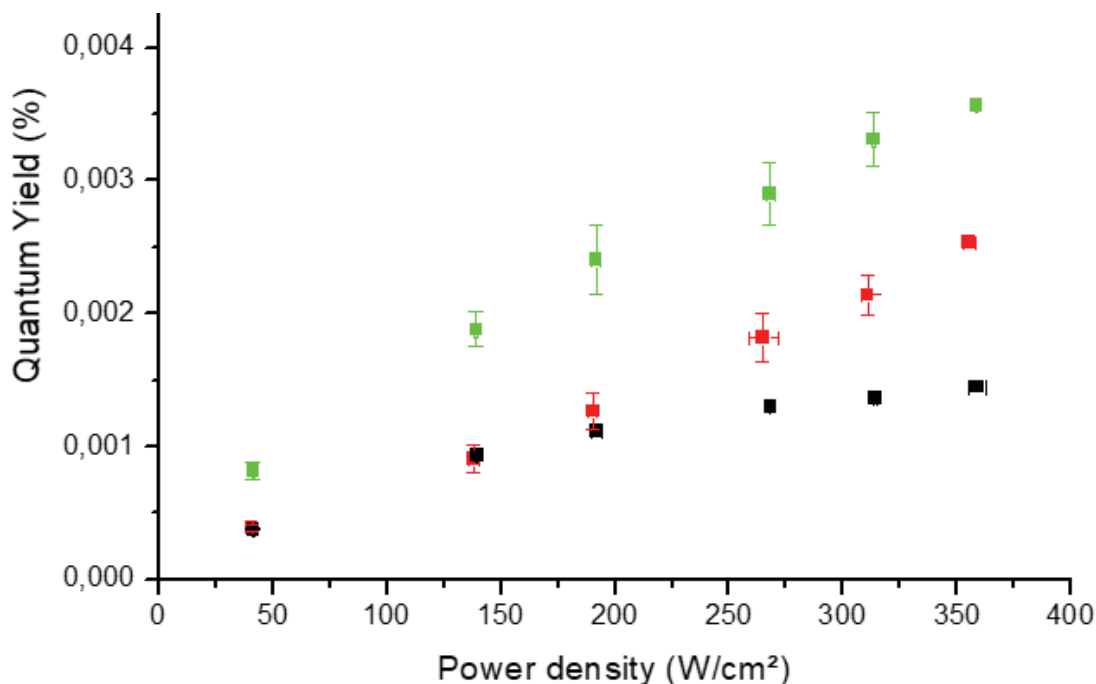


Figure 31. Comparative Power-dependent measurement of two ultrasmall core@shell UCNPs(5.5 nm) with respectively 20% (green) or 57% Yb (red). and one small core (7.5 nm) with 20% Yb (dark).

Noticeably, reference sample (core 20% Yb 7.5 nm) shows a curvature that can be attributed to a saturation effect with rising power. On the other hand, quantum yields of the two ultrasmall core@shell batches rise linearly with power density in this range of power (25-375 W cm⁻²). Among all samples ultrasmall core@shell with 20% Yb has the highest quantum yield. Nevertheless, for all these three samples, the overall quantum yield is spanning the 10⁻⁴ to 10⁻³ % range. As a result, quantum yield values recorded at a single excitation power cannot be used on its own to characterize the upconversion phenomenon and its efficiency. It should be given

as a function of the laser power. Moreover, it should be not considered as an absolute value, but more an “apparent quantum yield”. Ultrasmall core were not bright enough to be accurately treated in similar conditions.

To conclude, low quantum yields were obtained as expected, due to the ultrasmall size of the NPs. It should be noted that for all samples and laser power, 802 nm emission band contributes to at least 85% (85-90% depending on the laser power) of the global quantum yield.

IV Towards our own kinetic model

IV.1 Description of the model

Inspired by the simple kinetic model of Andersson-Engels described in the introduction of this chapter, our approach is based on the explicit description of all the kinetic events involved in ETU process up to 3P_0 level.

A crucial step is to define the pertinent species. Using the Dieke diagram (figure 32), one can see that thulium will give rise to 8 species (ground state and relevant excited states (3F_2 and 3F_3 levels are considered as a unique “ 3F ” level).) On the other way round, ytterbium will give 2 species. These are gathered in table 20. Detailed balance will also be employed meaning that at any time the total concentration of a dopant ion is constant. In other words, a constraint involving all Tm-species is applied $[Tm]^o = Cte = \sum_i [Tm_i^*]$; a similar constraint is defined for both Yb species.

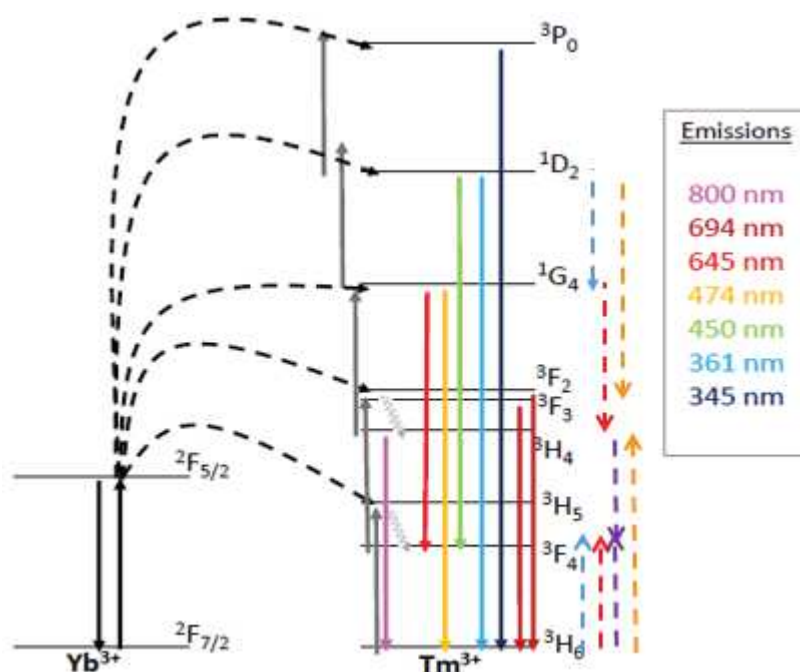


Figure 32. Description of the kinetic model

Table 20. Simplified labelling of the energy levels. Yb and Tm energy levels are respectively written in red and blue. Each constitutes a distinct “species” in the model.

$^2F_{7/2}$	$^2F_{5/2}$	3H_6	3F_4	3H_5	3H_4	$^3F_{2,3}$	1G_4	1D_2	3P_0
A	B	C	D	E	F	G	H	I	J

Translation of all the single arrows of the Dieke diagram into “chemical reaction rate” leads to implement thirty-nine processes. Importantly, it includes four Tm-Tm cross relaxations, but no back-transfers processes Tm-to-Yb. It should be noted that in our model (figure 32), no simplifying hypotheses have been made beside the choice of the processes:

- radiative processes are not separated from the non-radiative ones.
- ytterbium-to-thulium processes (“activation” processes) are not neglected regarding to the ytterbium relaxations ones.
- conservation equations of ytterbium and total thulium species are taken into account.
- no stationary state hypotheses are made.

The conservation equations enable the simulation of high power excitations as [Yb*] is not considered negligible regarding to [Yb].

However, no explicit description of the surface quenching is given: this will be introduced once the model is validated to fit experimental data. This preliminary model therefore does not take in account the size of the material under investigation. Its aim is only to reproduce the general shape of the power-dependent or pulse shape-dependent decays.

The methodology used rely on the expertise in Chemical Dynamics of the team at treating complex kinetic networks, either by fitting¹³ kinetic data or by simulating¹⁴ them in a multivariate analysis approach.

IV.2 Mathematical expression of the model

a-Ytterbium-centered processes (ph1: 980 nm photon)

- $A + \text{ph1} \rightarrow B$
- $B \rightarrow A$

b-Ytterbium-Thulium energy transfers and Thulium relaxation processes. As radiative- and non-radiative processes are first order, they are not distinguished in the model:

- $B + C \rightarrow D + A$
- $B + C \rightarrow E + A$
- $D \rightarrow C$
- $E \rightarrow D$
- $E \rightarrow C$
- $F \rightarrow E$
- $F \rightarrow D$
- $F \rightarrow C$
- $B + D \rightarrow G + A$
- $G \rightarrow F$
- $G \rightarrow E$
- $G \rightarrow D$
- $G \rightarrow C$
- $B + F \rightarrow H + A$
- $H \rightarrow G$
- $H \rightarrow F$
- $H \rightarrow E$
- $H \rightarrow D$
- $H \rightarrow C$
- $B + H \rightarrow I + A$
- $I \rightarrow H$
- $I \rightarrow G$
- $I \rightarrow F$
- $I \rightarrow E$
- $I \rightarrow D$
- $I \rightarrow C$
- $B + I \rightarrow J + A$
- $J \rightarrow I$
- $J \rightarrow H$
- $J \rightarrow G$
- $J \rightarrow F$
- $J \rightarrow E$
- $J \rightarrow D$
- $J \rightarrow C$

c-Thulium cross-relaxation processes

- $C + I \rightarrow H + D$
- $C + I \rightarrow F + F$
- $C + H \rightarrow F + D$
- $C + F \rightarrow D + D$
- $D + D \rightarrow C + F$

IV.3 Data mining of rate constant

A first basis to implement the model was to report rate constants extracted from the literature mainly from laser spectroscopy. Such data are gathered in the following tables:

Table 21. “Activation” i.e. Cross-relaxation rate constants between Yb and Tm, respectively labeled in red and blue

	Range of rate constant (cm ³ s ⁻¹)	Average rate constant k (cm ³ s ⁻¹)	Ref
${}^2F_{5/2} + {}^3H_6 \rightarrow {}^3H_5 + {}^2F_{7/2}$	-	$1.6 \cdot 10^{-18}$	15,16
${}^2F_{5/2} + {}^3H_6 \rightarrow {}^3F_4 + {}^2F_{7/2}$	$1.2 \cdot 10^{-17} - 1.8 \cdot 10^{-17}$	$1.5 \cdot 10^{-17}$	16,17
${}^2F_{5/2} + {}^3F_4 \rightarrow {}^3F_{2,3} + {}^2F_{7/2}$	-	$6.2 \cdot 10^{-16}$	15
${}^2F_{5/2} + {}^3H_4 \rightarrow {}^1G_4 + {}^2F_{7/2}$	$1.6 \cdot 10^{-18} - 2.7 \cdot 10^{-16}$	$1.4 \cdot 10^{-16}$	15,17
${}^2F_{5/2} + {}^3H_4 \rightarrow {}^3F_2 + {}^2F_{7/2}$	$8.8 \cdot 10^{-15} - 1.2 \cdot 10^{-14}$	10^{-14}	17

Table 22. Tm-Tm Cross-relaxation rate constants.

	Range of rate constant (cm ³ s ⁻¹)	Average rate constant k (cm ³ s ⁻¹)	Ref
${}^3H_6 + {}^1D_2 \rightarrow {}^1G_4 + {}^3F_4$	-	$5 \cdot 10^{-17}$	16,18
${}^3H_6 + {}^1D_2 \rightarrow {}^3H_4 + {}^3H_4$	-	$4.8 \cdot 10^{-17}$	16
${}^3H_6 + {}^1G_4 \rightarrow {}^3F_4 + {}^3H_4$	-	$7.5 \cdot 10^{-16}$	16
${}^3H_6 + {}^3H_4 \rightarrow {}^3F_4 + {}^3F_4$	$1.1 \cdot 10^{-16} - 4.2 \cdot 10^{-16}$	$1.9 \cdot 10^{-16}$	16,19
${}^3F_4 + {}^3F_4 \rightarrow {}^3H_6 + {}^3H_4$	-	10^{-18}	16,19
${}^3H_6 + {}^1G_4 \rightarrow {}^3F_4 + {}^3F_{2,3}$	Only mentioned, no value		18,20

Table 23. Excited state relaxation rate constants. Yb and Tm levels are respectively labeled in red and blue

transition	Range of rate constant (s ⁻¹)	Average rate constant k (s ⁻¹)	Ref
² F _{7/2} → ² F _{5/2}	340 – 760	530	12,15,18,21-23
³ P ₀ → ¹ D ₂	-	41.7	20
³ P ₀ → ¹ G ₄	-	1.35*10 ³	20
³ P ₀ → ³ F _{2,3}	-	1.39*10 ³	20
³ P ₀ → ³ H ₄	-	1.49*10 ³	20
³ P ₀ → ³ H ₅	-	41.7	20
³ P ₀ → ³ F ₄	-	8.19*10 ³	20
³ P ₀ → ³ H ₆	-	41.7	20
¹ D ₂ → ¹ G ₄	6 – 89.6	48	18,20
¹ D ₂ → ³ H ₄	164 – 821	493	18,20
¹ D ₂ → ³ H ₅	-	149	20
¹ D ₂ → ³ F ₄	376 – 5400	2.26*10 ³	18,20,22
¹ D ₂ → ³ H ₆	454 – 12500	5.58*10 ³	18,20,22,24
¹ G ₄ → ³ F _{2,3}	36 – 56.7	46.4	20,25
¹ G ₄ → ³ H ₄	70 – 222	137	18,20,22,25
¹ G ₄ → ³ H ₅	222 – 435.39	363	20,22,25
¹ G ₄ → ³ F ₄	100 – 1690	613	18,20,22,25-27
¹ G ₄ → ³ H ₆	495 – 12500	2.29*10 ³	18,20,22,24-27
³ H ₄ → ³ F ₄	55 – 1610	366	18-20,22,25
³ H ₄ → ³ H ₆	350 – 14300	2.28*10 ³	8,18,20,22,24,26,27
³ H ₄ → ³ H ₅	-	19.8	20
³ H ₅ → ³ F ₄	5.45 – 17000	1.1*10 ⁴	15,20,22
³ H ₅ → ³ H ₆	182 – 24000	1.2*10 ⁴	20,22
³ F _{2,3} → ³ H ₄	2.6 – 178000	1.1*10 ⁵	15,20,28
³ F _{2,3} → ³ H ₆	-	2.37*10 ³	20
³ F _{2,3} → ³ H ₅	-	189	20
³ F _{2,3} → ³ F ₄	-	65.6	20
³ F ₄ → ³ H ₆	90 – 300	169	19,20,25

IV.4 Preliminary results

Simulation of experimental lifetime measurement

From the first approximation of our model we started by checking whether it was possible to reproduce the shape of decays measured at LASIR. As an example we investigated the 475 nm emission band decays of BA7 and BA9 (figure 33).

It can be clearly observed that the shape of the decay can be reproduced with our simulation. However, the time scale is not consistent with the experiment.

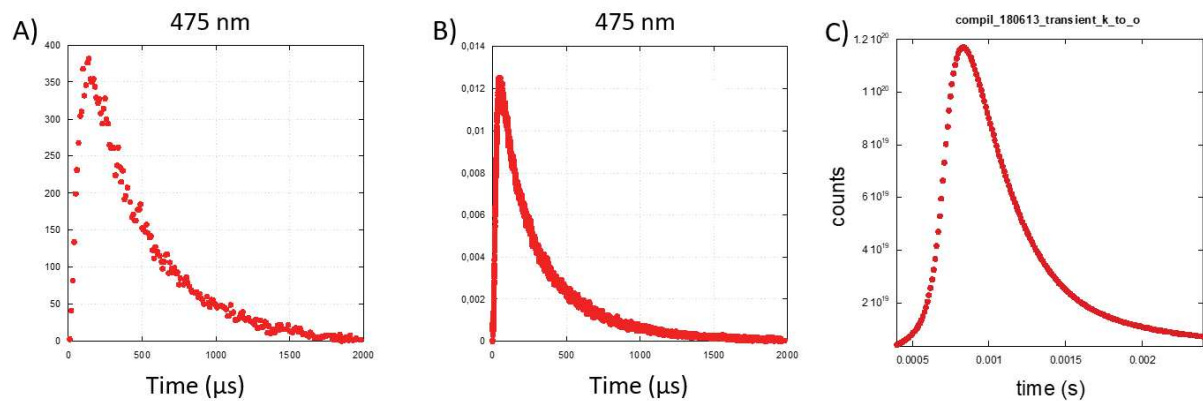


Figure 33. Comparison of 475 nm decay measurement on BA7 (A) and BA9 (B) with simulated one with our model (C)

Saturation effect on the 800 nm emission

Lifetime decays performed at LASIR are recorded under high laser power (MW to GW). Therefore, as we aim to explore the power-dependency, one remaining question is to know when the saturation regime is occurring.

In our model the total ytterbium excitation is monitored. However, as the pulse width at the LASIR is very short, one can neglect the processes that consume the ytterbium excited-state ($[Yb^*]$ or species “B” in the model) during the pumping of the system: the ytterbium excited-state concentration reaches therefore a PSS situation reflecting the absorption cross-section and the ytterbium excited-state lifetime. Thus, to simulate the effect of the application of instant pump pulse, one deliberately fixes a $[Yb^*]$ respecting the detailed balance:

$$[Yb]_0 = [Yb] + [Yb^*] = A + B = 21 \cdot 10^{21} \text{ atom cm}^{-3}. \text{ These data are gathered on table 24.}$$

Table 24. Concentration of Yb* (and Yb) used to simulate short pulses of various laser power initial ytterbium concentration: $[Yb]_0 = 21 \cdot 10^{21}$. Concentrations are given in atom cm^{-3} .

experiment	$[Yb^*]$	$[Yb]$	%Yb*
k	$2.1 \cdot 10^{21}$	$18.9 \cdot 10^{21}$	10%
l	$1.05 \cdot 10^{21}$	$19.95 \cdot 10^{21}$	5%
m	$0.525 \cdot 10^{21}$	$20.475 \cdot 10^{21}$	2.5%
n	$4.2 \cdot 10^{21}$	$15.8 \cdot 10^{21}$	20%
o	$8.4 \cdot 10^{21}$	$12.6 \cdot 10^{21}$	40%

Noticeably, using the ytterbium photophysical parameters (cross-section and excited-state lifetime), one can estimate the laser power required to reach such a Yb* PSS-concentration. We have observed a significant depopulation of the Yb ground state (species “A” in the model) only when the excitation power is higher than 500 W cm^{-2} (cases k, n and o).

The effect of the initial Yb* population on the 800 nm emission was obtained by following the population of the emitting level 3H_4 (named F in the model). On figure 24 are overlaid the time-dependent 3H_4 excited-state concentrations. Curves are labeled according to the “initial” Yb* concentration (from table 24).

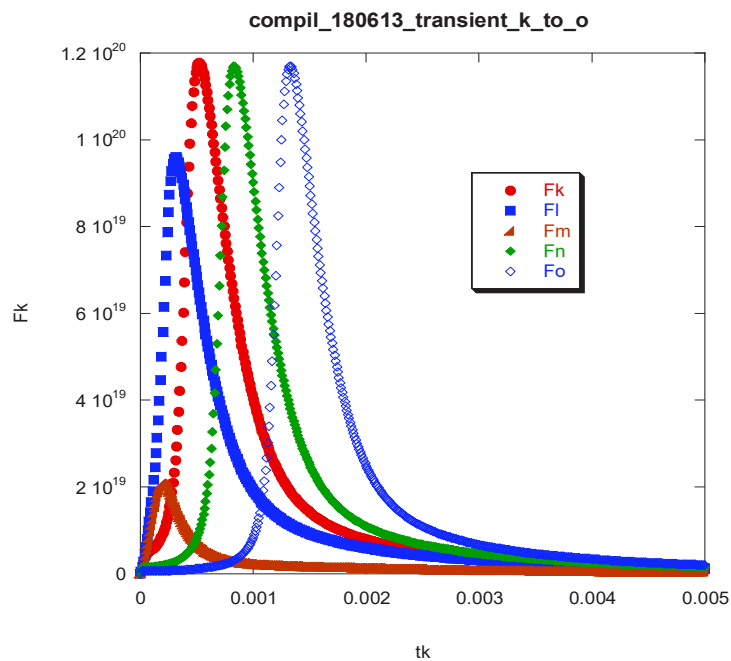


Figure 34. Results of the laser power simulation.

Two regimes can be distinguished: a first phase where the maximum concentration of the $^3\text{H}_4$ state” is increasing with $[\text{Yb}^*]$, or the excitation power; then a saturation regime where there is no apparent gain at increasing the power: the maximum amount of $^3\text{H}_4$ state available to generate the 800 emission remains globally constant.

The delayed rise of the $^3\text{H}_4$ state is expected as a signature of the ETU mechanism. For the last three curves this delay time drifts with the power. Such a result was not expected

Both phenomena have not been noticed yet on the LASIR experiments despite excitation powers falling in this critical zone. This can be due to poorly adapted parameters: the rate constants used have been extracted from data related to larger objects or macrocrystals. Next step will therefore be to fit the experimental curve and retrieve the “appropriate” rate constants. Some of these (transient excited state lifetimes) should then be compared to radiative rate constants computed from the Judd-Ofelt theory (but this requires absorption spectra). Eventually, especially in the high power excitation part, the probability of having more complex processes, such as the trimolecular CSU involving two Yb^* and one emitter’s state should not be eliminated.²⁹

V Conclusion

In the following chapter we could address various points:

- Exploring the photophysical behavior of UCNP:

Complete characterization of the luminescence was achieved with an approach towards standardization: from the absorption, to the emission intensity and lifetimes. Even estimation of the “efficiency” was achieved by measuring the quantum yield. However, the reader should be reminded that quantum yield and lifetime measured are not absolute values but apparent constants.

Moreover, an easy and cheap customization of a standard fluorometer can allow the simultaneous measurement of the absorption. Despite its importance for calibration purpose, the latter also afforded additional data, regarding the colloidal stability issues.

As UCNP are non-linear phosphors, standard quantifiers are probably inaccurate too describe these particles. Thus apparent “exponent”, “efficiency” (i.e. quantum yield) or “lifetimes” were measured under various conditions: these parameters (exponent, lifetime) were found to match the predictions obtained from the thulium Dieke diagram, and transitions originating from the same levels share common features. Yet, the understanding of the energy redistribution has still to be confirmed. The experiments recorded at the BAM can be considered as preliminary, and the choice of the experimental conditions could not be further optimized due to a lack of time: my internship there was limited to two months. Another alternative would be to use more intense laser square pulses in order to get more signal, even for the less efficient transitions. This could be achieved at LASIR by grouping the ns-pulses in trains of various durations.

- Case of ultrasmall UCNP :

A chemical parameter that was not considered at first emerged: the number of emitting atoms in an ultrasmall nanoparticle. Indeed for the range of size we explored, Indeed, according to calculations of their chemical parameters (table 3), 2.5 nm UCNP such as BA2 should have, in average, a single emitter per NP. Such a content makes these objects comparable to the upconverting molecular complexes described in the literature,³⁰ bridging the gap between these two domains.

This could impact the photophysics for our super-resolution goal. If the NP are really made of single emitters, they probably could blink without need of coupling with external shutter. On the other hand, single NP imaging will then become challenging, as for single emitter with long lifetimes, long durations of experiments will be required to get enough photons to have accurate analysis.

- Starting to elaborate a kinetic model:

Based on data coming from data mining of the literature, we were able to build the early stages of a 9-level kinetic model in order to explain the energy redistribution within an UCNP. Lifetimes data accumulated will be implemented to afford more realistic constants. Even if preliminary simulations show that decay can be reproduced in terms of shape, they are not accurate at the moment. Once the final model will be established, it could be used also to simulate the non-linear behavior (log-log plots).

VI Experimental section

Laser power calibration at IMRCP

A laser power calibration curve was established in such conditions. At first rising powers were monitored by rising arbitrary value (0-600) controlled by a potentiometer. Same experiment was performed by decreasing power. The calibration curve was established as an average of both values (power rise and power decrease).

Beam diameter was evaluated as being 3.5 mm (based on the numerical aperture of the fiber and the parameters of the collimating lens).

Power density was then implemented in the calibration curve from the following equation:

$$\text{Power density} = \frac{\text{Power}}{\text{Surface}} = \frac{\text{Power}}{4 \times \pi \times \left(\frac{\text{beam diameter}}{2}\right)^2}$$

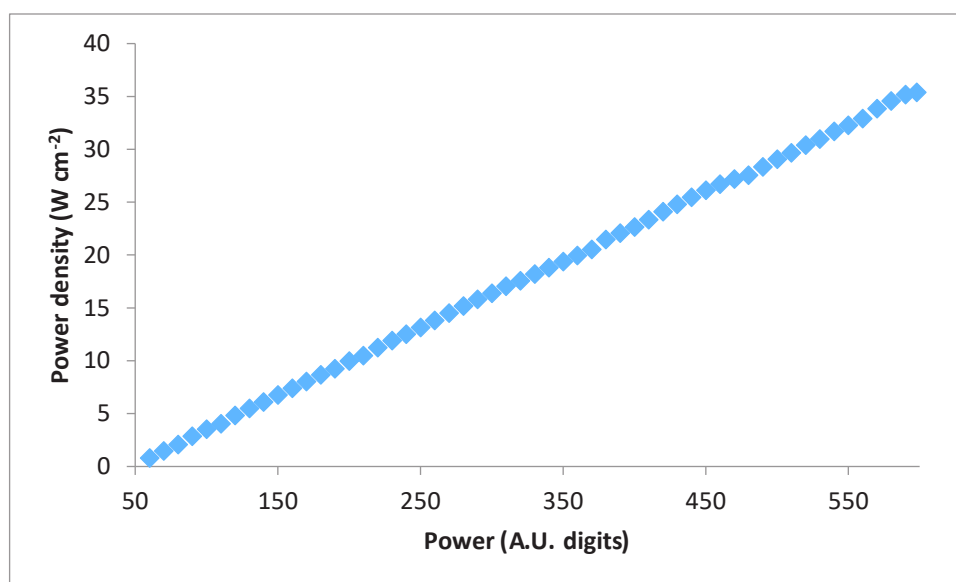


Figure 35. Calibration curve of multimode laser at IMRCP

Determination of NP content from absorbance (used in section II.1.1)

Diameter of the NPs obtained by analysis of TEM pictures is used to calculate the volume of these nanospheres (V_{TEM}).

Volume of the NaREF₄ unit cell (U_{NaREF4}) is extracted from XRD analysis and Rietveld refinements.

Therefore, the number of Rare Earth per NP (RE/NP) can be deduced by comparison of the volume:

$$N(RE/NP) = \frac{Z \cdot V_{TEM}}{U_{NaREF_4}}$$

Knowing the Rare Earth composition, the number of Yb/NP can then be determined as:

$$N(Yb/NP) = (\%Yb) \cdot N(RE/NP)$$

From the absorbance measured in solution, [Yb] in mol/L can be found, applying Beer-Lambert's law:

$$[Yb] = \frac{Abs(976 \text{ nm})}{\varepsilon_{976 \text{ nm}}(Yb)}$$

Thus, the concentration of NaREF₄ in mol/L can be calculated by:

$$[NaREF_4] = \frac{[Yb]}{N(Yb/NP)}$$

As a result, the number of UCNP per litre can be deduced by multiplying by Avogadro's number ($N_A=6.022 \times 10^{23} \text{ mol}^{-1}$):

$$[UCNP/L] = [NaREF_4] \cdot N_A$$

To determine NPs concentration in mg/mL, the formula weight (FW) has to be calculated, depending on the NP composition:

$$FW_{NaREF_4} = M(Na) + 4 \cdot M(F) + [(\%Gd) \cdot M(Gd) + (\%Yb) \cdot M(Yb) + (\%Tm) \cdot M(Tm)]$$

Then the concentration of UCNP in solution in mg/mL can be calculated as:

$$[NaREF_4@OA] = 100 \cdot \frac{[Yb] \cdot FW_{NaREF_4}}{(\%Yb)}$$

Knowing the content of the OA organic layer from TGA analysis (30%), we can therefore estimate the concentration of bare NP:

$$[NaREF_4]_{suspension} = \left[1 - \frac{(\%OA)}{100}\right] \cdot [NaREF_4@OA] = 0.7 [NaREF_4@OA]$$

By comparison with the initial concentration $[UCNP]_{theo}$ we can determine the concentration of settled NPs:

$$[NaREF_4]_{settled} = [UCNP]_{theo} - [NaREF_4]_{suspension}$$

The proportion of NP in solution can be deduced by:

$$\% NP \text{ in solution} = \frac{[NaREF_4]_{suspension}}{[UCNP]_{theo}}$$

Emission spectra and lifetimes acquisition at BAM

Emission spectra and lifetimes measurement at BAM were performed on FLS980 fluorometer from Edinburgh Instruments, fed by 976 nm CW laser with power range up to 124.4 W cm^{-2} . Sample were thermostated at 25°C . Measurements were done with slits bandpass $\Delta\lambda=10 \text{ nm}$.

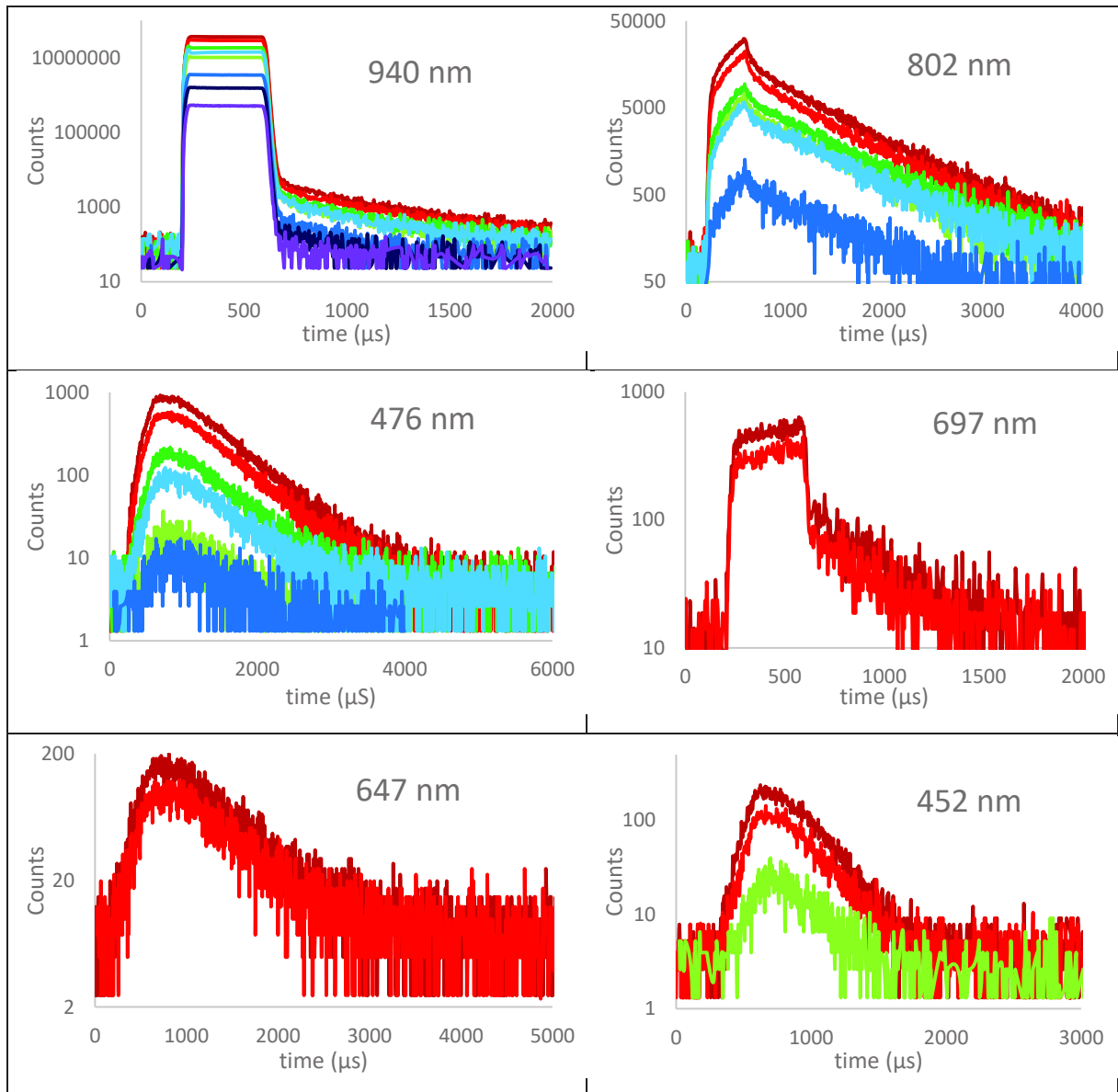
Quantum yield measurement procedure at BAM

Power-dependent quantum yield measurements were achieved with BAM home-designed setup. Before starting measurement, laser was warm-up for at least one hour. Quality criteria was to wait for laser stability $>99.5\%$ to initiate measurement. For each recording, the sample was first measured then immediately followed by blank solvent. Therefore, laser stability issue upon a succession of sample can be prevented. One measurement consisted in at first measurements performed by increasing the laser power, then by decreasing it. Experiment-to-experiment laser power variations are responsible of the error bars.

The complete emission spectrum of sample is reconstructed from the juxtaposition of smaller spectra recorded over different ranges of wavelength. For each range the gain is optimized to have an accurate signal along the full spectra. There is an overlap of at least 10 nm between successive ranges of wavelength to allow the quantitative comparison.

Eventually, the 976 nm absorbance (given in %) is simultaneously measured. It should remain constant among the different laser power. For my samples it stood at around 10%, the value depending on the nature of the samples.

Results of Power-dependent lifetime measurements at BAM

**Figure 36.** Power-dependent lifetime measurements of BA2

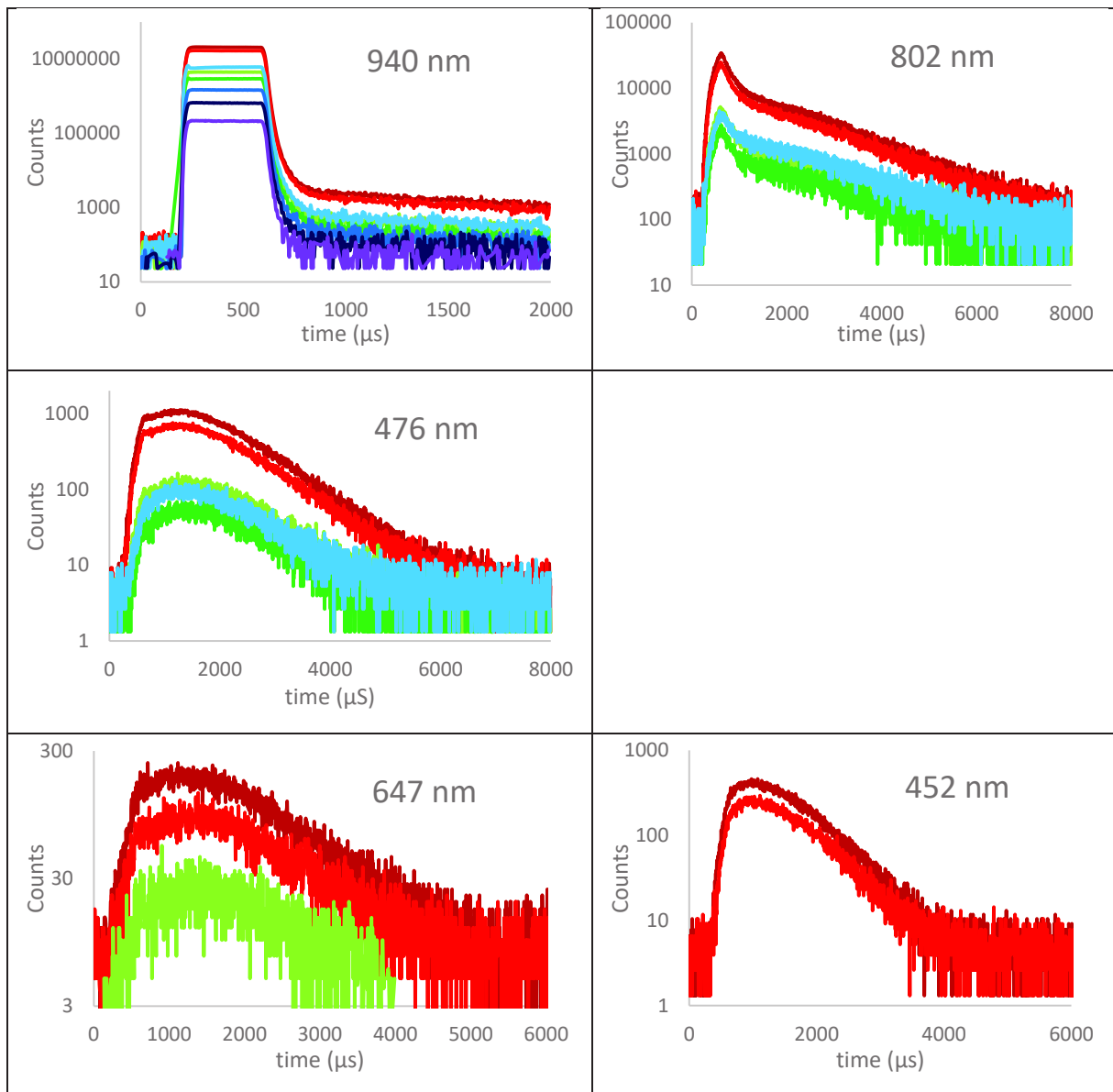


Figure 37. Power-dependent lifetime measurements of BA1

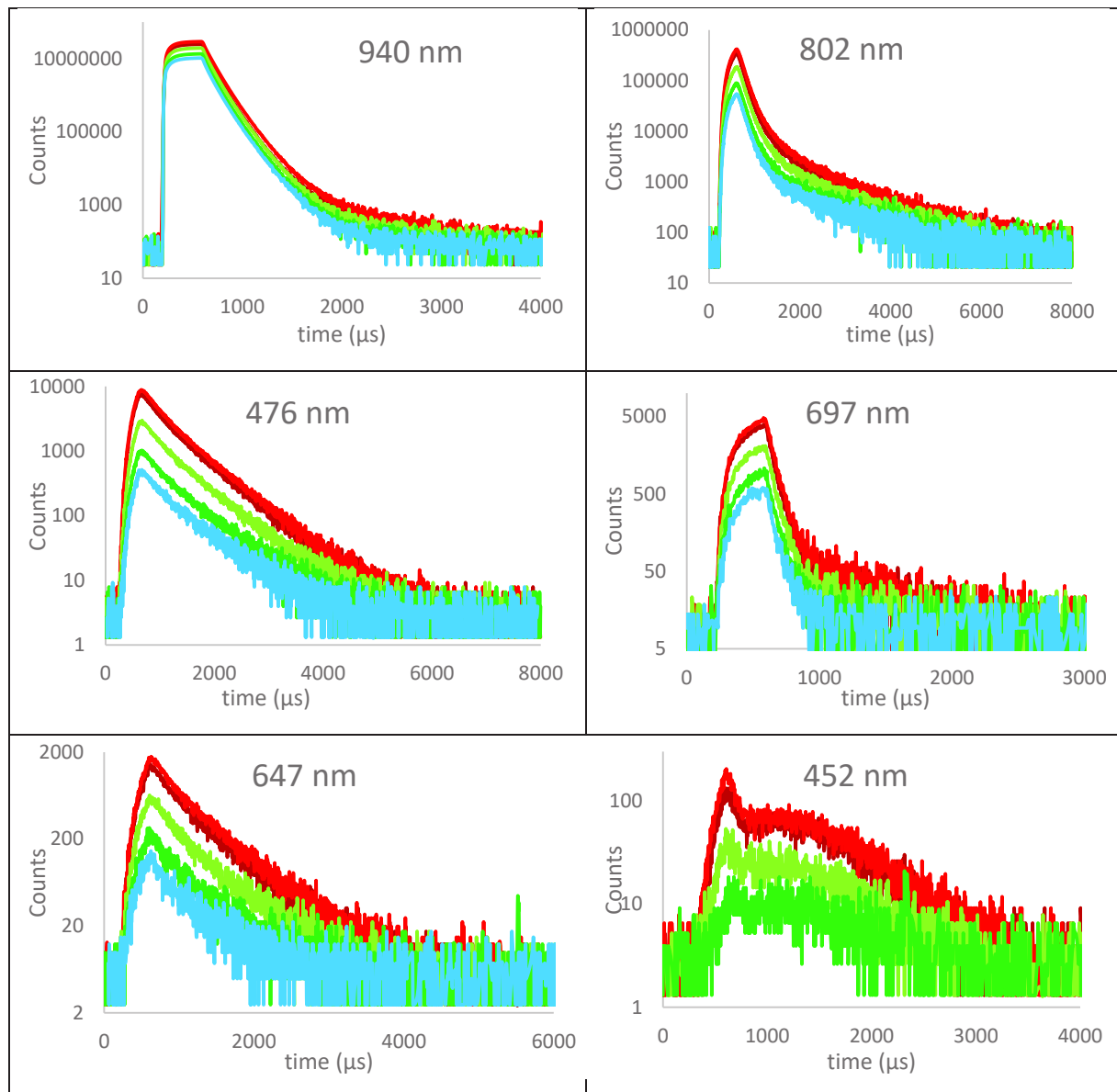


Figure 38. Power-dependent lifetime measurements of BA4

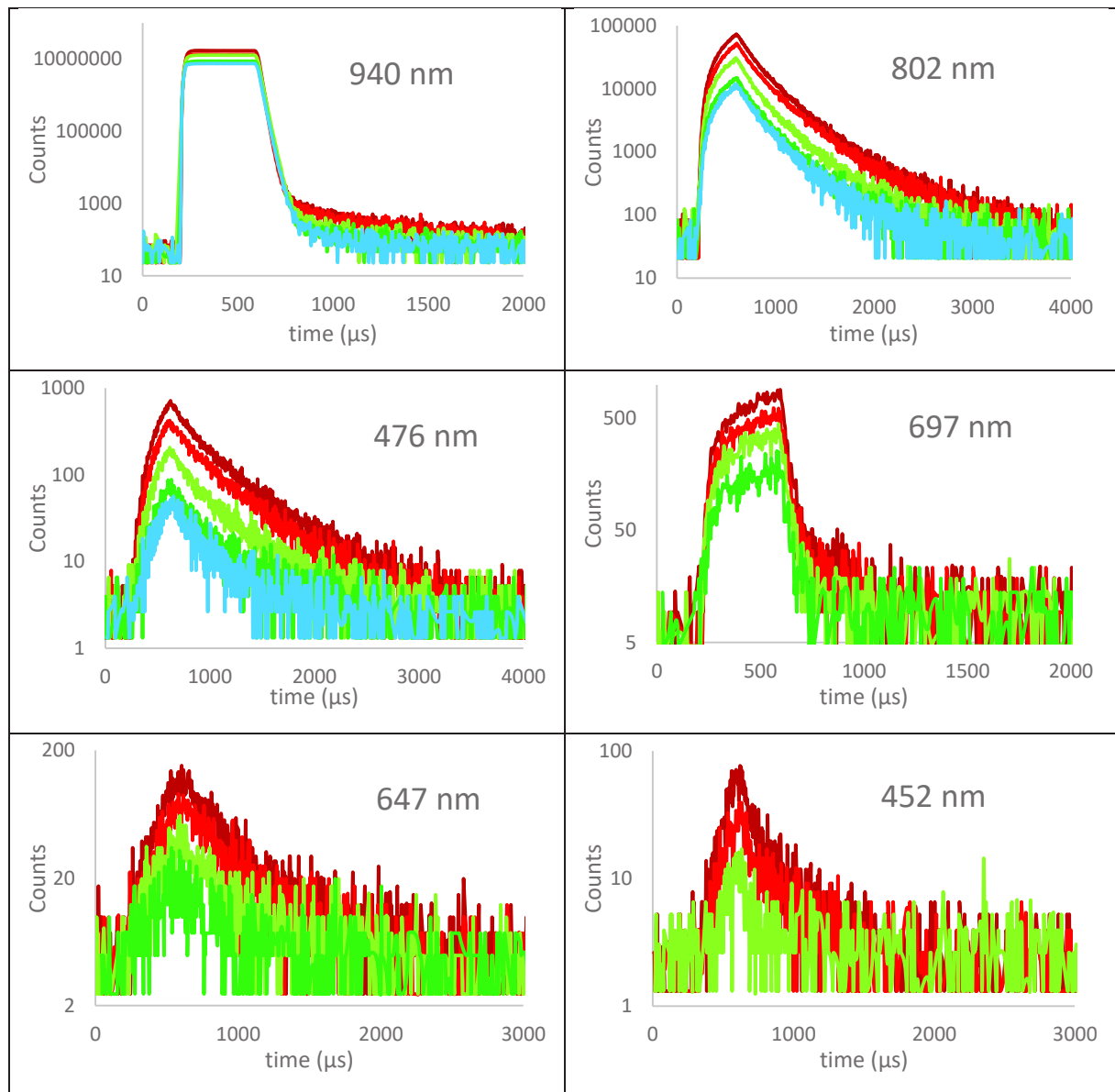


Figure 39. Power-dependent lifetime measurements of BA8

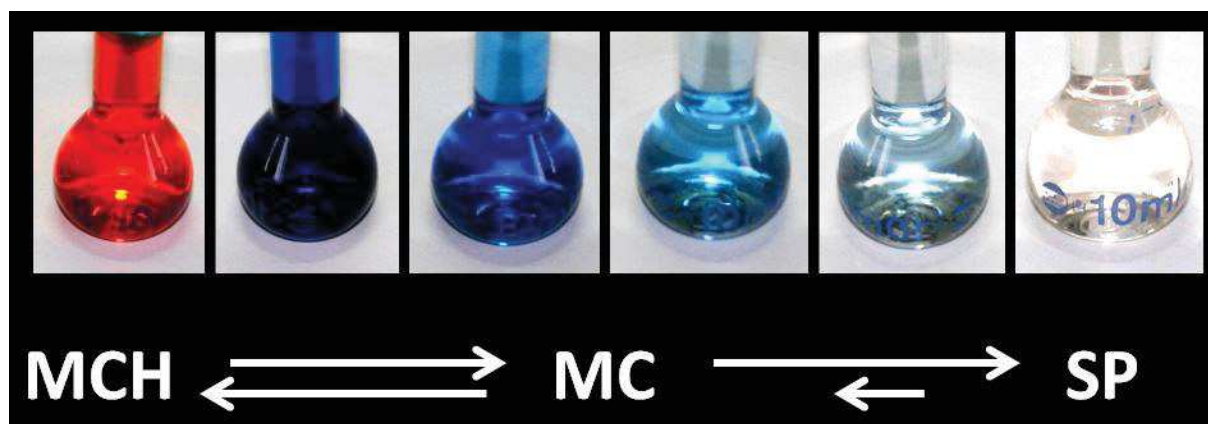
VII References

- 1 Kraft, M. *Spectroscopic characterization of upconversion nanomaterials with systematically varied material composition and surface chemistry*, Humboldt-Universität zu Berlin, (2019).
- 2 Zhang, H., Li, Y. J., Lin, Y. C., Huang, Y. & Duan, X. F. Composition tuning the upconversion emission in NaYF₄:Yb/Tm hexaplate nanocrystals. *Nanoscale* **3**, 963-966 (2011).
- 3 Liu, Y. J. *et al.* Amplified stimulated emission in upconversion nanoparticles for super-resolution nanoscopy. *Nature* **543**, 229-233 (2017).
- 4 Zhang, Y. Q. *et al.* Concentration quenching of blue upconversion luminescence in Tm³⁺/Yb³⁺ co-doped Gd₂(WO₄)₃ phosphors under 980 and 808 nm excitation. *J Alloy Compd* **709**, 147-157 (2017).
- 5 Liu, H. *et al.* Balancing power density based quantum yield characterization of upconverting nanoparticles for arbitrary excitation intensities. *Nanoscale* **5**, 4770-4775 (2013).
- 6 Chan, E. M., Gargas, D. J., Schuck, P. J. & Milliron, D. J. Concentrating and recycling energy in lanthanide codopants for efficient and spectrally pure emission: the case of NaYF₄: Er³⁺/Tm³⁺ upconverting nanocrystals. *The Journal of Physical Chemistry B* **116**, 10561-10570 (2012).
- 7 Strohhöfer, C. *Optical properties of ion beam modified waveguide materials doped with erbium and silver*, Utrecht University, PhD thesis, (2001).
- 8 Kaiser, M. *et al.* Power-dependent upconversion quantum yield of NaYF₄:Yb³⁺, Er³⁺ nano- and micrometer-sized particles—measurements and simulations. *Nanoscale* **9**, 10051-10058 (2017).
- 9 Gargas, D. J. *et al.* Engineering bright sub-10-nm upconverting nanocrystals for single-molecule imaging. *Nature Nanotechnology* **9**, 300 (2014).
- 10 Zhang, F. *Photon upconversion nanomaterials*. Vol. 416 (Springer, 2015).
- 11 Valeur, B. & Berberan-Santos, M. N. *Molecular Fluorescence: Principles and Applications*. (Wiley, 2013).
- 12 Hossan, M. Y. *et al.* Explaining the Nanoscale Effect in the Upconversion Dynamics of β-NaYF₄:Yb³⁺, Er³⁺ Core and Core–Shell Nanocrystals. *The Journal of Physical Chemistry C* **121**, 16592-16606 (2017).
- 13 Vallet, J., Micheau, J. C. & Coudret, C. Switching a pH indicator by a reversible photoacid: A quantitative analysis of a new two-component photochromic system. *Dyes and Pigments* **125**, 179-184 (2016).
- 14 Micheau, J. C., Cruz, J. M., Coudret, C. & Buhse, T. An Autocatalytic Cycle Model of Asymmetric Amplification and Mirror-Symmetry Breaking in the Soai Reaction. *ChemPhysChem* **11**, 3417-3419 (2010).
- 15 Liu, H. *et al.* Deep tissue optical imaging of upconverting nanoparticles enabled by exploiting higher intrinsic quantum yield through use of millisecond single pulse excitation with high peak power. *Nanoscale* **5**, 10034-10040 (2013).
- 16 Guy, S., Joubert, M. & Jacquier, B. Photon avalanche and the mean-field approximation. *Physical Review B* **55**, 8240 (1997).
- 17 Ostermayer, F. W., van der Ziel, J. P., Marcos, H. M., Van Uitert, L. G. & Geusic, J. E. Frequency Upconversion in YF₃:Yb³⁺, Tm³⁺. *Physical Review B* **3**, 2698-2705 (1971).

- 18 Li, L., Xin-Lu, Z. & Li-Xue, C. Intrinsic Bistability and Critical Slowing in $\text{Tm}^{3+}/\text{Yb}^{3+}$ Codoped Laser Crystal with the Photon Avalanche Mechanism. *Chinese Physics Letters* **26**, 064216 (2009).
- 19 Noginov, M., Vondrova, M. & Casimir, D. Analysis of intrinsic optical bistability in Tm-doped laser-related crystals. *Physical Review B* **68**, 195119 (2003).
- 20 Ivanova, S., Tkachuk, A., Mirzaeva, A. & Pellé, F. Spectroscopic study of thulium-activated double sodium yttrium fluoride $\text{Na}_{0.4}\text{Y}_{0.6}\text{F}_{2.2}:\text{Tm}^{3+}$ crystals: I. Intensity of spectra and luminescence kinetics. *Optics and Spectroscopy* **105**, 228-241 (2008).
- 21 Anderson, R. B., Smith, S. J., May, P. S. & Berry, M. T. Revisiting the NIR-to-visible upconversion mechanism in $\beta\text{-NaYF}_4:\text{Yb}^{3+}, \text{Er}^{3+}$. *The journal of physical chemistry letters* **5**, 36-42 (2013).
- 22 Villanueva-Delgado, P., Krämer, K. W. & Valiente, R. Simulating energy transfer and upconversion in $\beta\text{-NaYF}_4:\text{Yb}^{3+}, \text{Tm}^{3+}$. *The Journal of Physical Chemistry C* **119**, 23648-23657 (2015).
- 23 Bjurshagen, S. *et al.* Fluorescence dynamics and rate equation analysis in Er^{3+} and Yb^{3+} doped double tungstates. *Applied optics* **45**, 4715-4725 (2006).
- 24 Kale, V., Lastusaari, M., Hölsä, J. & Soukka, T. Intense UV upconversion through highly sensitized $\text{NaRF}_4:\text{Tm}$ (R: Y, Yb) crystals. *RSC Advances* **5**, 35858-35865 (2015).
- 25 Qin, G. *et al.* Power scaling of Tm^{3+} doped ZBLAN blue upconversion fiber lasers: modeling and experiments. *Applied Physics B* **82**, 65-70 (2006).
- 26 Collings, B. & Silversmith, A. Avalanche upconversion in $\text{LaF}_3:\text{Tm}^{3+}$. *Journal of luminescence* **62**, 271-279 (1994).
- 27 Arppe, R. *et al.* Quenching of the upconversion luminescence of $\text{NaYF}_4:\text{Yb}^{3+}, \text{Er}^{3+}$ and $\text{NaYF}_4:\text{Yb}^{3+}, \text{Tm}^{3+}$ nanophosphors by water: the role of the sensitizer Yb^{3+} in non-radiative relaxation. *Nanoscale* **7**, 11746-11757 (2015).
- 28 Gao, D. *et al.* Up/down conversion switching by adjusting the pulse width of red laser beams in $\text{LaF}_3:\text{Tm}^{3+}$ nanocrystals. *Optics letters* **40**, 3580-3583 (2015).
- 29 Zou, Q. *et al.* Cooperative and non-cooperative sensitization upconversion in lanthanide-doped LiYbF_4 nanoparticles. *Nanoscale* **9**, 6521-6528 (2017).
- 30 Charbonnière, L. J. Bringing upconversion down to the molecular scale. *Dalton Transactions* **47**, 8566-8570 (2018).

Chapter IV

Upconverting nanohybrid: towards super resolution



“Gardez le cap dans la tempête et tenez fermement la barre.” (Guy Roux)

“Truth will ultimately prevail where there is pains to bring it to light.”
(Georges Washington)

Contents

I	Introduction.....	227
I.1	Strategy for Blinking UCNP-based nanohybrid.....	227
I.2	Photochromic dyes	229
I.3	Organic negative T-photochromic dyes	231
I.4	Spiropyran dyes	233
I.4.1	Reversible photoacid	234
I.4.2	Negative photochromic hydrogels.....	235
I.4.3	Photoactivatable “Staples“	237
I.5	Aim of the chapter	238
II	Toward a negative photochromic spiropyran based UCNP nanohybrid.....	239
II.1	Strategy for dye integration: UCNP ligand exchange	239
II.1.1	Removal of OA	239
II.1.2	Different surface functionalization.....	240
II.1.3	Example of quantitative approach followed by NMR	242
II.1.4	Conclusion on the strategies to make nanohybrid.....	247
II.2	Choice of UCNP-dye couple	248
II.3	Synthesis of SP-grafted ligands	251
II.3.1	Triazine route	251
II.3.2	The amide route.....	253
III	Photochemical behavior of amido-BIPS	263
III.1	Parametrization of the dye: use of BIPS-GLT.....	263
III.2	Exploration of P _{1,38} polymer photochromism	268
IV	Towards UCNP@P _{1,38} nanohybrid for super-resolution.....	271
IV.1	Nanohybrid formation	271

IV.2	Impact of the Nanohybrid architecture on P _{1,38} photochemistry	272
IV.3	UCNP-induced Photoswitching of the P _{1,38}	273
V	Conclusion	275
VI	Experimental section	278
VI.1	Material and methods	278
VI.2	The photoisomerization experiments.....	278
VI.3	Protocol for UCNP ligand exchange	278
VI.4	Reactive dye BIPS-TCl ₂	279
VI.5	Model compound BIPS-GLT	280
VI.6	Polymer P _{x(39-x) x=1}	281
VI.6.1	Step 1.....	281
VI.6.2	Step 2.....	281
VI.7	Calculations of k _(MC→SP)	282
VII	References	283

I Introduction

I.1 Strategy for Blinking UCNP-based nanohybrid

As it has been seen in the introduction, UCNPs are notoriously non-blinking. While this property is of interest for tracking techniques, it is a major problem for the stochastic super-resolution microscopy we envision.

The approach we are developing is to equip the nanocrystal with an intermittent “shutter”: the luminescence of the resulting object would then switch randomly between an “ON” (bright) state to an “OFF” (dimmed) one. One possibility is to take advantage of the light emitted by the particle via a photochemical reaction: the system would then be completely autonomous.

UCNPs are now extensively used as “Nanolamps” typically to trigger irreversible photoreactions. Thus photo-uncaging as for drug release,¹⁻³ photopolymerization^{4,5} have been described. Photochromic dyes were also explored mostly P-photochromic systems.⁶⁻⁸ Few examples are found with T-photochroms.⁹⁻¹²

On the other hand, the use of photochromic dyes to control the emission of a nanoparticle has been shown in the group (P-photochrome and ZnO)¹³ and elsewhere (spiropyran and CdTe¹⁴ or CdSe@ZnS¹⁵; P-photochrome and quantum dots.^{16,17} To reach our goal, we planned to couple a UCNP to a suitable photochromic dye, whose photochemistry would be powered by the UCNP itself. Because the colored form of a photochromic organic dye has usually a spectrum that covers the UV and (part of) the visible range, some lines of the Ln-UCNP (particularly the NIR one) can be kept free of any perturbation and could be used to track the object.

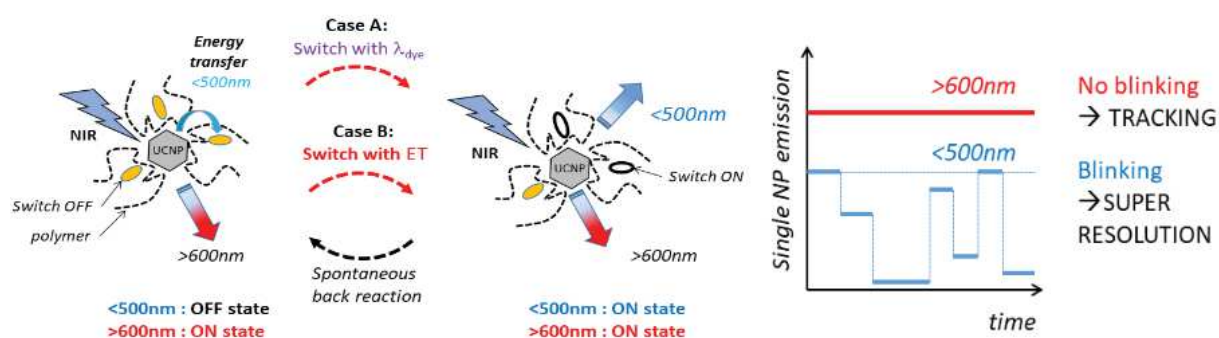


Figure 1. The BLINK project with the 2 treated cases to monitor the high ($<500\text{nm}$) and low ($>600\text{nm}$) energy emissions of the UCNP with a bound photochromic dye. **Case A** the dye is operated with an independent wavelength: the sample will be illuminated with NIR and λ_{dye} . **Case B:** the dye's photochemistry is UCNP-sensitized via RET: only NIR illumination is necessary. On the right, the resulting effect on both emissions at the single NP level. The dye's quenching dynamics affects only the emission $<500\text{nm}$.

The ideal dye should therefore meet the following criteria

- Because the re-emitted energy (in relative intensity: peaks height) decreases enormously from the NIR to the UV, the dye should be operated in the visible range,
- and, for the same reason (few or no UV light available), should reverse back to its original form spontaneously.

This fits the profile of a negative, T-photochromic compound.

The questions will then be how to keep the dye in close proximity to the nanoparticle, whatever the mechanism expected for the energy transfer between the two components, and how such an "immobilization" would impact the dynamics of the dye. We therefore chose a polymer-based nanohybrid structure benefiting from the expertise of the team in this field. To reach this point a dye with a suitable anchoring handle had to be developed and a capping polymer had to be selected.

I.2 Photochromic dyes

Photochromism is a general property, not related to a specific chemical feature.¹⁸ It is defined as a color change induced by light, and this color change must be reversible. That is, conditions reversing the coloration should exist.

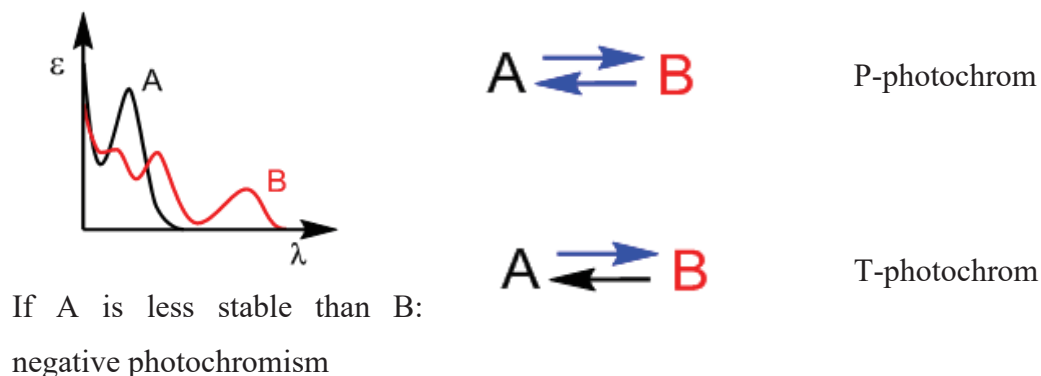


Figure 2. Spectral difference between the two isomers of a photochromic compound: B is the “low gap” isomer, A is the “high gap” one. Definitions of P- and T-photochromism: (Blue arrows photochemical processes; black arrow thermal process.

This property exists in inorganic materials (typically via photoinduced redox reactions)¹⁹ and organic compounds. Photochromic materials have been classified first according to the number of mandatory photochemical processes to achieve the color changes:

- *T-photochroms* require only one photochemical process: if the light is switched off, the material returns to its original state.
- *P-photochroms* are interconverted between the two states by light only: the color change persists in the dark.

Another level of classification is on the color of the most stable state that these materials can present:

- *Positive photochromism* gathers materials that are stable in the colorless form
- *Negative photochromic* materials are stable in the colored form.

Inorganic Photogray® glasses by Corning or organic Transition® by Essilor are typical examples of positive, T-photochromic materials.

Photochromism consists of photochemical reactions, described by *quantum yields* (Φ_{AB} for the $A \rightarrow B$ process, Φ_{BA} for the reverse), backed by *thermal* or “dark” reaction processes (k_1 and k_{-1}).

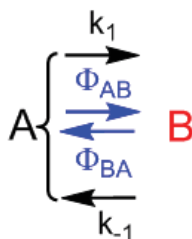


Figure 3. Kinetic processes describing photochromism. black: thermal forward (k_1) and backward (k_{-1}) Blue: photochemical processes: $A \rightarrow B$ and $B \rightarrow A$ quantum yields Φ_{AB} and Φ_{BA} .

Other important parameters are the extinction coefficients of the photoisomers, in particular at the wavelength used to trigger the process. The major kinetic issues come from Beer-Lambert’s law:

- in a solid material or in a non-/poorly stirred photoreactor, light is spatially unevenly absorbed thus concentration gradients, and potentially inner filter effects, occur;

- the fact that the starting material’s concentration evolves with time makes the apparent rate constant a function of time: as the photoreaction progresses the transformation becomes more and more sluggish. The photokinetic factor F , $F=A/(1-10^{-A})$ with A the total absorbance at the irradiation wavelength, is responsible of this property. Therefore, direct numerical fits of the kinetic curves are preferred to retrieve thermodynamic, kinetic and spectral parameters.²⁰

Because of the presence of backward reaction(s) (that can occur simultaneously as the forward process), the transformation is usually not complete: a *photostationary state (PSS)*, defined as the ratio of the two photoisomers’ final concentrations, is reached after an infinite irradiation time. Interestingly, for a simple A-to-B, “ideal” transformation, the initial slope of $d[A]/dt$, containing both forward and backward processes, can be very steep only because of efficient antagonist processes.

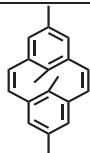

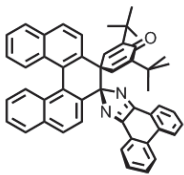
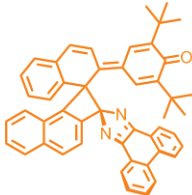
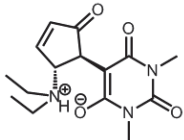
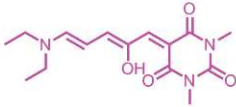
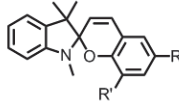
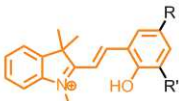
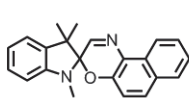
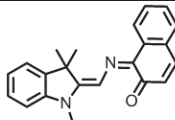
Photochromic materials have been developed mostly for optics (as in the above-mentioned example of the sunglasses). Optimization is guided by three criteria: the colorability (related to the proportions of the PSS and to the extinction coefficients of the species at the observation wavelength), the rate of coloration changes (linked to the quantum yield of the reaction and the rate constants of all processes) and the cycling ability (benchtop stability and photobleaching).

New applications of organic photochromic compounds as “photoswitches” can be found in Physics (from data storage to molecular electronics)²¹, Chemistry (photoswitchable catalysis or supramolecular chemistry)²² and Biology (optogenetics).²³ In particular, natural photochromic fluorescent proteins are used for superresolution microscopy.

I.3 Organic negative T-photochromic dyes

For organic compounds, photochromism is due to a photochemical rearrangement of the bonds. With the exception of hexaaryl-bisimidazole compounds (“lophines”) that are split in 2 radicals (homolytic σ -bond cleavage) or triphenylcarbinols (heterolytic C-OH bond cleavage), this reaction is essentially an isomerization (first order with respect to the organic material). The high HOMO-LUMO gap (i.e. the high-energy absorbing) isomer is the “colorless isomer”, the low HOMO-LUMO gap one, the “colored” one. The energy gap change is due to a deconjugation or to an aromatization of the structure. There is no specific architecture attached to photochromism and discovery of new compounds is usually based on serendipity. Furthermore, negative T-photochromic dyes were poorly explored, as, for the eyes, coloration is more easily detectable (and spectacular) than bleaching. Therefore, the desired property is shared only by a limited number of compounds. Most are gathered in table 1.²⁴

Table 1. Main families of negative, T-photochromic dyes

High energy form	Low-energy form	family
		dimethyl-dihdropyrene/ metacyclophane-diene
		Methylenequinone- imidazole
		“Donor-Acceptor Stenhouse adducts”
		Spiropyran
		Spiro-naphtooxazin

The dimethyl-dihdropyrene/metacyclophane-diene is an example of an “all carbon compound”. Its chemistry is limited due to a rather difficult access.²⁵

The “methylenequinone-imidazole” family was recently introduced by Jiro Abe’s laboratory.²⁶ This dye is the fruit of a long exploration of hexaaryl-bisimidazoles and related dyes and was developed to obtain fast switching rates. However, such molecules are prepared after very long syntheses, and some important oxidation steps are not compatible with further functionalization.

The “Donor-Acceptor Stenhouse adduct” (DASA) compounds are one the most recent family of negative, T-photochromic compounds discovered.²⁷ Spectrally very interesting with a single sharp band in the visible for the colored form and a UV-only spectrum for the colorless one, these compounds suffer from a photochromism that is very solvent dependent.

I.4 Spiropyran dyes

The spiropyran and spirooxazins are classically positive, T-photochroms, easy to prepare, some being commercially available. The spiropyran motif is usually called “BIPS” for “BenzoPyran-Indolenine-Spiro”²⁸, and is typically prepared by the Knoevenagel reaction between a salicylaldehyde and a Fischer base (methylene-indolenine). These molecules switch from closed “colorless” *spiro* forms SP to colored, open, flat merocyanine forms MC, starting by the heterolytic C-O bond cleavage followed by molecule unfolding steps. As a push-pull compound, the MC form exists under two mesomeric forms, a quinoid, non-aromatic one, and a zwitterionic, aromatic one, the latter being responsible for thermal ring closure by direct nucleophilic attack on the iminium moiety. Thus, the colorability improvement of these dyes aimed at favoring the quinoid form (annelation in the naphthooxazin series), reducing the charge density on the anionic atom (electron withdrawing group in the spiropyran series: “nitroBIPS”) or increasing the hindrance on the iminium ion (bulky substituents).²⁹ (figure 4).

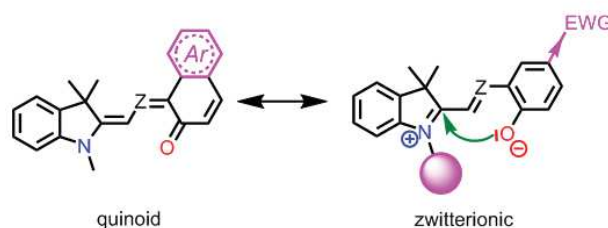


Figure 4. Merocyanin mesomeric forms and stabilization strategies to improve colorability. Annelation with an aromatic ring is used for spiro-oxazin series ($Z=N$).

Although more stable than spiropyran (better photostability), the intrinsic electron-deficient character of spirooxazins make them less sensitive to acidic guests (H^+ , M^{z+}) and therefore these dyes are much less represented in sensing/actuating applications.³⁰

The very large change in geometry, polarity and hydrophilicity made them essential in supramolecular sciences. Furthermore, the zwitterionic form can bind to metals or protons and several sensors applications exploit this particularity. These recent applications of spiropyran have been recently and exhaustively reviewed by Rafal Klajn.³¹

Protonation of the MC form induces large spectral blue-shifts, and usually destabilizes the closed SP form shifting all “dark” processes to the MCH^+ state. Interestingly, the compound is

then a negative, photochromic compound.³² This property is thus bound to the pK_a of the MCH^+ -phenol group: the higher the better. This goes against the classical optimization above-mentioned! The renewal of the exploration the negative photochromic compound was launched as such dyes are cheap, easily introduced in larger structures and present a very large spectral difference between colored and colorless forms.²⁴

Their sensitivity through the above-mentioned reactions with guests makes them suitable photoactivatable actuators or sensor units. Main applications are found in three directions described below.

I.4.1 Reversible photoacid

The protonated merocyanine form MCH^+ of a spiropyran can be considered as a reversible photoacid. In particular a simple water-soluble dye initially proposed by Li³³ was completely explored in our team for such a purpose (figure 5).³⁴ The photoreaction was initially written as



Therefore, the expected pK_a variation was considerable, from a phenol to a sulfonic acid. The study aimed at determining the number of relevant species to explain the observed pH drop, and also to quantify the “strength” of the photoacid, upon reaction with a weak base. The conclusions were *inter alia* that the protonation of the closed SP form (whose concentration builds up as the photocyclization progresses) eventually scavenge some protons, thus limiting the acidity window explored. This illustrates a common problem in photoswitchable chemicals: time-dependent speciation issues.

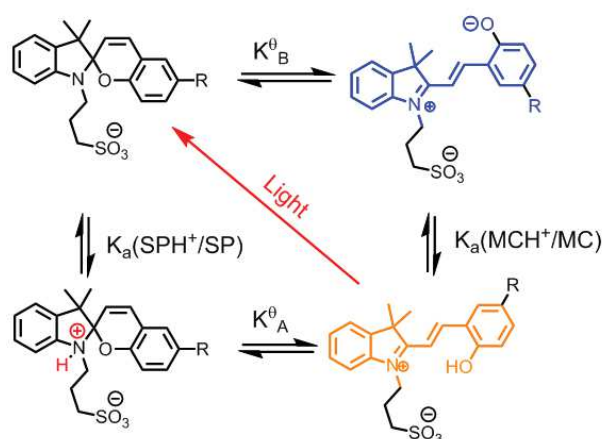


Figure 5. Kinetic scheme used to describe the “Li photoacid” by Vallet *et al.*³⁴

Nevertheless this simple photochromic compound is now commonly employed to trigger protonation reactions, for instance to trigger polymerizations.⁵

I.4.2 Negative photochromic hydrogels

The exchange of protons with the surrounding medium and the very large change of polarity and charge accompanying the MCH^+ -to-SP isomerization can be used to trigger photomechanical effects. In the literature, several hydrogels have been realized where the photochromism induces changes of swelling of the hydrogel. To achieve this, the usual strategy is to prepare a spiropyran-containing monomer. As explained above, the introduction of an esterified phenol group at the *para* position to the MCH^+ phenol increases its pK_a , therefore the working pH window (close to neutrality) is less aggressive. Therefore, most of the reports involve the acrylate of OH-BIPS, a spiropyran deriving from 4-hydroxysalicylaldehyde. Spectacular applications can be found as phototriggered microvalves for microfluidic circuits (figure 6).³⁵ Very active groups in this fields are in Japan (K. Sumaru),^{35,36} or in Ireland (D. Diamond).^{37,38} Great care about the local environments (“self-protonating hydrogels”) and electronic effects (pK_a engineering) are taken to increase the change rate between the “OFF” (swollen) and “ON” (shrunken) states.³⁷

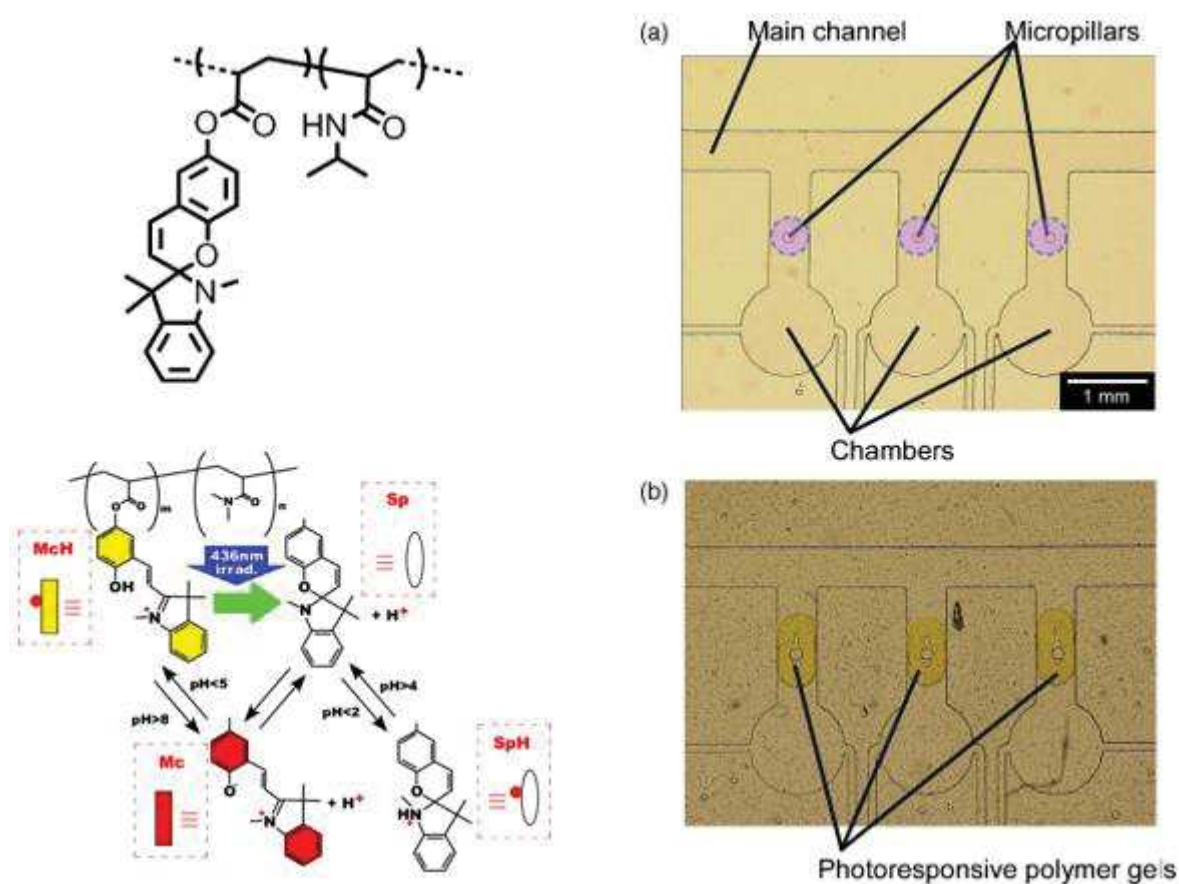


Figure 6. PNIPAM derived photochromic hydrogel developed by Sumaru *et al.* Left: Polymer used and speciation of the dye according to the pH.³⁶ Right : Example of microfluidic photosensitive valves.³⁵

Swollen states are typically due to the charged, open-forms. Interestingly, the number of pertinent species necessary to describe photochromism can be reduced depending on the pH window used. As an example, the group of S W. Thomas has recently described the behavior of spiropyran bound to water soluble polymers. Instead of four species (MCH⁺, MC SPH⁺ SP), the observed properties can be derived from a three species model SP, MC and MCH⁺ (figure 7).³⁹

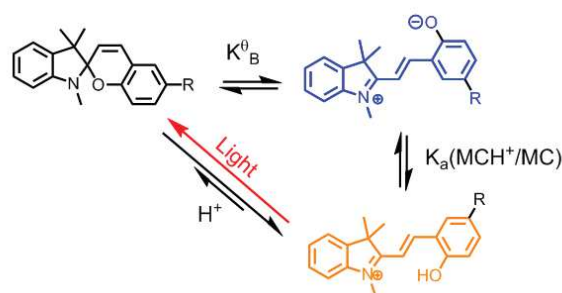


Figure 7. Speciation of the spiropyran embedded in a water-soluble polymer according to Feeney *et al.* in the pH window 5-9.

I.4.3 Photoactivatable “Staples”

This is not directly related to the negative photochromism but has to be considered when using spiropyran dyes. Indeed, beside their planar shape, the zwitterionic presents a very large dipole moment. Consequently they easily form aggregates via π -stacking.⁴⁰ Once aggregated, the dynamics of all processes can be extremely slowed. Thus, Achilleos *et al.* succeeded at the preparation of hollow nanocapsule based on this concept: a silica bead ATRP-macroinitiator is decorated by polymerization with a brush of polymerized spiropyran monomer (figure 8). Upon irradiation for a long time, the stacking of the MC-form induces a supramolecular reticulation of the polymer corona, sufficiently stable so that the supporting silica can be dissolved in HF. The result is a hollow capsule.⁴¹

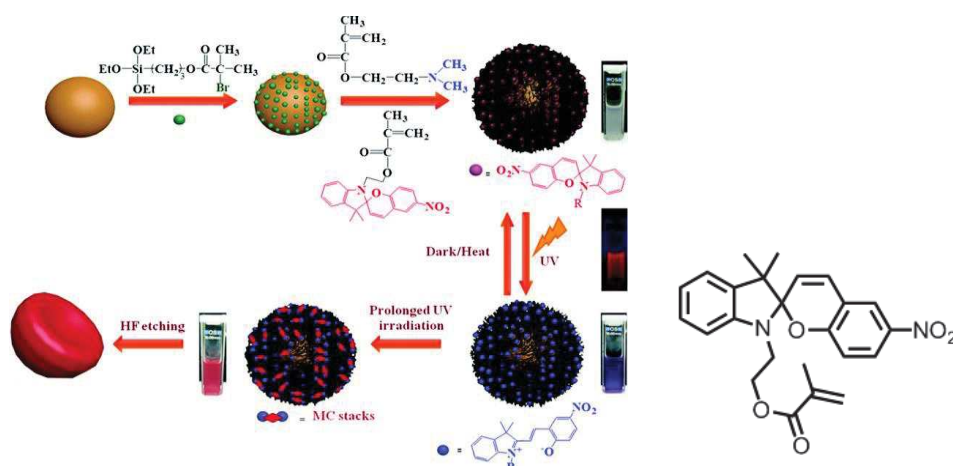


Figure 8. Preparation of a hollow capsule according to Achilleos *et al.*⁴¹, and photochromic monomer used for this objective.

I.5 Aim of the chapter

In view of what was explained in the introduction (chapter 1) we have chosen the following strategy for the grafting of the photochromic dye.

To simplify the encapsulation, we moved to a completely hydrophilic strategy involving the complexation of bare nanoparticles with a polyanionic ligand.⁴²

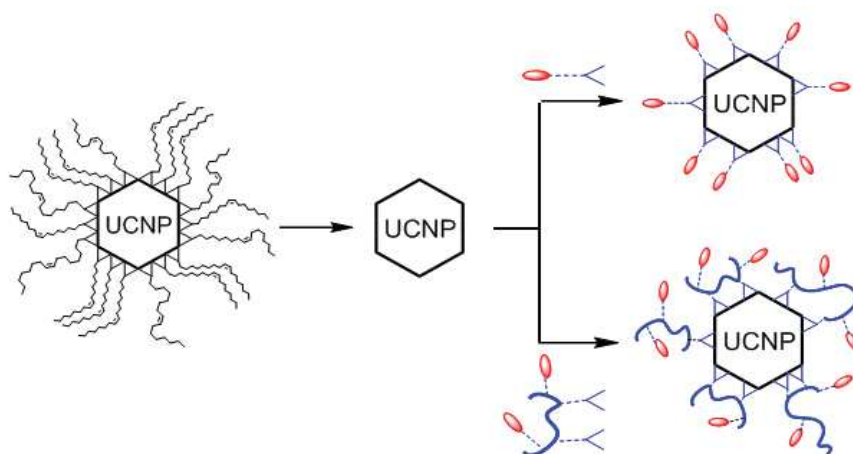


Figure 9. Strategies explored to build our nanohybrid

The technical specifications addressed in this chapter are the following (Table 2):

Table 2. Technical specifications towards UCNP-based blinking nanohybrid for super-resolution microscopy

Choice of UCNP	Choice of photochromic dye	Towards blinking nanohybrid
<ul style="list-style-type: none"> • Emission spectra adapted • UCNP brightness 	<ul style="list-style-type: none"> • Spectral overlap with UCNP • Photochromic behavior in water • Stability of the dye in water 	<ul style="list-style-type: none"> • Nanohybrid architecture <ul style="list-style-type: none"> - formation of the nanohybrid - characterization - post-functionalization possible? • Conservation of photochemical behavior in the nanohybrid • Validation of the dye photoswitching induced by UCNP emission • Is it a blinking nanohybrid? • Performance in super-resolution microscopy

II Toward a negative photochromic spiropyran based UCNP nanohybrid

II.1 Strategy for dye integration: UCNP ligand exchange

II.1.1 Removal of OA

According to Dong *et al.*'s procedure⁴³ introduced in chapter 1 (section water-solubilization), again OA removal was achieved via the NOBF_4 way. After uncapping the surface, UCNPs were isolated by precipitation with chloroform and centrifuged. The precipitation/centrifugation process was repeated 3 times in order to eliminate oleic acid and NOBF_4 derived side-products. Eventually, particles are stored as a suspension in DMF. They are soluble in water or DMF. Remarkably, when the bare UCNPs are dispersed in water, the observed pH is around 5 indicating a strong interaction of the particles with water as already noticed.⁴⁴

The UCNP@oleate (black, figure 11) IR spectrum is mostly dominated by the CH (2850 cm^{-1}) and the two carboxylates vibrations (1458 and 1558 cm^{-1}) of the oleate ligand. These two latter bands at 1458 and 1558 cm^{-1} are respectively characteristics for the symmetric and asymmetric stretch vibrations of carboxylate. According to S. Masur *et al.*⁴⁵ and G. Deacon *et al.*,⁴⁶ such a wavenumber separation (lower than 110 cm^{-1}) reveals that oleate ligand interaction with UCNP is due to a chelating bidentate interaction (figure 10).

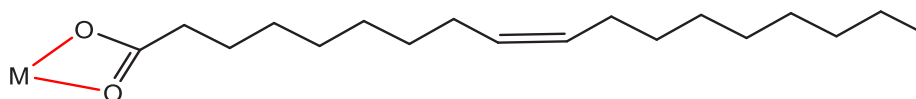


Figure 10. Schematic representation of the interaction between oleate and UCNP. M representing metal at the NP surface.

After treatment with NOBF_4 , and after repeated washings to eliminate reactants and side products, one can notice a complete modification of the spectrum. In particular, the oleic acid vibrations are quantitatively replaced by the DMF and BF_4^- (orange spectrum) one.

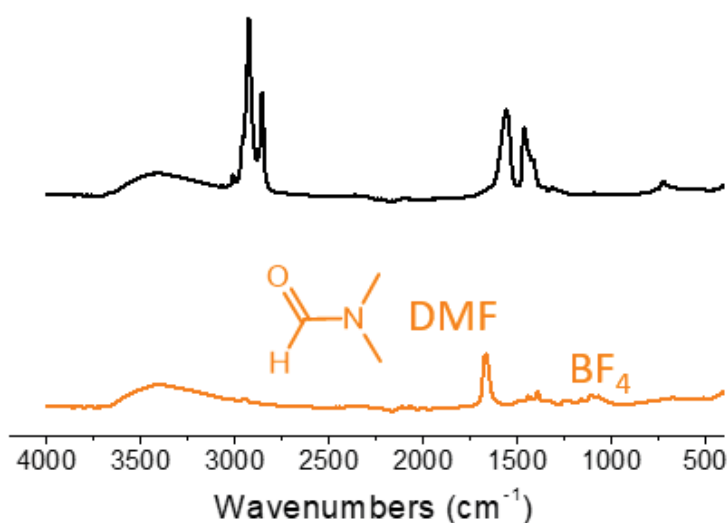


Figure 11. FTIR spectra of A) UCNP@OA. B) UCNP obtained after OA removal.

As a first proof of concept of the easy surface functionalization, we coated them with different kinds of ligands. We have chosen the stoichiometry commonly adopted but not rationalized (Dong and Mely),^{43,47} that is, using same concentration in mg mL^{-1} of bare UCNP and ligands, assuming that it represents a large excess of ligands (ex: 100 mg of ligand to treat 100 mg of bare UCNP).

II.1.2 Different surface functionalization

The isoelectric point of bare UCNPs being about 5.8, the particle can accommodate various types of ligands able to exchange electrostatic or coordination interaction with the surface. The coating is achieved by simple mixing, of a DMF suspension of bare nanoparticles with a solution of the desired ligand in an appropriate solvent. Particles were isolated by repeated centrifugation/redispersion in water. After dialysis against deionized water (2-days, membrane cutoff 12-14 kDa), aqueous suspensions were freeze-dried. As a first proof of concept of the easy surface functionalization, we coated them with different kinds of water-soluble ligands: monodentate (o-phosphorylethanolamine (AEP)) or polydentate ligands such as poly(allylamine hydrochloride), poly(acrylate)-*b*-poly(ethyleneoxide) (PAA-*b*-PEO), poly(vinylphosphonate) (PVPA) of poly(vinylphosphonate)-*b*-poly(ethyleneglycol) (PVPA-*b*-PEG). For most of them, such a procedure was followed by FTIR monitoring (figure 12), showing the spectroscopic features of the new ligand. Thus, phosphate or carboxylate characteristic vibrations were noticed when the ligands were AEP or PAA-PEO.

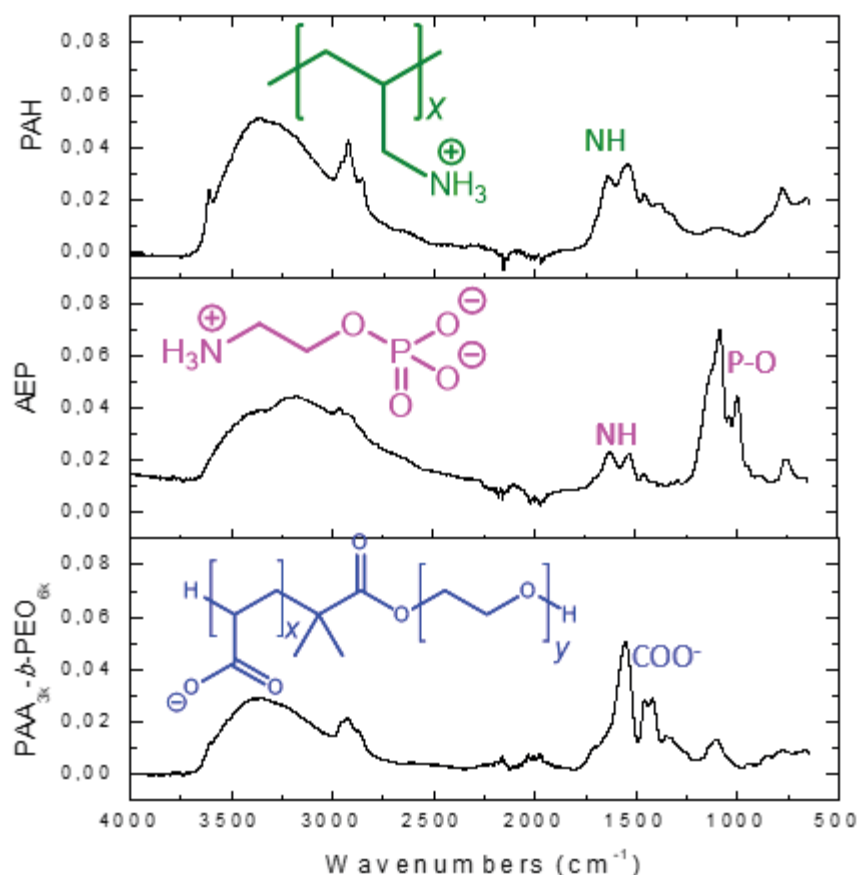


Figure 12. FTIR monitoring of oleate removal and UCNP capping with different surface agents. PAH: Poly(allylamine hydrochloride); AEP: o-phosphorylethanolamine; PAA-b-PEO: diblock Poly(acrylate)-b-poly(ethyleneoxide).

Physicochemical parameters of such new nanohybrids in deionized water could then be recorded (Table 3). The hydrodynamic diameter was obtained by DLS. Aquation of the surface leads to the formation of larger objects than when surface interacts with a ligand. Interestingly the smallest d_h was observed for AEP. Dissolution in water also affects the pH: the highly protonated PAH was found to give rather acidic solutions. Eventually we measured the zeta-potentials under these conditions: a positive potential was found for all the particles examined. The largest values were for the AEP and PAH ligands. Positive charge was found to be in agreement with the expected coordination of the ligands: AEP, interacting through the phosphate head with the nanoparticle's surface would therefore present the amino group to the aqueous solution.

Table 3. Nanohybrid physico-chemical parameters in water, as a function of the UCNP surface ligand.

d_h represents the hydrodynamic diameter.

Surface ligand		BF ₄ -DMF	PAH	AEP
d_h (nm)	Average intensity	930 ± 210	320 ± 130	210 ± 130
	Average Number	950 ± 195	180 ± 95	70 ± 30
	pH	5.14	3.88	5.20
	zeta-potential	+13.9 mV	+32.9 mV	+32.9 mV

Regarding the colloidal stability in water, polyallylamine appeared less efficient and NP settled down quickly. However, UCNP coated by PAA-PEG or AEP were highly soluble and stable for an indefinite time.

The polydentate PAA-PEG poses the risk of multi-NP encapsulation which is an issue for our goal of single NP localization for super-resolution. Additionally, PAA-PEG as hydrophilic stabilizer induces the management of the mixture of 2 ligands, a second one bearing the photochrome. AEP has strong interaction due to its phosphate and free amino group for further functionalization such as dye grafting. Despite the less-than-simple chemistry with AEP (soluble only in water), it was envisioned as the most promising ligand for accurate strongly UCNP-coupled ligand with easy functionalization.

It should be noted that in all cases, average hydrodynamic diameter is highly bigger compared to the one measure from TEM pictures on native nanoparticles (5.5 nm). This can be explained by the fact that NP were stored as dried powder over 6 months, leading to aggregation prior to this measurement of hydrodynamic diameter. It is just used for comparison among different surface ligand.

Another technique can also be used to prove the incorporation of a new ligand in the case of Y-based NPs: NMR, and specifically ³¹P-NMR was envisaged as a valuable tool.

II.1.3 Example of quantitative approach followed by NMR

Thanks to a collaboration with Marvin Langlais, Mathias Destarac and Olivier Coutelier from P3R team at IMRCP laboratory, a PVCL (poly(vinyl caprolactam) model polymer functionalized by a phosphonic acid, “TL-PVCL”,⁴⁸ was available (Figure 13). Following the

ligand exchange process described previously (sections II.1.1 & II.1.2), nanohybrid UCNP@TL-PVCL was prepared. Since lanthanides such as gadolinium (spin 7/2) are paramagnetic they seem to be unfit for standard NMR analysis in solution. Therefore, we decided to use NaYF₄ matrix in order to analyze the organic content at the surface of UCNP.

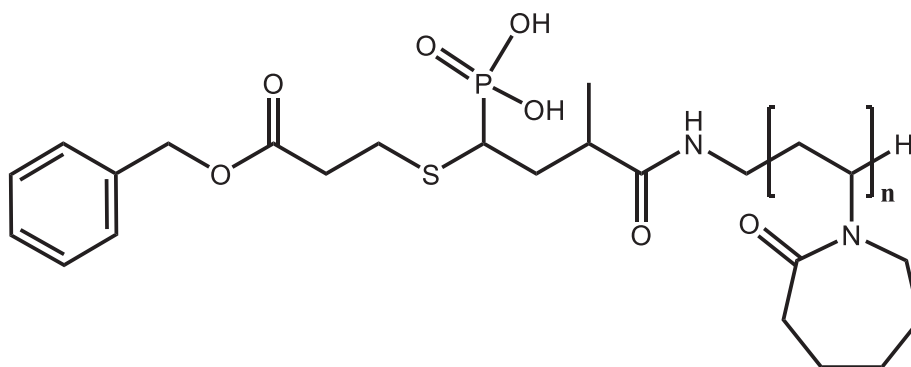


Figure 13. Chemical structure of TL-PVCL

Nanohybrid was built with Tm-doped NaYF₄ nanohexagons of 20 nm (see chapter 1), purified by successive centrifugation followed by dialysis. After freeze-drying, they were dispersed in D₂O.

II.1.3.1 Comparison of ¹H NMR spectra

¹H NMR of the nanohybrid was compared to the above described TL-PVCL (figure 14). Both spectra are similar, attesting the presence of the polymer with UCNP.

Therefore, an analysis in conditions of quantitative NMR was proposed to have a precise determination of the amount of polymer at the NP surface, knowing that each polymer chain is bearing only one phosphonate.

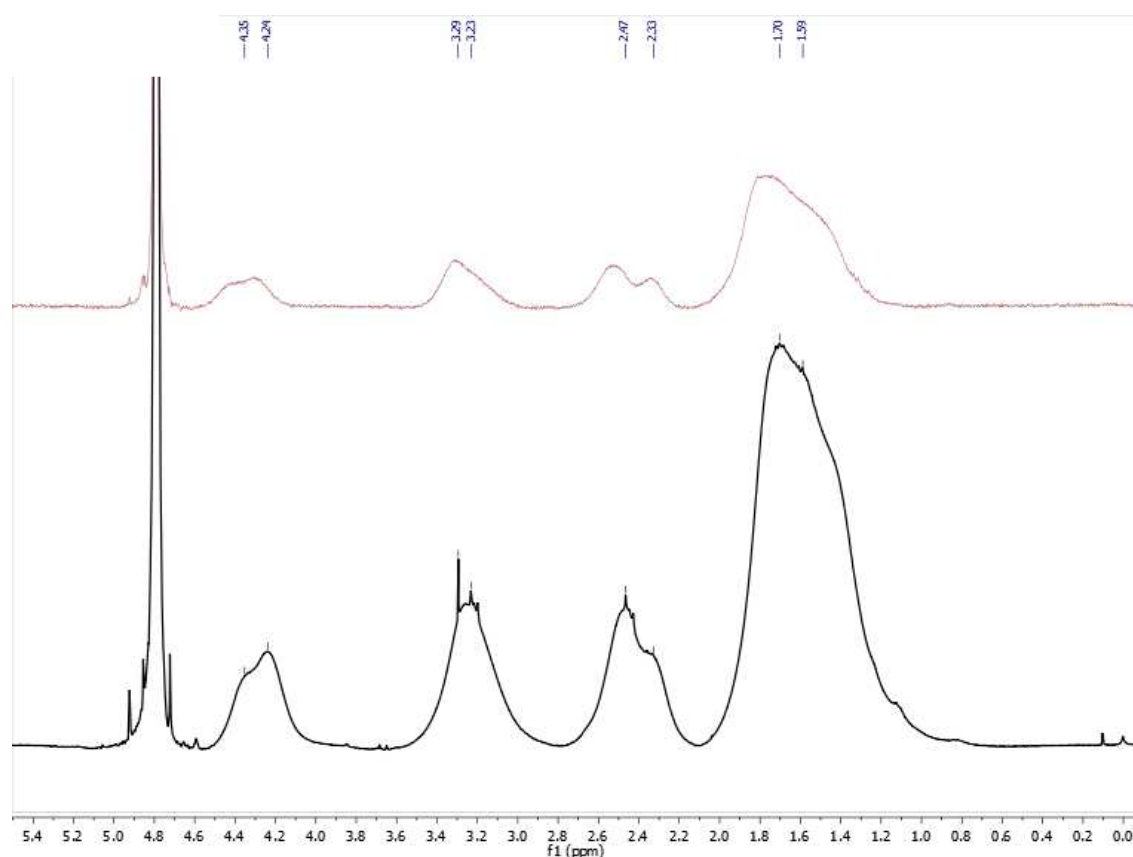


Figure 14. ^1H NMR of TL-PVCL (black) and the UCNP@TL-PVCL (red) in D_2O .

II.1.3.2 Towards quantitative ^{31}P NMR

Methodology

Quantitative NMR^{49,50} relies on the use of another compound, with signal differing from the compound to be quantified. Such standard has to be introduced in a well-known concentration, in the same range of concentration than the tested substance. Therefore, quantification can be deduced by comparing the integrations of the peaks, if the signal-to-noise ratio is higher than 10.

Usually, such a quantification is achieved by mixing directly the standard in the solution to analyze. However, in some special cases it can be isolated from the mixture by using a capillary insert, especially when the standard is not stable in the solvent or reacts with molecules in the solution. In our case, as phosphate and phosphonate have strong affinity to NP surface, it was decided to use a capillary insert to prevent any troubles. As a standard, we used NaH_2PO_4

compound which has a distinct ^{31}P signal at 0.08 ppm than the TL-PVCL expected at around 25 ppm.

However, the use of a capillary insert, enforces an additional calibration to correct the signal discrepancy between molecules in insert and in solution.

Calibration of the reference

The response of a capillary insert of NaH_2PO_4 in D_2O was calibrated by using a more usual standard for ^{31}P : cyclophosphamide monohydrate placed in D_2O solution of similar concentration, in an NMR tube. ^{31}P analysis is shown in figure 15. Integrations were respectively 3.95 and 1 for cyclophosphamide monohydrate and NaH_2PO_4 .

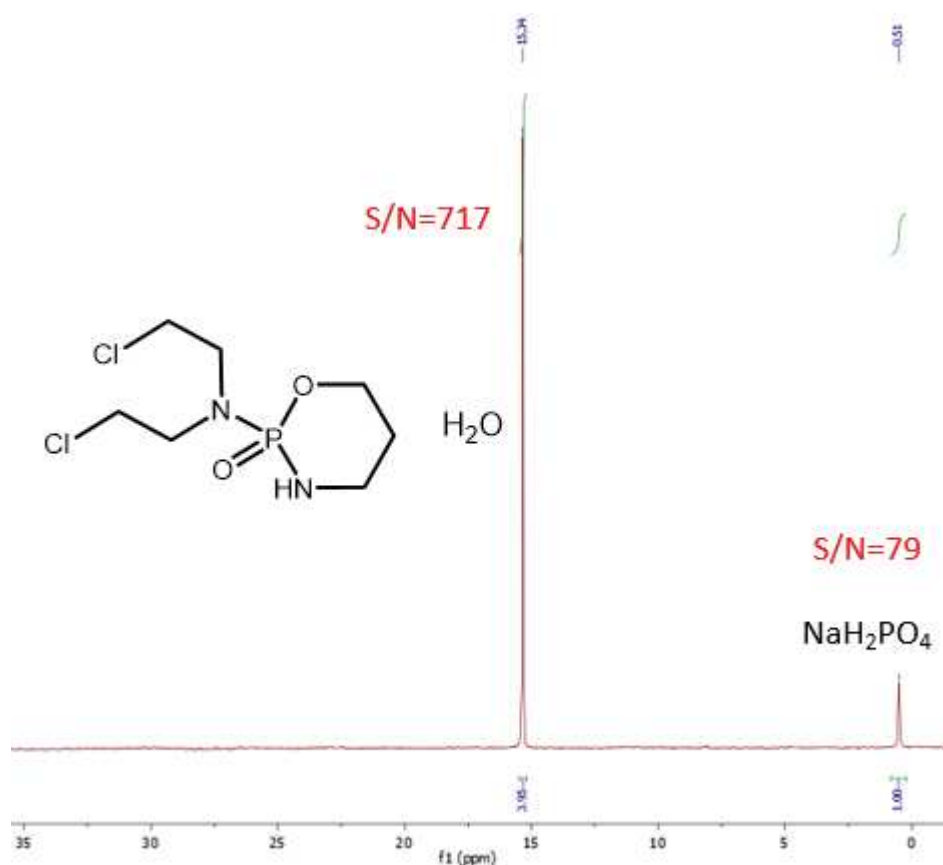


Figure 15. ^{31}P NMR in D_2O solution of cyclophosphamide monohydrate with a capillary insert containing D_2O solution of NaH_2PO_4 recorded with sequence “zig” adapted to quantification. Signal-to-noise ratio (S/N) are indicated to assess the validity of the quantitative condition (S/N must be >10).

This benchmarking allowed us to determine a response factor α from the known concentration of standard (Table 3) and the integration of peaks (figure 15):

$$\alpha = \frac{n(\text{cyclophosphamide}) / n(\text{NaH}_2\text{PO}_4)}{\text{Integration}(\text{cyclophosphamide}) / \text{Integration}(\text{NaH}_2\text{PO}_4)} = 0.1976$$

Table 4. Summary of solutions prepared for NMR quantification.

	NaH ₂ PO ₄	Cyclophosphamide monohydrate	UCNP@TL-PVCL
Concentration (mol/L)	2.124*10 ⁻³	1.838*10 ⁻³	(24.135 mg mL ⁻¹)
Volume (mL)	0.5225	0.4712	0.443
Number of moles mol)	1.11*10 ⁻⁶	8.66*10 ⁻⁷	(to determine)

Quantification of TL-PVCL by ³¹P NMR

Once the benchmarking validated for the capillary insert of NaH₂PO₄ in D₂O solution, we could then analyze our nanohybrid. A solution of 24.135 mg mL⁻¹ of nanohybrid in D₂O was placed inside an NMR tube (table 4). A sufficient number of scans was accumulated in order to get enough signal to have a S/N>10 (ca. 8 h of experiment on 500 MHz Bruker Avance). Result is shown on figure 16. Integrations were respectively 0.65 and 1 for UCNP@TL-PVCL and NaH₂PO₄.

Signals are globally in the same range for both samples. Thus, comparison is accurate. If the difference was more significant, we would have had to prepare a new solution of NaH₂PO₄ standard (less concentrated), to obtain signals of similar intensity than the TL-PVCL analyzed.

Therefore, we could determine the content of TL-PVCL (assuming that there is 1 phosphonate per polymer):

$$n(\text{TL} - \text{PVCL}) = n(\text{NaH}_2\text{PO}_4) \cdot \alpha \cdot \frac{\text{Integration}(\text{TL} - \text{PVCL})}{\text{Integration}(\text{NaH}_2\text{PO}_4)} = 1.43 \times 10^{-7} \text{ mol}$$

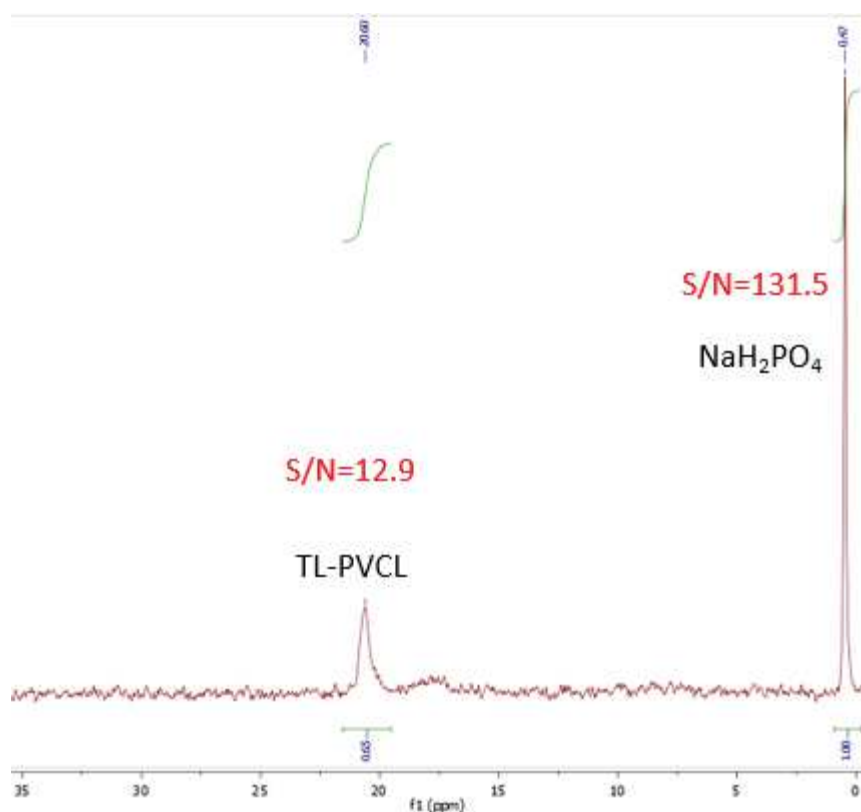


Figure 16. ^{31}P NMR in D_2O solution of UCNP@TL-PVCL recorded in quantitative conditions (with “zgif” sequence), with a capillary insert of NaH_2PO_4 as a standard.

II.1.4 Conclusion on the strategies to make nanohybrid

We demonstrated that a simple user-friendly method allows us to replace OA corona from the NPs surface and enables the storage for long time in DMF solution. Just as easily, the first ligand exchange with several ligands, only by a simple contact, was achieved. Preliminary results with more sophisticated process such as Flash Nano Precipitation (FNP)^{51,52} have been also initiated, but further study should complete this work.

By two analytical approaches, FTIR and NMR, we have shown that we can monitor the presence of a new ligand. Furthermore, since phosphorus does not belong neither to the organic shell nor to the inorganic core, ^{31}P -NMR in quantitative conditions allows the precise determination of ligand load as long as the latter carries suitable functional groups such as phosphate or phosphonate. However, such an NMR monitoring of the organic layer seems to be at the moment limited to NaYF_4 matrix, a method development to extend to paramagnetic elements such as gadolinium would be of interest to generalize it to all the NaREF_4 matrices. It

should be reminded however that NMR (albeit solid state NMR) can also be used to characterize the inorganic moiety.⁵³

Concerning our goal, we checked the feasibility and simplicity to set up new ligand at the UCNP surface. Attracted by the interest of phosphate or phosphonate due to their stronger affinity to lanthanides and their simple quantitative detection either by ³¹P NMR or ICP, we considered as a first choice the use of AEP (monodentate) and polycarboxylate (polydentate) ligand. The next point is the choice of the UCNP-dye couple.

II.2 Choice of UCNP-dye couple

Choice of UCNP adapted to SP dye

At first, we had to choose between “green-emitting” Er-based UCNP or the “blue-emitting” ones doped by Tm. As the photochromic shutter mentioned in the introduction of the chapter is rather limited to spiropyran, we compared the absorption spectra of such a dye, the water soluble (BIPS-SO₃)³⁴ with both kinds of UCNPs (figure 17) the absorption band of the MCH⁺, responsible for the negative photochromism and with its maximum at 420 nm, was found to overlap significantly with the visible emission of Tm-UCNPs. No such overlap was observed with the erbium particles justifying the dopant choice.

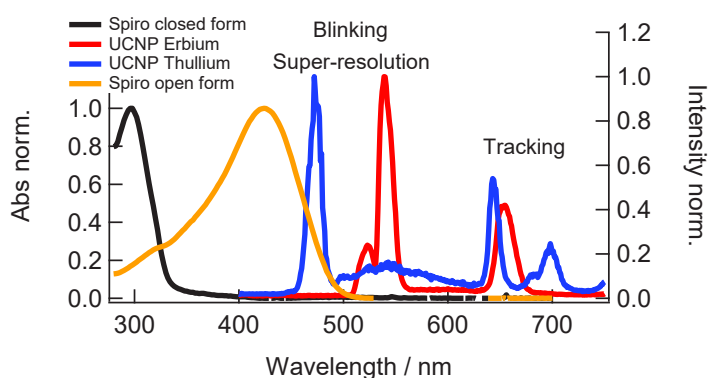


Figure 17. Overlap of UCNP emission spectra and dye absorption.

Therefore, we decided to use this dye and Tm-doped UCNP for our blinking UCNP project. As UCNP emission is dependent on the size of the NP, only “highly emissive” large NP are used in the present chapter, in order to maximize the chances of success. When the proof of concept

and the standardization of the protocol will be established, we will turn then to the use of ultra-small NP. As several experiments are required to evaluate the potential of such a nanohybrid, we focused on the use of the 20-nm nano-hexagons (see chapter 2) as their large stock (3 g) ensures homogeneity of the comparison with an identical batch of NP used for all the experiments.

The problem is now to connect the dye to the particle. Our strategy was to develop a modular architecture with a dye building block to be connected to a ligand building block (figure 18). The aim was to limit the organic chemistry and to offer a general protocol allowing for structural variations on the ligand part.

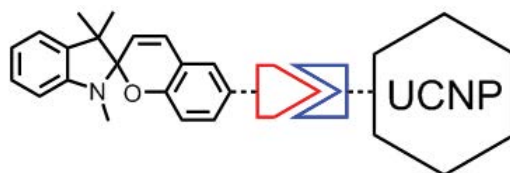


Figure 18. General architecture of the BLINK nanohybrid; the click approach should limit the chemistry onto the dye

Our bank of spiropyran

From previous studies in the lab, several spiropyrans were available. The main difficulty is that small dyes are usually not soluble in water, and that MC (or MCH^+) forms are solvatochromic. Therefore, predicting the perfect dye UCNP overlap would require specific syntheses to explore the behavior of the dye in water (H^+ sensitivity, negative photochromism, spectral overlap).

Tuning SP absorbance to overlap with the NP emission spectrum

NitroBIPS is one of the commercially available spiropyrans. A reduction of the nitro- to amino- group using tin(II) chloride has been described by Zimmermann *et al*⁵⁴ and was tested before this project started in the lab (figure 19). The intermediate amino-BIPS is rather fragile and therefore should be used immediately.

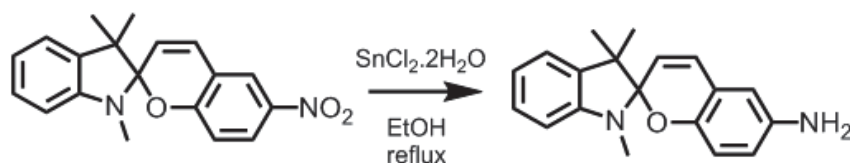


Figure 19. Nitro-BIPS to amino-BIPS reduction by Zimmermann *et al.*⁵⁴

This new functional group constitutes a convenient nucleophilic “handle” to graft this molecule. It is also accompanied by an umpolung of the electronic effect that should reinforce the negative photochromic property. This electron donating effect can be modulated by combining it with an electron-withdrawing one. Thus, from the tabulated Hammett parameters⁵⁵, transformation of the aniline into an amide group would make the amido-SP to behave as the non-substituted compound.

Choice of ligand

We have explored several possibilities, such as a triethoxy-silane derivative of spiropyran, which is currently evaluated by our collaborators. Here, only two examples will be presented: the first connector tried was trichlorotriazine. Due to limited success, we later moved to an amide connection (figure 20). These two routes will be detailed in the up-coming sections.

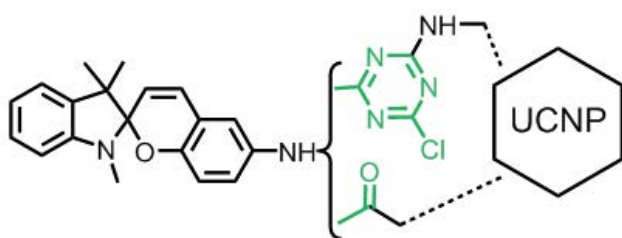


Figure 20. Synthetic strategies to anchor the spiropyran dyes onto an UCNP.

II.3 Synthesis of SP-grafted ligands

II.3.1 Triazine route

Conjugation of amines to polymers via a triazine moiety is well known in textile industry as it has been developed since the mid XXth century for dyestuff. The aim was that covalent dye grafting onto cellulose (or wool) prevent the color from fading away upon washing. An important dye family was released by ICI in 1956 (Procion® dyes). As a consequence, most of the associated literature is made of patents.

II.3.1.1 Use of SP-TCl₂

Preparation of BIPS-TCl₂

2,4,6-Trichloro-1,3,5-triazine (TCT) is a very electron deficient molecule able to undergo nucleophilic substitutions reactions leading to complete replacement of the chlorine atoms. Since a nucleophile is by definition an electron-rich reactant, each chlorine substitution is accompanied by an increase of the triazine ring's electronic density, changing deeply the reactivity of the new compound. This translates into the possibility to define reaction conditions to introduce substituents sequentially on the triazine ring.⁵⁶ Thus, dichloroaminotriazine derivatives are storable, stable for a short time in cold water, and grafting onto cellulose's OH groups occurs above room temperature.⁵⁷ Later, the first PEGylation reagents (non-specific!) were PEG-O substituted dichlorotriazine.⁵⁸

Crude material obtained by the SnCl₂ reduction of commercial nitro-BIPS was thus reacted with trichlorotriazine in acetonitrile at 0°C. Upon addition of diethylether, an orange precipitate was collected. ¹³C-NMR confirmed the monosubstitution product. Remarkably, the hydrochloric acid released by the reaction is scavenged by the dye itself, leading to the hydrochlorate of the functionalized open isomer. The reaction is efficient, and the reactive dye BIPS-TCl₂ was produced with a 53% yield over two steps (figure 21).

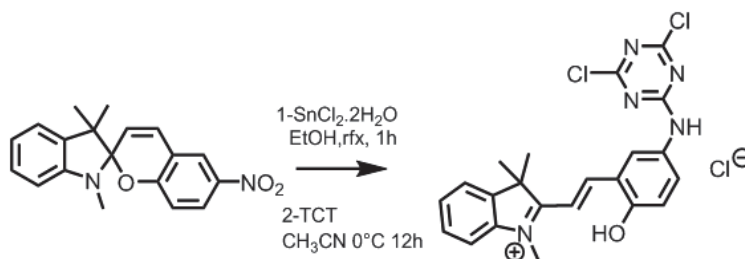


Figure 21. Preparation of the reactive dye BIPS-TCl₂

Spectral overlap

UV-visible spectrum of BIPS-TCI₂ was recorded in EtOH and compared to the emission spectra of Tm-doped UCNP (figure 22). This perfect overlap with the two blue emission (450 and 475 nm) was indeed promising.

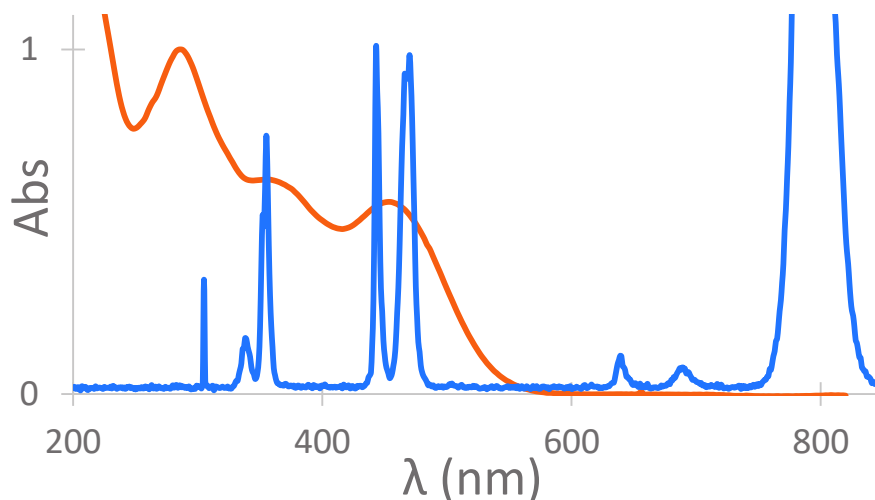


Figure 22. Overlay of the emission spectrum of Tm-doped UCNP (blue, normalized to 1 at 450 nm) with the absorption spectrum of BIPS-TCI₂ in ethanol.

Photochromic of BIPS-TCI₂ behavior in water

Attempt to make BIPS-TCI₂ soluble in water consisted in the monosubstitution of the triazine at room temperature with AEP. As previously shown AEP is a very good ligand for UCNP. Therefore, the aminoethylphosphate moiety was expected to bring water solubility as well as efficient binding ability. Difficulties came from the handling of reactive intermediates in water. Indeed, Both AEP and functionalized final products are soluble in water; their ionic character [and the chameleon-like character of the SP dye (able to change into MC, MCH⁺ forms)] made the purifications very tricky and impaired all attempts to separate the reaction products. Furthermore, to increase AEP nucleophilic reactivity, pH has to be risen up to 10. Under these conditions SP-TCI₂ was found to be very fragile, the chlorotriazine ring being prone to hydrolysis. Although pH-dependent, this reaction is expected to occur (much slowly) at other pH, including during crude material processing and purification. Thus, despite the isolation of the triazine monosubstitution products fraction, mass spectrum revealed that it was an intractable mixture of two products: some part was still bearing chloride, while the second

product consisted in hydrolysis product with hydroxy substitution instead of the chlorine substituent. Additionally, photoswitching attempt in water was unsuccessful. Therefore, this route was abandoned.

II.3.2 The amide route

As it has been mentioned in the general introduction, it is possible to use amphiphilic polymers or polyanionic polymers to make UCNP hydrophilic.⁴² These strategies are derived from what was developed for quantum dots, iron-oxide and other nanocrystals. One interesting route is the use of alternate copolymers of maleic anhydride and an alkene.⁵⁹ Indeed, the final object contains one reactive group per monomer, and therefore can be used as a scaffold to host several components. This strategy to “coat” nanoparticle was made popular by the works of Mattoussi,⁶⁰ Vancso,^{61,62} and Parak⁶³ and others^{64,65} and was adapted to photochromic dyes by Branda^{3,6} and Jovin.¹⁶

The advantages are mainly limited chemical manipulations once the chemical is bound to the polymer beside encapsulation of the nanoparticle.

We therefore explored a route to graft the dye onto poly(isobutylene-*alt*-maleic anhydride) (PIMA) through an amide bond less prone to hydrolysis than an ester one. An important issue is the final colloidal stability. The final polymer will carry carboxylate groups, so part of the stability is ensured thanks to electrostatic repulsion. However, this is pH- and ionic strength-dependent. Further stabilization can be gained by anchoring neutral hydrophilic chains. Instead of classically used oligo-ethylene glycol, we have chosen a small sugar-derived polyalcohol amine, namely D-glucosamine.⁶³ Because this solubilizing group is a small molecule, the elimination of unreacted material from the reaction mixture can be achieved by ultrafiltration. The general route we have developed is exposed figure 23. Beside the preparation of the polymer of interest, a model compound BIPS-GLT was prepared by reacting the amino-BIPS with glutaric anhydride. This compound was expected to be water soluble, so the photochromic properties of the isolated dye could be studied independently of the polymer.

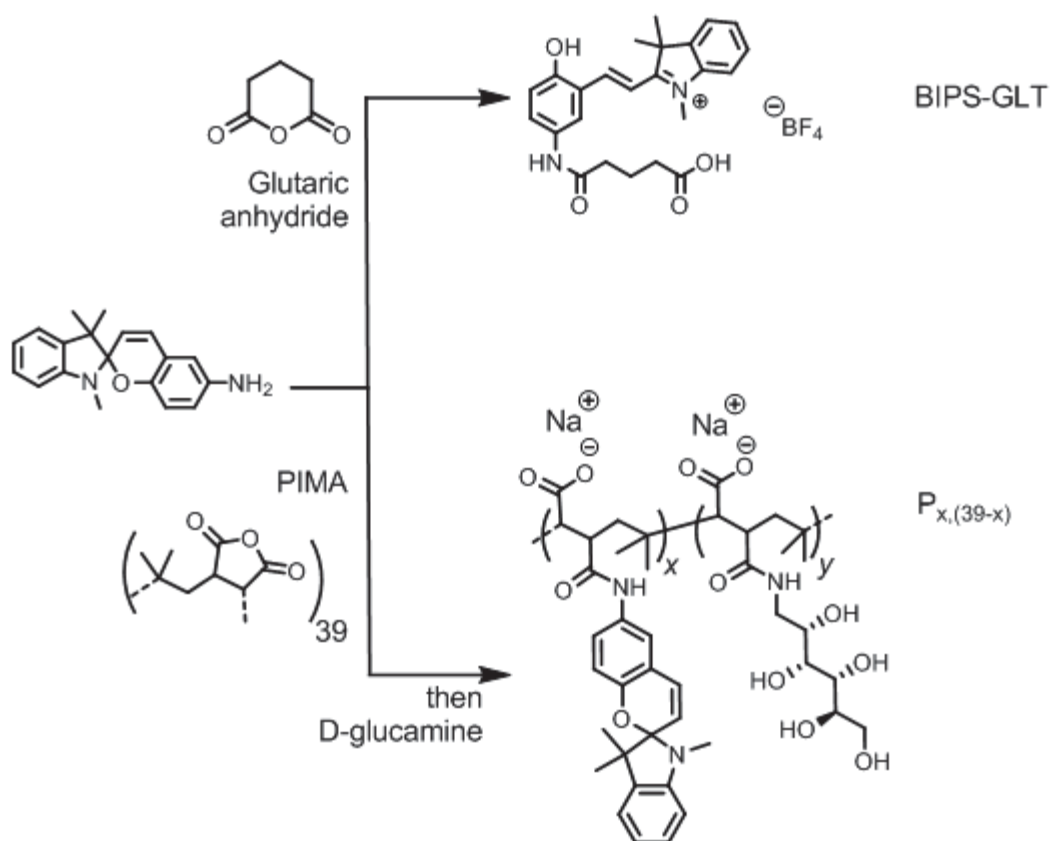


Figure 23. Strategy developed (BIPS-GLT) is a model compound. P_{x(39-x)} is a polymer incorporating x dyes per polymer molecule, starting from polymer chains comprising an average number of 39 monomers per chain.

II.3.2.1 Syntheses

Model compound BIPS-GLT

BIPS-GLT was prepared by reacting crude freshly prepared amino-BIPS with glutaric anhydride. The product was isolated as a tetrafluoroborate salt in its COOH and open, MCH⁺ form.

Polymer P_{x(39-x)} with x=1, P_{1,38}

The commercially available poly(isobutylene-*alt*-maleic anhydride), PIMA, is declared to have a molecular weight of 6 kDa, representing 39 (maleic anhydride-isobutene) monomers per chain. Our target was to incorporate 1 dye per molecule, then react all remaining anhydrides with D-glucamine. This was realized in a two-step process: first reacting PIMA with amino-BIPS in the presence of DIPEA in anhydrous DMF; then the crude intermediate was reacted

with an excess of D-glucamine in water. Final purification consisted in extensive washing by ultrafiltration on a cellulose membrane with a cut-off of 3 kDa. These washings aimed at the elimination of the excess of reagents and organic solvents and replacements of counter-cations with sodium. P_{1,38} was isolated after freeze drying.

II.3.2.2 BIPS-GLT characterization

NMR spectrum of the open form

The open form is characterized by a flat geometry and a strong push-pull effect. That is easily identified in the ¹H NMR spectrum (figure 24). Thus, the very high chemical shift of the double bond hydrogens and the degeneracy of the two CH₃ of the gem di-methyl group of the indolenine are in agreement with an open form: the strong unshielding is caused by the conjugation to the ammonium moiety, while the CH₃ are no longer diastereotopic: (only one singlet at $\delta=1.75$ ppm). Furthermore, the trans double bond geometry is confirmed by the magnitude of the J₃ coupling constant of the double bond hydrogens (signal at 8.45 ppm J=16 Hz).

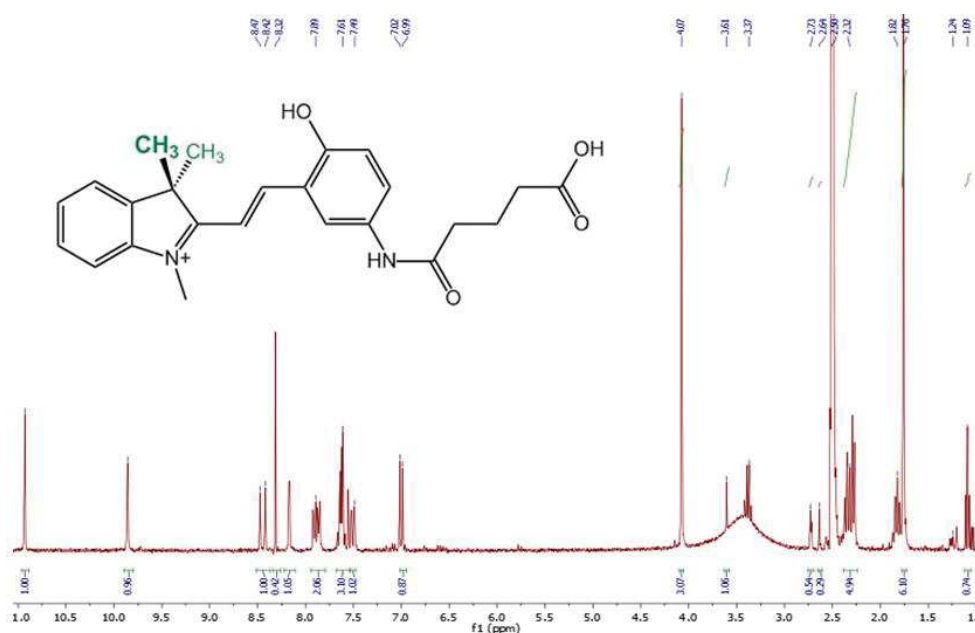


Figure 24. ¹H NMR spectrum of the open BIPS-GLT form.

UV-visible absorption spectra

Absorption spectrum (figure 25) of the BIPS-GLT shows in water A_{max}(MCH⁺) in blue area with $\lambda_{\text{max}} \approx 428$ nm. Even though we can notice strong overlap with 450 nm, a small overlap

is found at 475 nm, these two wavelengths corresponding to the two emission peaks of the “blue emission” of Tm-doped UCNP.

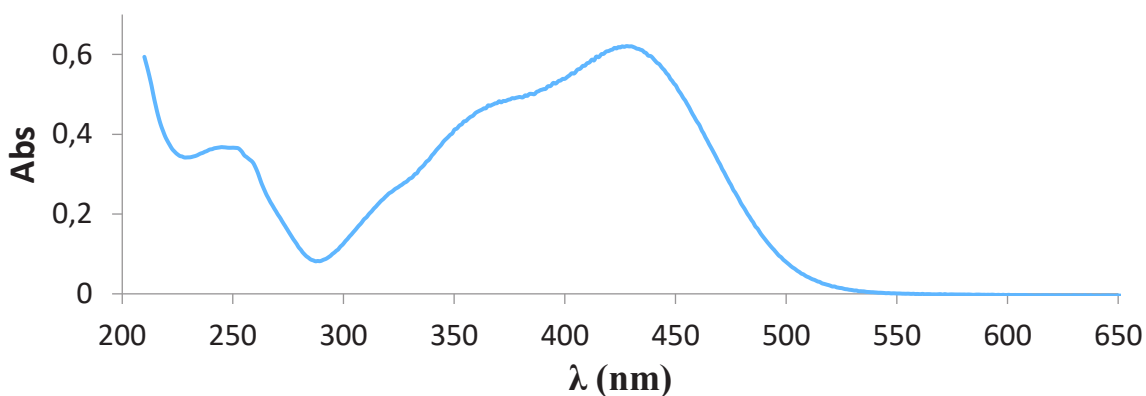


Figure 25. UV-visible spectrum of BIPS-GLT in H₂O at $2.8 \cdot 10^{-5}$ mol L⁻¹.

As BIPS-GLT has proven to be highly hygroscopic, determination of epsilon was made as early as the compound was dried. Four solutions of well-known concentration were independently prepared. Their absorption spectra were then acquired. Therefore, for each measured wavelength, plotting Abs as a function of the concentration gives directly the molar extinction coefficient $\epsilon(\lambda)$ as the slope of a linear fit function. Figure 26 shows the method, while table 5 gathers the result for some wavelength. The table clearly highlights that for energy transfer from UCNP, the 450 nm peak will more contribute due to better spectral overlap and dye absorption (ϵ).

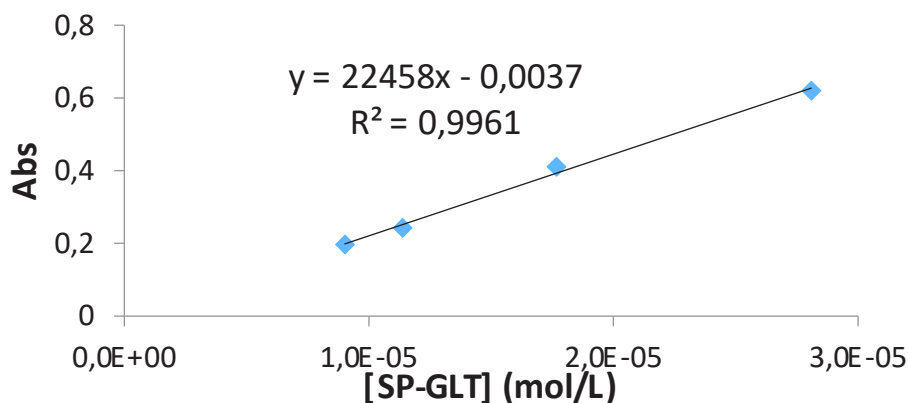


Figure 26. Determination of $\epsilon(\lambda_{\max})$ of SP-GLT.

Table 5. Value of epsilon obtained for wavelength of interest: at λ_{\max} and at the average wavelength of the two blue emissions of Tm-doped UCNP

λ (nm)	$\epsilon(\lambda)$ (L mol ⁻¹ cm ⁻¹)
427.5 nm (λ_{\max})	22500
450 nm (λ_1 (Tm))	19000
476 nm (λ_2 (Tm))	9400

These spectroscopic parameters were used to identify the dye once bound to the polymer

II.3.2.3 Polymer P_{1,38} characterization.

The extent of PIMA modification was controlled at each step. Thus, ¹H-NMR in DMSO was used to confirm the attachment of the dye onto the intermediate polymer.⁶⁶ Next, the glucamine grafting was proven by the same technique (¹H-NMR in D₂O or CD₃OD). Eventually, SEC analyses (Size-Exclusion Chromatography) confirmed the presence of the dye and helped to propose an apparent molecular weight (13100 Da).

II.3.2.3.1 Preparation of SP-grafted poly(anhydride) intermediate

Dye loading determination

¹H NMR of starting commercial product revealed some aromatic impurity (figure 27). We suggest it is coming from polymer end chain probably due to the initiator used. No details about the polymerization conditions employed could be found on the supplier's website (Sigma-Aldrich). Interestingly no peaks are found in the 5-8 ppm zone where some of dye signals are expected.

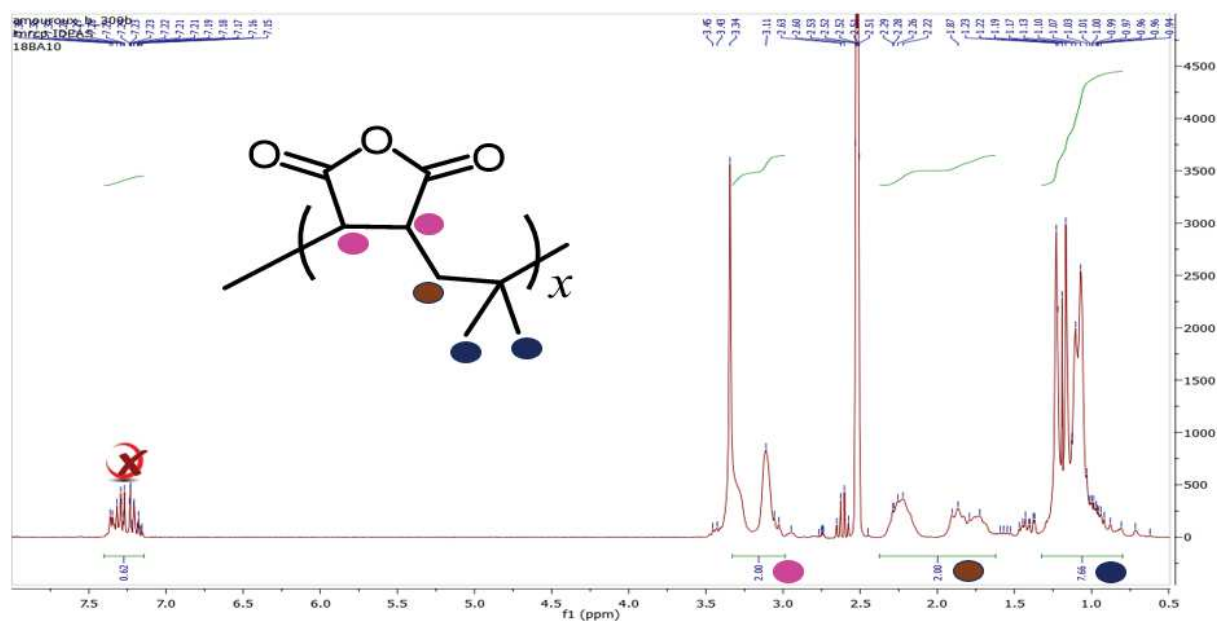


Figure 27. ^1H NMR of PIMA in $\text{DMSO-}d_6$. Peaks were attributed according to De Nolft *et al.*⁶⁷ and Li *et al.*⁶⁶

^1H -NMR spectrum of the intermediate of $\text{P}_{1,38}$ is shown figure 28. Signals attributed to the dye are clearly seen in the aromatic part and match rather clearly with the spectrum of the open form BIPS-GLT. Comparison of the integrations of SP content with the chain one allows the determination of the post-functionalization efficiency. Indeed, 1 H and 2 H signals of the aromatic signals of SP have respectively 0.02 integration, while it is 2 for the CH_2 (1.6-2.4 ppm) and the two CH (3.1-3.4 ppm) of the isobutylene-maleic anhydride monomer. There is 1% loading of SP. Therefore, assuming that PIMA has 39 monomers, there is, on average, around 0.39 dye per chain.

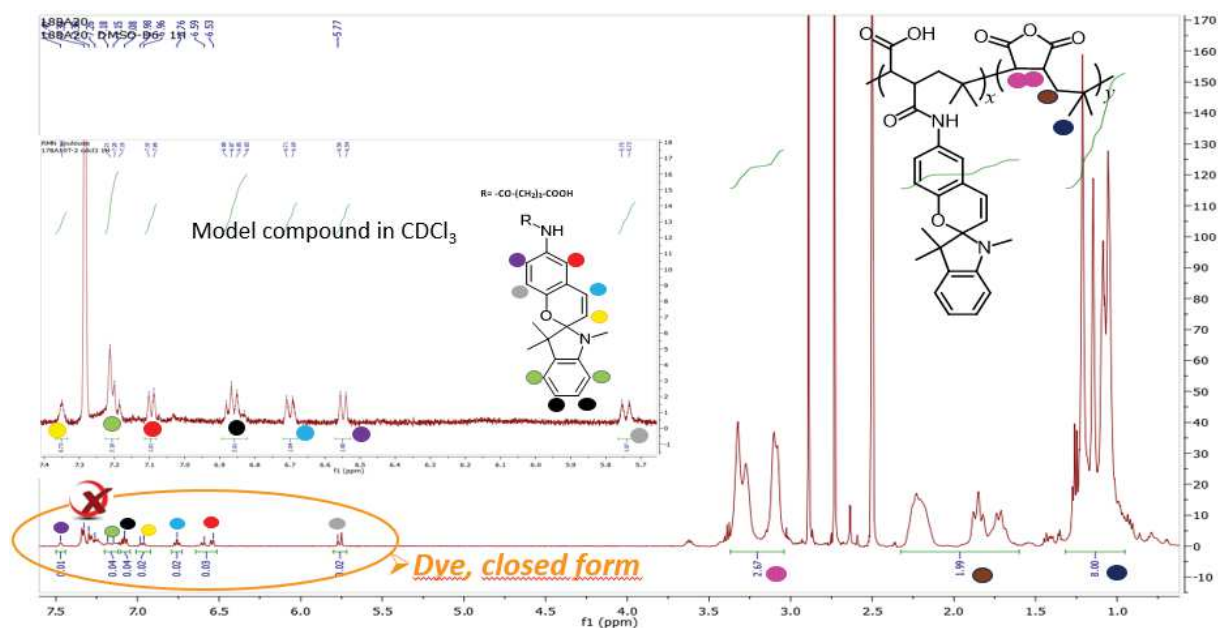


Figure 28. ^1H NMR of the intermediate of $\text{P}_{1,38}$ in DMSO. Offset: spectrum of the model compound BIPS-GLT. For the aliphatic part, broad signals from the polymer backbone were attributed according to.⁶⁷

UV-vis spectrum of the intermediate

Absorption spectrum of the amido-BIPS-loaded PIMA (figure 29) shows similar spectra than the BIPS-GLT. The visible band tails down to 550 nm, thus offering a nice overlap in DMF. The absorption at 450 nm will be used to monitor the SEC analysis in the following.

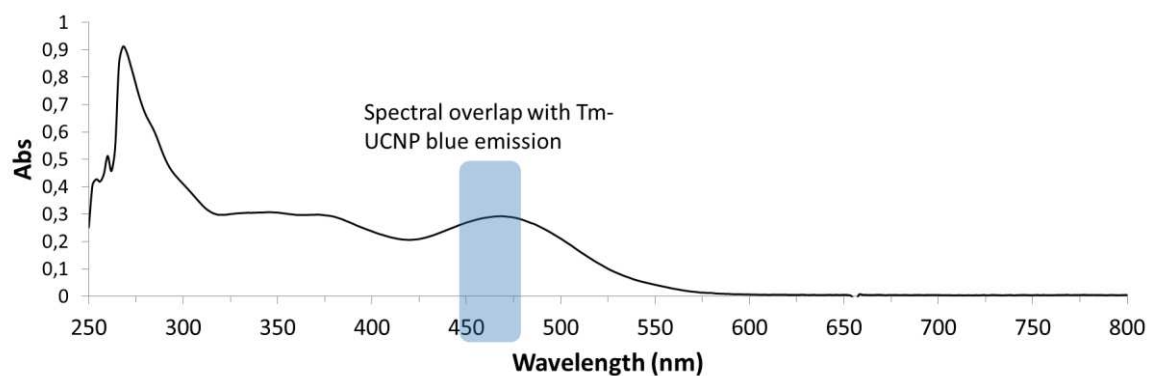


Figure 29. Absorption spectra of the intermediate of $\text{P}_{1,38}$ in DMF eluant for SEC. Blue rectangle indicates the positions of the two blue emissions of Tm-doped UCNP.

Validation of the grafting onto polymer: SEC analysis

The attachment of the dye onto the polymer can be assessed by SEC, by associating polymer elution properties and UV-visible detection of the dye absorption. The chromatograms are displayed in figure 30.

By using monitoring the refractive index, chromatograms of PIMA and our intermediate polymer show similar features. In particular the large change in RI at the very same elution time (ca 11 min) shows that the amount of grafted dyes does not affect polymer size. However, when monitoring the chromatography at 450 nm, the intermediate polymer shows an absorption that was not present in the initial one, revealing the presence of the new chromophore. As a result, the presence of covalently grafted SP-moieties onto polymer was validated.

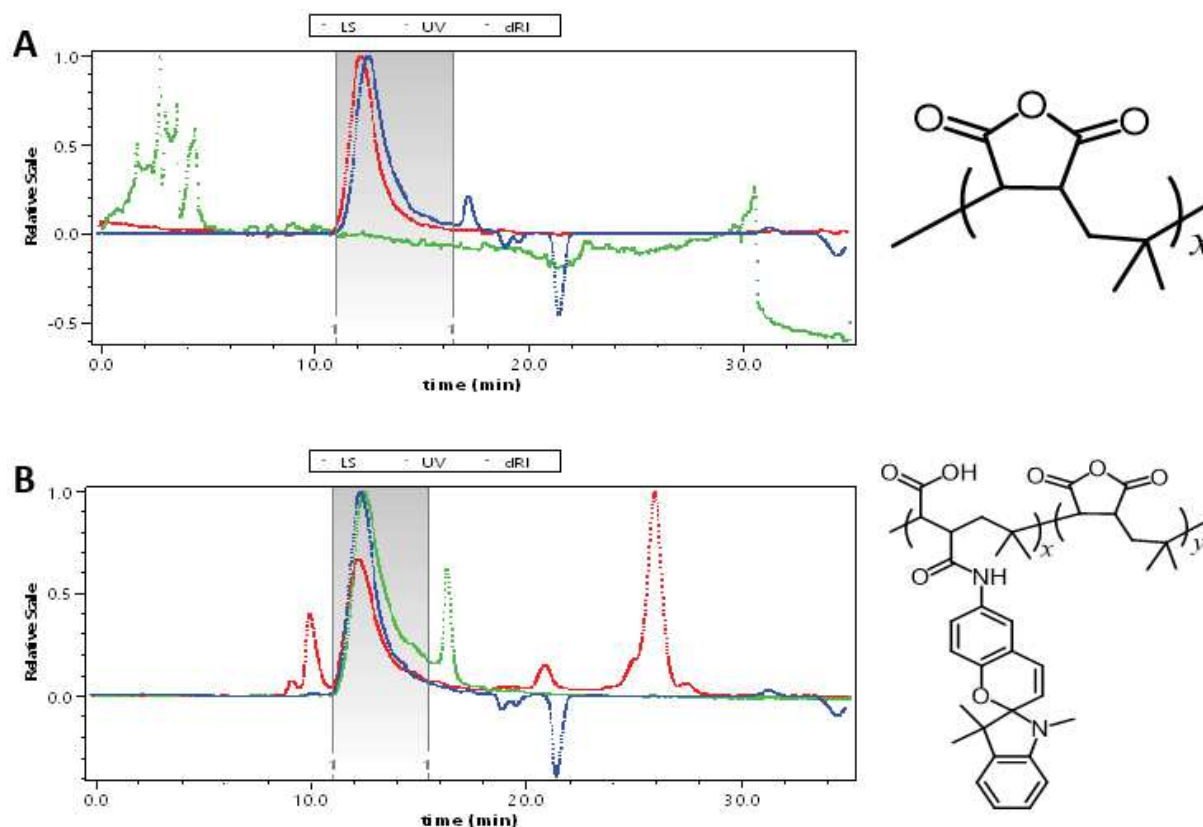


Figure 30. Results of SEC analysis in DMF. Detection by light scattering (LS), refractive index (dRI) and absorption at 450 nm (UV). Two polymers were compared in similar conditions, at a flow rate of 1 mL min^{-1} . A) PIMA. B) intermediate of $P_{1,38}$.

II.3.2.3.2 Synthesis of P_{1,38}

Determination of D-Glucamine loading

The efficiency of D-glucamine loading was again evaluated by ¹H NMR (figure 31).

Comparison of the integrations revealed that quantitative sugar incorporation onto polymer was achieved. However, it is no longer possible to quantify the dye content due to its low loading (0.39 dye per chain). Indeed, in polymer chemistry it is usually challenging to characterize end groups of the chain which generally represent 1 or 2 moiety per chain.

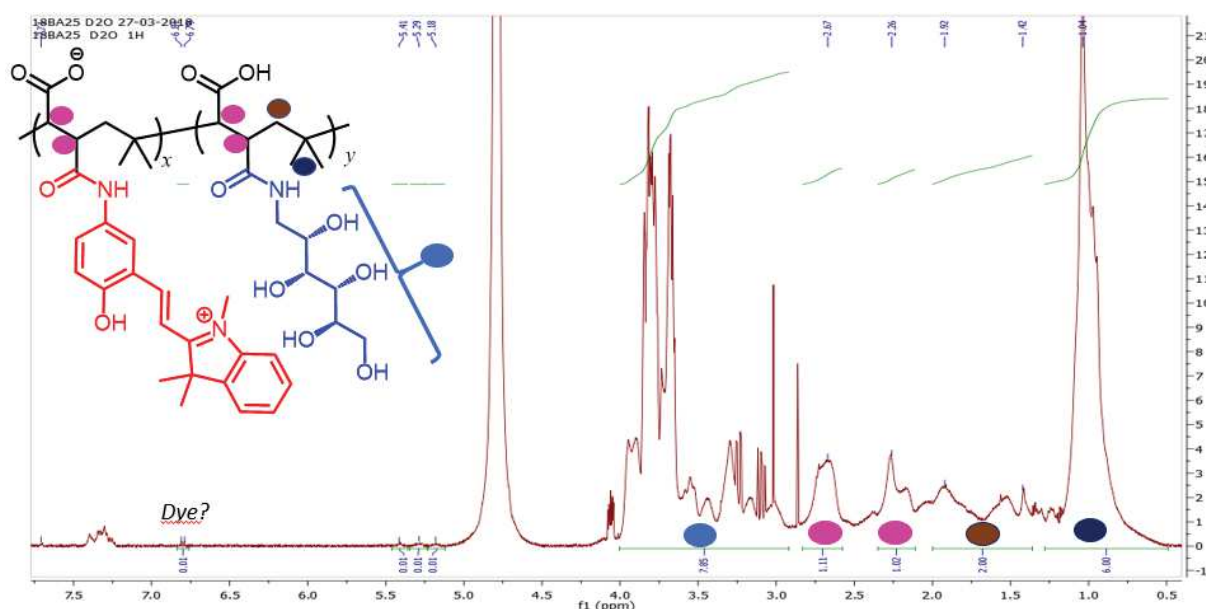


Figure 31. ¹H NMR of P_{1,38} in D₂O.

Validation of D-glucamine grafting

The final polymer was analyzed by SEC in water. As for the intermediate, the final P_{1,38}, a single peak in the chromatogram bearing the 450 nm absorption is obtained at an elution volume of 15 min (figure 32). Therefore, only one monomodal distribution of polymer has been obtained, the glucamine grafting seems to be homogeneous and quantitative.

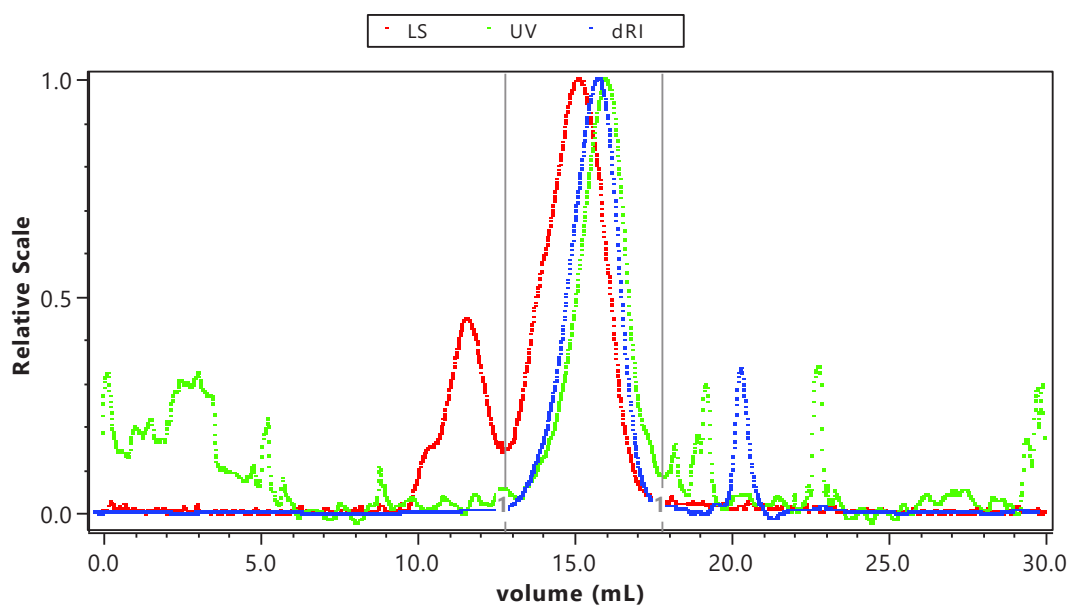


Figure 32. SEC analysis of P_{1,38} in water buffer (sodium azide, lithium nitrate, triethanolamine). Detection by light scattering (LS), refractive index (dRI) and absorption at 450 nm (UV).

Absorption spectra in water

The P_{1,38} has absorption spectrum (figure 33) shifted back to lower wavelength. It is due to SP solvatochromism. However, there still remains some overlap with the T_m blue emissions (especially for the 450 nm emission band, but not as ideal as it was in DMF).

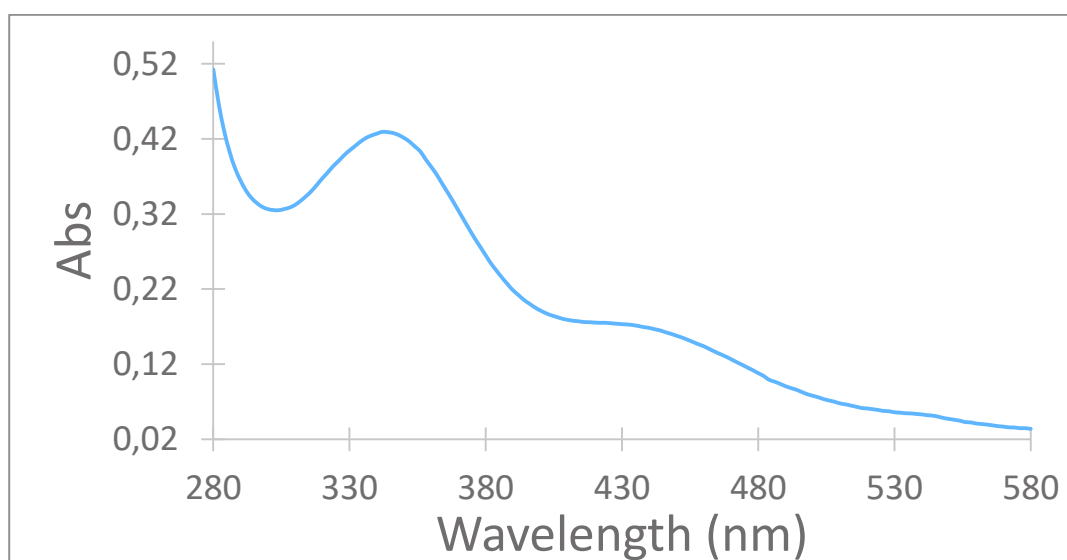


Figure 33. Absorption spectrum of P_{1,38} in water.

III Photochemical behavior of amido-BIPS

III.1 Parametrization of the dye: use of BIPS-GLT

Negative photochromism

When solutions of BIPS-GLT dye at $ca\ 5 \cdot 10^{-5}\ \text{mol L}^{-1}$ are prepared, the pH was found to spontaneously reach a value of about 5. Under such conditions, the photochromic behavior was investigated using monochromatic irradiation (LED 420 nm).

Under monochromatic irradiation at 420 nm, bleaching of the large broad band was observed with a simultaneous rise of a UV transition (figure 34). Mauser plot of these two transitions showed a nice correlation. This fact and the presence of an isosbestic point led us to simplify the kinetic scheme to a two-species-and- H^+ scheme such as $\text{MCH}^+ \rightarrow \text{SP} + \text{H}^+$.

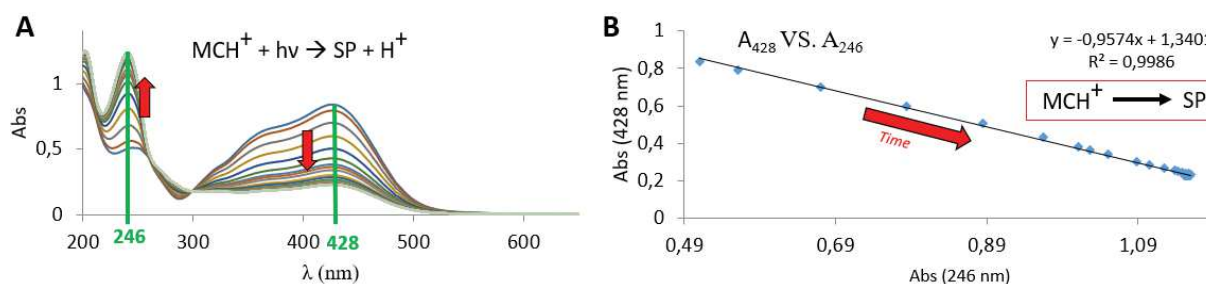


Figure 34. A) Kinetic monitoring of the photoinduced dye decoloration ($\lambda_{\text{irr}}=420\ \text{nm}$). B) Mauser plot of $\text{Abs}(428\ \text{nm})=f(\text{Abs}(246\ \text{nm}))$. $[\text{dye}]_0=3.25 \cdot 10^{-5}\ \text{mol L}^{-1}$ ($\text{pH}_0=5$, unbuffered)

Kinetic monitoring of a photoacid dye photochromism

The H^+ release was observed by the simultaneous monitoring of the pH of the dye solution and its visible absorption during the irradiation. During such a process, the pH of a dye solution at $5.2 \cdot 10^{-5}\ \text{mol L}^{-1}$ was found to decrease from 4.4 down to 4.17 as shown in figure 35. The MCH^+ form thus behaves as a photoacid, in a similar way to the sulfonate substituted one BIPS- SO_3 .^{12,34}

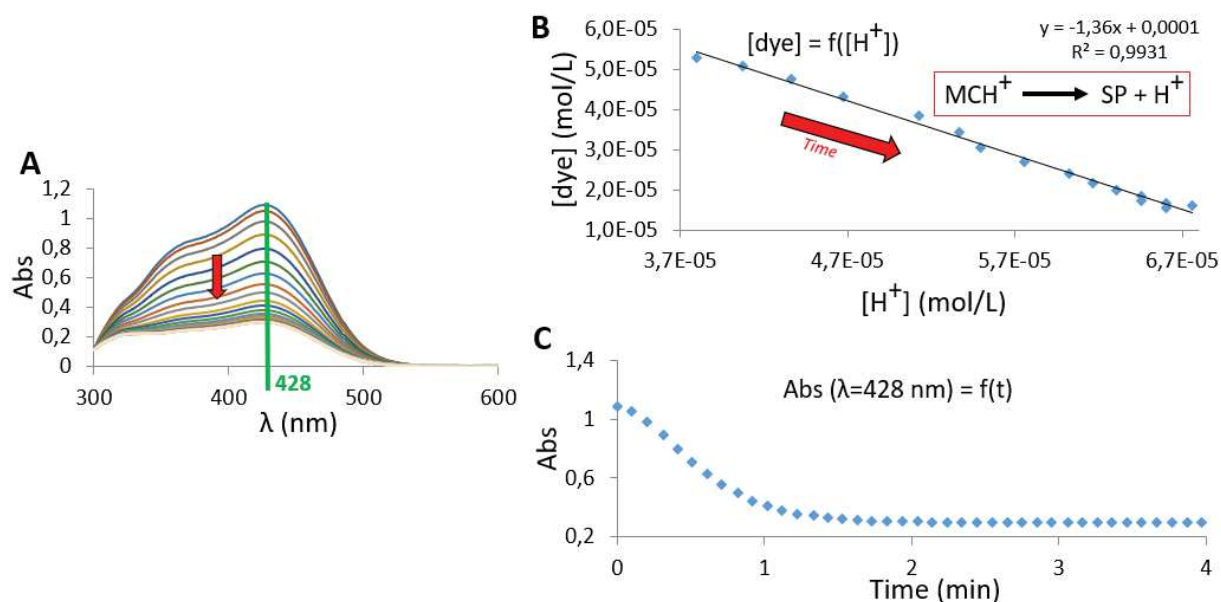


Figure 35. Kinetic simultaneous monitoring of pH and absorbance in solution. A) Overlap of absorbance spectra. B) Evolution of the [MCH⁺] as a function of the [H⁺] calculated from the pH measurements. C) Kinetic evolution of Abs(428 nm) as a function of the irradiation time. [dye]₀ = 5.2*10⁻⁵ mol L⁻¹.

Thermal back reaction

Once the PSS was reached, irradiation was stopped and UV-vis absorption of the solution was monitored (figure 36). Recovery of the absorption band occurs over a period of 20 minutes. The MCH⁺ vs [H⁺] plot and the kinetic trace (MCH⁺ vs time) show two distinct regimes: a first and fast recovery one with a quasi-linear evolution of MCH⁺ regarding to H⁺, then, the kinetic slows down. This second period where [H⁺] decreases not as fast as the [MCH⁺] rises is probably due to the speciation of the dye at these pH's close to 4 where the COOH group can ionize: the continued protonation of the SP form eventually leads to a deprotonation of the dye's COOH group, resulting in the building up of a buffer.

In non-buffered conditions, rate constants determinations would require the use of numerical modeling.

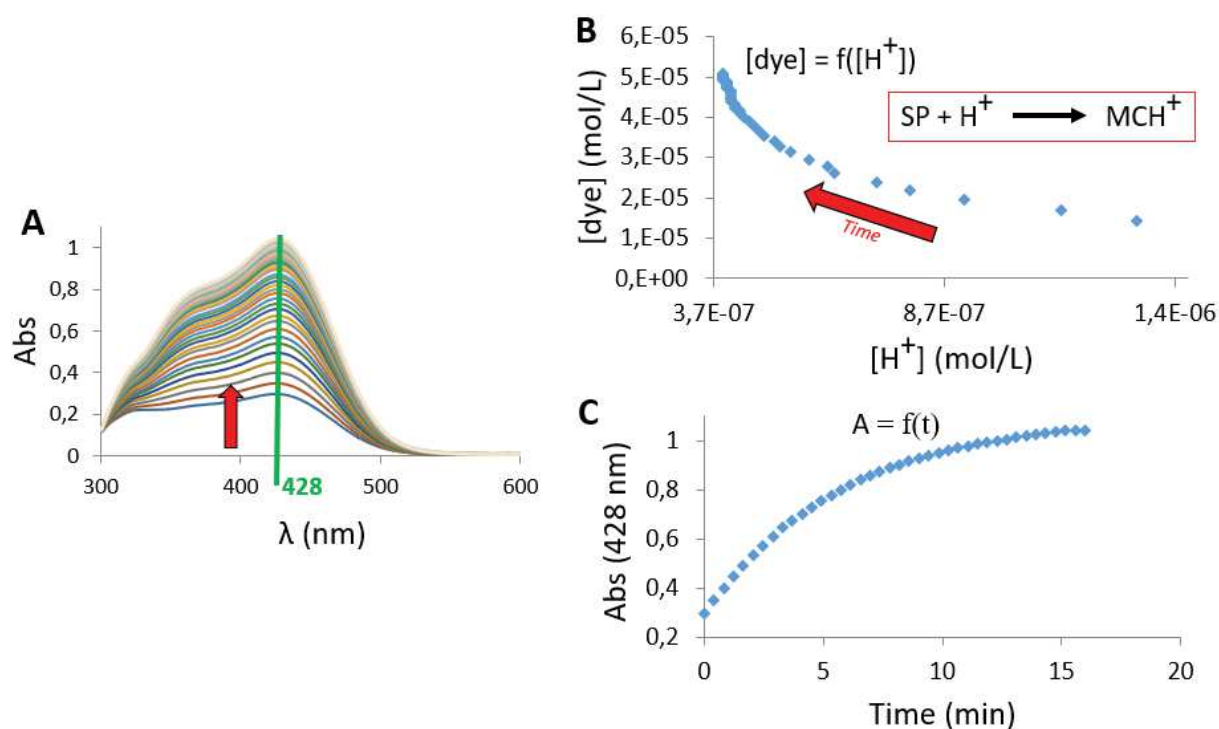


Figure 36. Thermal back reaction with simultaneous monitoring of pH and absorbance in solution. A) Overlap of absorbance spectra. B) Evolution of the $[MCH^+]$ as a function of the $[H^+]$ calculated from the pH measurements. C) Kinetic evolution of Abs(428 nm) as a function of time in dark. Same dye concentration as figure 35.

To conclude, BIPS-GLT model compound was shown to present the desired property in water: negative photochromism. The thermal back reaction was found to be rather slow and made complex by the interference of the pending COOH group. Such a feature is also expected for polymer P_{1,38}.

Dye stability in water

An important issue was the dye stability in water. Indeed, spiropyran are known to undergo a retro-Knoevenagel reaction,²⁴ that slowly hydrolyses the dye in the dark. Therefore, dye solutions were always freshly prepared before measurements.

The other point was the dye photostability: to assess this feature, the cycle “irradiation/recovery in the dark” was repeated 4 times (figure 37). The maximum absorbance at 428 nm was found to decrease slightly. One can incriminate classic oxidative dye bleaching

(in particular due to the presence of oxygen). No attempts were made to identify the photobleaching processes.

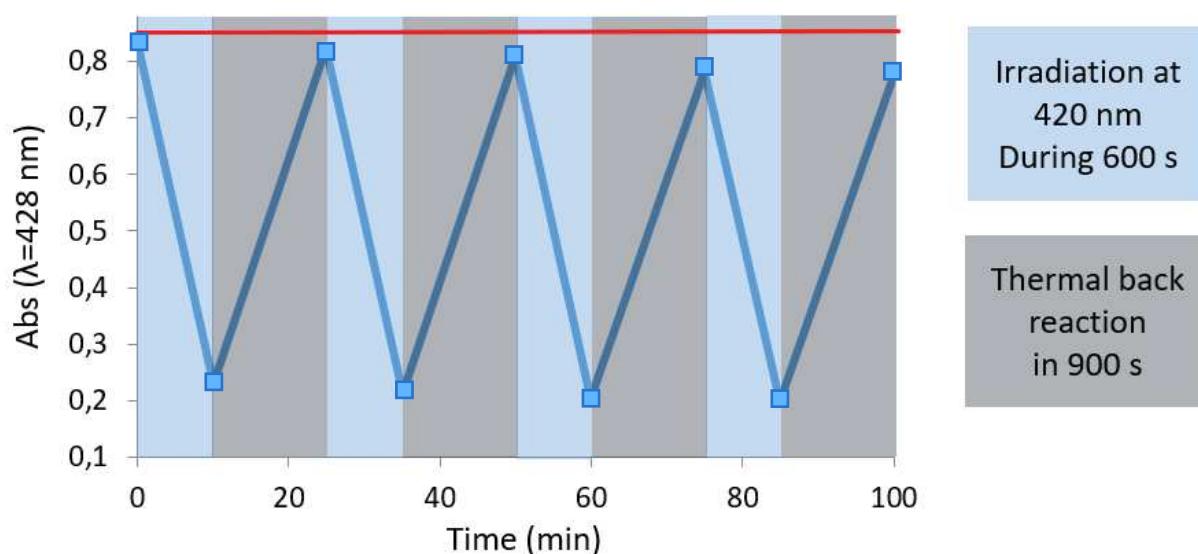
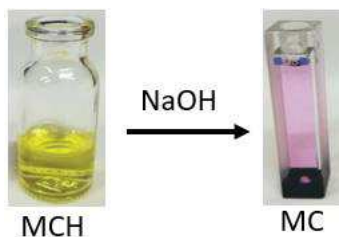


Figure 37. Photostability of the SP-GLT upon a sequence of bleaching (under 420 nm LED excitation) and thermal back reaction (in dark). The red horizontal line is for the initial absorbance.

Halochromism: MC → SP

As shown in the introduction, the MCH^+ form is in equilibrium with its conjugate base MC. We thus explored the effect of a pH change. Introduction of a large amount of NaOH (12 eq) caused a brutal color change from orange to purple, the latter color fading rather quickly. We monitored this transformation to retrieve some of the thermal back reaction parameters.



The initial spectrum is completely modified: the 420 nm band being replaced by a lower energy one at 532 nm. This band was attributed to the MC form. The monitoring of the absorption spectrum with time showed the rise of a transition in the UV region with a maximum at 241 nm attributed to SP (figure 38 A).

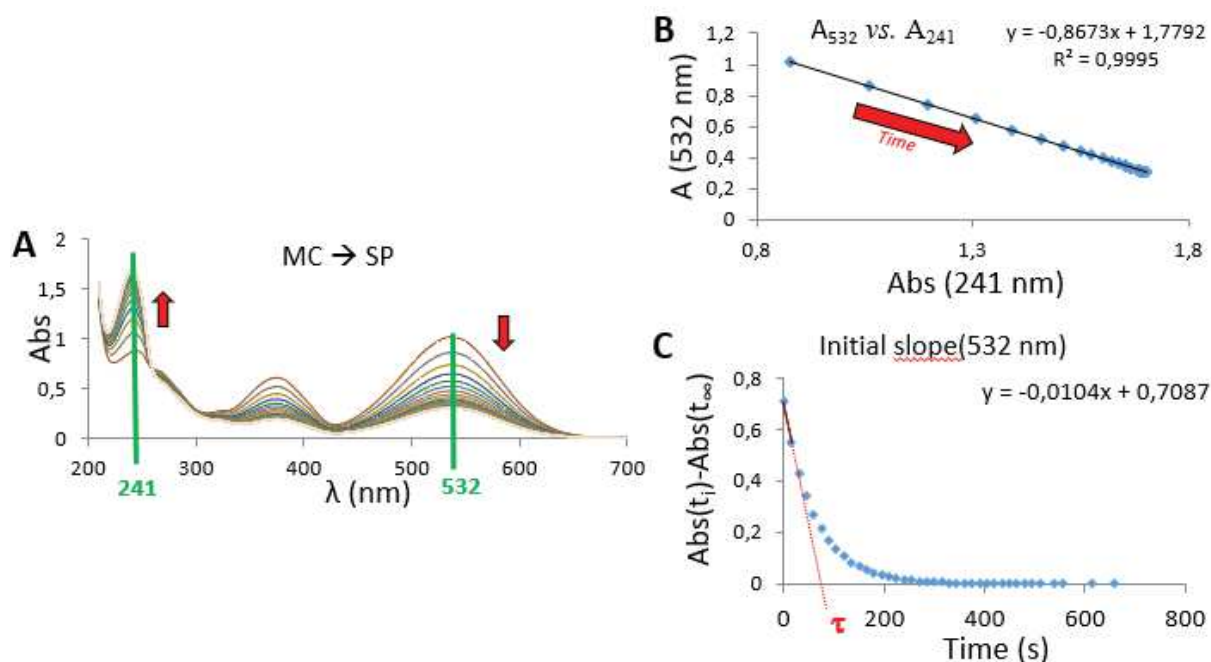


Figure 38. Monitoring of the absorbance in solution. A) Overlap of absorbance spectra. B) Mauser plot of $Abs(532\text{ nm})=f(Abs(241\text{ nm}))$. C) Kinetic evolution of the rescaled absorbance $Abs(t)-Abs(t_\infty)$ at 532 nm as a function of time.

Remarkably the pink solution is no longer photochromic: this property is restored only when the pH is lowered again, thus is bound to the MCH^+ form. Such a feature indicated that the photochromism occurs only over pH range where the MCH^+ form is the major one, therefore restricting the “useful” window to the acidic region: below 7. Because the thermal back reaction involves $[H^+]$, the extent of the photoisomerization will be limited by the rate of this “dark” process; one has to remember the definition of the position of the PSS: the more acidic the reaction medium, the less efficient (in terms of PSS) the photoisomerization.

Determination of $k_{(MC \rightarrow SP)}$

The reaction inducing the color disappearance is a two-species one written as $MC \rightarrow SP$, as justified by the presence of isosbestic points and the linear Mauser plot $Abs(532\text{ nm})$ vs $Abs(241\text{ nm})$ (figure 38 B). At infinite time we could notice that some color persisted indicating that an equilibrium mixture of SP and MC form was reached. To estimate the thermal back reactions $MC \rightarrow SP$ (k_1) and $SP \rightarrow MC$ (k_2) a requirement is to determine the absorption coefficient of the MC form. Considering that the deprotonation of the MCH^+ is quantitative and much faster than any other chemical process, we estimated the extinction coefficient (23700

$\text{cm}^{-1} \text{M}^{-1}$) from the absorbance extrapolated $t=0$ at 532 nm. The very simple initial slope approach was used to retrieve an estimation of the lifetime of the MC form (68 s). To extract the k_1 and k_2 rate constants we then exploited the PSS concentrations and definition.

$$K = \frac{k_1}{k_2} = \frac{[MC]_{\infty}}{[SP]_{\infty}} = \frac{A_{\infty}}{A_0 - A_{\infty}} = 0.35 \text{ and } \frac{1}{\tau} = k_1 + k_2 = \frac{1}{68} \text{ s}^{-1}$$

Thus, values of 0.011 s^{-1} (or $\tau_{\text{MC} \rightarrow \text{SP}}=92 \text{ s}$) and 0.031 s^{-1} (or $\tau_{\text{SP} \rightarrow \text{MC}}=33 \text{ s}$) were respectively obtained for k_1 (MC \rightarrow SP) and k_2 (SP \rightarrow MC).

III.2 Exploration of P_{1,38} polymer photochromism

Dye bleaching upon blue light irradiation

Acidified in aqueous solution, the polymer P_{1,38} absorption spectrum was characterized by two broad bands at 340 nm and 450 nm, the latter being comparable with the model dye BIPS-GLT (figure 38). Therefore, as expected, monochromatic 420-nm irradiation LED of such a solution induced the bleaching the visible part of the spectrum. Kinetic monitoring was made by reporting the absorbance at 450 nm and 474 nm (corresponding to the 2 blue emissions of UCNP) as a function of time (figure 39). Interestingly, as for the model compound, dye photoswitching is fast, with an estimated characteristic time $\tau \approx 13 \text{ s}$, indicating that a single MCH⁺ transition would be addressed by both Tm-emissions.

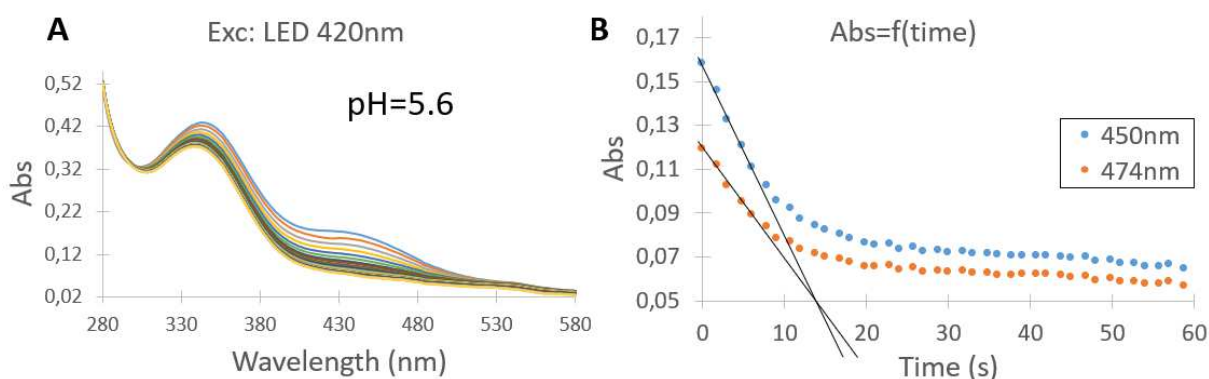


Figure 39. Bleaching of P_{1,38} at 3.51 mg mL^{-1} under 420 nm LED excitation, at pH=5.6. A) Overlap of the absorption spectra. B) Kinetic evolution of Abs at wavelengths corresponding to the two blue emission bands of Tm-doped UCNP

Thermal back reaction

As for BIPS-GLT, thermal back reaction in the dark was quite fast. Although not completed in 6 minutes, characteristic time τ can be approximated at around 3 minutes, even if the recovery was not achieved in the present case (figure 40).

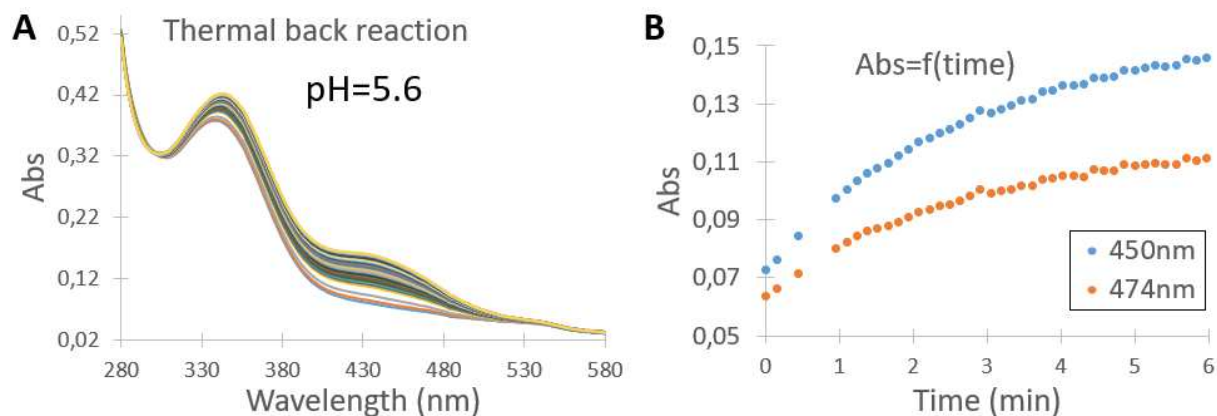


Figure 40. Thermal back reaction of $P_{1,38}$ at 3.51 mg mL^{-1} monitored in dark, without any irradiation, at pH=5.6. A) Overlap of the absorption spectra. B) Kinetic evolution of Abs at wavelengths corresponding to the 2 blue emission bands of Tm-doped UCNP.

Such a result can be compared to published data with related dyes. In particular in the work by M. Feeny *et al.*³⁹ was described the negative photochromism of water soluble non ionic polymer carrying variously substituted spiropyran chromophore. In this study the characteristic recovery time of electron rich spiropyran (MeO-SP-PEGMA) can be estimated at about 15 minutes. (figure 41)

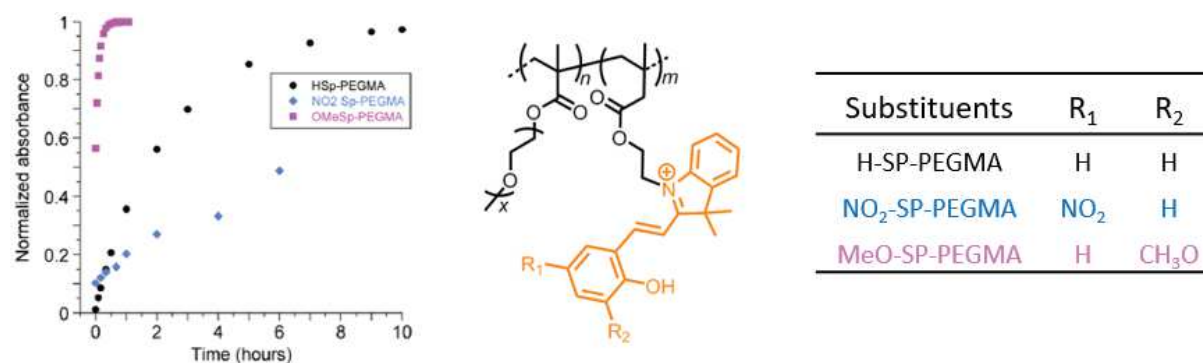


Figure 41. Reported kinetics of thermal recovery of various substituted spiropyran-loaded polymers by Feeny *et al.*³⁹

In our case, the effect of the *para*-amido group is therefore consistent with these reported results.

Photostability

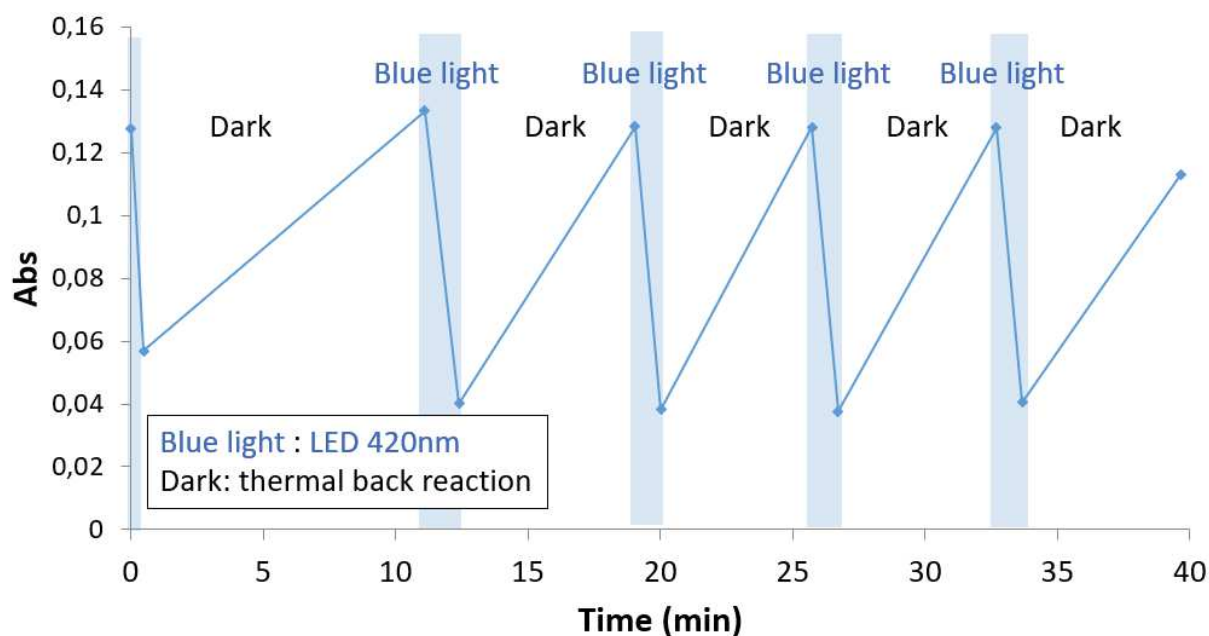


Figure 42. Photostability study on P_{1,38} via absorbance measurement upon repeated cycles of 420 nm irradiation / dark.

Upon repeated cycles discoloration/thermal recovery (figure 42), the photochromic polymer P_{1,38} shows slight decrease of the maximum of the absorbance: a loss of ca 10% is observed after 5 cycles. This behavior is in agreement with our previous results on the model dye BIPS-GLT.

Conclusion about P_{1,38} photochemical behavior in water

Altogether, it was proven that the T-negative-photochromic behavior of the model dye BIPS-GLT persisted once incorporated into the polymer P_{1,38}. Even though results are only qualitative as yet, we could evidence fast bleaching (characteristic time $\tau \approx 13$ s) of the dye under LED irradiation, and rather fast thermal back reaction in less than 10 minutes ($\tau \approx 3$ min) (figure 43).

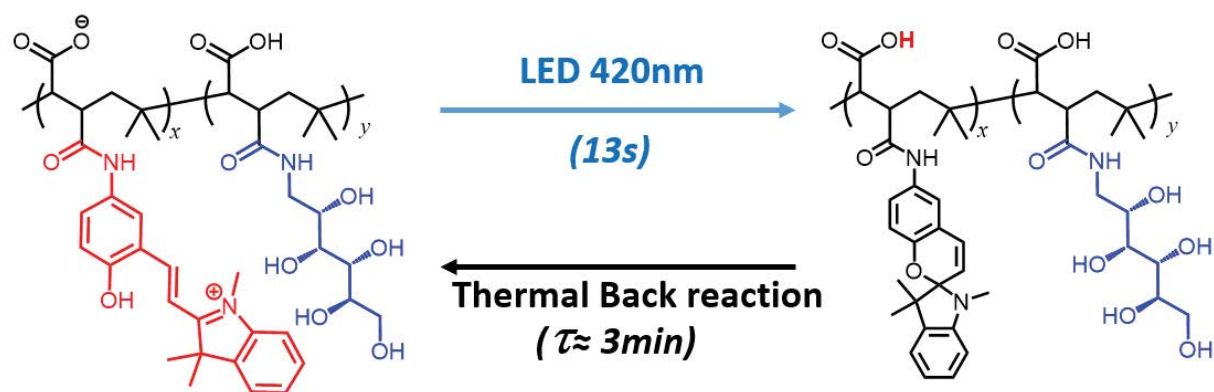


Figure 43. Summary of $P_{1,38}$ photochemical behavior

One question remains unanswered: does the SP have similar behavior in higher steric hindrance condition, while the polymer is surrounding a NP surface?

IV Towards UCNP@ $P_{1,38}$ nanohybrid for super-resolution

IV.1 Nanohybrid formation

Nanohybrid was prepared by using the simple procedure previously described (section II.1). To an aqueous solution of $P_{1,38}$ was introduced dropwise over 10 minutes a DMF or water solution of uncoated UCNPs (UCNP@ BF_4). We have used the conditions that were successful in section II. The stoichiometry was arbitrarily fixed following the rule “1 mg of ligand for 1 mg of UCNP”, assuming that it represents a large excess of ligands. After 30 min of vigorous magnetic stirring, the nanohybrid was purified by centrifugation. The purification procedure was voluntarily reduced to repeated centrifugations to avoid long exposure to large volume of water that might cause UCNP dissolution or dye hydrolysis. Such removal of free polymer in solution was achieved by 3 successive centrifugations in water (without the need for additional solvent of precipitation). Then, products were redispersed in water and immediately used for photochemistry experiments. Absorbance spectra revealed the presence of SP thus $P_{1,38}$, and the presence of UCNP was confirmed visually by shining a 980-nm handheld laser on the sample.

Due to the lack of time, we have not been able to go further in the analysis, it will be more discussed in the perspectives. However, it will be called as « nanohybrid » in the following

IV.2 Impact of the Nanohybrid architecture on P_{1,38} photochemistry

Compared to the polymer alone (figure 38), only the band at 340 nm can be clearly distinguished, the one of interest at 450 nm is noisy. Additionally, the shape of the curves suggests diffusion phenomenon in solution. This can be due to an unoptimized stability of the assembly UCNP@P_{1,38} in water.

Dye bleaching upon blue light irradiation

Figure 44 shows an attempt of dye bleaching on the nanohybrid.

Similar to P_{1,38}, photochemical experiments were reproduced with the « nanohybrid », at neutral pH, by using the blue LED (figure 43). Kinetic monitoring was made by reporting the absorbance at 450 nm and 474 nm (corresponding to the 2 blue emissions of UCNP) as a function of time. The kinetic monitoring show fast characteristic time. However, in the case of the nanohybrid, it is slightly longer (ca. 20 s vs. 13 s) compared to the polymer alone P_{1,38}.

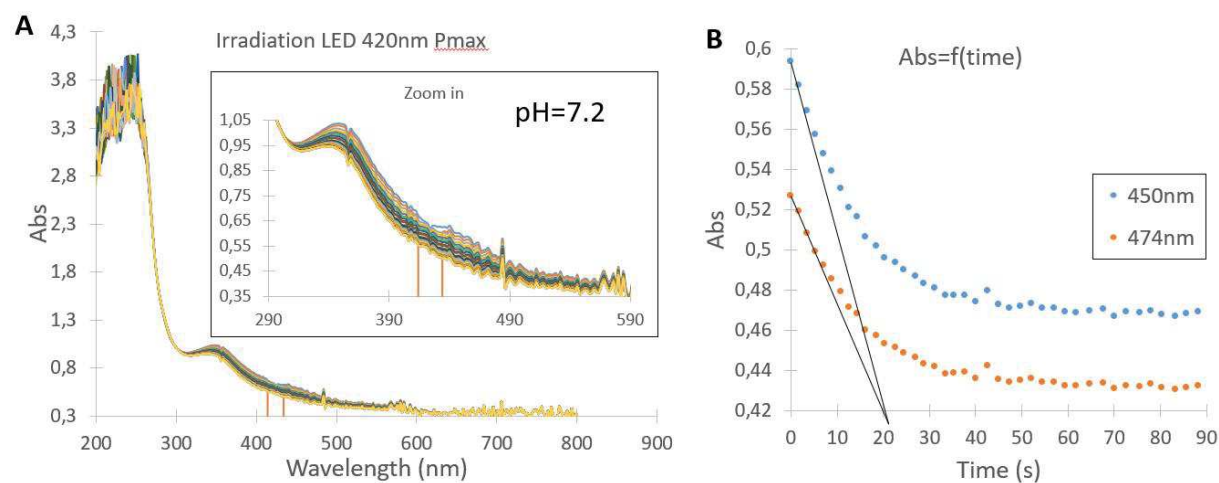


Figure 44. Bleaching of UCNP@P_{1,38} at [P_{1,38}]=0.718 mg mL⁻¹ under 420 nm LED excitation at pH=7.2. A) Overlap of the absorption spectra. B) Kinetic evolution of Abs at wavelengths corresponding to the two blue emission bands of Tm-doped UCNP.

Thermal back reaction

Similarly, to the polymer alone, thermal back reaction (figure 45) is still fast with a comparative characteristic time of around 3 min. Despite the noise, kinetic traces taken over the MCH^+ envelope are consistent, giving a single relaxation time of *ca* 3 min.

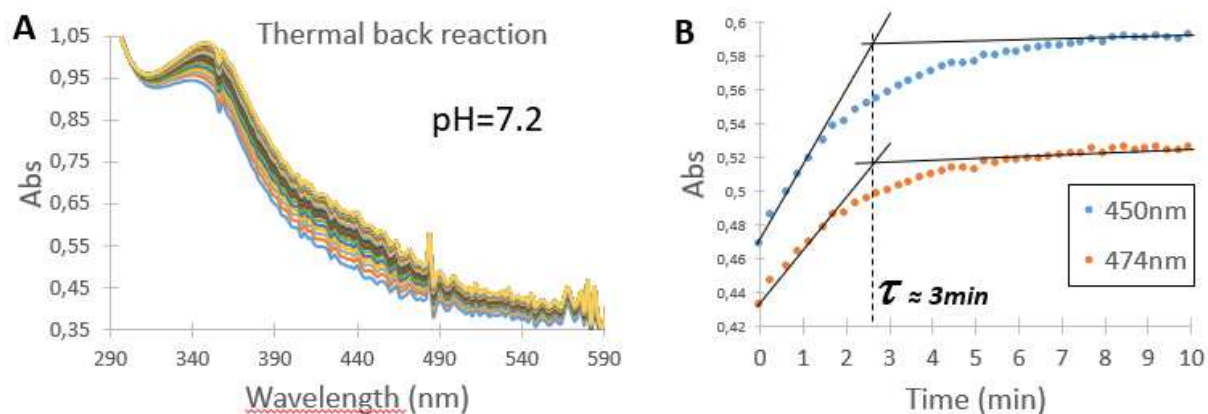


Figure 45. Thermal back reaction of UCNP@P_{1,38} at [P_{1,38}]=0.718 mg mL⁻¹ monitored in dark, without any irradiation. A) Overlap of the absorption spectra. B) Kinetic evolution of Abs at wavelengths corresponding to the 2 blue emission bands of Tm-doped UCNP.

IV.3 UCNP-induced Photoswitching of the P_{1,38}

Based on the demonstration of the conservation of dye photochromic behavior even after the nanohybrid assembly, next was the investigation of the feasibility of such photoswitching induced by the proper emission of UCNP. Thus, blue LED was replaced by 976 nm CW laser at 39.29 W cm⁻².

However, when applying the 980 nm excitation, no significant variation could be detected on the UV-visible spectrophotometer.

Two hypotheses can explain these observations:

-either UCNP emission in water is too weak to induce dye photoswitching (blue emission quantum yield too low, irradiated volume too small or back-isomerization rate increased due to local water overheating)

-or light fluctuation is occurring as expected at the single nanoparticle level but it is not detectable at the macroscopic one.

At this level, the proof of concept should come from a super resolution experiment, observing the actual luminescence of a single NP. To maximize the contrast between the “ON state” and the brightest state, ultrasmall UCNPs should be used.

Indeed, one can discuss two extreme cases. First, the unfavorable luminescence extinction via a “trivial quenching” or photon reabsorption mechanism. If we apply the hypotheses defining an absorption cross-section for the Beer Lambert law (i.e all photons falling with the cross-section σ of the dye are absorbed), then one can estimate the number of dyes n^* that would be required to completely quench the NP luminescence: $n^* = \frac{4\pi r_{NP}^2}{\sigma}$.

From a NP geometrical parameters (i.e the smallest NP of chapter III BA1 diameter=2.5nm) and the dye molar extinction coefficient $\epsilon \approx 22450 \text{ L mol}^{-1} \text{ cm}^{-1}$ or $\sigma \approx 3.7 \cdot 10^{-17} \text{ cm}^2$ one can get the following number $n^* \approx 5300$ dyes giving the unrealistic surface concentration of 250 dye.nm^{-2} ! If one considers a dye whose size would be comparable to an alkyl chain (diameter 0.2 nm) then the maximum surface concentration would be $8 \text{ molecules.nm}^{-2}$, close packed. With such a concentration, all dyes being switched off, the maximum extinction would be of 3% of the bare nanoparticle. Thus, trivial quenching can be considered as irrelevant for our purpose.

The second extreme case is a Förster quenching model. Förster radii commonly reported in the literature on UCNP are about 1 nm. Considering that dyes are bound to the surface of the particle we can calculate the volume of the sphere at the center of the NP that will be “out of reach” of any RET quenching. For an ultrasmall UCNP (ex BA1, diameter 2.5 nm) the diameter of this unquenched area is about 0.5 nm. Ratio of the total volume of the NP to this zone gives a factor of ca 100. That is, NP emission intensity would then vary over a significant range if dyes switch from the OFF, quenching state to the ON, unquenching state. One can also note that Förster spheres will start to overlap when the dye concentration is higher than about 10 dyes per particle. This approach is however very favorable as the centers of the dye molecules are not lying flat on the surface. Yet, this justifies the use of ultrasmall nanoparticles in order to maximize the amplitude of photoswitching. The main question is then the number of dyes per nanoparticle or the polymer loading per particle.

This implies to prove the architecture core UCNP@shell P_{1,38} resulting from the interaction of the polymer and the bare nanoparticle in water. In particular several points have to be addressed: Are we in the presence of a nanohybrid made of a single nanoparticle embedded within a corona of organic material or do we have larger aggregates. One suitable technique to efficiently address this issue is Field Flow Fractionation. In short, colloids to be analyzed are submitted to two perpendicular hydrodynamic fields, separating objects according to the magnitude of the interaction of the objects with the external perpendicular field. These techniques act like SEC chromatography for polymer. One particularly attractive mode is when the transverse field imposes sedimentation of the colloids: it is particularly adapted to nanohybrids with a dense inorganic core. Thanks to the coupling of DLS, RI and UV-Vis detectors, one could monitor the co-elution of UCNP and P_{1,38}, free polymer (the latter having a shorter elution time than a nanohybrid). We could not do it by lack of time. Moreover, it requires a long time of optimization of the parameters of acquisition and the method of analysis. Another interesting possibility is the preparative separation procedure proposed by the Regensburg team and involving electrophoresis. Beside the sorting out of crude nanohybrids, the agarose gel can be extracted to isolate the structures of interest.⁶⁸

Additionally, TGA should be required to determine the polymer content. A final characterization would be the determination of the number of UCNP encapsulated by nanohybrid.

V Conclusion

Compared to the initial technical specifications, we chose to work with the couple Tm-doped “blue-emitting” UCNP and orange-colored T-negative spiropyran absorbing blue light.

Dye structure was tuned in order to have a substituent in para of the phenol with a Hammett sigma value close to that of hydrogen to maximize the overlap. Thus, it relies on the use of poorly donating amino group. This lowering of the “electron-donor” behavior was achieved either by grafting triazine (by nucleophilic substitution) or carboxylic acid (through amide bond). Effectively, absorption spectra were shifted to the area of interest, in native solvent (EtOH for BIPS-TCl₂, DMF for BIPS-P_{1,38} intermediate). However, in both cases, when the dye is placed into water, the absorption is shifted back to lower wavelength due to

solvatochromism. As a result, the overlap occurs mainly with the 450 nm emission band of Tm, while the 475 nm one appears poorly usable. Issues with purification and lack of effective photochromic behavior for BIPS-TCI₂ forced us to abandon this route, despite the attractiveness of the selective post-functionalization of the triazine.

Concerning the amide route, we first designed a short ligand by coupling amino-BIPS to glutaric anhydride. This model compound was crucial as it allows us to determine the molar absorption coefficient of such a new kind of dye. Then, we could validate and explore its photochromism. Based on this first parametrization, we could then upgrade the method to form reactive polymer bearing SP via amide bond and explore the photochemistry. We decided at first to work with a low content of dye to prevent any stacking issue within the polymer. In order to enhance the hydrophilic behavior, this reactive polymer-based platform was fully functionalized by short hydrophilic molecules, D-glucamine.

Noticeably, such low dye-loaded polymer, P_{1,38}, conserved the same behavior than the model compound BIPS-GLT.

Then nanohybrid was built by the simplest approach, a direct mixing of P_{1,38} with bare UCNP. However, actual formation of such a nanohybrid architecture was not fully demonstrated by analytic method.

Despite the risks of modifications of the photochemical behavior of the dye due to the enhanced steric hinderance once the polymer anchored at the NP surface, the observations were again identical.

The dye chosen displays the desired negative photochromism when the MCH⁺ form is present. This implies that the blinking of the nanohybrid should occur over a defined pH window compatible with the dye speciation. That is, acidic but close to neutrality (from 5 to 7). While seemingly restrictive, this constraint will enable to introduce another discrimination parameter by combining sensing and super resolution properties. As an example, more fluctuations will be expected in acidic compartments such as tumors cells, or lysosomes.

Therefore, knowing that the dye is still photoswitchable, we turned our attention to the feasibility of such dye photoisomerization induced by UCNP emission under NIR excitation.

Unfortunately, by simple kinetics in solution with a standard UV-visible spectrophotometer, no change was detected. This phenomenon can have two origins:

-UCNP emission is too low in water to be able to switch efficiently the dye

-the photoswitching induced by UCNP emission is working, but it is happening as expected for the BLINK application: at the macroscopic level no light fluctuation is occurring, but at the single-NP scale there are fluctuation of intensity due to local variation of the dye isomerizations.

Further study such as single-NP observation with the confocal microscope established at LASIR should explore this way.

At this point, we are still far from success. Nevertheless, we have designed a strategy to prepare a nanohybrid architecture based on the electrostatic interaction of an anionic water-soluble polymer and a “naked” nanoparticle. Use of a commercially available polyanhydride leads to a simultaneous introduction of a functional group and a charged one. Thus, a multifunctional nanohybrid can be designed in a very straightforward way. We have also shown that it was possible to graft water-compatible, negative T-photochromic units onto such a polymer. Upon mixing with naked UCNPs, a mixed material was isolated in which the photochromic dye remained functional. However, we have not yet been able to characterize the actual nanohybrid architecture of the objects, and more importantly, to demonstrate unambiguously that the photon flux re-emitted by the UCNPs was sufficient to induce detectable dye photoswitching. However, even if the UCNP is not able to induce the dye isomerization, it can be achieved thanks to the use of a second, external excitation (figure 1 case A).

VI Experimental section

VI.1 Material and methods

Reagents were all of commercial source and used as received. Anhydrous DMF and THF were obtained by column drying using a M-Braun solvent purification system (courtesy of UMR5247 SPCMIB Toulouse).

NMR spectra were recorded on Bruker Avance 300 or 500 spectrometers using residual non-deuterated solvent as reference for the chemical shifts in ppm. Ultra-filtrations were performed using membranes with a 3 kDa cut-off.

UV-vis absorption spectra were recorded on a HP8451 or Analytik Jena Specord S 600 diode array spectrophotometers and photokinetics experiments on the HP8451 diode array spectrophotometer.

VI.2 The photoisomerization experiments

The solution to be photolyzed (2.5 mL) was stirred with a magnetic stirring bar in a 1 cm x 1 cm quartz cell placed in a thermostated sample holder (25°C). The light was introduced via an optical fiber from the top part (irradiation path of 2.5 cm). The irradiation light was obtained from a fibered 420 nm LED source (Mightex). If required, the pH was recorded *in-situ* using a microelectrode (H1083B Hanna Instruments).

VI.3 Protocol for UCNP ligand exchange

Preparation of bare UCNP

OA removal was achieved following the protocol established by Dong *et al.*⁴³ Typically 200 mg of UCNP@OA were dispersed in 4 mL of cyclohexane. To this solution was added 4mL of NOBF₄ dispersed in dried DMF (50 mg mL⁻¹). After at least 30 min of vigorous magnetic stirring, the solution was left to rest. Fast decantation reveals the presence of 2 phases, the upper-colored one containing organic compound is discarded. DMF fraction is purified by 3 successive centrifugations in DMF coupled to chloroform as precipitation solvent. Eventually last centrifugation in chloroform, followed by drying under vacuum leads to dry bare UCNP which were used for FTIR experiments. For storage they were dissolved in DMF.

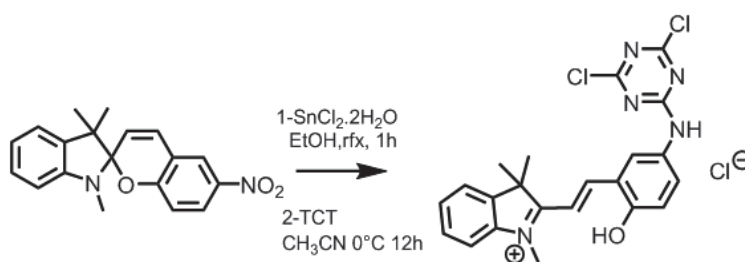
Capping with new stabilizer

200 mg of bare UCNP are dissolved in DMF or water (at 50 mg mL⁻¹), depending on the new stabilizer solubility. Stabilizer were introduced in aqueous solution at 50 mg mL⁻¹, assuming that it represents a large excess.

Purification was achieved by successive centrifugation with acetone as solvent of precipitation, then dissolved in water. Most of the nanohybrid were then purified by dialysis to remove free ligand. Then, nanoobjects were lyophilized and dispersed at a known concentration

For PIMA-derivative ligands used in the chapter, dialysis step was removed due to the risk of dye hydrolysis while exposed to water during such a long time.

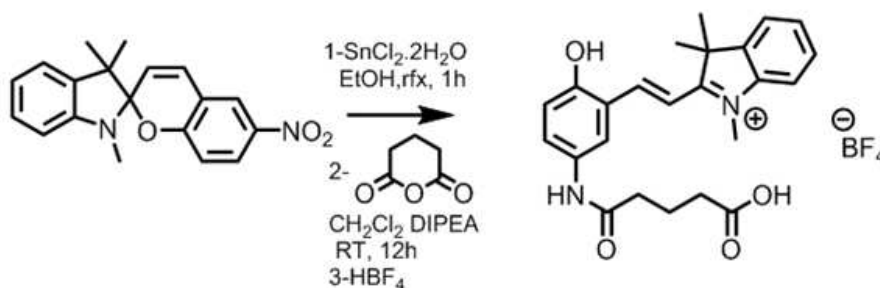
VI.4 Reactive dye BIPS-TCl₂



A solution of NitroBIPS (0.4 g, 1.2 mmol) and SnCl₂·2H₂O (1.6 g, 7 mmol) in ethanol (8 mL) was heated to reflux under argon for one hour. The orange reaction mixture was poured into 16 mL of 5 % sodium hydroxide and extracted three times with diethylether. The pale yellow organic phase was dried over MgSO₄ then evaporated to dryness leaving 0.367 g of a viscous green oily residue. Crude amino-BIPS was redissolved in 2 mL acetonitrile and a cold solution of TCT (tricholotriazine) (0.3 g, 1.6 mmol) was added dropwise at -5°C. The dark orange turbid mixture was left overnight in the freezer. Diethylether was added to achieve precipitation. The orange precipitate was filtered then dried in vacuo. Recrystallization from 1:2 mixture acetonitrile: acetic acid gave 0.160 mg of a bright orange powder (53%).

¹H NMR (500 MHz, DMSO-*d*₆) δ 11.24 (s, 1H), 10.74 (s, 1H), 8.47 (d, *J* = 16.4 Hz, 1H), 8.08 (d, *J* = 2.6 Hz, 1H), 7.89 (d, *J* = 24.0 Hz, 2H), 7.69 (d, *J* = 16.4 Hz, 1H), 7.64 (ddd, *J* = 6.5, 4.6, 1.5 Hz, 2H), 7.53 (dd, *J* = 8.8, 2.6 Hz, 1H), 7.11 (d, *J* = 8.8 Hz, 1H), 4.10 (s, 3H), 1.77 (s, 6H). ¹³C NMR (126 MHz, DMSO) δ 182.24, 157.28, 148.24, 143.74, 142.35, 132.16, 129.70, 129.48, 125.52, 123.32, 121.59, 117.50, 115.56, 113.09, 52.39, 34.76, 26.33.

VI.5 Model compound BIPS-GLT



A solution of nitro-BIPS (0.4 g, 1.2 mmol) and $\text{SnCl}_2 \cdot 2\text{H}_2\text{O}$ (1.6 g, 7 mmol) in ethanol (10 mL) was heated to reflux under argon for one hour. The orange reaction mixture was poured into 16 mL of 5 % sodium hydroxide and extracted by diethylether (3x30 mL). The pale yellow organic phase was dried over MgSO_4 then evaporated to dryness leaving a viscous green oily residue. Crude amino-BIPS was redissolved in 2 mL of dichloromethane, then 0.2 g of glutaric anhydride and 0.2 mL of DIPEA were added. The reaction mixture was stirred overnight, then 0.1 mL concentrated HBF_4 (56 %), was added dropwise before partition with acidified (HBF_4) water. Aqueous phase was extracted with dichloromethane, and organic phases dried over MgSO_4 . After evaporation to dryness the residue was purified by crystallization from CHCl_3 - Et_2O . Yield: 0.5g (84%) of a dark orange hygroscopic powder.

^1H NMR (300 MHz, $\text{DMSO}-d_6$) δ 10.93 (s, 1H), 9.86 (s, 1H), 8.45 (d, $J = 16.4$ Hz, 1H), 8.17 (d, $J = 2.5$ Hz, 1H), 8.03 – 7.78 (m, 2H), 7.69 – 7.59 (m, 2H), 7.58 – 7.45 (m, 2H), 7.00 (d, $J = 8.9$ Hz, 1H), 4.07 (s, 3H), 2.38 – 2.23 (m, 4H), 1.83 (q, $J = 7.4$ Hz, 2H), 1.76 (s, 6H).

HRMS ES⁺: m/z : 407.1965 [$\text{M}-\text{BF}_4$]

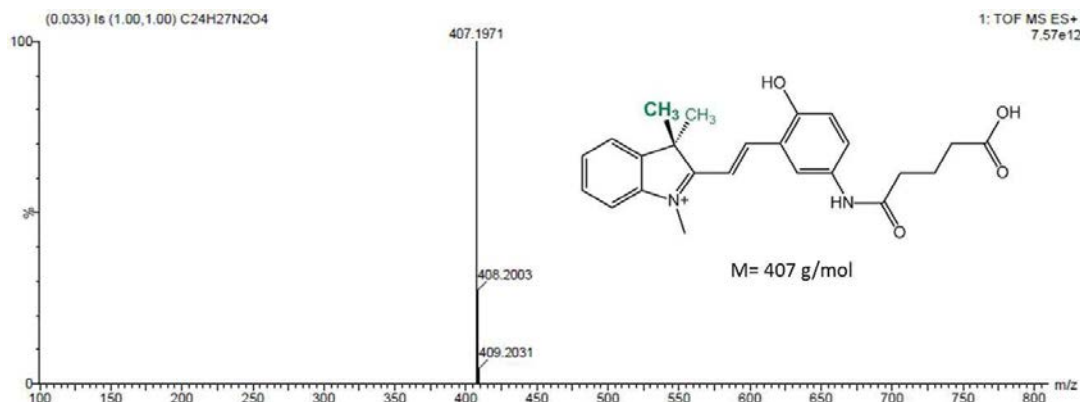


Figure 46. HR MS ES⁺ of the BIPS-GLT

VI.6 Polymer $P_{x(39-x)}$ $x=1$

VI.6.1 Step 1

A solution of nitro-BIPS (0.2 g 0.62 mmol) and $\text{SnCl}_2 \cdot 2\text{H}_2\text{O}$ (0.8 g, 3.5 mmol) in ethanol (4 mL) was heated to reflux under argon for one hour. The orange reaction mixture was poured into 10 mL of 5% sodium hydroxide and extracted by diethylether (3 x 30 mL). The pale-yellow organic phase was dried over MgSO_4 then evaporated to dryness leaving 0.160 g (*ca* 0.55 mmol) of a viscous green oily residue.

To a solution of PIMA (3 g, 19.5 mmol, 35.4 eq. *vs* intermediate amino-BIPS) in 20 mL of anhydrous DMF was then added the crude amino-BIPS dissolved in 4 mL DMF and DIPEA (0.1 mL, 0.55 mmol). The reaction was stirred overnight then was poured into a large excess of THF:diethylether⁶⁶ (4:60) to precipitate the polymer. After centrifugation, the pellet was redissolved in DMF and the precipitation procedure was repeated. Polymer was then vacuum-dried.

VI.6.2 Step 2

Crude intermediate polymer (0.2 g) was redissolved in DMF (3.5 mL) and a solution of D-glucamine (0.45 g, 0.25 mmol) in water (5.5 mL) was added. The homogeneous mixture was stirred overnight. After dilution with deionized water, the reaction mixture was ultra-filtrated, and washed 4 times with 10 mL water, then twice with brine (10 mL, 40 g L^{-1}). Then the chamber was filled with deionized water and washing were repeated at last 3 times, controlling the chloride content with silver nitrate test. The aqueous solution was then freeze-dried, giving 0.43 g of a fluffy pale-yellow powder.

VI.7 Calculations of $k_{(MC \rightarrow SP)}$

Initial slope method: $Y = -0.8673 x + 1.7792$

$$\tau = \frac{0.7087}{0.0104} = 68 \text{ s}$$

$$y^* = A_0 - A_\infty = 0.014 * 15 + 0.7087 = 0.8647$$

$$A_0 = 0.8647 + 0.307$$

$$\varepsilon_0 = \frac{A_0}{c_0} = \frac{1.17}{4.94 * 10^{-5}} = 23700 \text{ L mol}^{-1} \text{ cm}^{-1}$$

$$V_{1\infty} = k_1 \cdot [SP]_\infty$$

$$V_{2\infty} = k_2 \cdot [MC]_\infty$$

$$k_1 \cdot [SP]_\infty = k_2 \cdot [MC]_\infty$$

$$K = \frac{k_1}{k_2} = \frac{[MC]_\infty}{[SP]_\infty} = \frac{A_\infty}{A_0 - A_\infty} = 0.35$$

$$k_1 + k_2 = \frac{1}{\tau} = \frac{1}{68} \text{ s}^{-1}$$

Thus, it can be deduced the two rate constants:

$$k_1 = 0.011 \text{ s}^{-1} \rightarrow \tau_1 \approx 92 \text{ s}$$

$$k_2 = 0.031 \text{ s}^{-1} \rightarrow \tau_1 \approx 32 \text{ s}$$

VII References

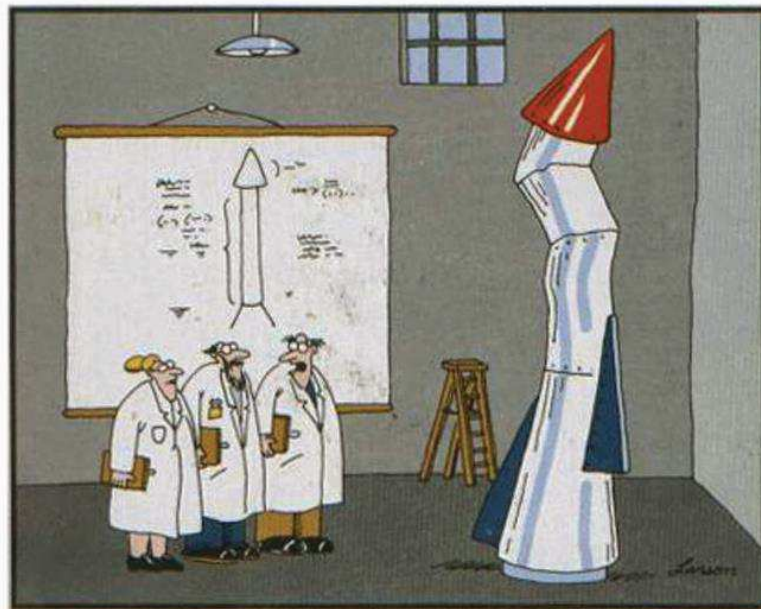
- 1 Wu, S., Blinco, J. P. & Barner-Kowollik, C. Near-Infrared Photoinduced Reactions Assisted by Upconverting Nanoparticles. *Chemistry–A European Journal* **23**, 8325-8332 (2017).
- 2 Wu, S. & Butt, H. J. Near-infrared-sensitive materials based on upconverting nanoparticles. *Advanced Materials* **28**, 1208-1226 (2016).
- 3 Wu, T. & Branda, N. R. Using low-energy near infrared light and upconverting nanoparticles to trigger photoreactions within supramolecular assemblies. *Chemical Communications* **52**, 8636-8644 (2016).
- 4 Bagheri, A., Arandiyani, H., Adnan, N. N. M., Boyer, C. & Lim, M. Controlled Direct Growth of Polymer Shell on Upconversion Nanoparticle Surface via Visible Light Regulated Polymerization. *Macromolecules* **50**, 7137-7147 (2017).
- 5 Fu, C., Xu, J. & Boyer, C. Photoacid-mediated ring opening polymerization driven by visible light. *Chemical Communications* **52**, 7126-7129 (2016).
- 6 Wu, T., Boyer, J.-C., Barker, M., Wilson, D. & Branda, N. R. A “plug-and-play” method to prepare water-soluble photoresponsive encapsulated upconverting nanoparticles containing hydrophobic molecular switches. *Chemistry of Materials* **25**, 2495-2502 (2013).
- 7 Boyer, J.-C., Carling, C.-J., Gates, B. D. & Branda, N. R. Two-way photoswitching using one type of near-infrared light, upconverting nanoparticles, and changing only the light intensity. *Journal of the American Chemical Society* **132**, 15766-15772 (2010).
- 8 Wu, W. *et al.* NIR-Light-Induced Deformation of Cross-Linked Liquid-Crystal Polymers Using Upconversion Nanophosphors. *Journal of the American Chemical Society* **133**, 15810-15813 (2011).
- 9 Zhang, B. F., Frigoli, M., Angiuli, F., Vetrone, F. & Capobianco, J. A. Photoswitching of bis-spiropyran using near-infrared excited upconverting nanoparticles. *Chemical Communications* **48**, 7244-7246 (2012).
- 10 Chen, Z. *et al.* Light Controlled Reversible Inversion of Nanophosphor-Stabilized Pickering Emulsions for Biphasic Enantioselective Biocatalysis. *Journal of the American Chemical Society* **136**, 7498-7504 (2014).
- 11 Lai, J., Zhang, Y., Pasquale, N. & Lee, K.-B. An Upconversion Nanoparticle with Orthogonal Emissions Using Dual NIR Excitations for Controlled Two-Way Photoswitching. *Angewandte Chemie International Edition* **53**, 14419-14423 (2014).
- 12 Li, W. *et al.* Noninvasive and Reversible Cell Adhesion and Detachment via Single-Wavelength Near-Infrared Laser Mediated Photoisomerization. *Journal of the American Chemical Society* **137**, 8199-8205 (2015).
- 13 Massaad, J. *et al.* Photocontrol of luminescent inorganic nanocrystals via an organic molecular switch. *Physical Chemistry Chemical Physics* **16**, 22775-22783 (2014).
- 14 Lee, E.-M., Gwon, S.-Y., Son, Y.-A. & Kim, S.-H. Luminescence switching of CdTe quantum dots in presence of water-soluble spironaphthoxazine. *Spectrochimica Acta Part A: Molecular and Biomolecular Spectroscopy* **97**, 699-702 (2012).
- 15 Zhu, L., Zhu, M.-Q., Hurst, J. K. & Li, A. D. Q. Light-Controlled Molecular Switches Modulate Nanocrystal Fluorescence. *Journal of the American Chemical Society* **127**, 8968-8970 (2005).
- 16 Díaz, S. A. *et al.* Water-Soluble, Thermostable, Photomodulated Color-Switching Quantum Dots. *Chemistry – A European Journal* **23**, 263-267 (2017).

- 17 Díaz, S. A. *et al.* Photoswitchable Water-Soluble Quantum Dots: pcFRET Based on Amphiphilic Photochromic Polymer Coating. *ACS Nano* **5**, 2795-2805 (2011).
- 18 C. Crano, J. & J. Guglielmetti, R. *Organic Photochromic and Thermochemical Compounds*. (2002).
- 19 Liu, N., Liu, S. & Geng, F. Two-dimensional tungstate nanosheets for constructing novel photochromic hydrogel with ultrahigh flexibility. *Journal of Materials* **4**, 144-148 (2018).
- 20 Deniel, M., Lavabre, D. & Micheau, J. in *Organic Photochromic and Thermochemical Compounds* 167-209 (Springer, 2002).
- 21 Irie, M., Fukaminato, T., Matsuda, K. & Kobatake, S. Photochromism of diarylethene molecules and crystals: memories, switches, and actuators. *Chemical reviews* **114**, 12174-12277 (2014).
- 22 Blanco, V., Leigh, D. A. & Marcos, V. Artificial switchable catalysts. *Chemical Society Reviews* **44**, 5341-5370 (2015).
- 23 Lin, W.-C. & Kramer, R. H. Light-Switchable Ion Channels and Receptors for Optogenetic Interrogation of Neuronal Signaling. *Bioconjugate Chemistry* **29**, 861-869 (2018).
- 24 Aiken, S., Edgar, R. J. L., Gabbutt, C. D., Heron, B. M. & Hobson, P. A. Negatively photochromic organic compounds: Exploring the dark side. *Dyes and Pigments* **149**, 92-121 (2018).
- 25 Jacquet, M. *et al.* Efficient Photoswitch System Combining a Dimethyldihydropyrene Pyridinium Core and Ruthenium(II) Bis-Terpyridine Entities. *Inorganic Chemistry* **56**, 4357-4368 (2017).
- 26 Yamaguchi, T., Kobayashi, Y. & Abe, J. Fast Negative Photochromism of 1, 1'-Binaphthyl-Bridged Phenoxy-Imidazolyl Radical Complex. *Journal of the American Chemical Society* **138**, 906-913 (2016).
- 27 Rifaie-Graham, O. *et al.* Wavelength-Selective Light-Responsive DASA-Functionalized Polymersome Nanoreactors. *Journal of the American Chemical Society* **140**, 8027-8036 (2018).
- 28 Bertelson, R. C. in *Organic Photochromic and Thermochemical Compounds* 11-83 (Springer, 2002).
- 29 Balmond, E. I. *et al.* Comparative Evaluation of Substituent Effect on the Photochromic Properties of Spiropyrans and Spirooxazines. *The Journal of Organic Chemistry* **81**, 8744-8758 (2016).
- 30 Gaeva, E. B. *et al.* Negative Photochromism of New Spirooxazine Derivatives in Acidified Solution. *Molecular Crystals and Liquid Crystals* **430**, 81-88 (2005).
- 31 Klajn, R. Spiropyran-based dynamic materials. *Chemical Society Reviews* **43**, 148-184 (2014).
- 32 Wojtyk, J. T. C. *et al.* Elucidating the Mechanisms of Acidochromic Spiropyran-Merocyanine Interconversion. *The Journal of Physical Chemistry A* **111**, 2511-2516 (2007).
- 33 Shi, Z., Peng, P., Strohecker, D. & Liao, Y. Long-lived photoacid based upon a photochromic reaction. *Journal of the American Chemical Society* **133**, 14699-14703 (2011).
- 34 Vallet, J., Micheau, J. C. & Coudret, C. Switching a pH indicator by a reversible photoacid: A quantitative analysis of a new two-component photochromic system. *Dyes and Pigments* **125**, 179-184 (2016).

- 35 Sugiura, S. *et al.* Photoresponsive polymer gel microvalves controlled by local light irradiation. *Sensors and Actuators A: Physical* **140**, 176-184 (2007).
- 36 Sumaru, K., Takagi, T., Satoh, T. & Kanamori, T. Photo-induced reversible proton dissociation of spirobenzopyran in aqueous systems. *Journal of Photochemistry and Photobiology A: Chemistry* **261**, 46-52 (2013).
- 37 ter Schiphorst, J., Saez, J., Diamond, D., Benito-Lopez, F. & Schenning, A. P. H. J. Light-responsive polymers for microfluidic applications. *Lab on a Chip* **18**, 699-709 (2018).
- 38 Ziólkowski, B., Florea, L., Theobald, J., Benito-Lopez, F. & Diamond, D. Self-protonating spiropyran-co-NIPAM-co-acrylic acid hydrogel photoactuators. *Soft Matter* **9**, 8754-8760 (2013).
- 39 Feeney, M. J. & Thomas, S. W. Tuning the Negative Photochromism of Water-Soluble Spiropyran Polymers. *Macromolecules* **51**, 8027-8037 (2018).
- 40 Krongauz, V. A. & Goldburt, E. S. Crystallization of poly(spiropyran methacrylate) with cooperative spiropyran-merocyanine conversion. *Macromolecules* **14**, 1382-1386 (1981).
- 41 Achilleos, D. S., Hatton, T. A. & Vamvakaki, M. Light-Regulated Supramolecular Engineering of Polymeric Nanocapsules. *Journal of the American Chemical Society* **134**, 5726-5729 (2012).
- 42 Cheng, Z. & Lin, J. Synthesis and Application of Nanohybrids Based on Upconverting Nanoparticles and Polymers. *Macromolecular Rapid Communications* **36**, 790-827 (2015).
- 43 Dong, A. *et al.* A generalized ligand-exchange strategy enabling sequential surface functionalization of colloidal nanocrystals. *Journal of the American Chemical Society* **133**, 998-1006 (2010).
- 44 Sedlmeier, A. & Gorris, H. H. Surface modification and characterization of photon-upconverting nanoparticles for bioanalytical applications. *Chemical Society Reviews* **44**, 1526-1560 (2015).
- 45 Masur, S., Zingsem, B., Marzi, T., Meckenstock, R. & Farle, M. Characterization of the oleic acid/iron oxide nanoparticle interface by magnetic resonance. *Journal of Magnetism and Magnetic Materials* **415**, 8-12 (2016).
- 46 Deacon, G. & Phillips, R. Relationships between the carbon-oxygen stretching frequencies of carboxylato complexes and the type of carboxylate coordination. *Coordination Chemistry Reviews* **33**, 227-250 (1980).
- 47 Muhr, V. *et al.* Particle-size-dependent Forster resonance energy transfer from upconversion nanoparticles to organic dyes. *Analytical chemistry* **89**, 4868-4874 (2017).
- 48 Langlais, M., Coutelier, O. & Destarac, M. Thiolactone-Functional Reversible Deactivation Radical Polymerization Agents for Advanced Macromolecular Engineering. *Macromolecules* **51**, 4315-4324 (2018).
- 49 Holzgrabe, U. Quantitative NMR spectroscopy in pharmaceutical applications. *Progress in Nuclear Magnetic Resonance Spectroscopy* **57**, 229-240 (2010).
- 50 Oxford, U. o. Quantitative NMR Spectroscopy. file:///G:/Pour%20Publi%20Izabela/RMN%20quantitative/quantitative-nmr_%20Oxford%202017.pdf, accessed on 15/06/2018 (2017).
- 51 Pinkerton, N. *et al.* Ionic Flash NanoPrecipitation (iFNP) for the facile, one-step synthesis of inorganic-organic hybrid nanoparticles in water. *Nanoscale* **9**, 1403-1408 (2017).

- 52 Pinkerton, N. M. *et al.* Quench ionic flash nano precipitation as a simple and tunable approach to decouple growth and functionalization for the one-step synthesis of functional LnPO 4-based nanoparticles in water. *Chemical Communications* **54**, 9438-9441 (2018).
- 53 Arnold, A. A. *et al.* Structure of NaYF₄ upconverting nanoparticles: a multinuclear solid-state NMR and DFT computational study. *The Journal of Physical Chemistry C* **117**, 25733-25741 (2013).
- 54 Zimmermann, T. & Brede, O. Ring transformations of heterocyclic compounds. XXIII. The UV irradiation product of photochromic 2,4,6-triaryl-1-(spiro[2H-1-benzopyran-2,2'-indoline]-6-yl)pyridinium salts - A phenolate betaine or a pyridinium substituted merocyanine dye? *Journal of Heterocyclic Chemistry* **40**, 611-616 (2003).
- 55 Hansch, C., Leo, A. & Taft, R. W. A survey of Hammett substituent constants and resonance and field parameters. *Chemical Reviews* **91**, 165-195 (1991).
- 56 Singla, P., Luxami, V. & Paul, K. Triazine as a promising scaffold for its versatile biological behavior. *European journal of medicinal chemistry* **102**, 39-57 (2015).
- 57 Bonneau, M. C. The Chemistry of Fabric Reactive Dyes. *Journal of Chemical Education* **72**, 724 (1995).
- 58 Abuchowski, A., McCoy, J. R., Palczuk, N. C., van Es, T. & Davis, F. F. Effect of covalent attachment of polyethylene glycol on immunogenicity and circulating life of bovine liver catalase. *Journal of Biological Chemistry* **252**, 3582-3586 (1977).
- 59 Di Corato, R. *et al.* Water solubilization of hydrophobic nanocrystals by means of poly(maleic anhydride-alt-1-octadecene). *Journal of Materials Chemistry* **18**, 1991-1996 (2008).
- 60 Wang, W., Aldeek, F., Ji, X., Zeng, B. & Mattoussi, H. A multifunctional amphiphilic polymer as a platform for surface-functionalizing metallic and other inorganic nanostructures. *Faraday Discussions* **175**, 137-151 (2014).
- 61 Jańczewski, D., Tomczak, N., Han, M.-Y. & Vancso, G. J. Synthesis of functionalized amphiphilic polymers for coating quantum dots. *Nature protocols* **6**, 1546 (2011).
- 62 Tomczak, N., Liu, R. & Vancso, J. G. Polymer-coated quantum dots. *Nanoscale* **5**, 12018-12032 (2013).
- 63 Lin, C.-A. J. *et al.* Design of an Amphiphilic Polymer for Nanoparticle Coating and Functionalization. *Small* **4**, 334-341 (2008).
- 64 Anderson, R. E. & Chan, W. C. W. Systematic Investigation of Preparing Biocompatible, Single, and Small ZnS-Capped CdSe Quantum Dots with Amphiphilic Polymers. *ACS Nano* **2**, 1341-1352 (2008).
- 65 Yen, S. K. *et al.* Design and Synthesis of Polymer-Functionalized NIR Fluorescent Dyes–Magnetic Nanoparticles for Bioimaging. *ACS Nano* **7**, 6796-6805 (2013).
- 66 Li, M.-J., Bertocchi, M. J. & Weiss, R. G. Photophysics of Pyrenyl-Functionalized Poly(isobutylene-alt-maleic anhydride) and Poly(isobutylene-alt-maleic N-alkylimide). Influence of Solvent, Degree of Substitution, and Temperature. *Macromolecules* **50**, 1919-1929 (2017).
- 67 De Nolf, K. *Optical properties of ion beam modified waveguide materials doped with erbium and silver* Master thesis thesis, Ghent University, Master thesis, (2012).
- 68 Hlaváček, A., Mickert, M. J., Soukka, T., Lahtinen, S., Tallgren, T., Pizúrová, N., Król, A., Gorris, H. Large-Scale Purification of Photon-Upconversion Nanoparticles by Gel Electrophoresis for Analogue and Digital Bioassays. *Analytical Chemistry* **91**, 1241-1246 (2019).

Conclusion



"It's time we face reality, my friends ...
We're not exactly rocket scientists".

“Of our elaborate plans, the end
Of everything that stands, the end
No safety or surprise, the end
I'll never look into your eyes... again”
(The Doors, « The end »)

L'objectif annoncé de ce travail de thèse était de mettre au point des nanoparticules luminescentes à clignotement contrôlé comme nouvelles sondes pour l'imagerie en super-résolution.

La mise au point bibliographique a permis de mettre en évidence l'intérêt de s'orienter vers des traceurs pouvant fonctionner dans l'infrarouge. Ceci permet de s'affranchir du problème majeur d'autofluorescence du matériel biologique dans les conditions standards d'observation. De plus, le rayonnement infrarouge présente un intérêt tant du point de vue optique avec une diminution des phénomènes de diffusion et une imagerie plus en profondeur dans les tissus, que du point de vue de la toxicité en passant outre les problèmes de photodégradations pouvant être occasionnés par des sources plus énergétiques (UV). De ce fait, le projet s'est naturellement focalisé sur l'utilisation de nanoparticules upconverting à base de lanthanides.

La séquence de précipitation des différents allotropes de NaREF_4 , en apparence ne conduisant qu'à des particules exploitables de grande taille a été mise à profit pour réduire la taille des particules.

Dans un premier temps nous avons appris à reproduire des nanoparticules standard. Puis, Nous nous sommes très rapidement orientés vers une composition originale de matrice hybride quasi-équimolaire $\text{Na}(\text{Yb-Gd})\text{F}_4$ pour augmenter l'efficacité de nos objets par l'amplification de l'absorption. Nous avons alors mis en place une démarche raisonnée permettant la réduction en taille successive de 15 nm vers 2 nm en améliorant le contrôle de la séquence d'Ostwald $\alpha \rightarrow \beta$. L'implémentation d'une méthode originale de cyclage de température à haute température grâce à l'utilisation d'un réacteur micro-onde s'est avérée fondamentale dans ce succès et ouvre désormais de nouvelles portes dans le domaine de la synthèse d'autres types de nanomatériaux, en particulier lorsqu'il s'agit de gérer deux allotropes. Une étude future de l'optimisation des paramètres du cyclage de température (durée des plateaux à T_{max} et T_{min} par exemple) pourrait sans doute permettre d'affiner encore plus le contrôle du « Ostwald focusing » et d'obtenir des distributions en taille encore plus étroite.

Cependant dans le cadre d'objets de type NaREF_4 , nous avons pu uniquement démontrer l'extrême reproductibilité sur des matrices de lanthanides de groupe II, ou des matrices hybrides groupe II- groupe III quasi-équimolaires. Des études supplémentaires seraient requises pour généraliser le procédé à des matrices composées uniquement de terres rares de groupe III comme NaYbF_4 , NaYF_4 ou NaLuF_4 . Une piste intéressante serait de reprendre les travaux de

Markus Haase pour le choix de la stoechiométrie, notamment le ratio Na/RE. En effet le groupe de Markus Haase propose une stoechiométrie spécifique pour les lanthanides de groupe II, et une seconde pour manipuler des éléments du groupe III.

De plus la forme de notre cyclage de température s'avère particulièrement adapté pour des mesures *in situ* lors du plateau à plus "basse température" (280°C). En effet il serait particulièrement intéressant d'avoir une mesure de taille, et/ou de luminescence en cours de chauffage. Des premières expériences dans ce sens ont pu être mises en place, avec notre partenaire Cordouan Technologies, avec l'adaptation d'une sonde DLS au cœur même du four micro-onde, mais l'optimisation de la méthode reste en cours.

Une autre optimisation future de ces nanoparticules, au moins aussi petites que des Quantum Dots standards, serait l'optimisation de croissance épitaxiale de coquille. En effet, bien que nos résultats soient suffisamment satisfaisant à ce stade quant au gain en efficacité d'upconversion sur nos coeur@coquille, les tailles obtenues nous suggèrent une absence de contrôle. Une campagne de mesure en synchrotron serait particulièrement intéressante pour confirmer la composition de la coquille que ce soit sur des objets déjà préparés ou suivi en cours de synthèse.¹ Plusieurs alternatives se présentent pour optimiser cette étape : un screening de conditions en suivant une démarche de plan d'expériences pour arriver rapidement à affiner nos paramètres actuels de synthèse, ou reprendre la stratégie de Markus Haase. Profitant d'une plus grande gamme de compositions compatibles avec la phase cubique que la phase hexagonale, cette approche repose sur la préparation de nanoparticules de phases cubiques ne pouvant pas donner de phase hexagonale. Ainsi une fois introduites avec les particules de cœur, ces graines sacrificielles cubique seront en théorie uniquement destinées à nourrir les particules de cœur pour former la coquille. Néanmoins dans le cadre de nos particules ultrapetites vient se poser la question de la taille : en effet l'écart de taille entre des cœurs de 2.5-3.3 nm et des graines sacrificielles (autour de 2 nm) étant particulièrement faible, la vitesse de dissolution des graines alfa sera-t-elle suffisamment plus rapide à haute température que celle des cœurs ? Dans le cas contraire cette approche ne fonctionnerait pas et on obtiendrait à nouveau des cœurs recouverts d'un mélange de précurseur de coquille et de matériau du cœur.

Dans le cadre du chapitre sur les nanolampes upconverting, nous avons pu étudier plus en détail le phénomène d'upconversion. Les propriétés photophysiques et la variété des réponses obtenues montre la difficulté de standardiser ce type de nanophosphores. Nous avons essayé de mettre en place une démarche analytique quantitative. Il nous est rapidement apparu important l'idée de mettre en place un standard de calibration pour la comparaison des mesures.

En effet l'absence d'un tel standard nous a amené sur le site des IMRCP à multiplier les expériences dans des conditions d'acquisition non comparables, mais adaptées à la caractérisation d'un lot à la fois. Le résultat étant à l'image de la partie stationnaire du chapitre 3, un foisonnement d'analyses sans possibilité de comparaison quantitative de lot à lot. Cependant nous avons pu montrer que de simples améliorations comme l'intégration d'un puissance-mètre pour la mesure *in situ* de l'absorption pendant l'acquisition de spectres d'émission étaient particulièrement intéressante pour cette démarche de rationalisation, permettant à la fois la caractérisation de l'absorption, difficile à observer sur des spectrophotomètres standards, la détermination de la teneur en sensibilisateur et donc la calibration par le nombre de sensibilisateur ou le nombre de nano-objets en solutions. Des informations sur la stabilité colloïdale comme la décantation peuvent également être obtenues de cette façon.

Les mesures temporelles menées au LASIR et au BAM ont permis d'apporter des premières données cinétiques comparables en mettant en place une méthode d'acquisition originale à temps constant. Néanmoins, ce mode de mesure est encore limité par le manque de signal obtenu pour nos particules de taille ultrapetite en particulier pour les émissions à haute énergie. Une nouvelle campagne de mesures avec un temps plus long (ex: 1h) pourrait permettre d'améliorer les choses. Une autre source d'amélioration majeure est le traitement du signal. En effet, malgré l'apparente forme de déclin de types biexponentiels, il a été particulièrement compliqué trouver un modèle de fit adéquat. Plusieurs méthodes ont été envisagées : la méthode multiexponentielle, non optimale, permet la comparaison de données cinétiques, alors qu'une méthode en intensité moyenne comme celle développée au LASIR permet de déterminer un temps de vie apparent mais n'a pas plus de sens du point de vue de la cinétique. L'ensemble des données collectées a pour but de mettre en place un modèle cinétique pour expliquer la dynamique complexe de redistribution de l'énergie au sein d'un UCNP. Il a été notamment présenté dans ce chapitre les prémices de ce modèle construit à partir de constantes de vitesses obtenues par l'analyse exhaustive de données publiées, mais par forcément adaptées au cas de nanoparticules. Une fois que ce modèle sera établi, il pourra permettre de fitter et simuler les expériences de temps de vie, mais aussi les diagrammes de type log-log plot UCNPs résultants d'études en régime stationnaire et communément présentées pour justifier du « nombre de photons » utiles au processus d'upconversion.

Enfin, le dernier chapitre traitait de l'application cible du projet BLINK: la mise au point de nanoparticules clignotantes pour la super-résolution.

L'idée ambitieuse était de coupler une particule UCNP avec des colorant photochromes réversibles présents à la surface. Ces derniers servant de "volet" sont sensés nous aider à reproduire nos « cinquante nuances de bleu ». Notre approche s'est déroulée en plusieurs étapes successives.

Nous avons tout d'abord démontré qu'il nous était très facile de « déshabiller » les UCNP de leur couche organique native, et de les recouvrir à façon, notamment pour des ligands présentant des phosphonates, phosphates, ou carboxylates. Nous avons utilisé deux méthodes analytiques pour suivre cet échange de ligand, l'infrarouge et la RMN quantitative.

Dans un second temps, nous avons explicité le choix du colorant photochrome T négatif utilisé: le spiropyrane. La sélection de substituants électroniquement « innocents » en s'appuyant sur un sigma de Hamett voisin de celui de l'hydrogène nous a conduits à nous focaliser sur des dérivés amino avec un faible caractère donneur de l'amine. De ce fait le comportement photochrome négatif du spiropyrane a été renforcé tout mettant en place un type de post-fonctionnalisation utilisable pour le projet.

En effet, en commençant par élaborer un composé modèle « BIPS-GLT » grâce à l'utilisation d'un anhydride court (anhydride glutarique) nous avons pu paramétrer la photochimie de ce nouveau colorant. Dans un second temps la même stratégie a été utilisée sur un poly(anhydride d'acide), permettant ainsi l'obtention d'une plateforme réactive, post-fonctionnalisable à façon. Afin d'augmenter l'hydrophilie du polymère et d'attester de la versatilité de la post-fonctionnalisation, nous avons créer un polymère entièrement fonctionnalisé par un faible taux de colorant (0,39 colorant par chaîne) et des D-glucamine. Ce dérivé de sucre a été choisi pour donner un caractère hydrophile important tout en limitant l'augmentation en taille du polymère, en gardant en tête l'idée que le nanohybride final UCNP@polymère doit rester suffisamment petit pour ne pas affecter la dynamique des éléments d'intérêt à sonder en microscopie super-résolution.

Une fois la validation de la méthode de synthèse et de la mise en place des protocoles de purification et d'analyse de cette plateforme polymère photochrome, nous avons pu vérifier que le polymère conservait le même comportement que le colorant de référence BIPS-GLT.

Nous avons alors enfin pu nous intéresser à la construction du nanohybride "clignotant" en assemblant ce polymère et des UCNP. Pour ce faire, nous avons sélectionné des particules de grande taille, plus émissive pour maximiser les chances de succès, préalablement décapées, sur lesquelles nous avons mis en présence le polymère photochrome. Ce protocole d'une simplicité extrême par simple mélange a ensuite été évalué en photochimie. Nous avons pu vérifier avec succès que même lorsque le colorant est ancré à la surface de nanoparticules il conservait un

caractère photochrome similaire au polymère libre. Cependant les premiers essais de photochimie non piloté par une source bleue externe mais par l'émission bleue des UCNP sous irradiation proche infrarouge se sont montrés infructueux. A ce stade, deux hypothèses s'opposent :

-soit il ne se passe rien parce que les UCNPs sont trop peu émissives, notamment dans l'eau ;
-soit, comme espéré, le colorant est bien photocommuté par la particule, mais au PSS (état photostationnaire) on ne voit rien à l'échelle macroscopique, il se produit uniquement des fluctuations à l'échelle de la particule unique, liées à la dynamique du colorant.

Les perspectives futures reposent sur l'observation en particule unique de ces nanohybrides au LASIR, où le setup dédié pour l'observation en particule unique dans des conditions d'upconversion a déjà été mis en place. Enfin de nouveaux polymères devraient être préparés, à des taux de chargement en colorant croissant, afin d'évaluer le potentiel de ces différents polymères pour faire fluctuer plus ou moins efficacement la lumière émise par les UCNP.

- 1 Liu, Q. *et al.* Quantifying the nucleation and growth kinetics of microwave nanochemistry enabled by in situ high-energy X-ray scattering. *Nano letters* **16**, 715-720 (2015).

| Annexes

Contents

I	Résumé du chapitre I	297
II	Résumé du chapitre II : Synthèse d'UCNP ultrasmall.....	299
III	Résumé du chapitre III: Nanolampes Upconverting	303
IV	Résumé du chapitre IV: Nanohybride upconverting vers l'imagerie super-résolue ...	307
V	Guide de lecture pour le suivi du chapitre 3	311

I Résumé du chapitre I

Mon sujet de thèse fait partie d'un projet financé par un projet ANR intitulé BLINK: nanoparticules luminescentes à clignotement contrôlé pour une application en microscopie de luminescence en super-résolution. Dès lors, mes travaux visaient au départ à concevoir des nanoparticules upconverting petites et lumineuses, adaptées à la microscopie en super-résolution, qui n'avaient pas été démontrées au début du projet (2016). Nous nous sommes concentrés sur l'imagerie stochastique, en particulier SOFI. En conséquence, le grand défi consiste à faire clignoter l'inclignotable UCNP.

L'idée était de coupler des UCNP ultrapetites à base de Thulium à un volet photochromique afin de construire un nanohybride pseudo-clignotant. L'émetteur Tm est choisi parce que l'émission bleue est plus adaptée à la commutation photo réversible du volet clignotant. De plus, cette sonde peut également être suivie grâce à son émission NIR.

Le présent manuscrit décrira comment mon travail a été mis en place afin d'aller vers cette application.

- Le chapitre 2 traite de la synthèse à partir de rien des nanoparticules UCNP, en portant une attention particulière à la réduction de la taille. Par rapport aux stratégies existantes, une matrice hybride originale de $\text{Na}(\text{Gd}_{42\%}\text{-Yb}_{57\%})\text{F}_4$, dopée à 1% de Tm, a été développée pour fournir des objets plus émissifs grâce à une absorption accrue.

-Le chapitre 3 présente les propriétés photophysiques des UCNP et une approche analytique originale pour proposer un nouveau modèle cinétique adapté à la migration du flux d'énergie entre les niveaux d'énergie des dopants.

-Au chapitre 4 seront développées des applications de l'UCNP en tant que nanolampes.

Dans un premier temps, les tentatives de caractérisation des nanolampes par une approche actinométrie chimique seront exposées.

Ensuite, une application vers une application de microscopie en super-résolution basée sur SOFI sera introduite: du choix et de la synthèse du volet photochromique à la conception du nanohybride hydrosoluble. Les premiers résultats concernant la faisabilité de cette application seront discutés.

II Résumé du chapitre II : Synthèse d'UCNP ultrasmall

Dans le présent chapitre, nous avons souligné l'importance de la composition, de la stratégie de mélange pour l'introduction de précurseurs et de l'appareil de chauffage afin d'atteindre une taille ultra-mince de phase hexagonale appropriée. En ce qui concerne ce nouveau sujet mis en œuvre en laboratoire, nous avons finalement acquis une bonne compréhension d'un mélange polymorphe complexe. La stratégie de réduction de la taille reposait sur l'optimisation couplée de la primo-précipitation et du chauffage à haute température. Le présent travail détaille la première synthèse micro-ondes, sans utilisation de trifluoroacétate, d'UCNP de cœur de phase bêta d'une taille inférieure à 5 nm dans un mélange de solvants couramment utilisé d'acide oléique et d'octadécène. La première description de l'approche de cyclage de températures assistée par un réacteur à micro-ondes et la validation empirique de la loi d'Arrhenius sur la synthèse de l'UCNP ouvrent de nouvelles perspectives pour la synthèse d'autres nanomatériaux. De plus, notre cyclage de températures assistée par micro-ondes est le premier protocole permettant une telle reproductibilité de la taille malgré la variation du contenu dopant (si la teneur en Yb est inférieure à 57%).

Cependant, certains autres paramètres critiques restent à explorer:

- l'utilisation de l'eau: les précurseurs des Terres Rare étant des chlorures, ils sont introduits dans l'eau. Une faible quantité d'eau associée à une vitesse de chauffage lente est nécessaire pour éviter, lors de l'échange du ligand $RE(OA)_3$, tout risque de projection de gouttes d'eau "piégées" dans le mélange huileux acide oléique/octadéc-1-ène. De plus, il peut éventuellement constituer une source de défaut dans la maille cristalline en amenant dans le cristal des atomes d'oxygène, dû par exemple à la formation éventuelle d'oxolanthanides pontés. Une alternative devrait être l'utilisation de précurseurs d'acétate directement solubles dans le « mélange huileux », sans nécessitant l'introduction d'eau dans le milieu

réactionnel. De plus, cette eau doit ensuite être éliminée, ceci est fait à 100 ° C sous flux d'argon. Cette «distillation» entraîne une baisse de la quantité du mélange acide oléique/octadec-1-ène, due à un azéotrope entre l'eau et l'acide oléique. En conséquence, la composition du solvant diffère de la composition initiale.

- l'utilisation de méthanol: une grande quantité de méthanol est utilisée pour l'introduction de sodium et de fluorure. Cette grande quantité de solvant volatile doit ensuite être évaporée. Ainsi, au début, les propriétés physicochimiques changent, en considérant le volume ajouté, à mesure que la composition OA:ODE /MeOH 1/1 soit atteinte après addition complète, et nous n'avons aucune idée de l'impact que cela aura sur la nucléation. D'un point de vue technique, ce méthanol est éliminé sous flux d'argon, ce qui est particulièrement long surtout dans l'approche à grande échelle et assez coûteux en ce qui concerne le volume de gaz inerte utilisé par synthèse. Une alternative devrait être l'utilisation d'oléate de sodium en tant que précurseur de sodium, ce qui permettrait de réduire de moitié le volume de MeOH, et/ou l'utilisation d'un évaporateur rotatif ou d'un appareil de distillation pour l'élimination du composé volatile sans perte de OA:ODE.

Cependant, la formation d'UCNP étant sous contrôle cinétique, chaque modification du protocole aura un impact sur la taille. Ainsi, les alternatives décrites ci-dessus vont générer une nouvelle analyse complète de la synthèse.

Néanmoins, les applications à grande échelle sont encore limitées pour le moment. Malgré une première tentative de chauffage conventionnel pour former des nanohexagones, cette approche est extrêmement délicate pour les UCNP ultrapetites: notre réacteur à micro-ondes a une capacité maximale de 20 mL. La montée en échelle avec notre appareil monomode ne peut être envisagée que par synthèse parallèle à partir d'un même lot de départ. Mais un tel processus soulève des questions sur le temps de réaction global et principalement sur le

vieillessement du lot initial. La principale limite de temps est la préparation fastidieuse de tubes de réacteur avec une étape de dégazage fastidieuse (environ 1h par tube).

Une application à grande échelle nécessiterait soit un réacteur monomode à flux continu, soit un réacteur multimode à grande échelle.

Ce dernier système existe déjà à l'échelle du litre. Cependant, les réacteurs pour lots de grande capacité ne sont pas une solution, car le refroidissement rapide était un facteur clé pour le cyclage de températures. Le fait de se tourner vers d'énormes conteneurs pose le problème de l'inertie thermique à l'intérieur du réacteur en fonctionnement. En conséquence, la seule alternative viable pour les synthèses à grande échelle devrait être basée sur un réacteur à flux continu microfluidique. Une telle configuration doit être conçue pour présenter un nombre de boucles à l'intérieur de la cavité monomode qui coïncide avec le nombre d'impulsions souhaitées à haute température.

Une grande variété de nanoparticules a été synthétisée au cours de ce projet de thèse: 2 gammes de taille d'UCNP en forme d'hexagone et diverses sphères de taille comprise entre 2,5 et 15 nm. Une fois cette bibliothèque d'UCNP synthétisée et entièrement caractérisée chimiquement, des recherches sur les propriétés photophysiques doivent être effectuées, en particulier sur celles ultrapetites. Ces détails seront traités dans le prochain chapitre.

Table 9. Résumé de la synthèse ou de la bibliothèque UCNP. Les synthèses réalisées avec un chauffe-ballon de puissance sont marquées en bleu, tandis que les roses ont été préparées avec un four micro-ondes monomode.

Composition	Diamètre (nm)	Quantité (g)	Temps de préparation
NaYF ₄ :Tm	35	0.6	1 jour
NaYF ₄ :Er	35	0.6	1 jour
NaYF ₄ :Tm	20	3	1.5 jours
NaYF ₄ :Er	20	3	1.5 jours
Na(Gd _{42%} -Yb _{57%})F ₄ :Tm	10	0.3	1 jour
Na(Gd _{42%} -Yb _{57%})F ₄ :Tm@NaYF ₄	15	0.6	2 jours
Na(Gd _{79%} -Yb _{20%})F ₄ :Tm	7.5	0.3	1 jour
Na(Gd _{42%} -Yb _{57%})F ₄ :Tm	15	0.3	1 jour
Na(Gd _{42%} -Yb _{57%})F ₄ :Tm	4.5	0.7	2 jours
Na(Gd _{79%} -Yb _{20%})F ₄ :Tm	2.5-3.5	0.7	2 jours
Na(Gd _{79%} -Yb _{20%})F ₄ :Tm@NaGdF ₄	5.5	1.4	1 semaine
Na(Gd _{42%} -Yb _{57%})F ₄ :Tm	2.5-3.5	0.7	2 jours
Na(Gd _{42%} -Yb _{57%})F ₄ :Tm@NaGdF ₄	5.5	1.4	1 semaine
Na(Gd _{42%} -Yb _{57%})F ₄ :Tm	3	3	1.5 semaines

III Résumé du chapitre III: Nanolampes Upconverting

Dans le présent chapitre, seront abordés différents points critiques:

- Rassembler la mesure des exposants de graphes log-log parmi les différents échantillons nous a permis de distinguer certains comportements. En effet, 3 groupes principaux de bandes d'émission se dégagent, avec un comportement d'exposant similaire (facteur de forme et de pente):

- 450 nm et 361 nm (et 344 nm)

- 474 nm et 645 nm

- 800 nm et 694 nm

En se référant au diagramme de Dieke, on peut voir que les bandes d'émission d'exposants similaires proviennent du même état excité (figure 22).

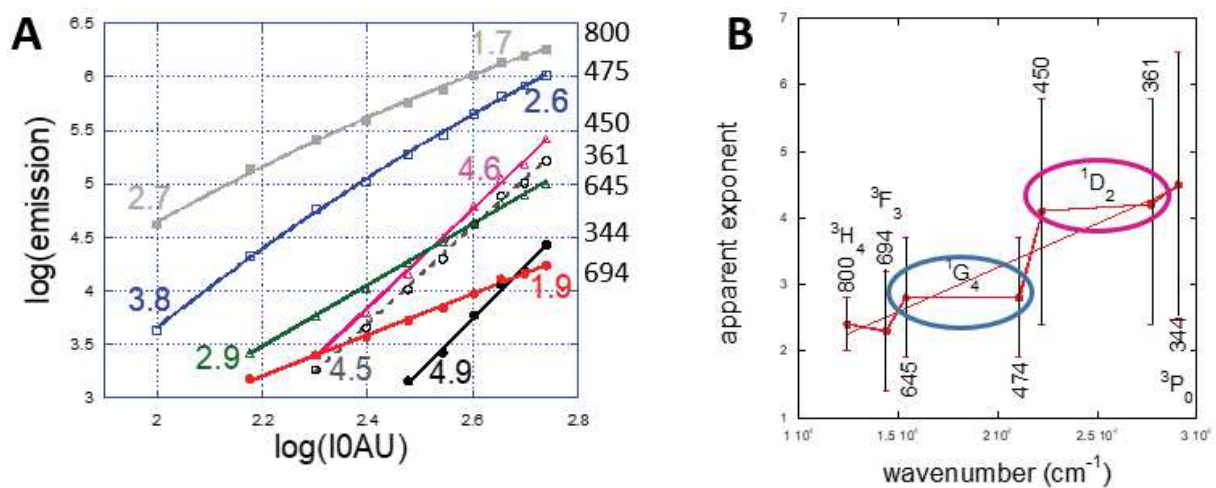


Figure 22. A: Comparaison des exposants moyens pour les échantillons ci-dessus décrits dans le chapitre. B: Corrélation entre la valeur de l'exposant et l'énergie de l'état excité initial.

Finalement, les échantillons pourraient être classés comme décrit ci-dessous (tableau 10):

Table 10. Classification des exposants de lots UCNP, en fonction de leur composition

	%Yb	%Tm	Matrice du coeur	coquille	800 nm exposant	475 nm exposant
BA11	57.38	1.02	Gd	-	2.25	2.30
BA15	57.35	0.99	Gd	-	2.25	2.30
BA12	57.38	1.02	Gd	100%Y	2.3	3.15
BA14	57.28	1.18	Gd	100%Y	2.3	3.15
BA6	57	1	Gd	100%Gd	2.32	2.80
BA17	57	1	Gd	100%Gd	2.32	2.80
BA16	57.35	0.99	Gd	100%Gd	2.40	2.70
BA7	20	1	Gd	100%Gd	2.85	

- Explorer le comportement photophysique des UCNP:

La caractérisation complète de la luminescence a été réalisée avec une approche de normalisation: de l'absorption à l'intensité d'émission et aux durées de vie. Même l'estimation de «l'efficacité» a été obtenue en mesurant le rendement quantique. Toutefois, il convient de rappeler au lecteur que le rendement quantique et la durée de vie mesurés ne sont pas des valeurs absolues mais des constantes apparentes.

De plus, une modification facile et peu coûteuse d'un fluoromètre standard peut permettre la mesure simultanée de l'absorption. En plus de son importance pour l'étalonnage des solutions, cette dernière fournit également des données supplémentaires sur les problèmes de stabilité colloïdale.

Comme les UCNP sont des luminophores extrêmement non linéaires, les quantificateurs standard sont probablement inexacts et mal adaptés pour décrire ces particules. Ainsi, les "exposants", "rendements quantiques" (ou "durées de vie" apparents ont été mesurés dans diverses conditions: il a été constaté que ces paramètres (exposant, durée de vie) correspondaient aux prévisions tirées du diagramme de Dieke du thulium et que les transitions partant du même diagramme. les niveaux partagent des caractéristiques communes. Cependant, la

compréhension de la redistribution de l'énergie à l'intérieur d'une nanoparticule reste à élucider. Les expériences enregistrées au BAM peuvent être considérées comme préliminaires, et le choix des conditions expérimentales n'a pas pu être optimisé davantage par manque de temps: mon stage y était limité à deux mois. Une autre solution consisterait à utiliser des impulsions laser carrées (top-hat) plus intenses afin d'obtenir plus de signal, même pour les transitions les moins efficaces. Cela pourrait être réalisé au LASIR en regroupant les impulsions ns dans des trains de différentes durées.

- Cas d'UCNP ultrapetites:

Un paramètre chimique qui n'a pas été pris en compte au début est apparu important pour la comparaison de différents lots: le nombre d'atomes émetteurs dans une nanoparticule d'ultrasmall. En effet pour la gamme de taille que nous avons explorée, en effet, selon les calculs de leurs paramètres chimiques (tableau 3), une UCNP de 2,5 nm telle que BA2 devrait avoir, en moyenne, un seul émetteur par NP. Un tel contenu rend ces objets comparables aux complexes moléculaires upconverting décrits dans la référence 30, comblant le fossé qui sépare ces deux domaines (complexes moléculaires et nanoparticules inorganiques).

Cela pourrait avoir un impact sur la photophysique pour notre objectif de super-résolution. Si les NP sont réellement constituées d'un seul émetteur, elles pourraient probablement clignoter sans couplage avec un obturateur externe. D'autre part, l'imagerie d'une seule NP deviendra alors difficile, car pour un émetteur ayant une longue durée de vie, des expériences de longue durée seront nécessaires pour obtenir suffisamment de photons pour une analyse précise.

- Commencer à élaborer un modèle cinétique:

Sur la base de données provenant du recoupement de constantes de vitesse provenant de la littérature, nous avons pu construire les premières étapes d'un modèle cinétique à 9 niveaux afin d'expliquer la redistribution de l'énergie au sein d'un UCNP. Les données accumulées sur la durée de vie seront mises en œuvre pour intégrer des constantes plus réalistes de nos objets. Même si des simulations préliminaires montrent que le déclin de luminescence peut être reproduit en termes de forme, elles ne sont pas précises pour le moment. Une fois que le modèle final sera établi, il pourrait également être utilisé pour simuler le comportement non linéaire (graphes log-log).

IV Résumé du chapitre IV: Nanohybride upconverting vers l'imagerie super-résolue

Par rapport aux spécifications techniques initiales, nous avons choisi de travailler avec le couple UCNP «émetteur bleu» dopé au Tm et le spiropyrane T-négatif de couleur orange absorbant la lumière bleue.

La structure du colorant a été ajustée afin d'avoir un substituant en para du phénol avec une valeur sigma de Hammett proche de celle de l'hydrogène afin de maximiser le recouvrement spectral. Ainsi, il repose sur l'utilisation de groupes aminés faiblement donneurs. Cet abaissement du comportement «donneur d'électrons» a été obtenu soit par greffage de triazine (par substitution nucléophile), soit d'acide carboxylique (par liaison amide). Effectivement, les spectres d'absorption ont été décalés vers la zone d'intérêt, dans un solvant natif (EtOH pour BIPS-TC1₂, DMF pour BIPS-P₁₁, intermédiaire). Cependant, dans les deux cas, lorsque le colorant est placé dans l'eau, l'absorption est renvoyée à la longueur d'onde inférieure en raison du solvatochromisme. En conséquence, le chevauchement se produit principalement avec la bande d'émission Tm à 450 nm, tandis que celle à 475 nm semble mal utilisable dû au faible recouvrement. Des problèmes de purification et de manque de comportement photochromique effectif pour BIPS-TC1₂ nous ont obligés à abandonner cette voie, malgré l'attrait de la post-fonctionnalisation sélective de la triazine.

Concernant la voie amide, nous avons d'abord conçu un ligand court en couplant l'amino-BIPS à l'anhydride glutarique. Ce composé modèle était crucial car il nous permet de déterminer le coefficient d'absorption molaire d'un nouveau type de colorant. Ensuite, nous pourrions explorer et valider son comportement photochrome. Sur la base de cette première paramétrisation, nous pourrions ensuite améliorer le procédé pour former un polymère réactif portant SP via une liaison amide et explorer la photochimie. Nous avons d'abord décidé de travailler avec une faible teneur en colorant afin d'éviter tout problème de π -stacking dans

le polymère. Afin d'améliorer le comportement hydrophile, cette plate-forme à base de polymère réactif a été entièrement fonctionnalisée par de courtes molécules hydrophiles, la D-glucamine.

Ce polymère à faible teneur en colorant, P_{1,38}, a conservé remarquablement le même comportement que le composé modèle BIPS-GLT.

Ensuite, le nanohybride a été construit selon la méthode la plus simple, un mélange direct de P_{1,38} et d'UCNP nu. Cependant, la formation réelle d'une telle architecture nanohybride n'a pas été complètement démontrée par la méthode analytique.

Malgré les risques de modifications du comportement photochimique du colorant en raison de l'encombrement stérique accru une fois le polymère ancré à la surface du NP, les observations étaient à nouveau identiques.

Le colorant choisi affiche le photochromisme négatif souhaité lorsque la forme MCH⁺ est présente. Cela implique que le nanohybride clignote pendant une fenêtre de pH définie compatible avec la spéciation du colorant. C'est-à-dire dans un milieu acide mais proche de la neutralité (valeur de pH de 5 à 7). Bien qu'apparemment restrictive, cette contrainte permettra d'introduire un autre paramètre de discrimination en combinant les propriétés de détection et de super-résolution. Par exemple, on s'attend à davantage de fluctuations dans les compartiments acides tels que les cellules tumorales ou les lysosomes.

Par conséquent, sachant que le colorant est toujours photochrome, nous avons porté notre attention sur la faisabilité d'une telle photoisomérisation du colorant induite par l'émission bleu d'UCNP sous excitation proche infrarouge (976 nm). Malheureusement, par simple suivi cinétique en solution avec un spectrophotomètre UV-visible standard, aucun changement n'a été détecté. Ce phénomène peut avoir deux origines:

- L'émission d'UCNP est trop faible dans l'eau pour pouvoir induire efficacement l'isomérisation du colorant ;

- La photo-commutation induite par l'émission UCNP fonctionne, mais elle se déroule comme prévu pour l'application BLINK: au niveau macroscopique, aucune fluctuation de la lumière n'est observable, mais à l'échelle d'une nanoparticule unique, il existe une fluctuation d'intensité due à la variation locale d'état d'isomérisation de colorant(s) à la surface d'une nanoparticule.

Des études complémentaires telles que l'observation en particule unique avec le microscope confocal mis en place au LASIR devraient explorer cette voie.

À ce stade, nous sommes encore loin du succès. Néanmoins, nous avons mis au point une stratégie pour préparer une architecture nanohybride basée sur l'interaction électrostatique d'un polymère anionique soluble dans l'eau et d'une nanoparticule "nue". L'utilisation d'un polyanhydride disponible dans le commerce conduit à l'introduction simultanée d'un groupe fonctionnel et d'un groupe chargé. Ainsi, un nanohybride multifonctionnel peut être conçu de manière très simple. Nous avons également montré qu'il était possible de greffer des unités T-photochromes négatives compatibles avec l'eau sur un tel polymère. Après mélange du polymère photochrome avec des UCNP nues, un matériau hybride a été isolé dans lequel le colorant conserve son comportement photochrome. Cependant, nous n'avons pas encore été en mesure de caractériser l'architecture nanohybride des objets et, plus important encore, de démontrer sans ambiguïté que le flux de photons réémis par les UCNP était suffisant pour induire une photo-commutation de colorant détectable. Cependant, même si l'UCNP n'est pas capable d'induire l'isomérisation du colorant, cela peut être réalisé grâce à l'utilisation d'une seconde excitation externe.

V Guide de lecture pour le suivi du chapitre 3

Summary of samples presented in chapter 3 (table 1).

(BA1 & BA4), (BA2 & BA5), (BA3 & BA7), (BA 11 & BA12), (BA13 & BA14), (BA15 & BA16) are respective pairs of core and core@shell originating from the same core.

Shape	Batch code	Core Na(Gd-Yb)F ₄ :Tm			shell	Size (diameter)
		%Gd	%Yb	%Tm		
Ultrasmall spheres	BA1	79	20	1	-	2.5 nm
	BA2	42	57	1	-	2.8 nm
	BA3	42	57	1	-	3.2 nm
	BA4	79	20	1	NaGdF ₄	5.5 nm
	BA5	42	57	1	NaGdF ₄	5.5 nm
	BA6	79	20	1	NaGdF ₄	5.7 nm
	BA7	42	57	1	NaGdF ₄	5.7 nm
	BA17	42	57	1	NaGdF ₄	5.5 nm
Small spheres	BA8	79	20	1	-	7.5 nm
	BA9	79	20	1	-	7.5 nm
	BA10	42	57	1	-	15 nm
	BA11	42	57	1	-	10 nm
	BA12	42	57	1	NaYF ₄	15 nm
	BA13	42	57	1	-	10 nm
	BA14	42	57	1	NaYF ₄	15 nm
	BA15	42	57	1	-	9.3 nm
	BA16	42	57	1	NaYF ₄	10.2 nm

Lanthanide-based Upconverting nanoparticles (UCNPs) show the fascinating property of converting low energy NIR photons into higher energy ones without requiring high laser fluences. This unique large anti-Stokes shift affords a higher signal-to-noise ratio than standard luminescent compounds. Associated to their photostability (non-blinking, non-bleaching), their size-independent emission spectrum and a limited toxicity, these inorganic materials have become an interesting tool in Biology besides Quantum Dots, especially for Bioimaging. However, the overall emission plummets sharply when the size is reduced. Therefore, efficient ultrasmall UCNPs are still challenging to obtain.

The present work is dedicated to the design of innovative nanohybrid structures based on NaREF₄ with ultrasmall sizes, in order to go towards super-resolution microscopy. Investigations were focused on three main issues.

At first, we will describe how a size reduction from 10-20 nm to sub-5 nm UCNP can be envisioned. An appropriate composition choice, coupled to an improvement of the common thermal coprecipitation pathway was setup. Especially, we have shown the importance of the conjunction of a mixing strategy for the primo-precipitation and accurate monitoring of the high temperature step. Here, the use of microwave-assisted synthesis was found to be crucial for a precise control of the Ostwald ripening through an original cycling heating.

Then, the photophysics of a library of different UCNPs were assessed in order to understand the complex energy redistribution within an NP, using different setups, home-made or thanks to collaborative work in specialized laboratories in Berlin or Lille. From these observations, the use of classic emission quantifiers was found to be inefficient and a first step towards a relevant kinetic model was initiated.

Eventually, nanohybrids based on a photochromic hydrophilic polymer have been elaborated. Selection of the appropriate dye, and preliminary exploration of the photokinetic properties of the polymer have been undertaken. This approach, coupling our ultrastable nanolamp to a photochromic shutter, is aimed at developing an innovative stochastic method to compete with the recent successes of the use of UCNPs for super-resolution via a STED approach.

Les nanoparticules Upconverting (UCNP) à base de lanthanides possèdent la propriété fascinante d'être capables de convertir des photons infrarouges en photons de plus haute énergie sans recourir à des fluences de laser élevées. Ce décalage Anti-Stokes conduit à rapport signal sur bruit meilleur que pour la luminescence classique. Associé à leur photostabilité (non clignotantes, non photolysables), un spectre d'émission indépendant de leur taille, une faible toxicité, ces matériaux inorganiques sont devenus un outil de choix en biologie, en particulier en imagerie biologique, à côté des Quantum Dots. Cependant, l'émission globale s'effondre rapidement quand la taille des UCNP est réduite. En conséquence la réalisation de particules ultra petites et efficaces reste un défi.

Le présent mémoire s'intéresse au design de structures nanohybrides fondées sur des particules ultra petites de NaREF_4 , avec pour objectif la microscopie super-résolue. Le travail s'est organisé en trois phases.

Tout d'abord nous avons étudié la réduction en taille des UCNP de 10-20 nm à moins de 5 nm, en se focalisant sur leur composition et l'amélioration du procédé de synthèse. En particulier nous avons montré l'importance de la conjonction du processus de mélange avec la conduite de l'étape à haute température. Pour cette dernière l'emploi du chauffage micro-onde, avec un cyclage en température original a permis de contrôler efficacement le mûrissement d'Ostwald.

La librairie de particules ainsi construite a permis d'étudier la photophysique des processus de redistribution de l'énergie au sein des particules sur des montages « maison » ou des équipements dédiés grâce à des collaborations avec des équipes de Berlin ou Lille. Il en ressort que les quantificateurs usuels de luminescence sont inadéquats pour décrire le phénomène d'upconversion. Aussi avons-nous débuté l'élaboration d'un modèle cinétique approprié.

Enfin, la construction de nanohybrides impliquant un polymère photochrome hydrophile a été explorée. La sélection du colorant approprié et les premières études photocinétiques ont été menées. Cette approche couplant nos « nanolampes » avec un « volet photochrome » a pour but de proposer une alternative innovante au développement de la super-résolution par STED.
